SCUOLA
NORMALE
SUPERIORE

Classe di Scienze

Corso di perfezionamento in **Astrochimica**

XXXIV ciclo

Computational development of models and tools for the kinetic study of astrochemical gas-phase reactions

Settore Scientifico Disciplinare CHIM/02

Candidato:

Dr. Bernardo Ballotta

Supervisione interna:

Prof. Vincenzo Barone

Relatori:

Prof. Emilio Martínez-Núñez

Dr. Sergio Rampino

ANNO ACCADEMICO 2022/2023

Acknowledgments

I wish to thank my supervisor Professor Vincenzo Barone of the Scuola Normale Superiore, my co-supervisors Dr. Sergio Rampino of the University of Padua and Professor Emilio Martínez-Núñez of the University of Santiago de Compostela, for guiding, encouraging and assisting me during these years and for providing me with all the necessary tools to carry out my research project.
I am very grateful to the technical staff of the Avogadro HPC center for all the technical assistance without which it would not have been possible to carry on my project.
I thank all the staff of the Scuola Normale Superiore services for constantly guaranteeing everyone to work in the best possible way.
I sincerely thank my fellow PhD students for the laughs they gave me and for introducing me to even just a small part of their world, which is now mine too.
Finally, I thank my loving family for always being there despite the difficulties.
I never wanted anything different, thank you.

Computational development of models and tools for the kinetic study of astrochemical reactions

PhD candidate: Bernardo Ballotta

Abstract

This PhD thesis focuses on the application and development of computational tools and methodologies for the modeling of the kinetics of gas-phase reactions of astrophysical interest in the interstellar medium (ISM). The complexity related to the investigation of chemical reactivity in space is mostly due to the extreme physical conditions of temperature, pressure and exposure to high-energy radiation, which in turn also lead to the formation of exotic species, like radicals and ions. Nevertheless, there is still much to be understood about the formation of molecules, the major issue being the lack of sufficient laboratory (experimental and computational) studies. A more detailed and accurate study of all the chemical processes occurring in the ISM will allow us to obtain the data necessary to simulate the chemical evolution of an interstellar cloud over time using kinetic models including thousands of reactions that involve hundreds of species. The collection of the kinetic parameters required for the relevant reactions has led to the growth of different astrochemical databases, such as KIDA and UMIST. However, the data gathered in these catalogues are incomplete, and rely extensively on crude estimations and extrapolations. These rates are of paramount importance to get a better comprehension of the relative abundances of the chemical compounds extrapolated by the astronomers from the spectral data recorded through the radio telescopes and the in-orbit devices, like the satellites. Accurate state-of-the-art computational approaches play a fundamental role in analyzing feasible reaction mechanisms and in accurately predicting the associated kinetics. Such approaches usually rely on chemical intuition where a by-hand search of the most likely pathways is performed. Unfortunately, this procedure can lead to overlook significant mechanisms, especially when large molecular systems are investigated. Increasing the size of a molecule can also increase the number of its possible conformers which can show a different chemical reactivity with respect to the same chemical partner. This brings to get very complex chemical reaction networks in which hundreds of chemical species are involved and thousands of chemical reactions can occur. During the last decades, a lot of effort has been done to develop computational techniques able to perform extensive and thorough investigations of complex reaction mechanisms. Such approaches rely on automated computational protocols which drastically decrease the risk of making blunders during the search for significant reaction pathways. Furthermore, the accurate characterization of the potential energy surfaces (PESs) critical points, like reactants, intermediates, transition states and products involved in the reaction mechanism, is crucial in order to carry out a reliable kinetic investigation. The kinetic analysis of an erroneous potential energy surface, would lead to gross errors in the estimation of the rate constants of the chemical species involved in the reaction. In order to avoid such errors, the combination of high-level electronic structure calculations via composite scheme can be helpful to get a more precise estimation of the energy barriers involved in the reaction mecha-

nism. It has been proven that "cheap"[1] composite schemes can achieve subchemical accuracy without any empirical parameters and with convenient computation times, making them perfect for the purpose of this thesis. In recent decades, many efforts have been made to develop theoretical and computational methodologies to perform accurate numerical simulations of the kinetics of such complex reaction mechanisms in a wide range of thermodynamic conditions that mimic extreme reaction environments as for combustion systems, the atmosphere and the ISM. Such methodologies are based on the ab initio-transition-state-theory-based master equation approach, which allows the determination of rate coefficients and branching ratios of chemical species involved in complex chemical reactions. This methodology allows to make accurate predictions of the relative abundances of the reaction products for complex reactions even under conditions of temperature and pressure not experimentally accessible, such as those that characterize the ISM. Based on these premises, this dissertation has been focused on the application of a computational protocol for the ab initio-based computational modeling and kinetic investigation of gas-phase reactions which can occur in the ISM. This protocol is based on the application of validated methodologies for the automated discovery of complex reaction mechanisms by means of the AutoMeKin[2] program, the accurate calculation of the energetic of the potential energy surfaces (PESs) through the junChS and junChS-F12a "cheap" composite schemes and the kinetic investigation using the StarRate computer program specifically designed to study gas-phase reactions of astrochemical interest in conjunction with the MESS program. Furthermore, this dissertation has been also focused on the development and implementation of StarRate, a computer program for the accurate calculation of kinetics through a chemical master equation approach of multi-step chemical reactions. StarRate is an object-based program written in the so-called F language. It is structured in three main modules, namely `molecules`, `steps` and `reactions`, which extract the properties needed to calculate the kinetics for the single-step reactions partecipating in the overall reaction. Another module, `in_out`, handles program's input and output operations. The main program, `starrate`, controls the sequences of the calling of the procedures contained in each of the three main modules. Through these modular structure, StarRate[3] can compute canonical and microcanonical rate coefficients taking into account for the tunneling effect and the energy-dependent and time-dependent evolution of the species concentrations involved in the reaction mechanism. Such protocol has been applied to investigate the formation reaction mechanisms of some complex interstellar polyatomic molecules, named interstellar complex organic molecules (iCOMs). More specifically, the formation of prebiotic iCOMs in space has raised considerable interest in the scientific community, because they are considered as precursors of more complex biological systems involved in the origin of life in the Universe. Debate on the origins of these biomolecular building blocks has been further stimulated by the discovery of nucleobases and amino acids in meteorites and other extraterrestrial sources. However, few insights on the chemistry which brings to the formation of such compounds is known.

Publications

Main author

1. B. Ballotta, T. D. Marforio, S. Rampino, V. Barone, A. Bottoni, E. Martínez-Núñez, L. Dore. Toward the detection of cyanoketene in the interstellar medium: new hints from quantum chemistry and rotational spectroscopy. *ACS Earth and Space.* 2023.

2. B. Ballotta, S. Rampino, E. Martínez-Núñez, V. Barone. Competition between abstraction and addition channels for the reaction between the OH radical and vinyl alcohol in the interstellar medium. *ACS Earth and Space.* 2023. **Submitted**

3. G. Nottoli, B. Ballotta, and S. Rampino. Local charge-displacement analysis. Targeting local charge-flows in complex intermolecular interactions. *J. Chem. Phys.*, 157, 084107, 2022.

4. B. Ballotta, S. Nandi, V. Barone and S. Rampino. Gas-Phase Formation and Isomerization Reactions of Cyanoacetaldehyde, a Prebiotic Molecule of Astrochemical Interest. *ACS Earth and Space.*, 5, 5, 1071-1082, 2021.

Co-author

1. S. Nandi, B. Ballotta, S. Rampino and V. Barone. A General User-Friendly Tool for Kinetic Calculations of Multi-Step Reactions within the Virtual Multifrequency Spectrometer Project. *Appl. Sci.*, 10(5), 1872, 2020.

This page would be intentionally left blank.

Contents

This page would be intentionally left blank.

List of Figures

List of Tables

List of Acronyms

ae	all electrons
AITSTME	Ab Initio Transition State based Master Equation approach
AMK	AutoMeKin
ASTRID	Aarhus STorage Ring
BBFS	Bond Breakage/Formation Search
CBS	Complete Basis Set
CC	Coupled Cluster
CM	Capture Model
COM	Complex Organic Molecule
CRESU	Cinétique de Réaction de Ecoulement Supersonique Uniforme
CSE	Chemical Significant Eigenvalue
CT	Capture Theory
CV	Core Valance
DFT	Density Functional Theory
DOS	Density Of States
DR	Dissociative Recombination
EC	Electron Correlation
EGME	Energy Grained Master Equation
Et	(Z) 1,2-Ethendiol
fc	frozen core
FCI	Full Configuration Interaction
GGA	Generalized Gradient Approximation
GMC	Giant Molecular Cloud
GUI	Graphical User Interface
HF	Hartree-Fock
HL	High Level
iCOM	interstellar Complex Organic Molecule
IEIE	Internal Energy Relaxation Eigenvalues
IR	Infrared
IRC	Intrinsic Reaction Coordinate
ISM	Interstellar Medium
KIDA	Kinetic Database for Astrochemistry
KMC	Kinetic Monte Carlo
LDA	Locked-Dipole Approximation
LL	Low Level
LSDA	Local Spin Density Approximation
MCTDH	Multi-Configuration Time-Dependent Hartree
MEP	Minimum Energy Path
MD	Molecular Dynamics
MP	Møller-Plesset
NMS	Normal Mode Sampling

ODE	Ordinary Differential Equation
PES	Potentail Energy Surface
PST	Phase Space Theory
QCT	Quasi-Classical Trajectory
RHF	Restricted Hartree Fock
RMS	Root Mean Square Error
ROHF	Restricted Open Shell Hartree-Fock
RP	Reaction Pathway
RPMD	Ring Polymer Molecular Dynamics
RRKM	Rice-Ramsperger-Kassell-Marcus theory
SCT	Small Curvature Tunneling
SED	Spectral Energy Distribution
SFP	Star Formation Process
Sgr B2	Sagittarius B2
SOS	Sum Of States
TS	Transition State
TSR	Test Storage Ring
TSSCDS	Transition State Search using Chemical Dynamics Simulations
TST	Transition State Theory
UHF	Unrestricted Hartree-Fock
VTST	Variational Transition State Theory
VMS	Virtual Multifrequency Spectrometer
Vy	Vinyl alcohol
WKB	Wentzel-Kramers-Brillouin
YSO	Young Stellar Objects
ZCT	Zero Curvature Tunneling
ZPE	Zero Point Energy

This page would be intentionally left blank.

Introduction

In the past, the idea that the interstellar medium (ISM) was a too hostile environment to host complex molecules was well established in the scientific community [4]. However, with technological progress and the construction of ever more accurate detection instruments, such as radio telescopes and satellites, it has been possible to identify emission and absorption signals traceable to organic molecules and to extrapolate the cosmic abundances of the chemical elements in the ISM with the aid of spectroscopy[5, 6]. Despite the low relative elementary abundances reported in table 1, in which the abundance of carbon, oxygen, and nitrogen is lower than that of hydrogen by factors of 10^{3-4} and that of heavier elements is lower by even greater factors[7], the formation of more complex molecular systems is possible even in the extreme thermodynamic conditions of the ISM.

Element	Relative abundance	Element	Relative abundance
H	1.00E0	Si	3.24E-05
He	8.51E-02	P	2.57E-07
Li	1.12E-11	S	1.32E-05
Be	2.40E-11	Cl	3.16E-07
B	5.01E-10	Ar	2.51E-06
C	2.69E-03	K	1.07E-07
N	6.76E-05	Ca	2.19E-06
O	4.90E-04	Sc	1.41E-09
F	3.63E-08	Ti	8.91E-08
Ne	8.51E-05	V	8.51E-09
Na	1.74E-06	Cr	4.37E-07
Mg	3.98E-05	Mn	2.69E-07
Al	2.82E-06	Fe	3.16E-05

Note: this table has been taken from the book Introduction to Astrochemistry [8] by S. Yamamoto.

Table 1: Cosmic abundance of elements

Over the years, astronomical observations have allowed the identification of many molecular species of different kinds in the ISM, from simple diatomics to much more complex polyatomic molecules, such as fullerenes and polyaromatic compounds. The

current practice is to call interstellar complex organic molecules (iCOMs) all the species formed by more than six atoms and including carbon. Currently, more than 200 molecules have been identified and collected in the CDMS (The Cologne Database for Molecular Spectroscopy [9, 10, 11]) and about four new molecules are identified each year as reported by McGuire in the census of the astrochemical molecules [12]. Figure 1 shows the cumulative number of interstellar molecules detected in the last 50 years together with the dates of the contributing facilities. It is apparent how the number of identifications subsequent to the birth of radio astronomy which took place around 1960 has considerably increased.

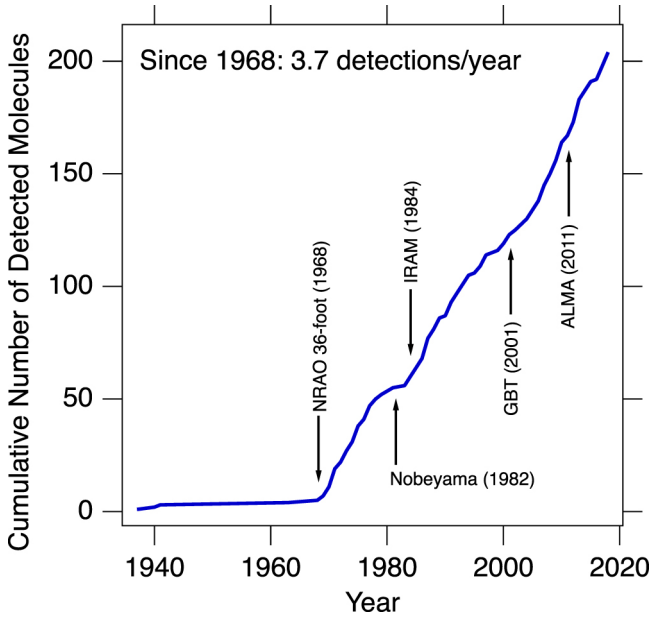

Figure 1: Cumulative number of known interstellar molecules over time.

Note: this plot has been taken from the paper [12] by B. McGuire.

The next sections are devoted to:

- a detailed description of the astrophysical context and the thermodynamic conditions in which iCOMs have been identified;
- a general description of the interstellar chemistry, in particular the two main environments in which chemical reactions can occurr in the ISM, namely gas-phase and grain surfaces;
- a general description and the main limitations of the experimental techniques available for the study of such reactions;
- a detailed description of the main computational techniques used to study the reaction mechanisms and the kinetics that lead to the iCOMs formation or destruction.

The Astrophysical Context

The Interstellar Medium and the Star Formation Process

The ISM is the region between the stars that contains large agglomeration of gas and tiny solid particles, called grains, with a very low typical density of H_2 (or H) of 10-100 cm^{-3} and a very low temperature of 10-100 K. It is approximately composed for the 99% of interstellar gas, and of its mass, about 75% is in the form of hydrogen, either molecular or atomic, with the remaining 25% as helium. Only a small amount of this matter, less than 1%, is composed of heavier elements, like C, N, O, called metals by astronomers.
The interstellar gas, also called nebulaes, consists partially of neutral atoms and molecules, as well as charged particles, such as ions and electrons.
These nebulaes are called diffuse molecular clouds and they are formed from the stellar ejecta under the influence of the gravity.
Although the detailed nature of these astrophysical objects is still only partially understood, even for the relatively close ones that belong to our own galaxy, they represent the starting point of the star formation process (SFP) graphically schematized in figure 2 [13].

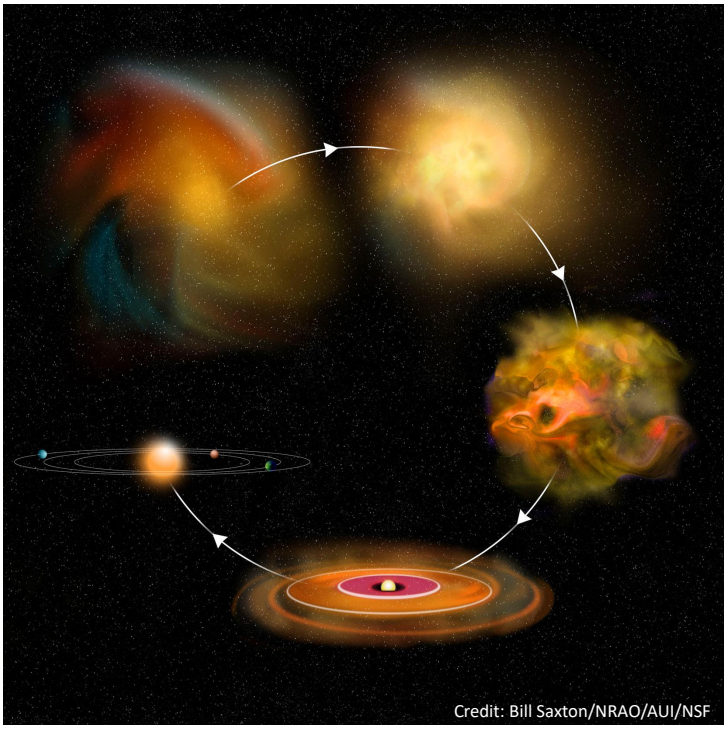

Figure 2: Graphical representation of the SFP.

Inspection of figure 2 shows how the relationship between stars and interstellar matter is cyclical because, as the clouds evolve, portions of them collapse to form new generations of stars with considerable portions of non-hydrogen matter in their outer regions. This

matter eventually finds its way into interstellar space because older stars release much of their matter either explosively, as in supernovae, or more gently. During SFP, star cores heat stellar matter by exothermic nuclear fusion reactions that produce elements more complex than hydrogen. Some chemical reactions and condensation into dust particles can therefore occur in relatively cold stellar atmospheres, especially as stars age. The matter emanating from these older stars contains atoms, molecules, and tiny dust particles composed of silicates or carbon. The harsh radiation field in interstellar space rapidly dissociates most of the molecules formed in stellar atmospheres, and the material leading to new generations of interstellar clouds becomes primarily atomic and particle in nature, although any very large molecules formed in stars can survive relatively unscathed.
The gravitational collapse of the diffuse clouds into dense clouds is considered to be the first stage of the SFP where temperature and density start to increase. More chemically important are dense clouds, where the gas density rises to 10^4 cm^{-3} and the temperature plunges to 10 K, for both gas and dust.
Note that the density of so-called dense clouds is only relatively high; on an absolute scale it is much lower than the lowest pressure reachable in laboratory. Here the hydrogen is overwhelmingly molecular in nature, and many polyatomic molecules can be detected. During this initial stage of the SFP, the formation of pre-stellar cores which will give rise to proto-stars occurs. At the very low temperature that characterizes pre-stellar cores (around 10 K) the atoms and molecules present in the gaseous phase freeze on the surfaces of the dust grains. During this phase and under these thermodynamic conditions, the hydrogenation reactions of the atoms and molecules frozen on the surface of the grain take place, which lead to the formation of frozen mantles mainly composed of water. However, even more complex species, such as iCOMs, have been detected in the pre-stellar regions. These molecules are supposed to have formed through gas phase reactions because at the very low temperatures of pre-stellar cores no gas-grain reaction could occur, only hydrogenation reactions, yet those molecules could not be released into the gas phase unless through non-thermal desorption processes.
Pre-stellar cores are involved in the SFP schematized by the 4 different stages shown in the Shu diagram shown in figure 2. Each stage has distinct observational characteristics corresponding to different ways in which the radiation is emitted by the source. The shape of the spectrum is generally called Spectral Energy Distribution (SED).

During the first phase (**Class 0**) a central proto-star and disk has formed, within a still infalling envelope of dust and gas. The temperature can reach 100 K provoking the sublimation of the grain icy mantles. The dust heated by the stellar radiation produces an emission spectrum, particularly bright in the infrared wavelength range. In these objects many iCOMs have been identified, however their synthesis is still debated. One possibility is that as the envelope heats up, atoms and radicals that had previously formed and frozen on the mantle acquire mobility and react on their surfaces to form iCOMs. At about 100 K the whole mantle sublimes, injecting the formed iCOMs into the gaseous phase. The other possibility envisaged by theoretical chemistry studies considers the formation of simple molecules, like radicals and ions, onto the grain surface formed during the pre-stellar phase and then injected into the gas phase at 100 K

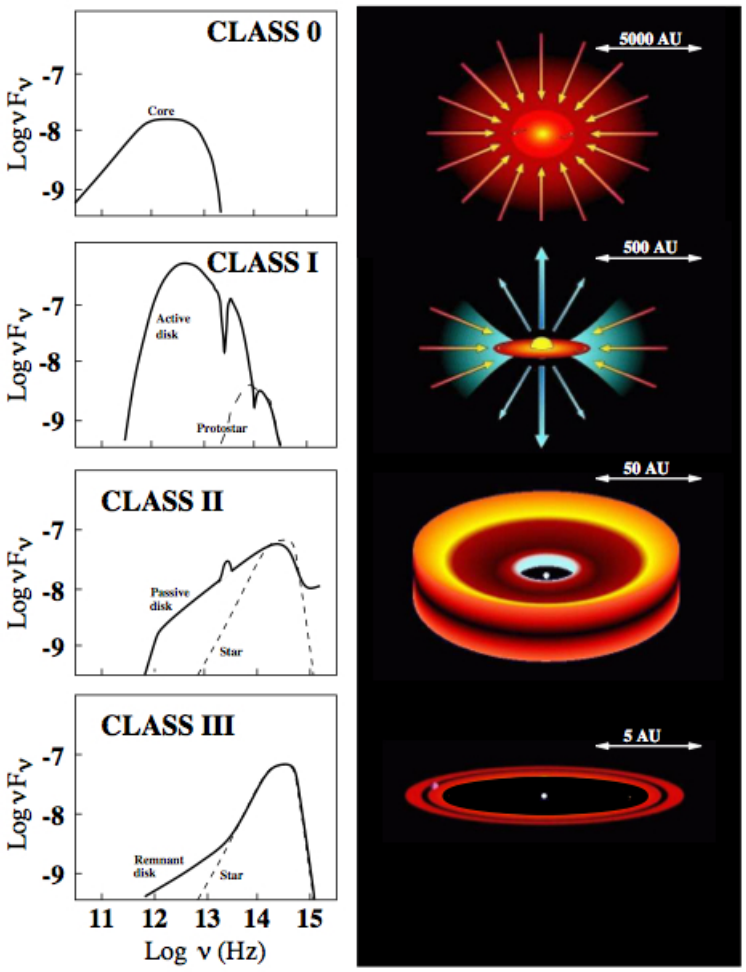

Figure 3: Illustration of the four classes of proto-stellar systems.

in which they can react to form iCOMs. This objects are also called hot corinos.
The second phase (**Class I**) is characterized by the fact that the protostar accretes material through the disk. At the same time, stellar wind (made of radiation and particles) is escaping along the rotational axis breaking the disk above and below, thus creating a bi-polar outflow. During this stage, the SED moves towards higher frequency with respect to the phase I and presents absorption features due to radiation absorbed by the disk material. Unfortunately very little is known about iCOMs in these regions.
In the third phase (**Class II**) the surrounding material has been blown away, leaving the protoplanetary material disk that will harbor the planet formation. The SED is peaked at still higher frequencies, being increasingly hotter. In this phase most of the radiation emitted by the star can escape from the disk.
In the final fourth phase of star formation (**Class III**) the star in the center has become a pre-main sequence star, now ready to burn hydrogen. The gaseous component of the disk has been now largely dispersed or accreted. A substantial amount of dust remains forming a debris disk of planetesimals and protoplanets. In this final stage of the star formation process the emerging SED is dominated by the radiation of the

star, though there is still a tail in the IR due to the remaining dust. Unfortunately also for **Class II** and **Class III** few iCOMs have been identified, and few information have been acquired so farabout their column densities and relative abundances.[14]

So, hot molecular cores and hot corinos are considered the precursors of high-mass and low-mass young stellar objects (YSOs), respectively.
They are both characterized for being strong emitters of high-energy rotational lines of rare molecular species at mm and sub-mm wavelengths.
They will determine the chemical richness of star-forming regions in the galaxy, which, as previously mentioned, are the main tracers of the spiral structure of our galaxy. Then, it is crucial to detect and study iCOMs in hot cores and hot corinos, which allows to obtain a better understanding of chemical processes that are taking place on them and to better comprehend the chemical compositions of the spiral structure of the galaxy.
For these reasons, it is crucial to increase the number of detections of COMs in high- and low-mass star–forming regions during the latest phases of star formation. The paradigmatic example is the giant molecular cloud (GMC) Sagittarius B2 (Sgr B2) located about 120 parsecs from the center of the Milky Way. This GMC is the largest molecular cloud in the vicinity of the core and one of the largest in the galaxy, spanning a region about 45 parsecs across. The total mass of Sgr B2 is about 3 million times the mass of the Sun. The mean hydrogen density within the cloud is 3000 atoms per cm^{-3}, which is about 20–40 times denser than a typical molecular cloud.

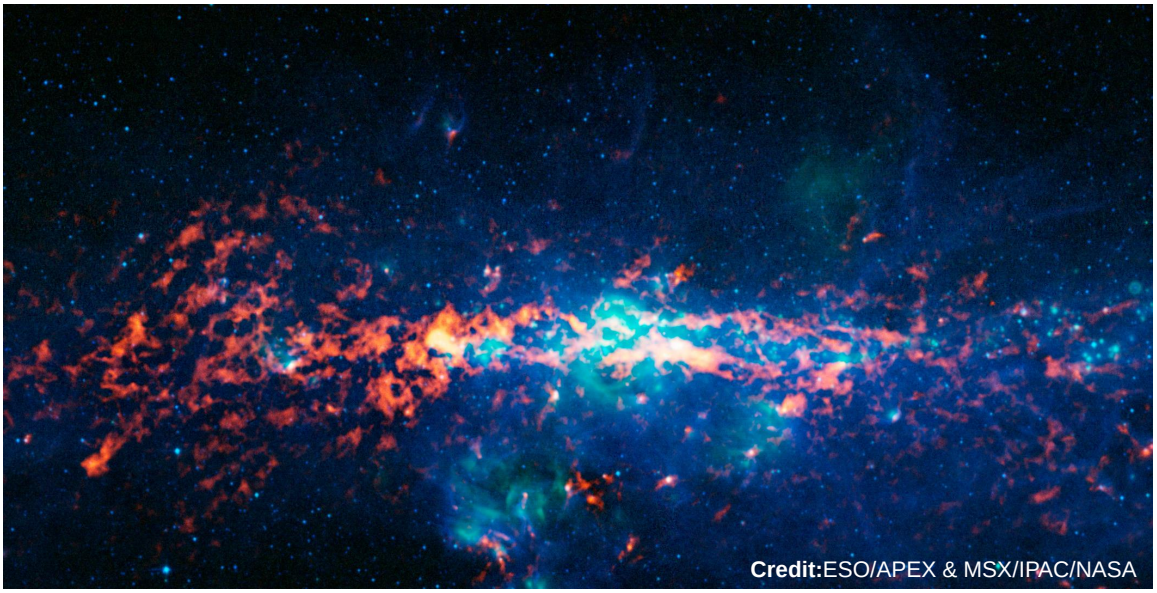

Figure 4: Sgr B2 seen by ATLASGAL, Chile.

Figure 4 shows a colour-composite image of the Galactic Centre and Sgr B2. The internal structure of this cloud is complex, with varying densities and temperatures. The cloud is divided into three main cores, designated north (N), middle or main (M)

and south (S) respectively. Thanks to these characteristics and to the proximity to the detection systems developed in the last decades, Sgr B2 is one of the most studied molecular clouds as regards the chemistry that characterizes it. In fact, in recent decades more than 100 molecular species have been identified within its cores.[15] Various kinds of COMs, like alcohols, esters and alkyl cyanides, have been detected. Recent analyses carried out by Brett McGuire showed that a high percentage of the organic molecules identified in the ISM were detected in star-forming regions. Figure 5 displays the percentage of interstellar molecules that were detected in each source type.

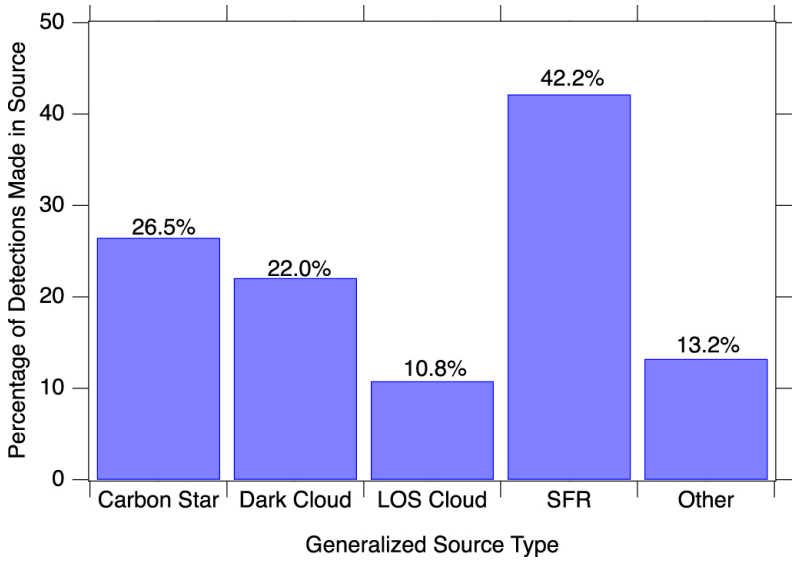

Figure 5: Percentage of known molecules detected in carbon stars, dark clouds, LOS clouds, and SFRs.

Note: this plot has been taken from the article [12] by B. McGuire.

These regions of the ISM have aroused considerable interest due to the numerous detections of iCOMs, considered as precursors of more complex prebiotic molecules involved in the origin of life in the Universe, e.g., these include amino acids (the building blocks of proteins), nucleobases (the building blocks of the genetic material), sugars and their derivatives (which play several roles, from the building blocks of DNA, RNA, and cell walls, to energy storage), amphiphiles (the building blocks of cell membranes), and several other families of organic compounds. The investigation of how the synthesis of iCOMs occurs in the harsh and extremely diversified conditions of the ISM is a pivotal challenge in the astrochemistry research field. Considerable efforts, both from an experimental and a computational point of view, have been made to understand through which chemical processes this category of molecules can be formed given the extreme conditions of the ISM.[16, 17]

Interstellar Chemistry

Because of the granular and gaseous nature of the ISM, the chemical processes that can occur are generally classified as: gas-phase and gas-grain processes. At very low densities, only binary ion-molecule or neutral-neutral gas-phase reactions can occur, they must be exothermic because of the very low temperatures with nearly-vanishing activation energies. The stabilization induced by the thermal bath is not possible because of the very low pressures, so, in the gas-phase the excess kinetic energy provided by the collision of the reactants has to be released after the formation of the dissociation products as vibrational energy, or through radiative emission stabilization which imply photons emission. The situation is different for gas-grain reactions, due to the 'third body stabilization' induced by the surface of the grain. Neutral-neutral reactions are possible even under these extreme conditions only if highly reactive chemical species (e.g., radicals) are involved. Three-body reactions only become significant at number densities above 10^{13} cm^{-3} such as those encountered in the atmospheres of stars and exoplanets. [18] Radiation-matter interaction can play a central role in the formation and destruction processes of molecules. Table 2 contains a list of the identified possible processes occurring in the ISM.
To obtain a reliable chemical model for very complex reactive systems such as molecular clouds, it is necessary to determine accurate reaction coefficients characterizing each individual reaction. So, due to the wide variety of conditions characterizing the ISM, also a large variety of chemical reactions can take place.[19]

Type of process	**Example**
Gas-grain interactions	$H + H + grain \rightarrow H_2 + grain$
Direct cosmic ray processes	$H_2 + \zeta \rightarrow H_2^+ + e^-$
Cation-neutral reactions	$H_2^+ + H_2 \rightarrow H_3^+ + H$
Anion-neutral	$C^- + NO \rightarrow CN^- + O$
Radiative associations (ion)	$C^+ + H_2 \rightarrow CH_2 + h\nu$
Associative detachment	$C^- + H_2 \rightarrow CH_2 + e^-$
Dissociative neutral attachment	$O + CH \rightarrow HCO^+ + e^-$
Neutral-neutral reactions	$C + C_2H_2 \rightarrow C_3H + H$
Radiative associations (neutral)	$C + H_2 \rightarrow C_2H_2 + h\nu$
Dissociative recombination	$N_2H^+ + e^- \rightarrow N_2 + H$
Radiative recombination	$H_2CO^+ + e^- \rightarrow H_2CO + h\nu$
Anion-cation recombination	$HCO^+ + H^- \rightarrow H_2 + CO$
Electron attachment	$H + e^- \rightarrow H^- + h\nu$
External Photo-processes	$C_3N + h\nu \rightarrow C_2 + CN$
Internal Photo-processes	$CO + h\nu \rightarrow C + O$

Table 2: List of chemical processes which can take place in the ISM.

Experimental limitations

The exotic nature of the chemical species involved in the afore mentioned reactions (e.g., radicals or ionic species), it is not always possible to perform suitable experiments to obtain reliable rate coefficients. Moreover experimental conditions are often too far from simulate the real conditions of the ISM. So, for these reasons, it is often necessary to rely on theoretical methods to determine accurate rate coefficients. Rate coefficients are of paramount importance to build chemical models to study the chemical evolution of the astrophysical objects. These models consist of a large number of rate equations; that is, ordinary differential equations (ODEs), each of one representing a given process to build-up or lessen the concentration of a particular chemical species. In time-dependent models, assumptions must be made concerning the starting conditions: the temperature, the chemical nature of the molecular species involved, like ionic, molecular or atomic, and the chemical abundances. Then the ODEs are integrated forward in time to generate molecular abundances at different ages of the cloud. There are at least two conditions that a successful model must respect: (i) it should include all those processes that are important in determining the molecular abundances, and (ii) the values of the rate coefficients included in the model should be accurate.[20] Various experimental techniques have been developed and employed to study the various types of reactions listed in table 2. For example, the CRESU (Cinétique de Réaction en Ecoulement Supersonique Uniforme) and ion trap techniques are used to study neutral-neutral and neutral-ion reactions at temperatures similar to those of cold cores. These techniques use mass spectrometry to measure changes in the concentrations of ionic reactants as well as the ionic products of the reaction. For neutral-neutral reactions, the CRESU technique with the Laval nozzle variant is often used to measure rate coefficients below 100 K, up to 13 K, but more generally 25 K.[21] Unfortunately, however, the pressures that this type of equipment can reach are still too high to simulate the conditions of the ISM. Dissociative recombination (DR) reactions are studied using several techniques like the storage ring and afterglow methods which both show merits and faults for the determination of the rate coefficients. The merged beam techniques employed at ASTRID (Aarhus, Denmark), TSR (Heidelberg, Germany) and CRYRING (Stockholm, Sweden) show limitations like the lack of control of the rotovibrational states of the product ions, which appear to have a different distribution with respect to temperatures relevant in the ISM[22] and the mass selection does not allow to separate the pairs of isomers and therefore to recognize them as different reaction products. The flowing afterglow method are carried out at room temperature and therefore, as discussed above, have limited validity for the ISM.[23] Furthermore, it is difficult to determine the branching ratios of a DR reaction, since rarely can all the product channels be quantified. Given the problems associated with experimental determinations of the branching ratios and rate coefficients of these reactions, a good alternative is to resort to predictions by high-quality ab initio calculations.

Computational approach

The simplest representation of chemical reactions requires that the most probable products are highlighted for a pair of reactants, without taking into account the reaction mechanism that leads to their formation as it can often lead to a high level of complication. The investigation of the energetics of the reactive PESs, *i.e.*, the thermochemistry, which contains a lot of information about the reaction mechanisms and all the reactive paths involved in a chemical reaction, is therefore fundamental to study the reactivity of the gas-phase reactions.[18] Therefore, accurate state-of-the-art computational approaches play a fundamental role in analyzing feasible reaction mechanisms. Such approaches usually rely on chemical intuition where a by-hand search of the more likely pathways is performed. Unfortunately, this procedure can lead to overlook significant mechanisms, especially when large molecular systems are investigated. Increasing the size of a molecule, also increases the number of its possible conformers, each of which can show a different chemical reactivity respect to the same chemical partner. This leads to very complex chemical reaction networks in which hundreds of chemical species are involved and thousands of chemical reactions can occur. The kinetic analysis of an erroneous potential energy surface, describing an incomplete chemical reaction scheme, would lead to gross errors in the estimation of the rate constants of the chemical species involved in the reaction. During the last decades, a considerable effort has been devoted to the development of computational techniques able to perform extensive and thorough investigations of complex reaction mechanisms. Such approaches rely on automated computational protocols, which drastically decrease the risk of making blunders during the search for significant reaction pathways. While the energetic characterization is a mandatory step to understand the possible routes open in the ISM, the definitive feasibility of the reaction paths under consideration is established by the rate at which they are expected to occur. The combined computational investigation of the thermochemistry and kinetics to study the chemical reactions relevant for the ISM and for which no experimental data are available is pivotal in astrochemistry to determine accurate rate coefficients. The computational protocols applied to carry out this kind of investigation start from a preliminary investigation of the reactive PES at relatively low computational level employing density functional theory (DFT) calculations for the identification of the chemical reaction pathways (RP) of interest. When all the RP have been computed, only those relevant at the ISM conditions are further computed at a higher level of theory in which improved energetics of each stationary point is determined. The accurate determination of the energetics is crucial to obtain reliable energy barriers along the RP which play a central role in the calculations of the reaction rates. It is of paramount importance to employ computational methodologies able to provide the chemical accuracy of the order of the kJ/mol in the determination of the energy barriers. So, it is necessary to rely on post-Hartree-Fock methods to recover the electron correlation (EC) energy which is essentially defined as the difference between the exact value of the Hamiltonian and its expectation value in the Hartree-Fock approximation for the state under consideration in the non relativistic approximation.[24] Several procedures have been developed to recover EC in order to compute accurate thermochemical data.[25, 26, 27] For small molecular systems,

like those of astrochemical interest, these procedures allow to obtain energetics close to the full configuration interaction (FCI) complete basis set (CBS) limit.[28] One of the most successful approaches is the extrapolated ab initio thermochemistry protocol also called HEAT protocol [29, 30, 31] for which a simplified version has been derived called CBS-CV based on the extrapolation to the CBS limit at the CCSD(T) level taking into account also for the core-valence corrections. However the evaluation of the higher-level contributions is still the rate-determining step of these methods and so for larger system more approximate composite methods are used to the desired chemical accuracy.[32, 33, 34, 35] For these reasons an effective, accurate and parameter-free composite scheme named junChS-F12, based on the explicitly-correlated F12 methods, has been applied in this dissertation.[1] It relies on cost-effective reference geometries obtained using the revDSD-PBEP86-D3(BJ) functional in combination with a triple-zeta basis set. Also a slightly modified version of this scheme has been developed for the computation of accurate reaction rates with special reference to astrochemical and atmospheric reactions.[36] It must be emphasized that most of the reactive systems analyzed in this dissertation involve open-shell radical reagents and closed-shell neutral molecules. From this interaction an open-shell reactive PES is obtained which may require an investigation through multireference methods. However it has been demonstrated that the composite schemes applied in this dissertation, in the abscence of a strong multireference contribution, outperform the most well-known model chemistries. After that thermochemistry has been accurately characterized, kinetic calculations are carried out to provide conclusive information on the feasibility of the suggested mechanisms as well as rate constants and the branching ratios of the products. The accurate computation of formation rates for these species at reduced computational cost is crucial in order to use them within global kinetic schemes. Different tools are available to compute accurate rate constants, like quantum dynamics calculations,[37] Multi-Configuration Time-Dependent Hartree (MCTDH),[38] Ring Polymer Molecular Dynamics (RPMD),[39] and Quasi-Classical Trajectory calculations(QCT).[40, 41] All these methods can give very accurate rate coefficients for small size systems composed typically by 3-4 atoms for quantum dynamics and 8-10 for MCTDH, RPDM and QCT. Unfortunately they require the knowledge of the whole PES which involves high computational time. Due to the system size and time limitations another powerful chemical kinetics tools is exploited: the transition state theory (TST). The transition state concept was first proposed in 1935 by Eyring [42] and Evans and Polanyi [43] and relies on the idea that there exists a transition state (TS) or "activated complex" that separates the reactants from the products. The main idea behind TST is that the reactants will move in the configurational space under the appropriate laws of motion, but the reaction will take place only if the system reaches the TS geometry. In fact, this configuration is characterized by a maximum along the reaction coordinate, but it is a minimum along all the other motions orthogonal to it, and therefore it is a first order saddle point along the multidimensional PES. There are two types of possible transition states: tight and loose. Tight TSs rules reactions with non-negligible barriers. Furthermore, if a saddle point exists but is too low in energy (e.g., below the downhill direction reactants), the dynamical bottleneck might be a tight transition state around the saddle point, or a loose transition state leading to a well between

the reactants and the saddle point. A loose transition state is made up of fragments that rotate freely or nearly freely in more than one dimension with regard to one another. It should be noticed that the existence of torsions, which are one-dimensional internal rotations, is not enough to make a transition state loose. A typical example is provided by bond fission reactions without intrinsic barrier (i.e., when the potential energy is monotonically uphill or monotonically downhill in the reverse association), which exhibit typical loose transition states. It should be clear that for loose transition states the conventional TST methodologies cannot be applied, since it is not possible to identify a TS structure. A variety of different models to overcome this limitation have been proposed, like the Phase Space Theory (PST). [44, 45] One of the advantage of TST is its applicability also to larger systems because it does not require the entire characterization of the PES, but only of some properties of few critical points. More specifically the equilibrium geometries, electronic energies, harmonic (or anharmonic) frequencies and zero-point energies. The accuracy of the rate constant depends on the accuracy of the electronic structure calculations and the sophistication of the TST. To apply the TST the reaction must be elementary, i.e. no reaction intermediates must be present in order to describe the chemical reaction. Anyway, the majority of chemical reactions imply intermediates because of their multi-step nature. So, they can be considered as networks of interconnected elementary steps contributing to the global kinetics. The TST model also has some limitations regarding its accuracy. Indeed, it has been demonstrated that the reactive fluxes obtained through TST are overestimated compared to the real ones obtained classically[46] This is due to the fact that in the TST framework the non re-crossing assumption is not valid. To overcome this problem and reduce the re-crossing phenomenon, the variational transition state theory (VTST) approach can be applied. In this case the transition state is no longer identified by the dividing surface which intersects a first order saddle point, but its position is variationally optimized to minimize the reaction rate. This minimizes the effects of re-crossing and gives a much more accurate result.[47] In addition, the thermal distribution of the reactants can play a key role in the quality of the kinetics calculation. In fact, for highly energized molecules involved in fast chemical reactions, the collisional stabilization process with the surrounding environment for the thermalization result to be lower than the reactive ones. Also the assumption that the Born-Oppenheimer approximation is valid for the entire dynamics process excludes all the possible spin forbidden reactions, while the classic treatment of nuclei dynamics leaves out all those reactions characterized by quantum effects, such as tunneling and non classical reflection. Lastly, TST, as it has been sketched here, does not take into account any pressure dependence of the rate coefficient. However, it has been demonstrated that for many gas-phase reactions, especially those involving small molecules, the rate coefficient can show a strong dependence on pressure. Finally, in order to describe the global kinetics of multistep reactions (taking into account also the pressure dependence) the Master Equation (ME) approach came out as one of the most effective models and it will be used and discussed throughout this thesis.

Aim and strategy

The aim of this dissertation is to develop a computational protocol for the accurate characterization of gas-phase reactive chemical systems of astrochemical interest. It is based on three main pillars: (i) an in-depth exploration of the several possible reaction pathways through an automated search carried out by means the AutoMeKin[2] program; (ii) the accurate characterization of their reactive potential energy surfaces applying composite schemes for energy refinement, and (iii) the kinetics calculation using the StarRate[3] program specifically designed to study astrochemical reactions. As for the first step, the goal is to be able to probe as completely as possible all the reaction paths involved in the reaction mechanism so as not to neglect reaction steps that could significantly influence the kinetics of the reaction. As regards the second step, the accurate energy refinement of the PES is performed through the application of reliable composite schemes which require reasonable computational times. For the last step, the calculation of reliable rate constants is carried out through the so called ab initio-transition-state-theory-based master equation approach (AITSTME). It is ab initio since it takes as input molecular properties calculated from first principles. These information are thus used in conjunction with TST coupled with a master equation approach in order to obtain rate constants and branching ratios of the species involved in the reaction mechanism. Hereafter the objectives of this thesis are defined and a related strategy to pursue them is sketched. In the introduction of each chapter the proper objectives will be recalled.

- Define a robust methodology to discover all the possible chemical reaction pathways for gas-phase reactions characterized by an initial barrierless association step in which the reactants are radical or ionic species.
- Use a validated methodology to compute accurate activation energies of the gas-phase reaction mechanisms.
- Develop a program to compute reliable rate constants based on the ab initio-transition-state-theory-based master equation approach and specifically designed to study astrochemical reactions.
- Apply the computational strategy to paradigmatic test case reactions in order to disclose their thermochemistry and kinetics, thus getting insights on their role in the astrophysical contexts.

Thesis outline

In this doctoral thesis, the development of a computer program for the calculation of rate constants and branching ratios for reactions of astrochemical interest will be presented. A general and robust strategy to successfully carry out the computational modeling of the PES and to calculate accurate rate constants for challenging gas-phase reactions will be also proposed. This thesis is structured as follows.

- Chapter 1: definitions and discussions of theoretical methodologies employed in this dissertation are given.
- Chapter 2: the development and the theoretical framework of the StarRate program is discussed, also several test case reactions are presented to show all the features implemented in it.
- Chapter 3: the paradigmatic case of the possible gas-phase formation and isomerization reaction of cyanoacetaldehyde a prebiotic molecule of astrochemical interest not yet detected in the ISM is presented to show how radiative emission can favour the association reaction between two radical fragments at very low pressures.
- Chapter 4: an alternative gas-phase formation reaction of cyanoketene, a prebiotic molecules of astrocheimcal interest not yet detected in the ISM, is presented to show how automated methods for the discovery of new reaction mechanisms can bring to new insights never considered before.
- Chapter 5: the reaction between vinylalcohol conformers and the radical hydroxyl is investigated to understand if it can be considered as a plausible reaction pathway for the formation of (Z)1,2-Ethendiol.
- Chapter 6: the reaction between two molecules relatively abundant in the ISM, the vinylalcohol and radical cyanide, is investigated in detail to understand the similar reactivity shown by the two conformers: *syn* and *anti* vinylalcohol.
- Chapter 7: the conclusions are presented, together with possible future improvements to the models and computational methods developed in the thesis.

Chapter 1

Theoretical and Computational Background

This Chapter introduces the methodology applied for the automated computation of reaction mechanisms together with the theoretical foundations of electronic structure and kinetic methods. In the next sections a concise description of the computational approaches used in this dissertation will be given. Hereafter, a description of the AutoMeKin software used to perform unsupervised searches of reaction mechanisms is presented. Some basics of the wavefunction theory and density functional theory (DFT) with an introduction to the composite scheme are presented. A deeper description of the chemical kinetics theories used to study unimolecular and bimolecular reactions like the transition state theory (TST) and the Rice-Ramsperger-Kassel-Marcus (RRKM) theory is given. Capture theory (CT) will be discussed to study barrierless bimolecular reactions along with master equation (ME) approach to solve chemical reactions involving multiple, interconnected potential wells. Models to compute the tunneling effect will be described, like the Eckart model, the Zero Curvature Tunneling (ZCT) model and the Small Curvature Tunneling (SCT) model. Taking into account the low pressures characterizing the interstellar medium, the radiative stabilization process will be addressed also taking into account its overall impact on iCOMs formation rates.

1.1 Reaction Mechanism Discovery with AutoMeKin

The complexity related to the investigation of chemical reactivity in space is mostly due to the extreme physical conditions of temperature, pressure and exposure to high-energy radiation leading to the formation of exotic species, like radicals and ions. Accurate state-of-the-art computational approaches play a fundamental role in analyzing feasible reaction mechanisms and into accurately predicting the associated kinetics. Such approaches usually rely on chemical intuition where a by-hand search of the more likely pathways is performed. Unfortunately, this procedure can lead to overlook significant mechanisms, especially when large molecular systems are investigated. Increasing the size of a molecule can also increase the number of its possible conformers which can show a different chemical reactivity with respect to the same chemical partner. This generates very complex chemical reaction networks in which hundreds of chemical species are involved and thousands of chemical reactions can occur. The kinetic analysis of an erroneous potential energy surface, describing an incomplete chemical reaction scheme, would lead to gross errors in the estimation of the rate constants of the chemical species involved in the reaction. During the last decades, a lot of effort have been done to develop computational techniques able to perform extensive and thorough investigations of complex reaction mechanisms. Such approaches rely on automated computational protocols which drastically decrease the risk of making blunders during the search for significant reaction pathways. This section will provide a detailed description of the AutoMekin program, an acronym for Automated Mechanisms and Kinetics, with particular attention to the implemented methods and its framework for the automated discovery of reaction mechanisms.

1.1.1 Method

AutoMeKin[2] is an updated version of tsscds2018 [48], a program for the automated discovery of reaction mechanisms. The three main pillars on which it is based are:

- Short-time reactive molecular dynamics simulations
- Post-processing analysis of the MD simulations
- Kinetics simulations

The program is based on the Transition State Search using Chemical Dynamics Simulations (TSSCDS) [49, 50] algorithm which exploits high-energy molecular dynamics simulations (MD) of molecules to trigger reactive events. MD simulations are run using the semiempirical methods implemented in the quantum chemistry program MOPAC2016 [51]. Subsequently, the algorithm can select and optimize those structures along the trajectories obtained through MD simulations that most closely resemble the transition state (TS) of a bond-breaking/bond-forming process. These structures are first optimized at the semiempirical level of theory, also called low-level (LL). Next, the structures of the most promising candidates are re-optimized by more refined wavefunction or DFT methods (the so-called high-level, HL) employing the Gaussian16 package [52]. Once the TSs are optimized, a reaction network can be constructed by

computing the intrinsic reaction coordinates [53] (IRCs) which connect TSs with minima. After that, kinetic Monte Carlo [54] simulations can be run to compute relative abundances as a function of time, energy or temperature. Let us now analyze in some detail how the TSSCDS algorithm works in terms of the six main steps composing the overall approach:

- **Step1: Optimization and frequency calculation of an initial structure at LL**
  The structure of a molecular system is optimized and frequency analysis is carried out using semiempirical methods like PM6 and PM7 [55] performed with MOPAC2016.

- **Step 2: Preparation of the ensemble of molecules for the MD simulations**
  The vibrational normal modes computed in the previous step are used to prepare a microcanonical ensemble of excited molecules. To do that the microcanonical normal mode sampling (NMS) [56] is used. This sampling technique creates an initial ensemble of T trajectories at the selected excitation energy. This energy should be sufficiently high so that the molecular system can experience several reactive processes within the simulation time. Alternatively, a canonical ensemble of excited molecules can be spawned, which avoids the computation of vibrational frequencies.

- **Step 3: Chemical dynamics simulations**
  The simulations are performed using a modified version of MOPAC2016. Since the molecular system is highly vibrationally excited, the dynamics is accelerated so only few hundreds of femtoseconds are needed to induce fragmentation or isomerization processes. To run MD with MOPAC the following keywords are needed:

  $$\textit{method velocity drc cycles} = \textit{ncycles t-priority} = \textit{1}$$

  where the *method* is the selected LL, which can be PM6, PM7 or any of the methods implemented in MOPAC, *velocity* is the initial velocity vector obtained in the second step, *drc* requests for a dynamic reaction coordinate calculation at constant energy that stops after *ncycles* steps and the cartesian coordinates and momenta are recorded every fs because *t-priority=1*. The time step for the integration of the trajectories is 0.5 fs.

- **Step 4: Reaction pathway search algorithm through BBFS**
  An algorithm is specifically designed in this work to find reaction pathways that involves bond breakage/formation. The algorithm is thus called bond breakage/-formation search (BBFS). It is based on the construction of the connectivity vector **C**:

  $$C^i = (C^i_{12}, C^i_{13}, ..., C^i_{(N-1)N}) \tag{1.1}$$

  where N is the number of atoms composing the molecular system. The element C^i_{jk} provides information about the connectivity between the atoms j and k of the

molecular system at the i^{th} step along the trajectory. The connectivity vector is defined through two additional vectors: $\mathbf{d}^i$ and $\mathbf{d}^{ref}$, which are, respectively, the interatomic distances at step i, and the reference distances between each pair of atoms obtained by the sum of the covalent radii of the atoms. The initial connectivity vector $C^{i=0}$ for $i = 0$ is defined from $\mathbf{d}^{i=0}$ and $\mathbf{d}^{ref}$ as:

$$C_{jk}^{i=0} = \begin{cases} 1 \text{ if } \delta_{jk}^{i=0} < 1 \\ 0 \text{ otherwise} \end{cases} \qquad \text{with } \delta_{jk}^{i=0} = \frac{d_{jk}^{i=0}}{d_{jk}^{ref}} \tag{1.2}$$

where the dimensionless parameter $\delta_{jk}^{i=0}$ is called normalized distance which provides a measure for the initial elongation of the interatomic distance between atoms j and k. The elements $C_{jk}^{j=0}$ are binary numbers, with values of one or zero for the pair jk indicating the existence or the abscence of a bond between both atoms. The way the connectivity vector is updated for any step i along the trajectory is described below. Once $\mathbf{C}$ has been set, a list of neighbors of each atom j are defined as those atoms n for which C_{jn}=1. In a similar way, a list of non-neighbors of j, or outer atoms, can be defined, which includes those atoms for which C_{jo}=0. Here and after, the indices n and o are reserved respectively to the neighbors and outer atoms of a given atom j.

– **Identification of reaction pathways**

The criteria adopted for identifying reaction pathways and updating the connectivity vector are the following:

* a reaction pathway takes place when, during a time interval Δt shorter than 20 fs, this condition is satisfied:

$$max(\delta^{(\Delta t)_{(jn)}}) > min(\delta^{(\Delta t)_{(jo)}}) \tag{1.3}$$

When Eq. 1.3 is fulfilled for the first time, the transition step is termed and denoted as $i^{\ddagger}$. When only one (j, n, o) combination of atoms satisfies Eq. 1.3 within Δt, the process is called a single reaction pathway.

* The three elements of the connectivity vector $C_{\alpha\beta}$ (with $\alpha\beta = jn, jo$,and no) will be updated according to the following condition:

$$C_{\alpha\beta}^{i^{\ddagger}+20} = \begin{cases} 1 \text{ if } \delta_{\alpha\beta}^{h} < 1 \\ 0 \text{ otherwise} \end{cases} \tag{1.4}$$

with h being any step within Δt. The condition of Eq. 1.4 means that, if the $\alpha\beta$ bond reaches an inner turning point within Δt at a distance shorter than $\mathrm{d}_{\alpha\beta}^{ref}$, atoms α and β are regarded as connected at the end of the time window (step $i^{\ddagger}$+20).

* If several (j, n, o) combinations fulfill the inequality given in Eq. 1.3 within the same Δt, the corresponding separate processes are merged and regarded as a single process, which is called a multiple reaction pathway. These processes may occur consecutively, or because of a complex rearrengement with usually more than three atoms involved. Some examples

are given below to illustrate the difference between single and multiple reaction pathways more clearly. In summary, the BFFS algorithm provides the following data for each trajectory:

· The number R of reactive pathways

· For each reaction pathway, the corresponding transition step $i^{\ddagger}$.

· the atoms involved in each reaction pathway.

– **Selection of TS guess structures**
The key point of the BBFS algorithm is to accurately obtain the transition step $i^{\ddagger}$; a process that has been explained above. Once $i^{\ddagger}$ has been determined, a number of structures are selected for each reaction pathway to increase the probability of TS optimization.

– **Avoiding multiple guess structures of the same TS in the same trajectory**
To avoid selecting multiple guess structures of the same TS in the same trajectory, the two local minima connected in a given RP are labeled with different codes as explained below. Each local minimum on the PES is represented in this work in terms of a connectivity vector **C**. The elements of **C** can be regarded as a binary number that can be converted into a decimal number. Both binary and decimal numbers are good labels for the minima; we use here decimal rather than binary codes. Then, assuming that, within an individual trajectory, two minima will be connected by the same TS, the vectors (A,B) and (B,A) denote, respectively, the direct and reverse processes that proceed through the same TS. Therefore, if a (A,B) process is found by BBFS, additional (A,B) processes or the corresponding reverse (B,A) processes are not taken into account anymore. Furthermore, two different minima may be connected by more than one TS. For these reasons, and to avoid missing different TSs connecting the same minima this procedure was only applied within a single trajectory.

- **Step 5: Partial and TS optimizations of the set of structures selected along each reactive pathway**
The structures selected in the previous step considered as good TS candidates are firstly partially optimized using MOPAC2016 freezing the atoms involved in the reaction pathway. After that, the structures are fully optimized with MOPAC using the eigenvector following method. When a TS is successfully optimized, geometries, energies and vibrational frequencies are recorded and added to a TS list. In order to avoid repetitions and undesired TSs, a screening of the list is performed to remove duplicates comparing energies, geometries and frequencies, and also those TS involving secondary process, likely those where the molecule has already fragmented but another reactive process is taking place between the fragments.

- **Step 6: TS optimization on the HL-PES**
The LL optimzed TSs obtained in the previous step are reoptimized using a HL

electronic structure method. AutoMeKin supports Gaussian16 to run HL calculations, but also other programs can be used. A flowchart of the TSSCDS method used in AutoMeKin is depicted in Figure 1.1. Shell and Python scripts and fortran programs have been developed to automate all the aforementioned steps.

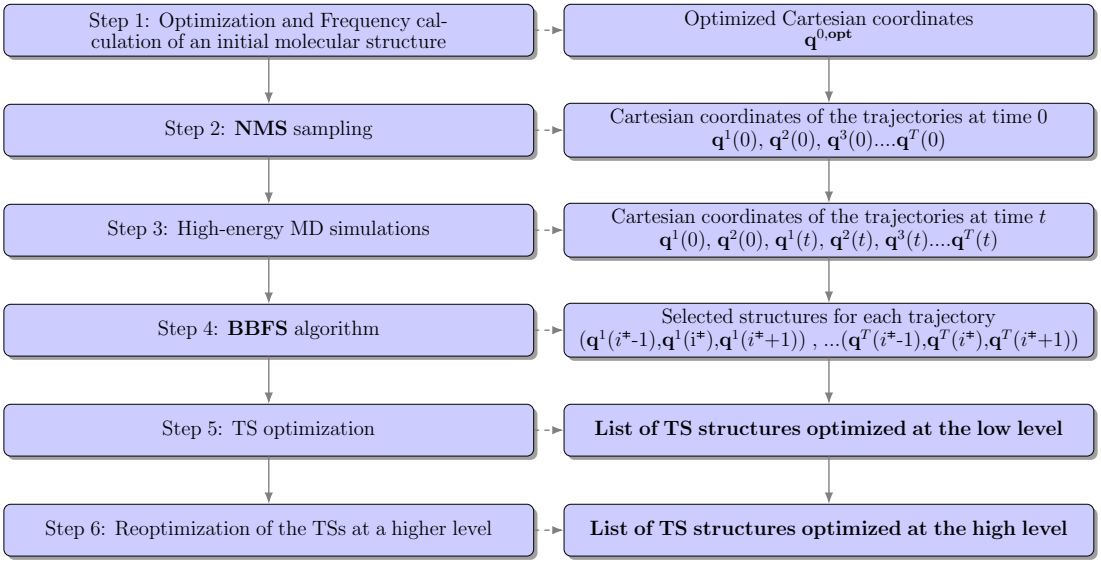

Figure 1.1: Scheme showing the main steps of the TSSCDS method.

1.1.2 Software structure

The program structure is based on two scripts to search for the reaction paths and to solve the kinetics at the LL and HL, which are **llcalcs.sh** and **hlcalcs.sh**, respectively. Both scripts are composed of different modules/programs written in the Bash shell scripting, Python3 and Fortran 90 to perform specific tasks. As shown in Fig 1.2, where a flowchart of **llcalcs.sh** is depicted, the script has several components. It starts executing **tsscds_parallel.sh** which submits a number of parallel and independent accelerated dynamics simulations using MOPAC2016. Then a given number of cycles or iterations (niter) of the loop shown on the left will be carried out.
After **tsscds_parallel.sh** has completed to run MD simulations, **irc.sh** screens the obtained structures to remove possible redundancies. After completion of the screening, IRC calculations are carried out in both forward and backward directions.
The last points of each IRC are the initial guesses of subsequent optimizations carried out by **min.sh**, a procedure whereby each TS is connected to the corresponding minimum energy structures. Thus, a reaction network is built, and each structure is labeled as either an intermediate, or a product. The construction of the reaction network and labeling of the different structures is performed by the **rxn_network.sh** script.
As shown in Figure 1.2, **rxn_network.sh** closes the loop, and its output is fed into **tsscds_parallel.sh**. In particular, the newly generated minima are needed by **tsscds_parallel.sh** because the ensembles of trajectories are initialized not only from

the starting structure but also from the new minima. When a maximum number of iterations is reached, the kinetics is solved using **kmc.sh**, which performs Kinetic Monte Carlo (KMC) simulations.

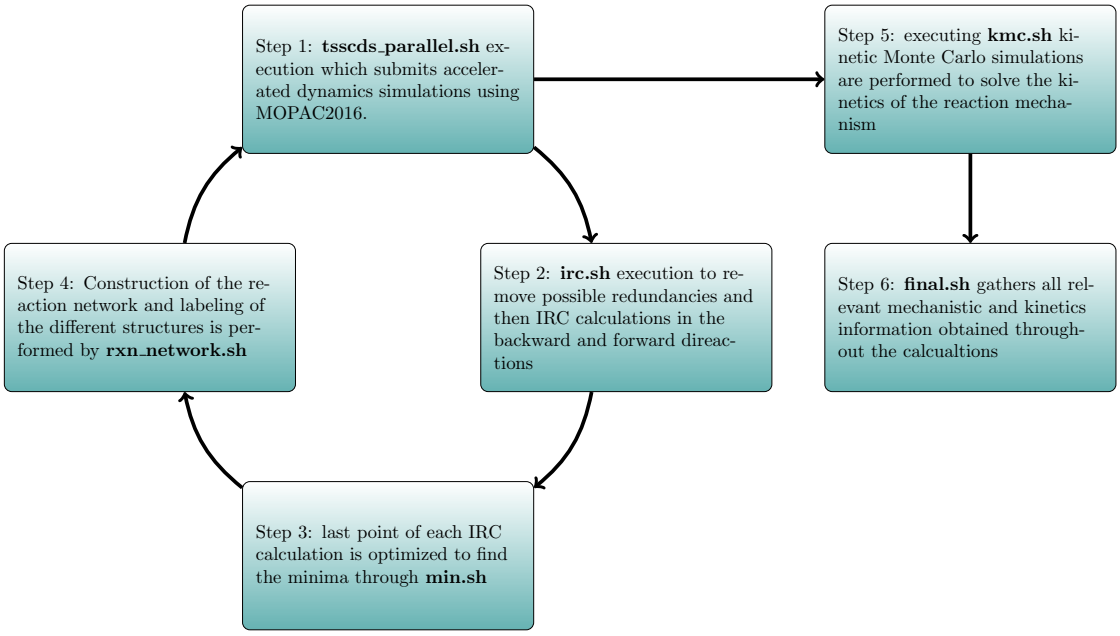

Figure 1.2: Flowchart of **llcalcs.sh** script.

Finally, **final.sh** collects all relevant mechanistic and kinetics information obtained throughout the calculations. As already mentioned, the reaction network and kinetic results can be also be obtained using an *ab initio*/DFT level of theory with G16. The high-level tasks are performed with **hlcalcs.sh**, which is the counter part of **llcalcs.sh** described previously. Low-level TSs optimized structures are now the initial guesses for the high-level optimization. In addition, the product fragments are now optimized to construct more accurate potential energy diagrams.
Therefore, the structure of **hlcalcs.sh** is somehow different from that of **llcalcs.sh**. Specifically, the different tasks carried out by each component of **hlcalcs.sh** are 1) high-level optimization of the TSs obtained at low-level (**TS.sh**); 2) high-level IRC calculations from the TSs optimized in the previous step (**IRC.sh**); 3) high-level optimization of the corresponding intermediates (**MIN.sh**); 4) construction of the high-level network (**RXN_NETWORK.sh**); 5) kinetics simulations on the high-level network (**KMC.sh**); 6) high-level optimization of the products (**PRODs.sh**) and 7) gathering of the important mechanistic and kinetics results (**FINAL.sh**).

1.1.3 Reaction network visualization through AMK tools

The identification of the astrochemical relevant reaction paths is aided by a graphic tool specifically designed for the visualization and analysis of the reaction networks generated through AutoMeKin, i.e. amk-tools.[57] The Python library amk-tools is a useful

package to parse and process the reaction networks obtained through AutoMeKin. After the reaction scheme is created by AutoMeKin, it is possible to graphically display the result of both the LL and the HL simulation.

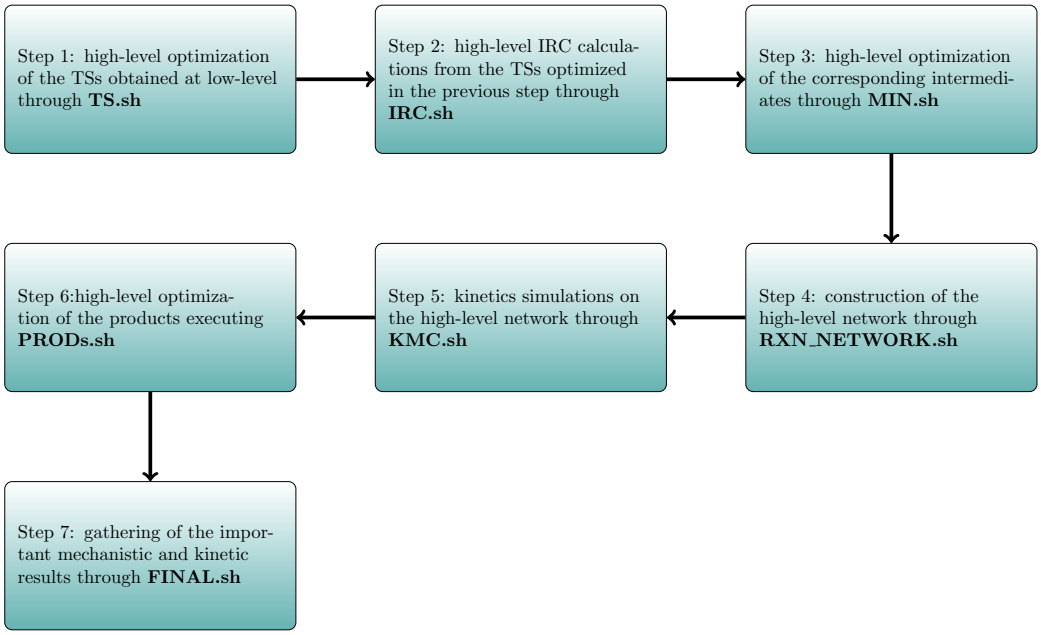

Figure 1.3: Flowchart of **hlcalcs.sh** script.

The standard procedure envisages initially the visualization of the reaction network obtained at a low level and then selects the structures which fall in within a user-defined energy range. Clearly we must take into account the inaccuracy that the PM6 and PM7 methods show in calculating the energy of the critical points. The best course of action is therefore to search for the reaction pathways of interest and select an energy range at least 30 kJ/mol higher than the highest energy critical point of the reaction pathway to be re-optimized. In this way the reoptimization of the reaction scheme will take into account only the structures within that energy range and not all the others. This will save the calculation time of the entire PES calculated at a low level. Thanks to amk-tools it is possible to visualize not only the energy profiles of the single reaction paths selected by the user through special flags from the command line, but also to visualize the 3D molecular structures of the critical points of the PES and of the normal vibrational modes of each of them. In Figure 1.4 an example of chemical reaction network built by amk-tools is shown. To make easier for the reader to understand the quality of the graphic, a reduced portion of a more complex reaction mechanism generated by AutoMeKin has been considered.

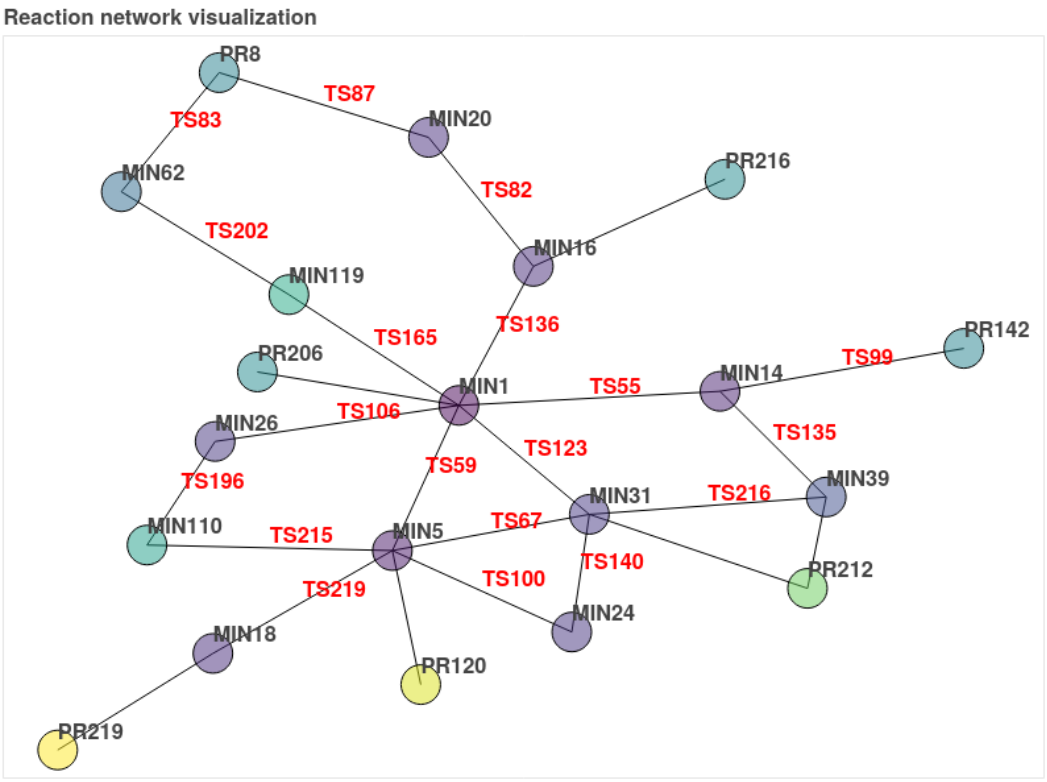

Figure 1.4: Example of chemical reaction network constructed by amk-tools. The nodes represent the minima and the products of the reaction mechanism, while the lines that connect the various nodes are the transition states for passing from one minimum to another.

1.1.4 Application in the astrochemical context

Given the large amount of mechanistic information obtainable through AutoMekin for gas phase reactions and beyond, its application to systems of astrochemical interest in which very exotic molecular species are involved, such as radicals and ions, is of great utility. One of the fundamental conditions for which these reactions can occur in the extreme conditions of the ISM is that there is no activation barrier. Usually, in fact, the initial fragments react in an uncontrolled way favoring the highly exothermic formation of association products, from which the reaction can then continue through numerous isomerization steps towards dissociation products. The strategy adopted with AutoMeKin was to start from the optimized structure of the low energy initial association product for computing all possible reaction paths with and without barrier to obtain all possible reactants that can lead to the formation of molecules of interest. In this way it is possible to obtain a long list of possible initial reactants and possible formation mechanisms of identified and not yet identified molecules in the interstellar medium thanks to the methodology implemented in AutoMeKin.

1.2 The molecular Hamiltonian

To understand the microscopic behavior of the molecules that make up macroscopic matter, it is necessary to rely on the fundamental theory of physics, quantum mechanics. Chemical reactions can be thought of as collisions between molecules that are actually quantum mechanical objects. During the reactions the electronic structure of the involved molecules undergoes changes that can only be understood through the use of quantum mechanics. The starting point is the Schrödinger equation

$$\hat{\mathcal{H}}|\Psi(\mathbf{r},t)\rangle = i\hbar\frac{\partial}{\partial t}|\Psi(\mathbf{r},t)\rangle, \tag{1.5}$$

where $\hbar = \frac{h}{2\pi}$, with h Planck's constant, $\hat{\mathcal{H}}$ the Hamiltonian operator and $|\Psi\rangle$ the wave function which fully describes a state of the system. Eq. 1.5 describes the time evolution of a N particles system, with coordinates $\mathbf{r} = \{\mathbf{r}_i\}, i = 1, \ldots, N$. The wave function itself has no physical meaning, but $|\Psi(\mathbf{r},t)|^2$ is the probability density of finding each particle at a given point and at a given time. $\hat{\mathcal{H}}$ is the Hamiltonian operator defined as the sum of the kinetic energy $\hat{T}$ and potential energy $\hat{V}$:

$$\hat{\mathcal{H}} = \hat{T} + \hat{V}, \tag{1.6}$$

in the case of an N particles, $\hat{\mathcal{H}}$ becomes:

$$\hat{\mathcal{H}} = -\sum_{i=1}^{N}\frac{\hbar^2}{2m_i}\nabla_i^2 + \sum_{i=1}^{N}\sum_{j>i}^{N}\frac{q_i q_j}{4\pi\varepsilon_0\left|\mathbf{r}_i - \mathbf{r}_j\right|}, \tag{1.7}$$

with m_i being the mass of the i-th particle and ∇^2 being the Laplacian operator acting on the coordinates of the i-th particle, and the second term of Eq. 1.7 includes the sum of two-particle Coulomb's interactions. As it can be observed, Eq. 1.7 is not explicitly dependent on time. For this reason, the wave function can be factorized as $|\Psi(\mathbf{x}_i,t)\rangle = |\Psi(t)\rangle\,|\Psi_x(\{\mathbf{x}_i\})\rangle$, where $|\Psi_t(t)\rangle = A\exp(-iEt)$. From this factorization is possible to obtain the time-independent (non-relativistic) Schrödinger equation:

$$\hat{\mathcal{H}}\,|\Psi(\{\mathbf{x}_i\})\rangle = E\,|\Psi(\{\mathbf{x}_i\})\rangle\,, \tag{1.8}$$

from which the energy can be obtained as the expectation value of $\hat{\mathcal{H}}$ as

$$E = \langle\Psi|\hat{\mathcal{H}}|\Psi\rangle \tag{1.9}$$

Two different kind of particles compose the chemical systems: electrons and nuclei. For a system with n electrons and N nuclei, the kinetic energy contributions can be separated into the electronic and the nuclear terms, $\hat{T}_e$ and $\hat{T}_n$. Different term contribute to the potential energy: electron-electron, nucleus-nucleus and electron-nucleus potential energy terms $\left(\hat{V}_{ee}, \hat{V}_{nn}, \hat{V}_{en}\right)$.

The $\hat{V}_{en}$ term couples electrons and nuclei, making the system not separable into electron-dependent and nuclei-dependent wave functions.
Thus, the molecular Hamiltonian is:

$$\hat{\mathcal{H}} = -\sum_{i=1}^{n}\frac{1}{2}\nabla_i^2 - \sum_{k=1}^{N}\frac{1}{2M_k}\nabla_k^2 - \sum_{i=1}^{n}\sum_{k=1}^{N}\frac{Z_k}{|\mathbf{r}_i - \mathbf{R}_k|} + \sum_{i<j}^{n}\frac{1}{|\mathbf{r}_i - \mathbf{r}_j|} + \sum_{k<l}^{N}\frac{Z_k Z_l}{|\mathbf{r}_k - \mathbf{R}_l|} \quad (1.10)$$

where Z_k are the atomic numbers and $\mathbf{r}$ and $\mathbf{R}$ are the electronic and nuclear coordinates, respectively. The non-separability of the wave function into electronic and nuclear parts limits the applicability of Eq.1.10, mainly to very simple systems, like atoms composed by nuclei and one electron, but molecules are more complex systems composed by several electrons To study this kind of systems it is necessary to introduce additional approximations.

1.2.1 The Born-Oppenheimer approximation

The Born-Oppenheimer approximation, a special case of the so-called adiabatic approximation, is crucial in quantum chemistry. It is based on the fact that nuclei are much heavier than electrons (about 1800 times more) and therefore they move more slowly.
In this way, nuclear kinetic energy can be neglected and the internuclear repulsive interaction term can be considered as a constant. So, given all these assumptions, the electronic Hamiltonian for an N electron system can be defined as

$$\hat{\mathcal{H}}_{\text{elec}} = -\sum_{i=1}^{n}\frac{1}{2}\nabla_i^2 - \sum_{i=1}^{n}\sum_{k=1}^{N}\frac{Z_k}{r_{ik}} + \sum_{i<j}^{n}\frac{1}{r_{ij}}, \quad (1.11)$$

where $r_{ik} = |\mathbf{r}_i - \mathbf{R}_k|$ and $r_{ij} = |\mathbf{r}_i - \mathbf{r}_j|$. The consequence of this approximation is that electronic and nuclear dynamics are separable.
$\mathbf{R}$ can be considered as a parameter inside the electronic wave function, as can be seen by the following equation

$$\hat{\mathcal{H}}_{\text{elec}} \left|\psi(\mathbf{r};\mathbf{R})\right\rangle = E_{\text{elec}} \left|\psi(\mathbf{r};\mathbf{R})\right\rangle \quad (1.12)$$

Assuming to be able to solve Eq. 1.12 for each nuclear configuration $\{\mathbf{R}\}$, the total molecular wave function $|\Psi(\mathbf{r};\mathbf{R})\rangle$ can be expanded on the basis of $|\psi_q(\mathbf{r};\mathbf{R})\rangle$

$$\left|\Psi(\mathbf{r};\mathbf{R})\right\rangle = \sum_q \chi_q(\mathbf{R}) \left|\psi_q(\mathbf{r};\mathbf{R})\right\rangle \quad (1.13)$$

Inserting Eq. 1.13 into Eq. 1.12 and projecting onto the ψ_q basis set (integrating only on electronic coordinates), we can evaluate how the different terms of $\hat{\mathcal{H}}$ act on the $\chi_q(\mathbf{R})$ and $|\psi_q(\mathbf{r};\mathbf{R})\rangle$. In particular the kinetic energy operator of nuclei $-\sum_k \frac{\hbar^2}{2M_k}\nabla_k^2$ is not diagonal on the $|\psi_q(\mathbf{r};\mathbf{R})\rangle$ basis. The Born-Oppenheimer approximation now consists in neglecting the off diagonal terms of this operator and therefore decoupling the electronic dynamics from the nuclear one. In general, this assumption is an extremely mild one, and it is entirely justified in most cases. It is worthwhile emphasizing that this approximation has very profound consequences from a conceptual point of view: without the Born-Oppenheimer approximation, for example, we would lack the concept of molecular structure and potential energy surface.

1.2.2 Variational principle

In quantum chemistry one of the most important principles (on which many computational methods are based on) is the variational principle. It states that, given a normalized trial wave function $|\Phi\rangle$, for which $\langle\Phi \mid \Phi\rangle = 1$, the expectation value of the Hamiltonian is always an upper bound of the actual ground state energy, so $\langle\Phi|\hat{\mathcal{H}}|\Phi\rangle \geq E_0$. When $|\Phi\rangle$ is identical to the ground state wave function, $|\Phi_0\rangle$, $\langle\Phi_0|\hat{\mathcal{H}}|\Phi_0\rangle = E_0$. The challenge is to find a good trial wave function. One possibility to build up a wave function for a multi-electron system would be the product of single electron wave functions of non interacting single electron spin-orbitals $|\chi(\mathbf{x})\rangle = |\Psi(\mathbf{r})\rangle|\omega(\sigma)\rangle$, where the spin function $|\omega(\sigma)\rangle$ can assume two values, $|\alpha\rangle$ or $|\beta\rangle$. In this way, however, Pauli's principle would not be respected, *i.e.*, or cannot guarantee that a multi-electronic wave function must be anti symmetric with respect to the exchange of two electrons. A better choice is provided by the so called Slater determinant:

$$\Psi_{SD}\left(\mathbf{x}_1, \mathbf{x}_2, \ldots, \mathbf{x}_N\right) = \frac{1}{\sqrt{N!}} \begin{vmatrix} \chi_1\left(\mathbf{x}_1\right) & \chi_2\left(\mathbf{x}_1\right) & \cdots & \chi_N\left(\mathbf{x}_1\right) \\ \chi_1\left(\mathbf{x}_2\right) & \chi_2\left(\mathbf{x}_2\right) & \cdots & \chi_N\left(\mathbf{x}_2\right) \\ \vdots & \vdots & & \vdots \\ \chi_1\left(\mathbf{x}_N\right) & \chi_2\left(\mathbf{x}_N\right) & \cdots & \chi_N\left(\mathbf{x}_N\right) \end{vmatrix} = |\chi_1\chi_2\cdots\chi_N| \tag{1.14}$$

If it satisfies anti symmetry requirements, and consequently the Pauli principle, since changes sign upon exchange of two electrons.

1.2.3 Hartree-Fock method

Starting from the Slater determinant, it is possible to derive the Hartree-Fock method (HF), also called self-consistent field method, for the determination of the wave function and the energy of quantum many-body systems. To do that, we must compute the quantity $\left\langle \Psi_{SD}|\hat{\mathcal{H}}|\Psi_{SD}\right\rangle$, that is

$$V_{NN} + \sum_{i=0}^{N_{\text{elec}}} h_i + \sum_{i=0}^{N_{\text{elec}}} \sum_{j>i}^{N_{\text{elecc}}} J_{ij} - K_{ij} \tag{1.15}$$

where h_i collects the one-electron terms and $J_{ij} - K_{ij}$ two-electrons ones. These terms are defined as $h_i = \left\langle \chi_i \left| \hat{T}_e + \hat{V}_{en} \right| \chi_i \right\rangle$, $J_{ij} = \left\langle \chi_i\chi_j \left| r_{ij}^{-1} \right| \chi_i\chi_j \right\rangle$ and $K_{ij} = \left\langle \chi_i\chi_j \left| r_{ij}^{-1} \right| \chi_j\chi_i \right\rangle$. The two latter terms come from $\hat{V}_{ee}$ acting on the wave function, where r_{ij} is the distance between the i-th and j-th electrons. Here J_{ij} is the Coulomb integral and represents the electrostatic interaction between two charge densities $|\chi_i|^2$ and $|\chi_j|^2$ while K_{ij}, called the exchange integral, arises from the anti symmetric nature of the Slater determinant. Both J_{ij} and K_{ij} are positive, and therefore if $i = j$ their contribution vanishes, preventing any spurious self-interaction effect, which would come from J_{ii}. The core of the Hartree-Fock theory is the application of the variational method to this independent particle model. By proceeding in this way, J_{ij} and K_{ij} integrals can be expressed as single-electron operators, defined by the spin-orbitals themselves:

$$J_j\chi_i(\mathbf{x}) = \chi_i(\mathbf{x}) \int \frac{|\chi_j(\mathbf{x}')|^2}{|\mathbf{x}-\mathbf{x}'|} d\mathbf{x}' \tag{1.16}$$

$$K_j\chi_i(\mathbf{x}) = \chi_j(\mathbf{x}) \int \frac{\chi_j^*(\mathbf{x}')\,\chi_i(\mathbf{x}')}{|\mathbf{x}-\mathbf{x}'|} d\mathbf{x}' \tag{1.17}$$

In other words, it turns out that Hartree-Fock theory is a mean-field theory, *i.e.*, each electron feels the averaged effect of the other electrons by means of these one-electron operators. Collecting these two terms plus h_i, one obtains the Fock operator which may be defined for a given spin direction σ, either up or down (α, β), as:

$$\hat{F}^\sigma |\chi_i^\sigma\rangle = \left[\hat{h} + \sum_{j,\sigma'} \hat{J}_j^{\sigma'} - \delta_{\sigma\sigma'} K_j^\sigma\right] |\chi_i^\sigma\rangle = \varepsilon_i^\sigma |\chi_i^\sigma\rangle \tag{1.18}$$

where ε_i^σ are the energies associated with the i-th spin-orbital with spin σ. These are the unrestricted HF (UHF) equations, in which each electron is allowed to occupy a different spatial orbital thanks to the separation related to the electron's spin. Neverthless the two sets of orbitals are still coupled by the Coulomb's term. For a closed-shell molecule, *i.e.*, same number of spin α and β electrons, the previous equation becomes

$$\hat{F} |\chi_i\rangle = \left[\hat{h} + \sum_j \hat{J}_j - K_j\right] |\chi_i\rangle = \varepsilon_i |\chi_i\rangle \tag{1.19}$$

in which each spin-orbital is filled by two electrons, one spin up and one spin down. This give rise to the restricted HF (RHF) theory. One could also take a midway by forcing doubly occupied orbitals to behave as RHF and the remaining ones as UHF, which leads to the restricted open-shell (ROHF) method. The total RHF and ROHF wavefunctions are also eigenfunctions of the total squared spin operator $\hat{S}^2$, while the UHF ones are not.

1.2.4 Electron correlation

A consequence of the mean-field approximation is that each electron feels only the averaged effect of the other ones, so the energy value obtained is far from giving the exact solution because an appropriate evaluation of the electronic correlation (EC) is missing.
The EC correction is generally defined as the difference between the exact energy and the HF energy:

$$E_{\text{corr}} = E_{\text{exact}} - E_{HF}. \tag{1.20}$$

EC can be classified as Coulomb's and Fermi's correlation, for interactions between electrons with parallel or antiparallel spins, respectively. In the RHF framework, a given spin orbital can only be populated by two electrons with antiparallel spins, due to Pauli's principle. Thus, Coulomb correlation is possible between electrons both in the same space orbital and in different ones. On the other hand, Fermi correlation can only occur between electrons in different orbitals, which makes it smaller than

the previous one. EC can also be classified as static or dynamic. The dynamic EC takes into account the instantaneous correlation of electrons while the static one is associated with quasi-degenerate states (spin orbitals of similar energy). Dynamic EC is more important for electrons in the same orbital, while static EC is more important between electrons in different orbitals. So, in this context, UHF can recover more static correlation than RHF.

1.2.5 Møller-Plesset perturbation theory

The Møller-Plesset (MP) perturbation theory is one method that could be used to recover electronic correlation. This method treats correlation as a minor perturbation $\hat{\mathcal{H}}'$ to the reference HF Hamiltonian $\hat{\mathcal{H}}^{(0)}$, which allows one to construct a perturbed Hamiltonian.

$$\hat{\mathcal{H}} = \hat{\mathcal{H}}^{(0)} + \lambda\hat{\mathcal{H}}', \tag{1.21}$$

where λ is a dimensionless real parameter that controls the size of the perturbation and $\hat{\mathcal{H}}^{(0)} = \sum_i \hat{F}_i$.
The perturbed Schrödinger equation to solve is then

$$\left(\hat{\mathcal{H}}^{(0)} + \lambda\hat{\mathcal{H}}'\right)|\Psi\rangle = E|\Psi\rangle \tag{1.22}$$

Since the eigenvalues and eigenfunctions of Eq. 1.22 are continuous functions of λ, it can be expanded in series:

$$E(\lambda) = \sum_{k=0}^{\infty} \lambda^k E^{(k)}, \tag{1.23}$$

$$\Psi(\lambda) = \sum_{k=0}^{\infty} \lambda^k \left|\Psi^{(k)}\right\rangle \tag{1.24}$$

where each term of the expansion is an order of the correction, and the terms of the wavefunction are orthogonal between them.
Substituting Eq. 1.23 and Eq. 1.24 into Eq. 1.22 one obtains:

$$\begin{aligned}\left(\hat{\mathcal{H}}^{(0)} + \lambda\hat{\mathcal{H}}'\right)\left(\left|\Psi^{(0)}\right\rangle + \lambda\left|\Psi^{(1)}\right\rangle + \lambda^2\left|\Psi^{(2)}\right\rangle + \ldots\right) = \\ \left(E^{(0)} + \lambda E^{(1)} + \lambda^2 E^{(2)}\ldots\right)\left(\left|\Psi^{(0)}\right\rangle + \lambda\left|\Psi^{(1)}\right\rangle + \lambda^2\left|\Psi^{(2)}\right\rangle + \ldots\right)\end{aligned} \tag{1.25}$$

Then, collecting the terms by orders of λ:

$$\begin{aligned}\hat{\mathcal{H}}^{(0)}\left|\Psi^{(0)}\right\rangle &= E^{(0)}\left|\Psi^{(0)}\right\rangle \\ \hat{\mathcal{H}}^{(0)}\left|\Psi^{(1)}\right\rangle + \hat{\mathcal{H}}'\left|\Psi^{(0)}\right\rangle &= E^{(0)}\left|\Psi^{(1)}\right\rangle + E^{(1)}\left|\Psi^{(0)}\right\rangle \\ \hat{\mathcal{H}}^{(0)}\left|\Psi^{(2)}\right\rangle + \hat{\mathcal{H}}'\left|\Psi^{(1)}\right\rangle &= E^{(0)}\left|\Psi^{(2)}\right\rangle + E^{(1)}\left|\Psi^{(1)}\right\rangle + E^{(2)}\left|\Psi^{(0)}\right\rangle\end{aligned}$$

and so on.

Møller-Plesset methods are labeled as MPn where n is the order of the correction where the expansion is truncated. In the MP formalism to compute the successive corrections it is possible to use the knowledge of the previous ones. The usual ones are MP2, MP3 and MP4. It can be shown that the n-th correction to the energy is $E^{(n)} = \left\langle \Psi^{(0)} \middle| \hat{\mathcal{H}}' \middle| \Psi^{(n-1)} \right\rangle$. Since MP methods are not variational the energy is not an upper bound to the exact one.

1.2.6 Coupled cluster theory

Coupled cluster (CC) theory is nowadays widely recognized by the quantum chemistry community as being one of the most powerful and most accurate microscopic formulations of the quantum many-electron problem, even if it was originally formulated for the quantum-chemical treatment of nuclear matter. After its introduction into electronic structure theory, it became one of the most powerful schemes for high-accuracy computations. CC theory is based on the use of an exponential ansatz for the wavefunction

$$|\Psi_{CC}\rangle = \exp(\hat{T})\,|\Psi_{HF}\rangle \tag{1.26}$$

where $\hat{T}$ is the so called cluster operator, which is an excitation operator and consists of the weighted sum of all excitations,

$$\hat{T} = \hat{T}_1 + \hat{T}_2 + \ldots \hat{T}_{N_{\text{elec}}} \tag{1.27}$$

$\hat{T}_1 + \hat{T}_2 + \ldots$ denote the weighted sums of single, double, etc., excitations with the unknown parameters given by the weighting coefficients that are usually referred to as amplitudes. The exponential ansatz in Eq. 1.26 ensures size-consistency and size-extensivity of the electron-correlation treatment even within a truncated scheme that does not include all excitations. CC theory, therefore, is, by construction, a size extensive approach. Size consistency of a method means that the energy of two molecules separated by an infinite distance is the same as the sum of the energies individually calculated for each molecule, *i.e.*, $E_{AB} = E_A + E_B$ for $r \longrightarrow \infty$. Instead, size extensivity means that correlation energy scales correctly (linearly) with the size of the system.
CC theory demonstrates its advantages only when used with a truncated cluster operator. The usual choices are $\hat{T} = \hat{T}_1 + \hat{T}_2$ (CC singles and doubles (CCSD)), $\hat{T} = \hat{T}_1 + \hat{T}_2 + \hat{T}_3$ (CC singles, doubles, triples (CCSDT)), and $\hat{T} = \hat{T}_1 + \hat{T}_2 + \hat{T}_3 + \hat{T}_4$ (CC singles, doubles, triples, quadrupoles (CCSDTQ)), etc. CC higher than CCSD are computationally very expensive. The third order excitations can be added perturbationally giving rise to the CCSD(T) method, often referred as the "gold standard" in quantum chemistry.

1.2.7 Explicitly correlated methods

The main issues related to the electron correlation methods are the slow basis set convergence so that very large basis sets are often required to obtain converged results. This basis set problem arises because the expansion in products of limited 1-electron

functions does not describe well the shape of the wave function at small to intermediate values of interelectron distance r_{12}, since it does not satisfy the electronic wave function cusp condition:

$$\left.\frac{\partial \Psi}{\partial r_{12}}\right|_{r_{12}=0} = \frac{1}{2}\Psi\left(r_{12}=0\right) \tag{1.28}$$

This problem can be avoided by including terms in the wave function that depend explicitly on r_{12} and thus can describe the cusp properly. Early implementations used a linear R_{12} correlation factor, and a number of so-called R_{12}-methods were developed. An alternative is the Slater-type function $F_{12} \sim \exp\left(-\gamma r_{12}\right)$ which yields much better basis set convergence and numerical stability. The methods which employ this kind of function are called the F12 methods. Both MP2-F12 and CCSD(T)-F12 methods have a large number of ansatz and approximations available.[58, 59, 60] For the MP2-F12, the so-called diagonal fixed amplitudes approximation (FIX) is the recommended one because it guarantees size consistency and orbital invariance making the use of localized orbitals no longer necessary. The error introduced by this approximation depends on the system and the property calculated but is in general rather small. For CCSD-F12 two main approximations exist, namely F12a and F12b. The CCSD-F12a approximation tends to overestimate the correlation energy, while CCSD-F12b is systematically below the basis set limit. For what concern the perturbative treatment of the triples correction, the explicit correlation has not been implemented yet. Usually a trick is employed to speed-up the convergence in the (T) energy contribution with respect to the basis set size. For example in the Molpro[61, 62, 63] package the ratio of the MP2-F12 and MP2 correlation energies is used to estimate a scaling factor for the perturbative triples correction, as follows

$$\Delta E_{(\mathrm{T}^*)} = \Delta E_{(\mathrm{T})} \frac{E^{\mathrm{corr}}_{\mathrm{MP2-F12}}}{E^{\mathrm{corr}}_{\mathrm{MP2}}} \tag{1.29}$$

This is based on the assumption that explicit correlation affects the energy of the triples in the same way as the MP2 correlation contribution.

1.2.8 Density functional theory

In the previous sections, a description of the wave function methods to compute electronic energy and to take into account the EC has been provided. Here below the derivation of the Density Functional Theory (DFT) is sketched. DFT is based on the electron density $\rho(\mathbf{r})$, which depends on three spatial variables. It can be derived from a wave function Ψ

$$\rho(\mathbf{r}) = N \int \ldots \int d\mathbf{x}_1 d\mathbf{x}_2 \ldots \mathbf{x}_N \Psi^*\left(\mathbf{x}_1, \ldots, \mathbf{x}_N\right) \Psi\left(\mathbf{x}_1, \ldots, \mathbf{x}_N\right) \tag{1.30}$$

$\rho(\mathbf{r})$ is non-negative, it vanishes at infinity and gives the total number of electrons N when integrated over the real-space coordinates $\mathbb{R}^3$

$$\int \rho(\mathbf{r}) d\mathbf{r} = N \tag{1.31}$$

The cusps of the density are the positions of nuclei, and their heights define the nuclear charges.
The energy of a molecular system can be expressed as a functional of $\rho(\mathbf{r})$ as a sum of various terms

$$E[\rho] = V_{NN} + E_e[\rho] = V_{NN} + V_{eN}[\rho] + J_e[\rho] + T[\rho] + E_{xc}[\rho], \tag{1.32}$$

where V_{NN} is the nucleus-nucleus interaction and $E_e[\rho]$ is the electronic energy as a functional of the electron density.
$E_e[\rho]$ is the sum of the electron-nucleus interaction V_{eN}, electron-electron interaction J_e, $T[\rho]$ is the electronic kinetic energy and of the exchange-correlation term $E_{xc}[\rho]$.
However, it can be shown that the system can be completely defined by the electron density in its ground state. The Hamiltonian is completely determined by the number of electrons and the potential V_{eN}, usually called "external" potential. The relation between ρ and the energy of the system was demonstrated in the first Honenberg and Kohn theorem, which ensures the existence of a universal energy functional of the electronic density. In their second theorem they proved that the energy can be obtained by means of the variational principle, starting with a trial density, $\tilde{\rho}$, so that $E[\tilde{\rho}] \geq E[\rho]$.[64] Although $E[\rho]$ is proved to exist and to be universal, it is unknown. This is due to the fact that $T[\rho]$ and $J_e[\rho]$ functionals cannot be explicitly written in terms of $\rho(\mathbf{r})$. To overcome this problem, Kohn and Sham ingeniously considered a fictitious system, of non-interacting electrons moving within an "external" potential (V_{eN})[65], which can be exactly described by a Slater determinant made up by auxiliary Kohn-Sham (KS) spin-orbitals. It requires a constraint, that the electron density derived from these auxiliary functions is the same as the one of the DFT

$$\rho_{KS}(\mathbf{r}) = \sum_i \int |\chi_i(\mathbf{x})|^2 \, d\sigma = \rho(\mathbf{r}) \tag{1.33}$$

Next, the difference in kinetic energy between the real and the fictitious ($T_s[\rho]$) system is added to the exchange-correlation term to give

$$E_{xc}[\rho] = E'_{xc}[\rho] + T[\rho] - T_s[\rho] \tag{1.34}$$

Now, only $E_{xc}[\rho]$ is unknown. To make the realization of DFT possible, several functionals, which led to the rise of several methods, have been designed to determine $E_{xc}[\rho]$. Usually they are all based on the the separation of $E_{xc}[\rho]$ into a term for exchange and another for correlation, $E_{xc}[\rho] = E_x[\rho] + E_c[\rho]$. Then each DFT method relies on certain approximations to compute each part. There are hundreds of DFT methods, but no systematic way to improve functionals. According to the fundamental ingredients in each method, Perdew and Schmidt proposed a classification into five families.[66] The resulting "Jacob's ladder" of DFT is a classification connecting the "hell" of non-interacting electrons to the "heaven" of chemical accuracy. The higher one climbs the ladder, the more accurate the results will be, but at a higher computational effort. The rungs of the ladder are as follows, in ascending order of complexity:

- the local spin density approximation (LSDA) assumes that $\rho(\mathbf{r})$ is a slowly changing function of $\mathbf{r}$, so that the uniform electron gas model is able to describe the non-uniform density system locally

- the generalized gradient approximation (GGA), introduces corrections accounting for the non uniformity of ρ through the gradient of the electron density
- the meta-GGA family, which adds higher order corrections based on higher order derivatives of the electronic density
- the hybrid DFT methods improve the highly local nature of the previous families by mixing some "exact" exchange energy computed following the HF method with the KS auxiliary spin-orbitals
- the double-hybrid DFT methods include some (dynamical) correlation estimated by perturbative methods like MP2 at a higher computational cost

1.2.9 Dispersion correction

Usually DFT functionals are corrected in order to properly describe London dispersion forces. This is necessary because, except for double-hydrid functionals for which the addition of correlation is due to perturbative corrections, dispersion is not well described by DFT methods. To improve the description of medium range interactions, the most used methods to take into account the dispersion corrections are the Grimme's methods, D3[67, 68] and D3(BJ)[69]. The D3(BJ) version includes the Becke-Johnson damping function, which controls the overlap between short and long range interactions, as the former is described by DFT. The equation for D3 correction is given by:

$$\Delta E_{\text{disp}}^{\text{D3}} = -\frac{1}{2} \sum_{n=6,8} \sum_{A \neq B} s_n \frac{C_n^{AB}}{R_{AB}^n} f_{\text{damp}}\ (R_{AB})$$

where s_n is a scaling factor which depends on the chosen functional, C_n^{AB} are the nth order dispersion parameters for each AB atom pair, R_{AB} are the AB inter-nuclear distances and $f_{\text{damp}}\ (R_{AB})$ are damping functions.

For what concerns the D3(BJ) correction, the equation becomes

$$\Delta E_{\text{disp}}^{\text{D3(BJ)}} = -\frac{1}{2} \sum_{n=6,8} \sum_{A \neq B} s_n \frac{C_n^{AB}}{R_{AB}^n + f_{\text{damp}}^n\ (R_{AB}^0)}$$

Here, $f\left(R_{AB}^0\right) = a_1 R_{AB}^0 + a_2$ where a_i are fit parameters called BJ parameters and $R_{AB}^0 = \sqrt{\frac{C_8^{AB}}{C_6^{AB}}}$.

1.2.10 Composite schemes for molecular energies

As mentioned in the Introduction, composite schemes are methods for the accurate calculation of molecular electronic energies or structural parameters. They are based on the combination of different types of electronic structure calculations that employ high levels of theory in conjunction with small basis sets or low levels of theory with large basis sets. Through this combination it is possible to obtain a more accurate

estimate of the various individual contributions that can affect the total energy, such as the electron correlation, the effect of the basis sets and the interaction of the core-valence electrons. These methods are often based on the principle of additivity which involves calculating the various contributions separately at the highest possible level of theory, and then combining them all together. Composite schemes save computational time as they provide less computationally intensive calculations while maintaining a high level of accuracy. In the next paragraph a formal presentation and description of the so called "cheap" composite schemes, namely junChS and junChS-F12 is provided.

1.2.11 junChS and junChS-F12

For both junChS and junChS-F12 schemes, the starting point is the optimization of molecular structures at the DFT level, employing the revDSD-PBEP86-D3(BJ) double hybrid functional in conjunction with the jun-cc-pVTZ basis set. Then, from such optimized structure, the cheap composite schemes are applied to obtain the refined electronic energy of the molecular system under investigation.
The general idea on which both schemes are based is the calculation of all the contributions reported in Eq. 1.35 through single point calculations using the DFT optimized structure. The workflows for junChS and junChS-F12 schemes are reported in Fig 1.5

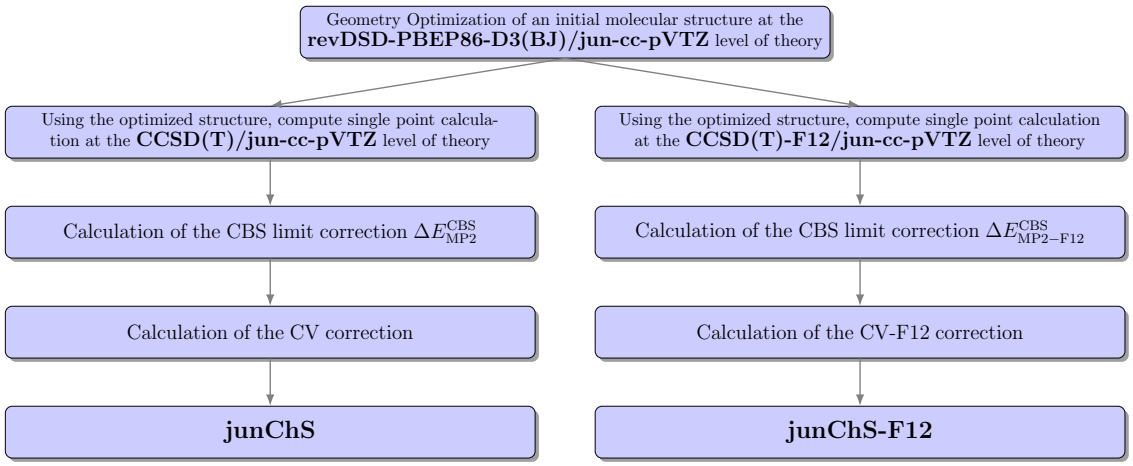

Figure 1.5: junChS and junChS-F12 workflows.

More specifically the single point energies are computed using CCSD(T) with a triple ζ quality basis set in conjunction with CBS limit and additive CV corrections computed at MP2 level of theory. Both schemes rely on the use of partially augmented basis sets. Then the anharmonic ZPE is evaluated through generalized second order vibrational perturbation theory.
The junChS and junChS-F12 electronic energy calculation are based on the following expression

$$E_{\mathrm{jChS(-F12)}} = E_{\mathrm{CCSD(T)}(-F12)} + \Delta E^{\mathrm{CBS}}_{\mathrm{MP2}(-F12)} + \Delta E_{\mathrm{CV(-F12)}} \tag{1.35}$$

where $E_{\mathrm{CCSD(T)}}$ and $E_{\mathrm{CCSD(T)}-F12}$ are computed in conjunction with the jun-cc-pVTZ basis set.

Corrections for the CBS limit are computed using the two-point extrapolation formula

$$\Delta E^{(n)}_{\mathrm{MP2(-F12)}} = \Delta E^{\infty}_{\mathrm{MP2(-F12)}} + \frac{a}{n^3}, \tag{1.36}$$

This term considers the valence correlation energy extrapolated to the basis set limit, which leads to the following explicit expression

$$\Delta E^{\infty}_{\mathrm{MP2}(-F12)} = \frac{n^{n-1}E^{\mathrm{MP2(-F12a)}/nZ} - n^n E^{\mathrm{MP2(-F12a)}/(n-1)Z}}{n^{n-1} - n^n} - E^{\mathrm{MP2(-F12a)}/(n-1)Z} \tag{1.37}$$

This term considers the valence correlation energy extrapolated to the basis set limit, in which n=T,Q.
Finally, the core-valence correction is recovered at MP2(-F12) level of theory as the difference between all electron and frozen core calculations, *i.e.*,

$$\Delta E_{\mathrm{CV(-F12)}} = E_{\mathrm{MP2(-F12)}}(\mathrm{ae}) - E_{\mathrm{MP2(-F12)}}(\mathrm{fc}) \tag{1.38}$$

using the cc-pwCVTZ basis set.

1.3 Gas-Phase Chemical Kinetics

As one of the oldest branches of physical chemistry, the aim of chemical kinetics is to provide a detailed understanding of the evolution of chemical reactions by assigning specific rate constants to all the steps involved in the reaction mechanism. As already mentioned in the Introduction, theoretical kinetics is fundamental to investigate chemical processes that are difficult to explore experimentally, such as those which occur in combustion, atmospheric and interstellar environments. However, to do that, it is necessary to make some assumptions. Gas phase chemical kinetics is based on fundamental concepts and approximations derived from statistical and quantum mechanics applied to molecular processes such as chemical reactions, which are:

- the microscopic reversibility principle, which states that microscopic detailed dynamics of particles is time-reversible because the microscopic equations of motion are symmetric with respect to the inversion of time. This principle is strictly related to mechanical quantities like transition probabilities, trajectories and cross sections. The following is the general expression for the microscopic reversibility principle [70]

$$p_1{}^2\sigma_{12} = p_2{}^2\sigma_{21} \tag{1.39}$$

  in which p_1 and p_2 are the momenta of the colliding particles and σ_{12} and σ_{21} are the differential cross section for the forward and reverse processes. For macroscopic systems as an ensemble of elementary processes the consequence of time-reversibility is that for each individual process there is a reverse process, and in a state of equilibrium the average rate of each process is equal to the average rate of its reverse process.

- the detailed balance principle, which is formulated for kinetic systems that can be decomposed into elementary processes, for which, at equilibrium, the forward process is in equilibrium with its reverse process for each elementary process[71]. Detailed balance can be formulated through the following expression

$$\frac{k_{\text{for}}}{k_{\text{rev}}} = \frac{Q_{\text{P}}}{Q_{\text{R}}} e^{-\Delta E_0/k_B T} = K(T) \tag{1.40}$$

  That is, the ratio of the total rate constants for the forward and reverse reactions is a constant which depends only on temperature T. Q_{P} and Q_{R} are the total partition functions of the reactants and the products. k_{for} and k_{rev} assume the following expressions

$$k_{\text{for}} = \sum_i \sum_f k_{if} x_i \tag{1.41}$$

$$k_{\text{rev}} = \sum_i \sum_f k_{fi} x_f \tag{1.42}$$

x_i is the fraction of the reactants in state i and x_f the fraction of products in state f.

Detailed balance can be derived from microscopic reversibility by making use of the connection between cross sections and rate constants

$$k_{\text{for}} = \int_{p_1} \int_{\Omega} v_1 \sigma_{12} \text{f}\left(p_1\right) \text{d}^3 p_1 \ \text{d}^2\Omega \tag{1.43}$$

$$k_{\text{rev}} = \int_{p_1} \int_{\Omega} v_2 \sigma_{21} \text{f}\left(p_2\right) \text{d}^3 p_2 \ \text{d}^2\Omega \tag{1.44}$$

where $\text{d}^2\Omega$ is the product scattering angle, whose integration converts the differential scattering cross section into a total cross section, and thereby, it includes all possible contributions to k_{for} or k_{rev} that occur for a fixed initial translational momentum p_1 or p_2.

- the infinite sink approximation, which states that in a highly diluted system the dissociation of an isomer, or reaction intermediate, is considered as an irreversible process, since the probability of a second effective collision between the two product fragments is extremely unlikely due to the rarefied nature of the system itself[72].

Given all these assumptions, many landmarks have been reached during the historical progression of chemical kinetics, like the steady-state approximation of Bodenstein and Lind and the Lindemann-Hinshelwood mechanism involving activated molecules for unimolecular dissociation or isomerization reactions. Also theoretical models for calculating the specific rate constants like transition state theory (TST) for pressure-independent thermal rate constant and the Rice-Ramsperger-Kassel-Marcus theory for microcanonical and pressure dependent rate constants. In general, the calculation of reliable rate constants often involves two separate steps: (i) calculation of the potential energy surface (PES) for electronically adiabatic processes, also called Born-Oppenheimer reactions, or calculation of multiple PESs and their couplings for electronically non-adiabatic reactions also called non-Born-Oppenheimer reactions, and (ii) the calculation of the rate constants using the kinetic models mentioned above and in the Introduction. Neverthless, for complex multi-well interconnected chemical reaction mechanisms involving several chemical species, the most powerful framework is the master equation, *i.e.*, the set of coupled rate equations for all the steps in the mechanism, to compute the time evolution and the rate coefficients of all the possible reaction channels[73].

1.3.1 Single-step reactions

Transition state theory

Generally a single step reaction is represented as

$$A + B \longrightarrow P$$

Where A and B are the reactants and P the products. The rate of change of the abundances of reactants and products is called the reaction rate law and is given by the following expression

$$\text{rate } = \frac{d[P]}{dt} = k[A][B], \tag{1.45}$$

where $[P]$, $[A]$, $[B]$ are the abundances of the species involved in the reaction and k is the reaction rate constant, for which its dependence on the temperature is defined by the Arrhenius equation:

$$k = A \exp\left(-\frac{E_a}{k_B T}\right) \tag{1.46}$$

where A is the pre-exponential or "frequency" factor, which is a measure of the rate at which collisions occur and may be temperature-dependent, E_a is the activation energy which can be roughly interpreted as the minimum energy that the reactants must have to form products, k_B is Boltzmann's constant and T the temperature. If a reaction obeys the Arrhenius equation, then the Arrhenius plot ($\ln k$ versus $\frac{1}{T}$) should be a straight line with the slope and the intercept being -$\frac{E_a}{k_B}$ and A, respectively, as shown in Figure 1.6.

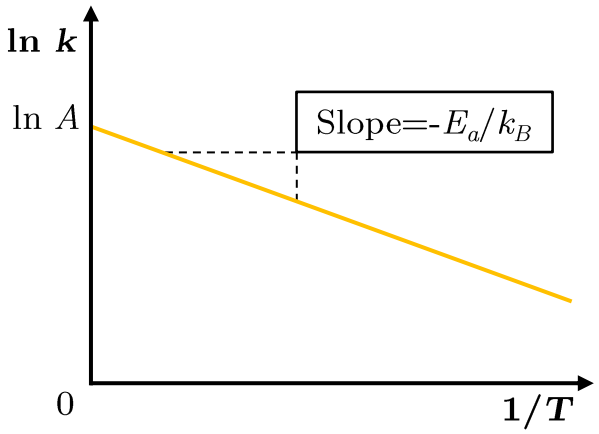

Figure 1.6: Arrhenius plot

The Arrhenius equation describes the rate constant for a reaction from reactants to products ignoring any mechanistic consideration like the presence of intermediates

along the reaction pathway. TST, also referred to as "activated-complex theory", explains the reaction rates of elementary chemical reactions. With activated-complex, it is meant an unstable arrangement of atoms that exists momentarily at the peak of the activation energy barrier and it is usually called TS. This theory, based on concepts and quantities derived from statistical mechanics, provides an expression of k making some assumptions:

- there is chemical equilibrium between reactants and the "activated complex"
- once a molecule has reached the TS it may either come back to reactants or evolve into products
- if it crosses the TS, the system can only evolve into products.

The main result of TST is the following expression for the thermal rate coefficient:

$$k(T) = \frac{k_B T}{h} \frac{Q^{\ddagger}}{Q_R} \exp\left(-\frac{E_a}{k_B T}\right) \tag{1.47}$$

where $Q^{\ddagger}$ and Q_R are the partition functions of the transition state and reactants, respectively. These functions are fundamental to calculate the thermodynamic properties of the molecular system and are usually computed in the rigid-rotor harmonic-oscillator (RRHO) approximation, which allows to decouple the translational, rotational, vibrational and electronic degrees of freedom. So the total partition function for all the species involved in the reaction will be computed in this way

$$Q_{tot} = Q_{trans} Q_{rot} Q_{vib} Q_{elec} \tag{1.48}$$

where Q_{trans}, Q_{rot}, Q_{vib} and Q_{elec} are translational, rotational, vibrational and electronic partition functions. This approximation could lead to errors, for example in molecules with hindered rotations characterized by low-frequency vibrational modes, where one molecular fragment rotates relative to another around a bond [74].
TST can be applied to reactions involving tight and loose transition states to compute the rate. However, the fundamental limitation of the TST is the overestimation of their rate. This is because the TST counts each crossing of the TS as a reaction, so one molecule turning over and another crossing multiple times and truly reacting once, are all considered reactive events in the TST framework. It happens for both, tight and loose TS. Anyway, for loose TSs, due to the fact that the molecular configuration of the TS, or "activated-complex", cannot be univocally identified, the application of the variational principle for the computation of the rate coefficient is made necessary. In this framework, the TS is defined as the dividing surface that minimizes the flux of reactive molecules passing from reactants to products per unit time. So with this principle, the position of the TS along the reaction coordinate is chosen as the one that minimizes the canonical rate coefficient. In this way the recrossing effect is partially corrected and a better estimation of the rate can be obtained.

Rice-Ramsperger-Kassel-Marcus

As mentioned in the previous section, a molecule that effectively reacts must have a high internal energy which must at least overcome the barrier between reactants and products. In the gas phase the internal energy of the molecules can increase or decrease thanks to collisions with the other molecules that make up the bath gas. Therefore, for a gas phase reaction, the combination of two steps represent a reaction:

- the collision between the molecules of the reactive system A with the particles of a thermal bath M can increase or decrease the internal energy of the molecules, *i.e.*,

$$A + M \rightleftharpoons A^* + M$$

  * indicates the internal excitation.

- the actual reactive event

$$A^* \longrightarrow P$$

This assumption is the basis of the Lindemann-Hinshelwood mechanism formulated by Frederick Lindemann, Cyril Hinshelwood and also by Herman Carl Ramsperger, which supposed and verified experimentally that such two-step mechanism has a non-negligible dependence on pressure and it is able to explain the dynamics of gas-phase unimolecular reactions. In the high pressure limit, collisional activation and deactivation are very fast, so the rate-determining step of the mechanism is the reaction itself and the rate coefficient will be the rate coefficient of the reaction event. Since this does not involve the bath gas, the overall rate coefficient will be independent of pressure. We have the opposite situation in the low pressure limit, the rate-determining step is the collisional activation and deactivation step, which is very slow. It makes the overall rate coefficient proportional to the bath gas pressure. For intermediate pressure values, the k follows a falloff regime. In this framework, the internal states of the molecule A and its excited state A^* are regulated by the microscopic rates of collisional energy transfer from energy level E_j to another level with energy E_i, *i.e.*, $R(E_i, E_j)$, and the microscopic rate of reaction $k(E_i)$ from a level with E_i. Given that only molecules having an energy higher than the activation energy can react, the evolution over time of the population of molecules capable of reacting because of that will be given by the following expression:

$$\frac{dx_i(t)}{dt} = [M] \sum_{j=0}^{\infty} (R_{ij}x_j - R_{ji}x_i) - k_i x_i(t). \tag{1.49}$$

From this expression it is possible to obtain information about the phenomenological rate coefficient, *i.e*, the rate constant for a specific reaction that can be measured as a function of temperature and pressure. Eq. 1.49 can be considered as the most

basic form of the master equation. It can be solved only if information about $k(E_i)$ and the collisional energy transfer R_{ij} are known. It is possible to compute the collisional energy transfer through classical trajectories simulations, which requires a lot of computational effort. In general, $k(E_i)$ is described by Rice-Ramsperger-Kassel-Marcus (RRKM) theory which is the most commonly employed and widely accepted approximate description of the dynamics of the reaction step defined by the following fundamental equation for the rate constant

$$k(E) = \frac{N^{\ddagger}(E - E_0)}{h\rho(E)} = \frac{\int_0^{E-E_0} d\varepsilon^{\ddagger} \rho^{\ddagger}\left(E - E_0 - \varepsilon^{\ddagger}\right)}{h\rho(E)} \tag{1.50}$$

where $N^{\ddagger}(E - E_0)$ is the sum of states from 0 to $E - E_0$ for the TS (computed by excluding the normal mode with imaginary frequency under the assumption that the motion along the reaction coordinates is separable from that of the other modes), vibrational ZPEs of reactants and the TS. The sum of states of the TS can be expressed as an integral of its density of states over the translational energy of the reaction coordinate $\varepsilon^{\ddagger}$.

1.3.2 Unimolecular reactions

As already mentioned, an important class of reactions that frequently occurs in gas phase chemical processes are the unimolecular reactions, which are first-order reactions where the reactants acquire energy for reaction through collisions. This is one of the most conceptually simple types of reactions in chemistry and presents several mechanisms that are helpful in understanding many reactive systems. Dissociation or isomerization of the molecule may be considered as characteristic examples of such reactions.

Dissociation

A dissociation reaction is a decomposition process that starts from an initial reactant to arrive at the formation of multiple products. As consequence of the 'infinite sink' approximation, in the gas-phase the dissociation reactions are considered as irreversible processes and can be schematized in this way

$$A \xrightarrow{k_d} B + C$$

where k_d is the rate constant for the dissociation process. The phenomenological rate equation which defines the rate of change of the relative abundances of the chemical species involved in the reaction are:

$$\frac{d[A]}{dt} = -k_d[A] \qquad \frac{d[B]}{dt} = k_d[A] \qquad \frac{d[C]}{dt} = k_d[A]$$

TST or RRKM theory are usually used to compute k_d.

Isomerization

Isomerization is the simplest case of reversible reaction which describes the interconversion between two chemical species like A and B and is generally represented as

$$A \underset{k_b}{\overset{k_f}{\rightleftharpoons}} B$$

where k_f and k_b are the reaction rate constants for the forward and reverse isomerization processes, which can be computed through TST or RRKM theory.
The phenomenological rate equations which define the rate of change of the relative abundances during the isomerization reaction are:

$$\frac{d[A]}{dt} = -k_f[A] + k_b[B] \qquad \frac{d[B]}{dt} = k_f[A] - k_b[B]$$

1.3.3 Bimolecular reactions

In general, a bimolecular reaction is a chemical process which takes place between two substances A and B and which can lead to the formation of one or more products C_1 , ..., C_n, by passing through one or more reaction steps, which can be represented in the following form

$$A + B \underset{k_b}{\overset{k_f}{\rightleftharpoons}} C_1 + \cdots + C_n$$

The phenomenological rate equations which defines the rate of change of the relative abundances during the above mentioned bimolecular reaction are:

$$-\frac{d[A]}{dt} = -\frac{d[B]}{dt} = k_f[A][B] - k_b \prod_{i=1}^{n} [C_i]$$

where $[A]$, $[B]$, $[C_i]$ are the concentrations of the species involved, k_f and k_b are the forward and reverse temperature-dependent rate constants (or rate coefficients), respectively.
The equilibrium constant, K, for the process depends on the quotient Q_K of the forward and reverse rate constants defined by

$$Q_K = \frac{k_f}{k_b} = \frac{\prod_{i=1}^{n}[C_i]}{[A][B]} \tag{1.51}$$

The temperature-dependent equilibrium constant is defined by

$$K = Q_K^{\circ}(T) \exp\left[-\Delta G_T^{\circ}/RT\right] \tag{1.52}$$

where R is the gas constant, Q_K° is the value of the reaction quotient at the standard state and $\Delta G_T^\circ(T)$ is the standard-state Gibbs free energy of reaction at temperature T and it is defined as

$$\Delta G_T^\circ(T) = \Delta H_T^\circ(T) - T\Delta S_T^\circ \tag{1.53}$$

In general, the free energy change upon reaction is

$$\Delta G = RT \ln \frac{Q_K}{K} \tag{1.54}$$

If the free energy change is zero, the reaction is at equilibrium. If ΔG_T° or ΔG is negative, the reaction may be called exergonic, and if either of these quantities is positive, the reaction may be called endergonic [75].

Association

An important class of bimolecular reactions is the association, where two initial reactants A and B can form a single product C, generally this kind of reaction is represented in reversible form as

$$A + B \underset{k_b}{\overset{k_f}{\rightleftharpoons}} C$$

where k_f and k_b are the forward association rate and the backward re-dissociation rate. This type of reaction is usually involved in most of the chemical reactions of atmospheric, astrophysical and combustion interest that can occur in the gaseous phase. In the case of association processes involving activation barriers, RRKM, TST or VTST are reliable models for calculating k_f and k_b. In the case of barrierless reactions, collisional models, also called capture models, represent a valid alternative for calculating the rates.

1.3.4 Barrierless reactions

Collision theory

The collision theory provides simple and useful models to obtain insights about the temperature and energy dependence of the bimolecular rate constants. The collision between an atom or molecule A at an internal state i with another atom or molecule having an internal state j can give several possible outcomes. They can interact through:

- Elastic collision: the two colliding partners do not undergo any arrangement or change in the internal state or translational energy, only the direction of their relative motion changes.
- Inelastic collision: the two reactants do not rearrange their relative connectivity, but only their internal states.

- Reactive collision: the two colliding partners rearrange their connectivity to form new molecules with different internal energy distribution.

In reactive collisions, where a beam of $A(i)$ molecules with relative velocity V_R colliding a scattering zone containing $B(j)$, it is possible to define the state-selected rate constant k_{ij} and the reaction cross section σ_{ij} as following

$$k_{ij}\left(V_{\mathrm{R}}\right)=V_{\mathrm{R}}\sigma_{ij}\left(V_{\mathrm{R}}\right) \tag{1.55}$$

The average reaction cross section σ_r is obtained by averaging over all the reactants internal states:

$$\sigma_r=\sum_{i,j}w_i^{\mathrm{A}}w_j^{\mathrm{B}}\sigma_{ij}\left(V_{\mathrm{R}}\right) \tag{1.56}$$

where w_i^{A} and w_j^{B} are the Boltzmann weighting factors of the i^{th} and j^{th} reactant's internal states, respectively. The thermal rate constant for the process is obtained by averaging $V_R\sigma_r$ over an equilibrium Maxwell-Boltzmann distribution of V_R

$$k=\beta\left(\frac{8\beta}{\pi\mu}\right)^{1/2}\int_0^\infty dE_{\mathrm{rel}}E_{\mathrm{rel}}\sigma_{\mathrm{r}}\left(E_{\mathrm{rel}}\right)\exp\left(-\beta E_{\mathrm{rel}}\right) \tag{1.57}$$

where

$$E_{\mathrm{rel}}=\mu V_{\mathrm{R}}^2/2 \tag{1.58}$$

is the relative translational energy, with μ being the reduced mass of relative translational motion.
It is also useful to define the reaction probability P_R as a function of the impact parameter b, which is defined as the distance of closest approach between the two molecules in the abscence of interparticle forces. The probability of reaction decreases to zero for large b. Actually, we can consider a value of $b=b_{max}$ after which the reaction probability is negligible, and the reaction cross section is given by

$$\sigma_r=2\pi\int_0^{b_{\max}}P_R(b)bdb \tag{1.59}$$

The simplest model is to consider the reactants as hard spheres that do not interact with each other if the intermolecular distance is larger than the arithmetic average d of their diameters, and so $P_R(b>d)=0$, but that react at all shorter distances so $P_R(b>d)=1$ [75]. For this case the reaction cross section is πd^2, and by applying Eq. 1.3.4 one finds that the reaction rate equals

$$k(T)=\left(\frac{8}{\pi\mu\beta}\right)^{1/2}\pi d^2 \tag{1.60}$$

An improvement of this model is the capture model (CM) or reactive hard spheres model in which it is assumed that the reaction occurs if $\mu V_{LOC}^2/2$ exceeds a threshold

energy E°, where V_{LOC} is the relative velocity along the line of centers, *i.e.*, in the direction connecting the centers of the two spheres.
CM is used also to describe the 'barrierless' processes considering the strong long-range attractive forces between reactants. In this way, the interaction potential can be expressed as an expansion series of the distance R between the colliding particles

$$V_R = \sum_n -\frac{C_n}{R^n} \tag{1.61}$$

The leading power n, as well as the interaction coefficient C_n for a given reaction system, depends on the nature of the interaction. For collisions which involve reactants with a non-zero impact parameter a centrifugal term needs to be added to the potential to account for the relative orbital motion of the two fragments. This leads to the formulation of an effective potential of the form

$$V_{\text{eff}} = \frac{L^2}{2\mu R^2} - \sum_n \frac{C_n}{R^n} \tag{1.62}$$

where the angular momentum L can be written as

$$L = \mu V_R b \tag{1.63}$$

where μ is the reduced mass of the system, v the relative velocity of the colliding species, and b the impact parameter.
A paradigmatic case of barrierless reaction is the collision of an ion with a neutral molecule, for which the Langevin model can be employed. It assumes that the ion is a point charge and the molecule is a sphere with polarizability α. This model assumes that at long range only the ion-induced dipole attractive term in the potential is important; the effective potential is then given by

$$V_{\text{eff}} = \frac{L^2}{2\mu R^2} - \frac{1}{2}\frac{\alpha q^2}{R^4} \tag{1.64}$$

where R is the distance between collision partners, q is the charge of the ion, and L is the orbital angular momentum. The first term in Eq. 1.64 is the centrifugal potential, and the second term is the ion-induced dipole potential defined by a general expression C_4/R^4 as indicated in Eq. 1.62. Sustituting Eq. 1.63 and using Eq. 1.58 we obtain

$$V_{\text{eff}}(R) = E_{\text{rel}}\left(\frac{b}{R}\right)^2 - \frac{1}{2}\frac{\alpha q^2}{R^4} \tag{1.65}$$

The effective potential in Eq. 1.65 has a single maximum at a radius $R*$ given by

$$R_* = \frac{1}{b}\left(\frac{\alpha q^2}{E_{\text{rel}}}\right)^{1/2} \tag{1.66}$$

and the effective potential at the maximum is

$$V_{\text{eff}*} = \frac{{E_{\text{rel}}}^2 b^4}{2\alpha q^2} \tag{1.67}$$

The critical impact parameter b_* is obtained from $V_{\text{eff}}*$ and is given by

$$b_* = \left(2\alpha q^2/E_{\text{rel}}\right)^{1/4} \tag{1.68}$$

and the cross section is

$$\sigma = \pi {b_*}^2 = \pi \left(\frac{2\alpha q^2}{E_{\text{rel}}}\right)^{1/2} \tag{1.69}$$

If $E_{\text{rel}} < V_{\text{eff}}*$ the centrifugal barrier cannot be penetrated and no reaction occurs. If $E_{\text{rel}} = V_{\text{eff}}*$, the ion can move inside the centrifugal barrier, and the reaction probability is assumed to be equal to unity. So, substituting in Eq. 1.55 the expression of the cross section defined by Eq. 1.69, the relative velocity expressed as $V_R = (\frac{2E_{rel}}{\mu})^{\frac{1}{2}}$ and after some rearrangements, we obtain the temperature and velocity independent Langevin rate constant

$$k_{\text{L}} = q\sqrt{\frac{\pi\alpha}{\varepsilon_0\mu}}, \tag{1.70}$$

where ε_0 is the permittivity of free space and q is the ionic charge.
Capture theory methods sought to adapt the Langevin equation to include the effects of temperature, polarizability, dipole moment, and orientation of the reactants on the rate coefficient. One of this attempts was the 'locked' dipole (LD) orientation method. The LD method assumes that the dipole of the polar molecules locks at zero angle ($\Theta = 0$) when approaching the ion, yielding rate coefficients higher than those predicted by the Langevin model. A further extension of the LD method is the average dipole orientation (ADO) theory which suggests that the orientation of the dipole with respect to the ion can be treated as having an average value rather than being permanently locked. ADO reaction rate coefficients can be calculated using

$$k_{\text{ADO}} = q\sqrt{\frac{\pi\alpha}{\varepsilon_0\mu}} + \frac{q\mu_{\text{D}}c}{\varepsilon_0}\sqrt{\frac{1}{2\pi\mu k_{\text{B}}T}}, \tag{1.71}$$

As can be seen in Eq. 1.71, the ADO model builds upon the Langevin equation by adding a term that accounts for the dipole moment and temperature dependence of the rate coefficient, giving rise to the inverse trend with temperature that has been observed experimentally in many ion-polar molecule reaction systems. The parameter c accounts for the average orientation of the dipole of the neutral reactant with respect to the ion ($c = cos\bar{\Theta}$) and depends on both the ratio $\mu/\alpha^{1/2}$ and the temperature of the system.
An analogue of the Langevin ion-dipole model for neutral reactions without a barrier, like the radical-radical reactions, is the Gorin model which replaces $-\alpha q^2/2r^4$ in Eq. 1.64 by $-(C_6/r^6)$ where C_6 is a constant. With the Gorin model, the thermal rate constant is given by

$$k_{\text{Gorin}}\,(T) = \sqrt{\frac{\pi}{\mu}}2^{11/6}\Gamma\left(\frac{2}{3}\right)(C_6)^{1/3}\,(k_{\text{B}}T)^{1/6} \tag{1.72}$$

In this model a centrifugal barrier is predicted at much smaller R than that of the Langevin model, which makes reactions between neutral molecules less likely than ionic reactions to be dominated by the long-range force law.
All CMs are based on the assumption that a collision event will yield products with unit probability, if the reactants have enough energy to surmount the centrifugal barrier. The simplicity and the approximations employed in these models give rise to several limitations. The main drawback of CMs is that they do not account for interactions that happen at short range. This is due to the fact that the CM considers only the likelihood that two reactants form a reaction complex, based on their long-range attraction. In this way, it is not possible to predict the branching ratios of different reaction pathways when more than one product channel is available. Discarding the description of short-range interactions does not allow to take into account the presence of submerged barriers which can influence the likelihood of a reaction proceeding to products. Moreover, the non-inclusion of short-range interactions, and the assumption that all captured reactants go on to form products, make the results obtainable by CMs upper limits of the reaction rate coefficient for a given system. However, CMs play an important role in predicting the rate coefficients of many important astrochemical processes for which there is no reliable experimental data at the relevant low temperatures[76].

1.3.5 Tunneling models

The tunneling effect is a quantum mechanical phenomenon in which particles, e.g, electrons or atoms, can pass through a potential energy barrier, which according to classical mechanics this would not be possible. This effect has been studied in the physics of electrons or atoms, in solid state physics and also in the context of the escape of α particles from the nucleus, only later it has been appreciated as a factor conditioning chemical reactions [77, 78, 79, 80, 81]. The first to mention the role of the tunneling in chemical reactions were Applebey and Ogden in 1936[82], later in 1938 Bell discussed more about it at the Faraday Discussion[83], proposing it as a possible cause of the non-linear trend of Arrhenius plots. A lot of theoretical and experimental work has been done to address the problem of the tunneling effect on chemical reactions, and several models have been proposed, such as the one-dimensional Eckart model and the multidimensional models Zero Curvature Tunneling (ZCT) and Small Curvature Tunneling (SCT), which present a different degree of accuracy in the theoretical evaluation of the tunneling effect in chemical reactions.

One-dimensional models

Eckart model

Tunneling effects can be conveniently included by introducing the so called transmission probability $P_{\text{tunn}}(E')$ in RRKM's formulation of $k(E)$:

$$k(E) = \frac{\int_{-V_0}^{E-V_0} \rho^{\ddagger}\left(E - E'\right) P_{\text{tunn}}\ \left(E'\right) \mathrm{d}E'}{h\rho(E)} \tag{1.73}$$

where V_0 is the classical energy barrier for the forward reaction.
Note that now the integral is extended also to energies below the reaction threshold E. Analytical expressions for $P_{\text{tunn}}(E')$ can be obtained by using model potential shapes. In this dissertation one of these, the unsymmetric Eckart potential, has been widely used[84]. For such potential, the transmission probability is given by the following expression:

$$P_{\text{tunn}}(E') = \frac{\sinh(a)\sinh(b)}{\sinh^2((a+b)/2) + \cosh^2(c)} \tag{1.74}$$

where a, b and c are parameters defined by:

$$a = \frac{4\pi\sqrt{E' + V_0}}{h\nu_i\left(V_0^{-\frac{1}{2}} + V_1^{-\frac{1}{2}}\right)} \qquad b = \frac{4\pi\sqrt{E' + V_1}}{h\nu_i\left(V_0^{-\frac{1}{2}} + V_1^{-\frac{1}{2}}\right)} \qquad c = 2\pi\sqrt{\frac{V_0 V_1}{(h\nu_i)^2} - \frac{1}{16}}$$

Here, V_1 is the classical energy barrier for the reverse reaction, and ν_i is the magnitude of the imaginary frequency of the saddle point. One-dimensional tunneling models such as the Eckart model are often used in kinetic modeling and are implemented in most kinetic calculation programs, such as MESS [85], MESMER[86], MultiWell[87, 88], Polyrate[89] and also in StarRate[90, 3].

Multidimensional models

In general, multidimensional models for quantum tunneling rely on the definition of a reaction path as the portion of the PES comprised by the reaction coordinate connecting two minima and the transverse vibrational mode defined by the turning points on the concave side of the reaction path. Along this reaction path the decay probability density $|\psi|^2$ in a classically forbidden region is described by the exponential $e^{-2\theta}$, derived by the Wentzel-Kramers-Brillouin (WKB) approximation, where θ is the action integral generally defined as

$$\theta = \int_{\text{tunnelling region}} \mathrm{d}\xi \, |p_{\xi,\,\text{eff}}| \tag{1.75}$$

where ξ it is a measure of the distance along the tunnelling path and $p_{\xi,\,\text{eff}}$ is the ξ-component of the effective momentum.

Zero Curvature Tunneling

The ZCT approximation involves a one-dimensional tunnelling calculation, it is actually a multidimensional tunnelling approximation because the vibrationally adiabatic potential used along the reaction path involves contributions from the transverse modes. Anyway, in ZCT the tunneling path is approximated as coinciding with the Minimum Energy Path (MEP) and neglects its curvature for which the action integral $\theta(E)$ can be written in this way

$$\theta^{\mathrm{MEP}}(E) = h^{-1} \int_{s_<(E)}^{s_>(E)} ds \left\{ 2\mu(s) \left[V_{\mathrm{a}}^{\mathrm{G}}(s) - E \right] \right\}^{\frac{1}{2}} \tag{1.76}$$

where μ is the reduced mass of the system, $s_<(E)$ and $s_>(E)$ are the left and right classical turning points at which the vibrationally-adiabatic ground-state potential $V_{\mathrm{a}}^{\mathrm{G}}(s)$ given by

$$V_{\mathrm{a}}^{\mathrm{G}}(s) = V_{\mathrm{MEP}}(s) + V_{\mathrm{int}}(s) \tag{1.77}$$

takes on a value equal to

$$V_{\mathrm{a}}^{\mathrm{G}}(s) = E \tag{1.78}$$

$V_{\mathrm{MEP}}(s)$ is the potential energy along the minimum energy path and $V_{\mathrm{int}}(s)$ denotes the total zero-point energy at the reaction coordinate s value

$$V_{\mathrm{int}}(s) = \sum_{i=1}^{3N-7} \frac{1}{2} \hbar \omega_i(s) \tag{1.79}$$

with $\omega_i(s)$ denoting the frequency of mode i and the sum is over all vibrational modes orthogonal to the reaction coordinate at s.

Small Curvature Tunneling

In the SCT approximation the action integral $\theta(E)$ is defined in this way

$$\theta(E) = h^{-1} \int_{s_<(E)}^{s_>(E)} ds \left\{ 2\mu_{\mathrm{eff}}(s) \left[V_{\mathrm{a}}^{\mathrm{G}}(s) - E \right] \right\}^{\frac{1}{2}} \tag{1.80}$$

The action integral is evaluated over the classically forbidden regions, that is, for regions in which the total energy is lower than the effective potential, which is V_a^G. The coupling between the reaction coordinate and the rest of degrees of freedom is included in the effective mass $\mu_{\mathrm{eff}}(s)$. When coupling is included $\mu_{\mathrm{eff}}(s) \leq \mu$, so the action integral is smaller and the tunneling probability is larger. In SCT, the effective mass is defined as

$$\mu_{\mathrm{eff}}^{\mathrm{SC}}/\mu = \min \left\{ \begin{array}{l} \exp\left\{ -2\bar{a}(s) - [\bar{a}(s)]^2 + (\mathrm{d}\bar{t}/\mathrm{d}s)^2 \right\} \\ 1 \end{array} \right. \tag{1.81}$$

where

$$\bar{a} = |\kappa(s)\bar{t}(s)| \tag{1.82}$$

in which $\kappa(s)$ is the reaction-path curvature

$$\kappa(s) = \left\{ \sum_{m=1}^{F-1} \left[B_{mF}(s) \right]^2 \right\}^{1/2} \tag{1.83}$$

and $\bar{t}(s)$ is the turning point

$$\bar{t} = \left[\frac{\hbar}{\mu\bar{\omega}(s)}\right]^{\frac{1}{2}} = \left(\sum_{m=1}^{F-1}\left[\frac{B_{m,F}(s)}{\kappa(s)}\right]^2 [t_m(s)]^{-4}\right)^{-\frac{1}{4}} \tag{1.84}$$

of an harmonic oscillator with frequency

$$\bar{\omega} = \left(\sum_{m=1}^{F-1}\left[\frac{B_{m,F}(s)}{\kappa(s)}\omega_m(s)\right]^2\right)^{\frac{1}{2}} \tag{1.85}$$

where $B_{m,F}(s)$ are the reaction-path curvature coupling elements between the reaction coordinate s and a mode m perpendicular to it[91].
$t_m(s)$ are the individual turning points of all the normal modes perpendicular to the reaction path

$$t_m(s) = \pm\left[\frac{\hbar}{\mu\omega_m(s)}\right]^{\frac{1}{2}} \tag{1.86}$$

and the last term on the right hand side of Eq. 1.81 is calculated using central-finite differences

$$\left(\frac{\mathrm{d}\bar{t}}{\mathrm{d}s}\right)^2 = \sum_{m=1}^{F-1}\left(\frac{dt_m(s)}{ds}\right)^2 = \sum_{m=1}^{F-1}\left(\frac{t_m\left(s+\delta s_{\mathrm{H}}\right) - t_m\left(s-\delta s_{\mathrm{H}}\right)}{2\delta s_{\mathrm{H}}}\right) \tag{1.87}$$

with a step size given by $\delta s_{\mathrm{H}} = N_{\mathrm{H}}\delta s$, where N_{H} is the step along the MEP between Hessian calculations.
The tunneling transmission probabilities called semiclassical adiabatic ground-state probability $P^{\mathrm{SAG}}(E)$ are calculated by the following expression:

$$P^{\mathrm{SAG}}(E) = \begin{cases} 0, & E < E_0 \\ \{1+\exp[2\theta(E)]\}^{-1}, & E_0 \le E \le V^{\mathrm{AG}} \\ 1 - P^{\mathrm{SAG}}\left(2V^{\mathrm{AG}} - E\right), & V^{\mathrm{AG}} \le E \le 2V^{\mathrm{AG}} - E_0 \\ 1, & 2V^{\mathrm{AG}} - E_0 < E \end{cases} \tag{1.88}$$

where V^{AG} corresponds to the maximum of the energy barrier. Various kinetics programs have implemented multidimensional tunnel models, such as Polyrate[89], Pilgrim[92], and MultiWell[87, 88]. The theoretical framework described in this section is also the one implemented in the Pilgrim program.

1.3.6 Molecular stabilization processes

Typically in the gas-phase we have to deal with the two initial reactants A and B and the molecules M constituting the thermal bath thanks to which collisional stabilization can take place to favor the formation of complexes or reactive intermediates involved in a chemical reaction. To stabilize such intermediates, a second stabilization mechanism is possible thanks to the radiative emission. However it is strongly disadvantaged since under standard pressure conditions the collisional process is much faster than

the radiative one. Neverthless, in the low pressure regime, the collisional stabilization of the reaction complexes or intermediates is strongly disadvantaged precisely because the collision probability is greatly reduced. For this reason, under these zero-pressure conditions, the radiative emission plays a determining role in the stabilization of the complexes or intermediates formed by the bimolecular association reactions.

Collisional energy transfer

The most widely used model to compute the collisional energy transition probabilities $P(E|E')$ is the so-called exponential down model, its formulation is a consequence of the partitioning of the energy space which is illustrated later in this dissertation in Section 1.1.7. The basic assumption is that the energy transfer probability depends only on the internal energy of the molecule without taking into account its collisional history, it is calculated through this expression

$$P(E_i|E_j) = C(E_j)\mathrm{e}^{-\frac{E_j - E_i}{\langle \Delta E \rangle_d}} \tag{1.89}$$

where $E_j > E_i$, $C(E_j)$ is a normalization constant, and $\langle \Delta E \rangle_d$ is the average energy transferred per collision in a downward direction. The transition probabilities for energy transfer in the upward direction can be obtained via detailed balance.
Other models with different transition probability distributions have been proposed, such as Gaussian models and double exponential models. It has often been noted that classical trajectory simulations as well as experimental data suggest that the exponential down model is perhaps not the most accurate for describing collisional transition probabilities and that models with longer tails are more accurate[86].

Radiative emission

The collision of an ion A^+ or a radical species $A^{\cdot}$ with a molecule typically results, at least initially, in the formation of an ion-molecule complex AB^+, or for the radical species into a radical intermediate because of the formation of a chemical bond between the two reactants. The stabilization of this complexes through the removal of the excess energy above the dissociation limit occurs in the direct competition with its dissociation back to reactants or no to other products. At ordinary pressures the stabilization of this complex occurs through collisional stabilization processes. However, radiative emission provides an additional stabilization route which becomes dominant in the low pressure limit[93]. Thus for pressures below about 10^{-5} mbar one must generally consider a reaction scheme which involves combination of a bimolecular complex formation step

$$A^+ + B \xrightarrow{k_f} \left[AB^+\right]^* \tag{1.90}$$

a unimolecular redissociation step

$$\left[AB^+\right]^* \xrightarrow{k_b} A^+ + B \tag{1.91}$$

a collisional stabilization step

$$\left[AB^+\right]^* + M \xrightarrow{k_c} AB^+ + M \tag{1.92}$$

and a radiative stabilization step

$$\left[AB^+\right]^* \xrightarrow{k_r} AB^+ + h\nu \tag{1.93}$$

It is possible to develop an effective bimolecular rate constant k_{eff} for the loss of reactants given by 1.94 based on the outcomes of the experimental investigation of systems similar to those mentioned above.

$$k_{\text{eff}} = \frac{k_f \left(k_r + k_c[M]\right)}{k_b + k_r + k_c[M]} \tag{1.94}$$

Which, performing a Taylor series expansion about $[M] = 0$ yields

$$k_{\text{eff}} = \frac{k_f k_r}{k_b + k_r} + \frac{k_f k_b k_c[M]}{\left(k_b + k_r\right)^2} \tag{1.95}$$

If a zero-pressure limit is assumed to simulate the ISM pressure conditions it is necessary to consider $[M] = 0$. So, the effective bimolecular rate constant becomes

$$k_{\text{eff}} = \frac{k_f k_r}{k_b + k_r} \tag{1.96}$$

where k_f and k_b can be determined using capture models depending on the nature of the reactants and the detailed balance principle. The radiative rate constant k_r within the harmonic approximation for any distribution of vibrational states is given by

$$k_r\left(\text{ s}^{-1}\right) = \sum_{i=1}^{N_m} \sum_{n=0}^{\infty} 1.25 \times 10^{-7} n P_i(n) I_i(\text{ km/mol}) \nu_i^2 \left(\text{ cm}^{-1}\right) \tag{1.97}$$

where N_m is the number of vibrational modes, $P_i(n)$ is the probability of vibrational mode i being in level n, I_i is the i absorption intensity for the $v = 0$ to $v = 1$ transition of mode i and ν_i is the ith vibrational frequency. Therefore, a technique for figuring out $P_i(n)$ and the various IR absorption intensities is needed in order to determine the radiative rate constant *apriori*. The radiative rate constant can instead be computed for the canonical distribution with the equivalent total energy for moderately large molecules since the canonical and microcanonical distributions are sufficiently comparable. Similar to the microcanonical case for which

$$P_i(n, E, J) = \frac{\rho_{\text{vib}}^{N-1,i}\left(E - BJ^2 - nh\nu_i\right)}{\rho_{\text{vib}}\left(E - BJ^2\right)} \tag{1.98}$$

where $\rho_{\text{vib}}^{N-1,i}$ is the DOS for the complex in the absence of the ith degree of freedom and BJ^2 is the rotational energy, the canonical distribution function is substituted for $P_i(n)$ during the evaluation of the radiative rate constant for the canonical case

$$P_i(n,T) = \exp\left(-\frac{h\nu_i n}{k_B T}\right)\left[1-\exp\left(-\frac{h\nu_i}{k_B T}\right)\right] \tag{1.99}$$

where T is the temperature, h the Planck constant and k_B the Boltzmann constant[94]. In the astrochemical context, the radiative emission assumes primary importance in the stabilization process of the radical and ionic association complexes and also of the various reaction intermediates. Given the low pressures characterizing the ISM (between 10-100 molecules/cm^3 corresponding to 10^{-18}-10^{-19} atm) it is possible to hypothesize that the collision stabilization is not effective. It is at this juncture that stabilization by radiative emission becomes fundamental. In particular for radical association reactions, in which the association product can only stabilize by radiative emission. It is important to underline that this stabilizing effect increases in importance as the size of the system increases, *i.e.*, the number of atoms composing the molecules as the number of available vibrational modes increases, therefore it also increases. For this reason it is possible to state that in the case of COMs formation reactions, the radiative emission can condition the values of formation rate constants in a decisive way.

1.3.7 Multi-step reactions

Multi-step reactions are those reactions which, in order to lead to the formation of the reaction products, require several intermediate elementary steps, even interconnected to each other, which combined can generate various formation reaction paths having one or more single-step reactions in common. The study of the kinetics of these interconnected multi-step reaction networks is of great importance in gas phase chemistry since the chemical species involved are connected through multiple pathways having different rate constants which can significantly condition the overall kinetics of the reaction mechanism considered.

Chemical Master Equation

The theoretical formulation of the chemical master equation is based on mathematical concepts derived from probability theory and on the description of energy transfer processes and chemical reactions as stochastic processes classified as Markovian processes. In general, the theoretical framework to study the time evolution of complex multi-component systems characterized by stochastic Markov processes is the Chapman-Kolmogorov equation which represents the starting point for the derivation of the master equation. The purpose of this section is not to delve into the theoretical mathematical aspects on which the formulation of ME is based, but rather to provide a description more related to the chemical application of this mathematical tool. However, to obtain such information it is possible to find a rich literature concerning the theoretical foundations of the master equation.
Both the collisional energy transfer stabilization and the chemical reactivity can be defined as time-homogeneous Markovian stochastic processes. Therefore, to study the time evolution of these phenomena it can be studied by applying is possible to apply

the master equation approach and defining as a stochastic variable the energy E in an interval E+dE, which defines the internal energy that the molecules can assume.
To model the molecule collisions in this energy interval the following assumptions are made:

- The reactants are dilute in a bath gas and the number of collisions undergone by a typical reactant molecules depend only on the length of the time period τ.
- The probability of a molecule undergoing collision in a sufficiently small time interval τ is proportional to the length of the time interval, $\omega(E)\tau + o(\tau)$.
- The probability that more than one collision occurs in τ is $o(\tau)$.

Given all the previous assumptions and considering the collisional energy transfer process as homogeneous, it is possible to study the probability distribution function for energy at time t and to formulate the master equation for the energy transfer

$$\frac{\partial}{\partial t}p\left(E_i,t\right) = \int \omega\left(E_j\right) P\left(E_i \mid E_j\right) p\left(E_j,t\right) dE_j - \omega\left(E_i\right) p\left(E_i,t\right) \tag{1.100}$$

where $P\left(E_i \mid E_j\right)$ was already defined in 1.89 as the collisional transition probability. In order to include in the ME equation also the chemical reactivity it is necessary to compute the microcanonical rate coefficient, $k(E)$, through the RRKM theory reported in the previous sections. Chemical reactivity is considered as a loss of population from the energy space of reactants. The ME then becomes

$$\frac{\partial}{\partial t}p\left(E_i,t\right) = \omega \int_0^\infty P\left(E_i \mid E_j\right) p\left(E_j,t\right) dE_j - \omega p\left(E_i,t\right) - k\left(E_i\right) p\left(E_i,t\right) \tag{1.101}$$

Due to the fact that the right-hand side is linear in the population density, the equation can be written in a more compact form as

$$\frac{\partial}{\partial t}p(E,t) = \hat{M}p(E,t) \tag{1.102}$$

where the operator $\hat{M}$ represents the combined effects of energy transfer and reaction, and will be referred to as a transition operator 1.102. One possible approach to solve this equation is the technique of separation variables to separate time from the energy variable which leads to the expansion

$$p(E,t) = \sum_i c_i \phi_i(E) e^{\lambda_i t} \tag{1.103}$$

where c_i are numerical coefficients, λ_i and $\phi_i(E)$ are the eigenvalues and eigenfunctions of the operator $\hat{M}$:

$$\hat{M}\phi_i(E) = \lambda_i \phi_i(E) \tag{1.104}$$

So, to solve Eq 1.104 it is possible to use the classical approach based on the diagonalization technique of the matrix representation of the operator $\hat{M}$ to obtain eigenvalues

and eigenvectors. The other widely used method to solve ME is through stochastic approaches, like kinetic Monte Carlo simulations and the Gillespie algorithm[95]. It can be done through an energy grained approach for which eigenvalues and eigenvectors are computed assuming that the energy space is partitioned into a set of contiguous intervals, or grains. The grain size must be chosen in order to minimize the discretization error and also because to reach the convergence the grain size must be significantly smaller than $\langle \Delta E \rangle_d$. Moreover, the grain size must be small enough such that the microcanonical rate coefficients, transition probabilities, densities of states, and normalization constants do not vary significantly across the grain. To calculate the mean energy of a grain, ϵ_i, it is necessary to determine the number of states that fall within the grain, N_i, also called sum of states (SOS). The density of states (DOS) function must take into account the discrete nature of the rovibrational states. This is most often done using a direct count algorithm such as Beyer-Swinehart algorithm [96] for directly computing harmonic oscillator, or the Stein-Rabinovitch algorithm [97] for anharmonic and hindered rotors oscillators, or the Wang-Landau algorithm [98] for computing quantum densities of states for fully coupled anharmonic systems. Briefly, this algorithm involves the division of the energy axis into a set of contiguous intervals, which, to avoid confusion with the energy grains of the ME, will be referred as cells. It is then determined in which of these cells rovibrational states lie. So, for each cell the number of rovibrational states is computed and they are summed to give N_i for the grain. The grain energy and the associated rate coefficient for reactive loss are formed by taking averages of these quantities over the grain.
Then a ME for the grain distribution, $p_i(t)$, also called an energy grained master equation, or EGME can be written and has the form

$$\frac{d}{dt}p_i(t) = \omega \sum_{j=1}^{m} P_{ij}p_j(t) - \omega p_i(t) - k_i p_i(t) \tag{1.105}$$

or in more compact matrix form,

$$\frac{d}{dt}\mathbf{p} = [\omega(\mathbf{P} - \mathbf{1}) - \mathbf{K}]\mathbf{p} \tag{1.106}$$

where $\mathbf{P}$ is the matrix of transition probabilities, $\mathbf{1}$ is the identity matrix, $\mathbf{K}$ is a diagonal matrix of microcanonical rate coefficients, ω is the collision frequency and $\mathbf{p}$ is the population distribution vector. Finally, setting $\mathbf{M} = \omega(\mathbf{P} - \mathbf{1}) - \mathbf{K}$, the EGME can be written in the compact form

$$\frac{d}{dt}\mathbf{p} = \mathbf{M}\mathbf{p} \tag{1.107}$$

where $\mathbf{M}$ will be referred to as the transition matrix. The solution of this equation provides the time dependence of $\mathbf{p}$ and has the form

$$\mathbf{p}(t) = \mathbf{U}e^{\mathbf{\Lambda}}\mathbf{U}^{-1}\mathbf{p}(0) \tag{1.108}$$

where $\mathbf{p}(0)$ is the initial population vector, $\mathbf{U}$ is a matrix whose columns are the right eigenvectors of $\mathbf{M}$, and $\mathbf{\Lambda}$ is a diagonal matrix of the corresponding eigenvalues.

Eigenvalues are often referred to as the Chemically Significant Eigenvalues (CSEs). Along with their corresponding eigenvectors, they describe the time evolution of the system as it approaches equilibrium. The CSEs are those that correspond to the experimentally observed phenomenological rates measured in typical kinetics experiments, since they describe reaction and interconversion between the different molecular configurations on the PES. The remaining eigenvalues, those that are much more negative than the CSEs, correspond to collisional relaxation on very short time scales, and are often referred to as the Internal Energy Relaxation Eigenvalues (IEREs)[99].
In Figure 1.7 a graphic representation of a generic reactive multi-step system is shown.

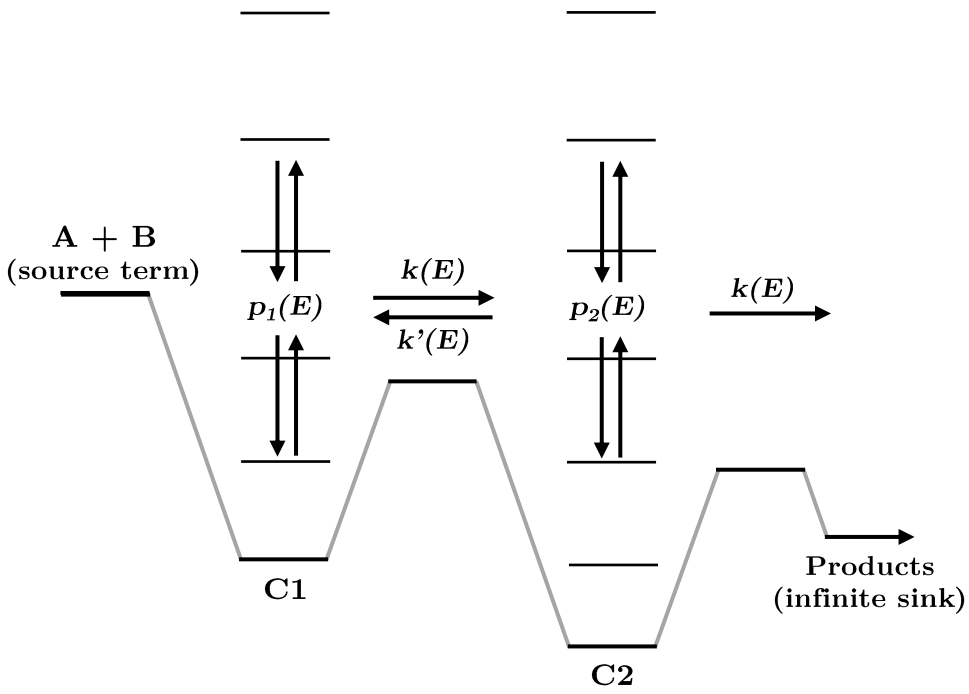

Figure 1.7: Graphical representation of multi-step reaction and EGME model.

The major problem in applying the master equation to an association reaction is that the bimolecular nature of association introduces nonlinearities, which make the master equation hard to formulate and to be solved. Any such solution needs careful analysis to extract a quantity that will serve as an association rate coefficient. An approach to determine the association rate coefficient is to modify the ME by adding a source term

$$\frac{d}{dt}\mathbf{p} = \mathbf{M}\mathbf{p} + \mathbf{g}(t) \tag{1.109}$$

where the vector $\mathbf{g}$ represents the rate at which individual grains are populated by the association reaction. A number of approaches have been made to tackle this problem and they can be broadly classified into three main groups: steady-state methods, linearization or homogeneous methods, and source or inhomogeneous methods.
One of the most used methods is the method of linearization by pseudo approximation

of the first order, in which the quantity of one of the two reactants is considered, much larger superior than that of the other.
Taking into account all the elements previously described in the various sections, more sophisticated ME models can be constructed by combining three elements, namely simple dissociation, isomerization, and the linearized or homogeneous source term to study a wide range of gas-phase reactions characterized by very different temperature and pressure conditions.

Chapter 2

StarRate: a computer package for modeling the kinetics of astrochemical reactions

The theoretical framework and the structure of the StarRate program is described in this Chapter as an implementation of the work started by Nandi et al[100]. A comprehensive illustration of kinetic simulations for a wide class of reactions, including dissociative recombination and radiative association processes, shows that StarRate is an effective tool for calculating reliable phenomenological rate coefficients and branching ratios useful to predict the relative abundances of the interstellar molecules detected in the ISM as products of complex multi-step reaction mechanisms. The program is written in the F language, a subset of the Fortran 95 language. It has been conceived in the object-based programming paradigm and it shows a modular structure. It is indeed based on four main modules `in_out`, `molecules`, `steps` and `reactions` which handle the molecular species, the elementary steps and the entire reaction scheme. Data parsing is performed through a python script, `G2R.py`, and all the information necessary to run the kinetics calculation are collected through an XML format interface which allow interoperability with popular electronic-structure packages and with the graphical interface of the Virtual Multifrequency Spectrometer (VMS). This Chapter is based on an article already published [3]. At the end of the chapter, more recent and future implementations are discussed that allow a wider range of reaction types to be studied.

A General User-Friendly Tool for Kinetics Calculations of Multi-Step Reactions within the Virtual Multifrequency Spectrometer Project

2.1 Introduction

Calculation of chemical kinetics in the gas phase by accurate theoretical models is extremely important in research areas like atmospheric chemistry, combustion chemistry and astrochemistry. As a matter of fact, the accurate prediction of reaction rates and the evolution of the involved species in a given set of physical conditions is a key feature for understanding the presence of a molecular or ionic species in that environment. Sometimes the reactions involved are too fast to be tracked by laboratory experiment or the associated physical conditions are simply not reproducible, hence the understanding of those reactions relies on accurate theoretical treatments capable of predicting the evolution of the species involved in a reaction network.
A rigorous treatment of the time evolution of a chemical reaction should be based on quantum-dynamics calculations modeling the motion of the involved nuclei on ab initio potential-energy surfaces [101, 102, 103]. However, exact quantum-dynamics methods are only applicable to very small systems made up of 3 or 4 atoms (see for instance Refs. [104, 105, 106]). For the remaining systems – the vast majority – one can either opt for approximate methods, such as the Multi-Configuration Time-Dependent Hartree (MCTDH) [107] or the Ring Polymer Molecular Dynamics [108] (which can however extend this limit only marginally), or for a (quasi-)classical treatment of the nuclear motion [109, 110, 111].
On the other hand, a less expensive yet reliable route to chemical kinetics is the adoption of statistical models, such as the popular transition-state theory (TST) in one of its variants, which successfully exploits information on the energetics of a limited set of important points of the potential energy surface to predict the kinetics of chemical reactions. The usual procedure in this framework involves the calculation of transition states and intermediates of a given reactions and a description of the motions at molecular level of these species. Then classical or semiclassical transition state theory (TST) is applied to calculate the reaction rates of each of the elementary steps making up the whole reaction (the Rice-Ramsperger-Kassel-Marcus (RRKM)[112, 113, 114] theory, shortly summarized in the following, is usually adopted for unimolecular reactions in the gas-phase). Finally, the time evolution of the relative abundances of each of the reactant, intermediate and product species is calculated using methods based on either master-equation or stochastic approaches.
In this paper, we discuss the implementation of the computer program StarRate for kinetics calculations of multi-step chemical reactions, and its integration in the graphical interface of the user-friendly, multipurpose framework Virtual Multifrequency Spectrometer (VMS) [115]. The Virtual Multifrequency Spectrometer (VMS) is a tool that aims at integrating a wide range of computational and experimental spectroscopic techniques with the final goal of disclosing the static and dynamic physical-chemical properties of molecular systems, and is composed of two parts: VMS-Comp, which

provides access to the latest developments in the field of computational spectroscopy [116, 117], and VMS-Draw, which provides a powerful graphical user interface (GUI) for an intuitive interpretation of theoretical outcomes and a direct comparison to experiment [118]. We discuss the integration of StarRate within the VMS tool and illustrate some features of the developed software through two important reactions: the single-step interconversion of hydroxyacetone and 2-hydroxypropanal, and the more challenging multi-step dissociation of vinyl cyanide. It is worth mentioning here that the reported calculations were performed to the purpose of illustrating the developed computational software, and that providing new accurate results on the above reactions for comparison with experiment is beyond the scope of this work.
The article is organized as follows. Section 2.2 is devoted to computational details of the developed software. In Sections 2.3 and 2.4, we address the kinetics for the above mentioned reactions. In Section 2.5, conclusions are drawn and perspectives are outlined.

2.2 Computational details: StarRate and the VMS tool

StarRate is an object-based, modern Fortran program for modeling the kinetics of multistep reactions. At its current stage of development, StarRate targets multi-step unimolecular reactions (which can however dissociate, irreversibly, to multiple products).From a technical point of view, the program is written in the so-called 'F language' [119, 120], a carefully crafted subset of Fortran 95, and is conceived in an object-based programming paradigm. As described in deeper detail in Ref. [100], StarRate is structured in three main modules, namely `molecules`, `steps` and `reactions`, which reflect the entities associated with a multi-step chemical reaction. All of these modules contain a defined data-type and some related procedures to access and operate on it. The main program, StarRate, controls the sequences of the calling of the procedures contained in each of the three main modules.
Another important module of StarRate is `in_out`, which handles the input and output operations of the program. Input data are accessed by StarRate through an XML interface based on the same versatile hierarchical data structure that is adopted by VMS. At the beginning, the user has to prepare a very simple input file encoding a reaction scheme (see the starrate.inp box in Fig. 2.1) and gather all the files, one for each molecular species, containing data deriving from electronic-structure calculations. These can be either in an internal standard format or directly output files of quantum-chemistry packages,as exemplified in Fig. 2.1 for the case of the Gaussian package. Currently StarRate supports output files from this quantum-chemistry package (.log extension), though support for other popular electronic-structure programs is presently being pursued (see also Refs. [121, 122] on the issue of interoperability and common data formats in quantum chemistry). Then a Python script is run which extracts data from the output files generated by the quantum-chemistry calculations and, driven by the reaction scheme, collects the information in the proper sections of the XML file.
The structure of the XML interface is schematized in Fig. 2.2. The whole XML doc-

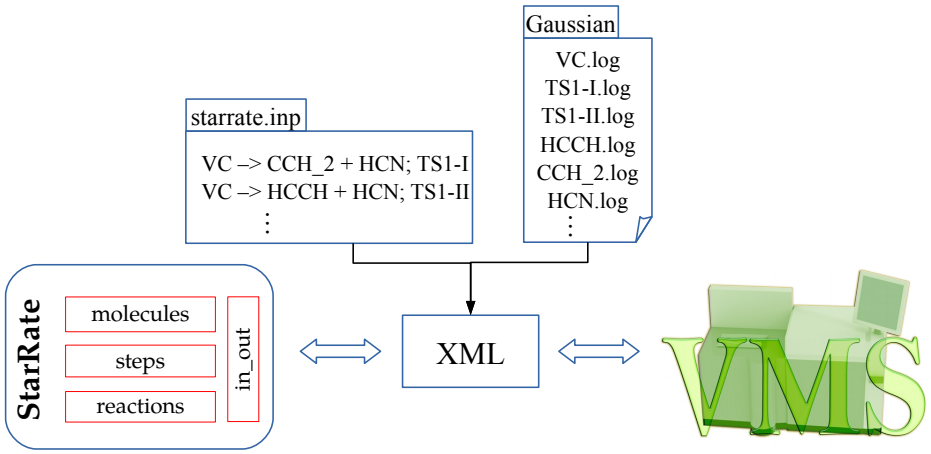

Figure 2.1: Diagram showing the interoperability between electronic-structure calculations, StarRate, and VMS through a dedicated hierarchical data structure XML interface.

ument develops under a root element named `escdata`. The `escdata` has one child element for each molecule named `section_run`. Each of these elements contains three nodes: `program_info`, `section_system`, and `system_single_configuration_calculation`. All the information regarding a molecule is handled by these three sibling nodes. The `program_info` node contains two subnodes which keep track of quantum chemical software name and .log file location. The `section_system` node contains basic information which does not require quantum chemical information (*viz.*, molecular charge, spin multiplicity, atom label, atomic numbers, rotational constants). The last sibling, `system_single_configuration_calculation` contains information which requires quantum chemical calculations (*viz.*, vibrational constants, SCF energy, density of state data). Finally, the last `section_run` collects information on physical conditions and on the reaction under study. For illustrative purposes, the actual .xml file for the reaction studied in Section 2.3 is given as supplementary material.
Once the XML has been generated, the StarRate program comes into play. The module `in_out` reads the XML file (a well-built external Fortran library, `FoX_dom` [123], is used for XML parsing) and saves the data for each molecule and step as structured arrays of the `molecules` and `steps` modules, respectively. Some information such as vibrational frequencies, rotational constants, electronic energy, are collected from the electronic-structure calculations; some other information such as densities of states (see later on) and single-step microcanonical rate coefficients are either also read as input data or computed internally to StarRate. Lastly, the `reactions` module solves the kinetics for the overall reactions using a chemical master equation method. At the end of the calculations, VMS is used to access, visualize and analyze the data produced thanks to the shared XML interface (see Fig. 2.1).

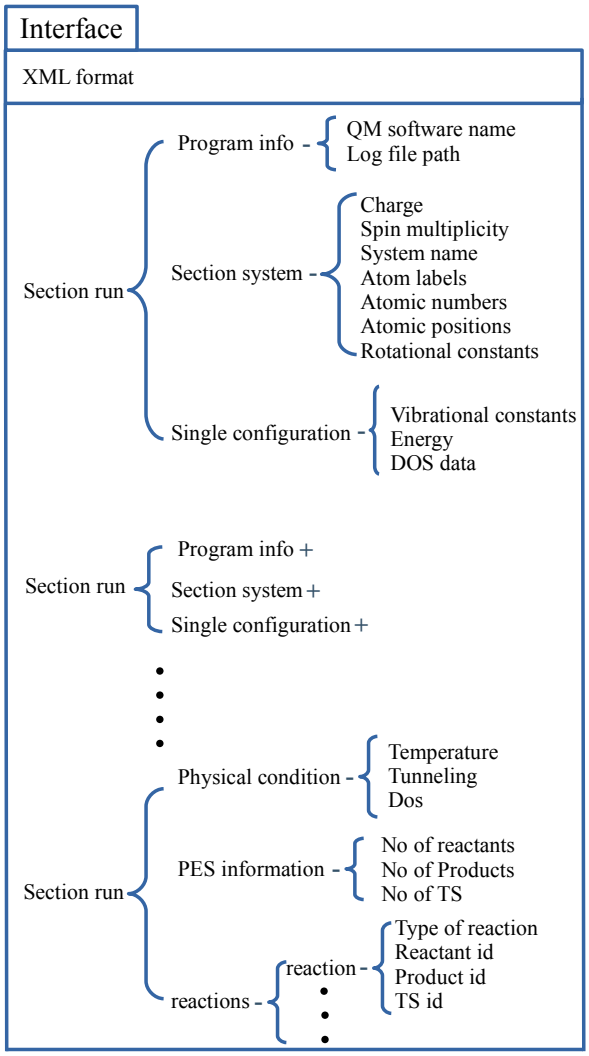

Figure 2.2: Hierarchical data structure of the XML interface.

2.3 Single-step reactions

The interconversion reaction between hydroxyacetone and 2-hydroxypropanal is an important reaction in the context of atmospheric chemistry because the hydroxyacetone represent the simplest form of photochemically oxidised volatile organic compounds [124]. In a recent study, Sun et al. [125] have considered the interconversion mechanisms on several hydroxycarbonyl compounds, and much attention has been focused on the interconversion reaction between hydroxyacetone and 2-hydroxypropanal. This isomerization reaction can occur through three different mechanisms, 2 high-barrier multistep processes and, as shown in Fig. 2.3, a direct mechanism via double hydride shift involving a low-barrier concerted transition state. In their work, Sun et al. also supposed that hydroxycarbonyl compounds can adsorb solar radiation, as carbonyl compounds, from 320 to 220 nm and then undergo an internal conversion to the vibrationally excited ground state with an energy more than sufficient to overcome the isomerization barrier, and computed RRKM microcanonical rate coefficients in order to

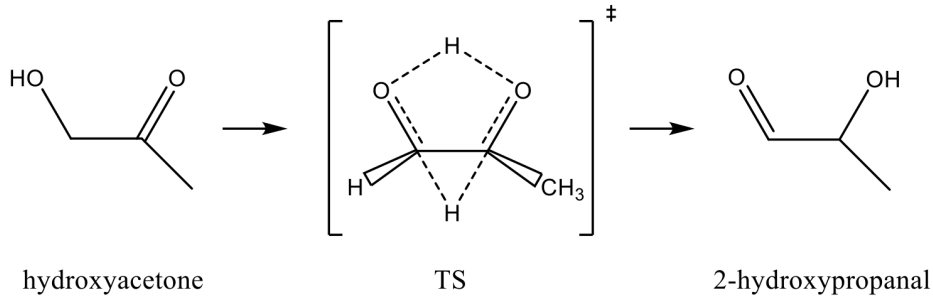

Figure 2.3: Direct isomerization reaction mechanism between hydroxyacetone and 2-hydroxypropanal.

understand how much the isomerization reaction is favored with respect to collisional deactivation and fragmentation processes at a given excitation energy.
Within the RRKM theory [112, 113, 114], the microcanonical rate coefficient for the reaction of Fig. 2.3 is given by the equation [126]

$$k(E) = \frac{N^{\ddagger}(E)}{h\rho(E)} \tag{2.1}$$

where

$$N^{\ddagger}(E) = \int_0^E \rho^{\ddagger}(E')\ \mathrm{d}E' \tag{2.2}$$

In Eqs. 2.1 and 2.2, h is Planck's constants, $N^{\ddagger}(E)$ is the sum of states of the transition state (TS) (computed by excluding the normal mode with imaginary frequency under the assumption that the motion along the reaction coordinates is separable from that of the other modes), and $\rho(E)$ and $\rho^{\ddagger}(E)$ are the density of states (DOS, i.e. the number of rovibrational states per energy interval) of the reactant molecule and transition state, respectively. As apparent, a central quantity in this framework is the molecular rovibrational density of states of the involved molecular species. This can be easily worked out by convoluting its rotational and vibrational counterparts [127]. In the present version of the program, a classical expression is used for the rotational DOS (see [100] for details), while the vibrational DOS is evaluated at uncoupled anharmonic level by adoption of the Stein-Rabinovitch[128] extension of the Beyer-Swinehart algorithm[129]. An improved version of Eq. 2.1 accounts for the tunneling correction by using a modified version of the sum of states $N^{\ddagger}(E)$ of the TS. A common and efficient way of including tunneling is by means of the asymmetric Eckart barrier [130]. Within this model, the sum of state of the transition state is redefined by

$$N^{\ddagger}_{\mathrm{tunn}}(E) = \int_{-V_0}^{E-V_0} \rho^{\ddagger}(E - E')P_{\mathrm{tunn}}(E')\ \mathrm{d}E' \tag{2.3}$$

where $N^{\ddagger}_{\mathrm{tunn}}(E)$ is a tunneling-corrected version of the sum of state of the TS and V_0 is the classical energy barrier for the forward reaction. The quantity $P_{\mathrm{tunn}}(E')$ is the tunneling coefficient at the energy E', and is given by the expression

$$P_{\mathrm{tunn}}(E') = \frac{\sinh(a)\sinh(b)}{\sinh^2((a+b)/2) + \cosh^2(c)} \tag{2.4}$$

where, a, b and c are parameters defined by:

$$a = \frac{4\pi\sqrt{E' + V_0}}{h\nu_i(V_0^{-\frac{1}{2}} + V_1^{-\frac{1}{2}})},\ b = \frac{4\pi\sqrt{E' + V_1}}{h\nu_i(V_0^{-\frac{1}{2}} + V_1^{-\frac{1}{2}})},\ c = 2\pi\sqrt{\frac{V_0 V_1}{(h\nu_i)^2} - \frac{1}{16}}\,. \tag{2.5}$$

Here, V_1 is the classical energy barrier for the reverse reaction, and ν_i is the magnitude of the imaginary frequency of the saddle point (in Eqs. 2.5, $h = 1$ if the energies are expressed, as in this work, in cm^{-1}).
For illustrative purposes, we computed the microcanonical rate coefficient for the direct and inverse reaction of Fig. 2.3, both with and without tunneling correction. To this purpose, the three molecular species were modeled by density-functional theory with the B2PLYP-D3/jun-cc-pVTZ model chemistry. According to our calculations, the forward reaction is exoergic by 1719 cm^{-1} with a barrier of 16448 cm^{-1} (the barrier for the backward reaction is 14729 cm^{-1}). The resulting microcanonical rate coefficients $k(E)$ are plotted in Fig. 2.4 (on a logarithmic scale) for the forward (blue line) and backward (red line) reaction as a function of the energy relative to the hydroxyacetone zero-point energy. In the same figure, the dashed curves are the tunneling-corrected ones. As apparent, the tunneling correction enhances the reaction rate both in the forward and backward direction, more visibly nearby the threshold region, thus lowering the actual value of the reaction threshold in both directions.

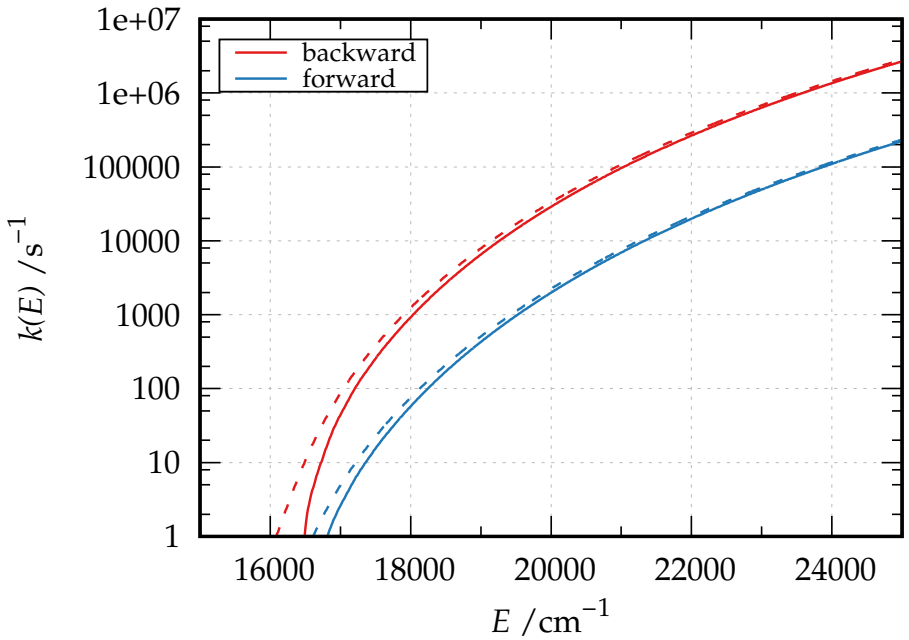

Figure 2.4: Microcanonical rate coefficients for the backward (red color) and forward (blue color) isomerization reaction of hydroxyacetone and 2-hydroxypropanal (Fig. 2.3) as a function of the energy relative to the reactant zero-point energy. Dashed lines are the tunneling-corrected versions of the rate coefficients.

The thermal rate coefficient can easily be computed from the microcanonical rate

coefficients using the following equation:

$$k(T) = \frac{1}{Q(T)} \int_0^\infty k(E)\rho(E)e^{-E/k_\mathrm{B}T}\mathrm{d}E \ , \tag{2.6}$$

with $Q(T)$ being the partition function of the reactant species. The computed thermal rate coefficients for the forward reaction (isomerization reaction of hydroxyacetone to 2-hydroxypropanal) in the temperature range 151-501 K are given as Arrhenius plot ($\log_{10} k(T)$ versus $1/T$) in Fig. 2.5. Results are reported both neglecting (blue

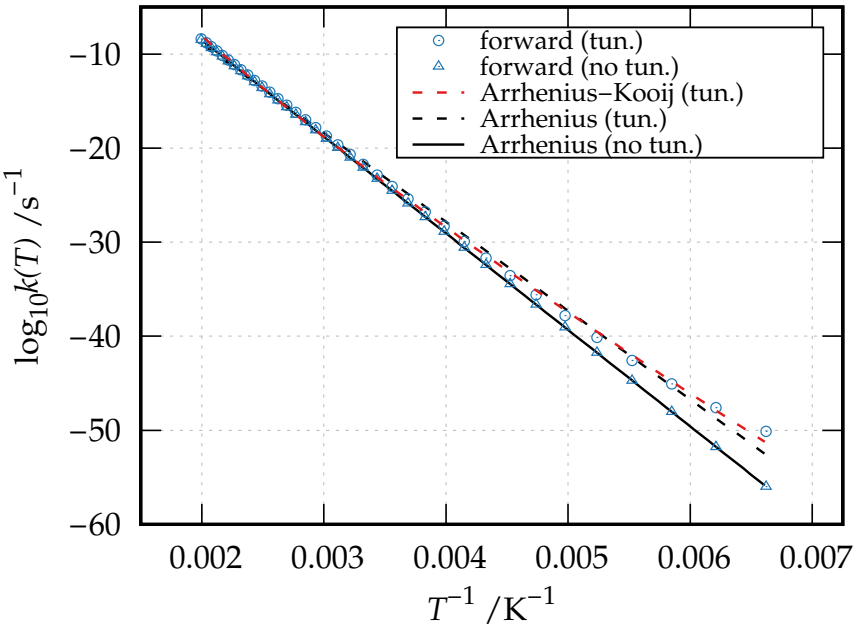

Figure 2.5: Arrhenius plot of the computed thermal rate coefficient (both neglecting and including tunneling) for the isomerization reaction of hydroxyacetone to 2-hydroxypropanal (Fig. 2.3) and of the Arrhenius and Arrhenius-Kooij best-fitting curves.

triangles) and including (blue circles) tunneling. These data can be fitted to the popular Arrhenius equation:

$$k(T) = Ae^{-\frac{E_\mathrm{a}}{RT}} \tag{2.7}$$

(with A being the pre-exponential factor, E_a the activation energy, and R the gas constant) or to the more refined Arrhenius–Kooij formula [131] (also known as modified Arrhenius equation [132]) allowing for a temperature dependence of the pre-exponential factor:

$$k(T) = \alpha(T/300)^\beta e^{-\gamma/T} \ , \tag{2.8}$$

which essentially implies a linear variation of the activation energy with the temperature, $E_\mathrm{a}/R = \gamma + \beta T$. The Arrhenius best-fitting curve for both the tunneling-corrected and no-tunneling data are shown in Fig. 2.5 as dashed black line and solid black line,

respectively. The Arrhenius-Kooij best-fitting curve for the tunneling-corrected data is also reported as a red dashed line in the same Figure, while the best-fitting parameters together with the associated coefficient of determination R^2 are given in Table 2.1.

Arrhenius (Eq. 2.7), no tunneling			
A (s^{-1})		E_a/R (K)	R^2
1.01×10^{12}		23636.0	1.0000
Arrhenius (Eq. 2.7), with tunneling			
A (s^{-1})		E_a/R (K)	R^2
9.12×10^{9}		21752.9	0.9973
Arrhenius–Kooij (Eq. 2.8), with tunneling			
α (s^{-1})	β	γ (K)	R^2
1.20×10^{1}	21.4	16000.4	0.9992

Table 2.1: Results of the fit of the Arrhenius and Arrhenius–Kooij equations to the computed thermal rate coefficients for the isomerization reaction of hydroxyacetone to 2-hydroxypropanal in the temperature range 151-501 K.

As evident from Fig. 2.5 and Table 2.1, the Arrhenius equation perfectly fits the thermal rate coefficients calculated by neglecting tunneling, yielding a $R^2 = 1.0000$ and an activation energy of 16428 cm^{-1} that compares well with the computed reaction barrier. On the contrary, the tunneling-corrected thermal rate coefficients show a deviation from linearity with decreasing temperatures. As a result, the Arrhenius expression yields a worse best-fitting curve ($R^2 = 0.9973$) and a lower activation energy of 15120 cm^{-1}, while a better fitting is obtained through the Arrhenius-Kooij equation ($R^2 = 9.9992$), which gives an activation energy of 14839 cm^{-1} at $T = 250$ K and of 13352 cm^{-1} at $T = 150$ K.

2.4 Multi-step reactions

The dissociation of vinyl cyanide (VC, C_3H_3N), is particularly interesting because it involves multiple reaction channels and different sets of products (HCN, HNC, HCCH, and $:CCH_2$) and hence it serves as a very good test case for master-equation based kinetic models. The potential-energy surface for this reaction has been investigated in a recent work by Homayoon et al. [133] through *ab initio* CCSD and CCSD(T) calculations with the 6-311+G(2d,2p) and 6-311++G(3df,3pd) basis sets. In the same work, a reaction scheme involving ten unimolecular steps, three of which reversible, was proposed. The ten reaction steps are summarized in Table 2.2, while the associated reaction diagram is given in Fig. 2.6.
As shown in Fig. 2.6 and Table 2.2, VC can directly dissociate to product sets $:CCH_2$ + HCN and HCCH + HCN through steps 1 and 2 (the only direct dissociation paths),

	Reaction step	E_a /cm^{-1}
1	VC $\xrightarrow{k_{1f}}$:CCH_2 + HCN	35185
2	VC $\xrightarrow{k_{2f}}$ HCCH + HCN	41271
3	VC $\underset{k_{3f}}{\overset{k_{3b}}{\rightleftharpoons}}$ Int1-III	20076
4	Int1-III $\xrightarrow{k_{4f}}$ HCCH + HCN	32947
5	VC $\underset{k_{5f}}{\overset{k_{5b}}{\rightleftharpoons}}$ Int1-IV	37494
6	Int1-IV $\xrightarrow{k_{6f}}$ HCCH + HNC	12521
7	VC $\underset{k_{7f}}{\overset{k_{7b}}{\rightleftharpoons}}$ Int1-V	36724
8	Int1-V $\xrightarrow{k_{8f}}$:CCH_2 + HNC	19727
9	Int1-III $\xrightarrow{k_{9f}}$:CCH_2 + HNC	31128
10	Int1-III $\xrightarrow{k_{10f}}$ HCCH + HNC	32912

Table 2.2: Reaction steps involved in the dissociation mechanism of vinyl cyanide considered in this work. The associated activation energies (relative to the zero-point energy of the reactant of each step) are also given.

or lead to formation of reaction intermediates Int1-III (the most stable one), Int1-IV, and Int1-V, further evolving to products. On the other hand, product HNC can only be formed via indirect dissociation paths involving the above mentioned intermediates. A screenshot of VMS showing the structures of all the molecular species involved in this reaction is given in Fig. 2.7.
Within a master-equation approach (see for instance [134]), to determine the time evolution of the relative abundance of the involved species, initially a matrix, **K**, is set up by opportunely combining the microcanonical rate coefficients at a specified energy. In particular, the diagonal elements K_{ii} contain the loss rate of species i, while the

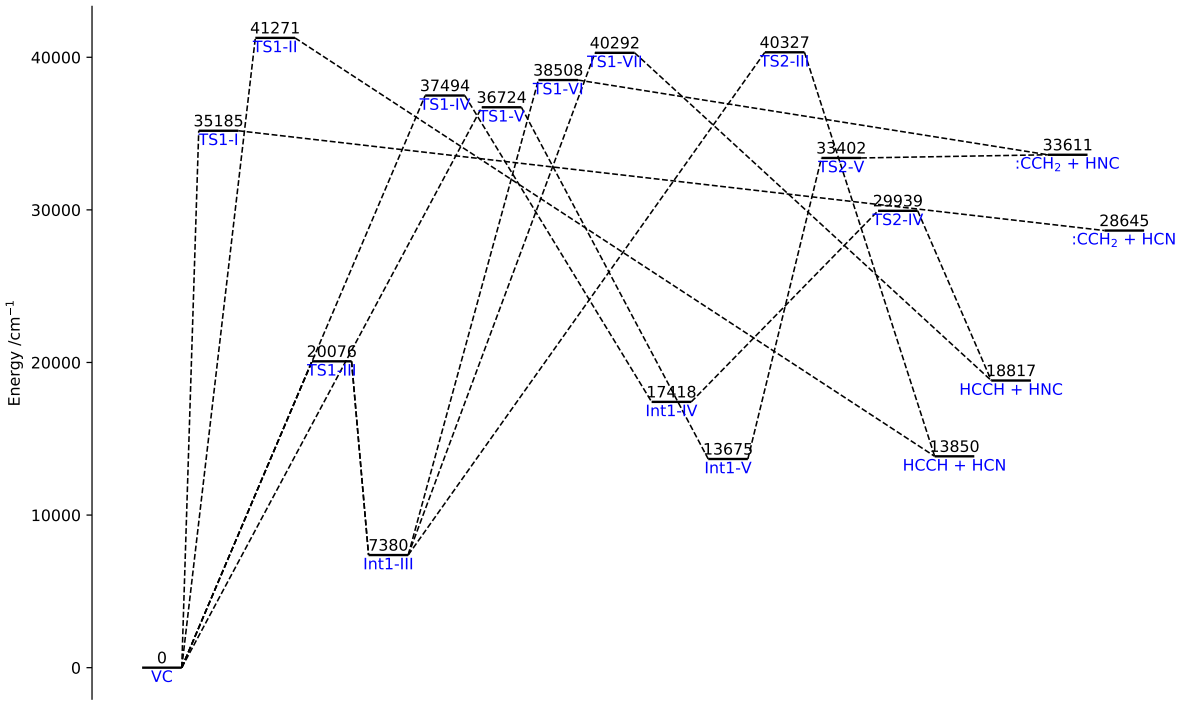

Figure 2.6: Reaction diagram for the dissociation of vinyl cyanide yielding HCN, HNC, :CCH_2, and HCCH. All energies are relative to the reactant zero-point energy.

off-diagonal elements K_{ij} contain the rate of formation of species i from species j. The rate of change in the concentration of each species is given by the vector differential equation:

$$\frac{\mathrm{d}\mathbf{c}}{\mathrm{d}t} = \mathbf{K}\mathbf{c} \tag{2.9}$$

where $\mathbf{c}$ is the vector of the concentrations of the species at time t. This is a linear differential equation and can be solved by diagonalization of $\mathbf{K}$. In terms of the eigenvector matrix $\mathbf{Z}$ and eigenvalue vector $\mathbf{\Lambda}$, the solution of Eq. 2.9 reads:

$$\mathbf{c}(t) = \mathbf{Z}e^{\mathbf{\Lambda}t}\mathbf{Z}^{-1}\mathbf{c}(0) \tag{2.10}$$

where, $\mathbf{c}(0)$ is the concentration vector at $t = 0$. In this model, a fundamental hypothesis is that collisional relaxation occurs on time scales much shorter than those that characterize phenomenological kinetics [135]. It is worth mentioning here that a more general version of the master equation would involve diagonalizing a much larger matrix explicitly including collisional relaxation [134]. However, if the above mentioned hypothesis holds, the resulting eigenvalues would appear in two separated sets: one made up by so-called internal energy relaxation eigenvalues (IEREs) and one made up by so-called chemically significant eigenvalues (CSEs). These last eigenvalues, that relate to the phenomenological kinetics of interest in interstellar space and atmospheric studies, would be identical to those obtained by solving Eq. 2.9.
By using the methodology described, we computed the evolution of species with respect to time through the StarRate program using the structural parameters of the species given in Ref. [133], and computing the microcanonical rate coefficients through Eq.

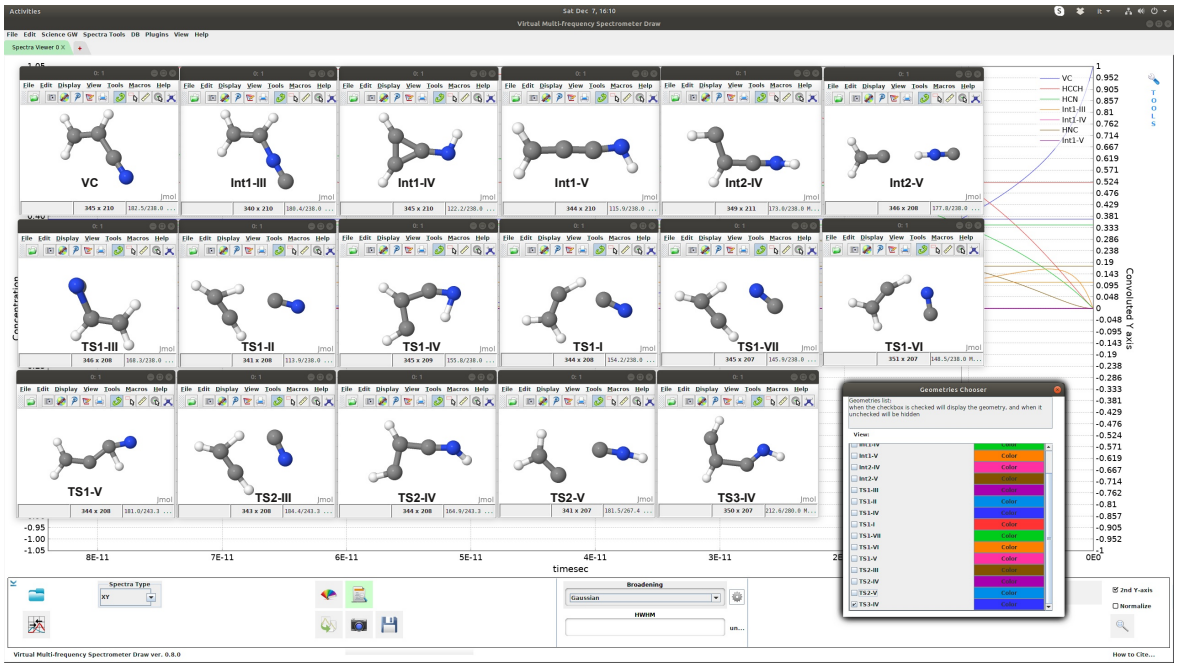

Figure 2.7: Structures of the reactant molecule (top left corner), intermediates (remaining frames in the top row), and transition states (second and third rows) visualized through the VMS software.

2.1. For the reader's convenience, we give the full form of the matrix **K** for this reaction (please note that expressions in square brackets, though spanning several rows, relate to single matrix elements and are shown as such to give a compact picture of the matrix):

$$
\begin{pmatrix}
 & \text{VC} & \text{HCCH} & :\text{CCH}_2 & \text{HCN} & \text{Int1-III} & \text{Int1-IV} & \text{HNC} & \text{Int1-V} \\
\text{VC} & -\begin{bmatrix} k_{1f}+k_{2f} \\ +k_{3f}+k_{5f} \\ +k_{7f} \end{bmatrix} & 0 & 0 & 0 & k_{3b} & k_{5b} & 0 & k_{7b} \\
\text{HCCH} & k_{2f} & 0 & 0 & 0 & [k_{4f}+k_{10f}] & k_{6f} & 0 & 0 \\
:\text{CCH}_2 & k_{1f} & 0 & 0 & 0 & k_{9f} & 0 & 0 & k_{8f} \\
\text{HCN} & [k_{1f}+k_{2f}] & 0 & 0 & 0 & k_{4f} & 0 & 0 & 0 \\
\text{Int1-III} & k_{3f} & 0 & 0 & 0 & -\begin{bmatrix} k_{3b}+k_{4f} \\ +k_{9f}+k_{10f} \end{bmatrix} & 0 & 0 & 0 \\
\text{Int1-IV} & k_{5f} & 0 & 0 & 0 & 0 & -[k_{5b}+k_{6f}] & 0 & 0 \\
\text{HNC} & 0 & 0 & 0 & 0 & [k_{9f}+k_{10f}] & k_{6f} & 0 & k_{8f} \\
\text{Int1-V} & k_{7f} & 0 & 0 & 0 & 0 & 0 & 0 & -[k_{7b}+k_{8f}]
\end{pmatrix}
$$

In our calculations, the initial concentration of VC was taken as 1.0 and the concentration of other species was set to 0.0. The relative abundances of the involved species as a function of time are plotted for two energies, namely $E = 51764\ \text{cm}^{-1}$ and $E = 62000\ \text{cm}^{-1}$, in Figs. 2.8 and 2.9, respectively.

By inspection of the plots, a first remark is that there is a sudden spike of the concentration for Int1-III in a very small time range for both energies. This is because Step 3 involves a low activation energy (20076 cm^{-1}) compared to Int1-IV (37494 cm^{-1}) and Int1-V (36724 cm^{-1}), and the intermediate Int1-III is relatively stable compared to the other two (the stability of Int1-III is also reflected by the long sigmoidal tail of the plot). At the considered energies, these last two species are virtually never present

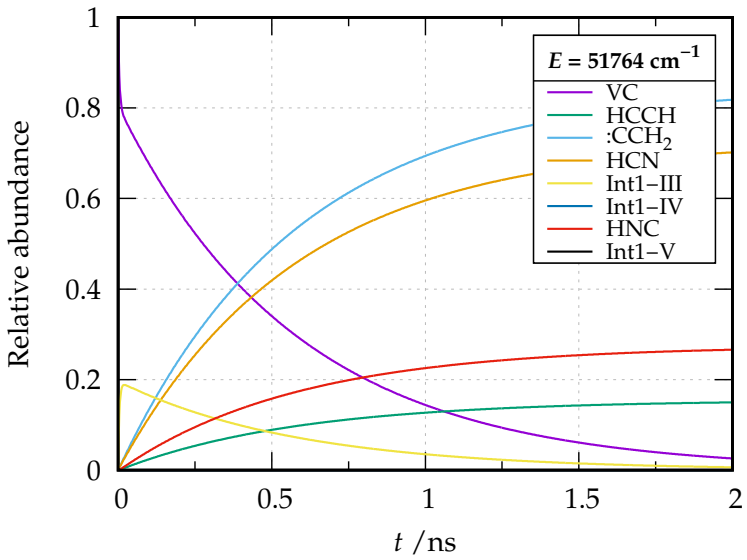

Figure 2.8: Relative abundance of the species involved in the dissociation of vinyl cyanide as a function of time at energy $E = 51764$ cm^{-1} relative to the reactant zero-point energy.

and as soon as formed evolve into products. The reaction paths involving these two intermediates (the only ones leading to formation of HNC) become increasingly important at $E = 62000$ cm^{-1}; in fact, while the branching ratio HCN/HNC tends to a value of about 2.5 at $E = 51764$ cm^{-1}, a branching ratio of 1.9 is obtained at $E = 62000$ cm^{-1}. The predicted branching ratio at $E = 51764$ cm^{-1} nicely compares with the experimental estimate of 3.3 of Ref. [136] and the theoretical one of 1.9 of Ref. [133] (where, however, only vibrational densities and sum of states were taken into account in the calculation of the microcanonical rate coefficients), substantially improving over former theoretical calculations yielding a branching ratio of over 120 [137].
An interesting feature offered by VMS, is that of visualizing matrices in a 'heat-map' fashion through a color palette reflecting the actual value of the elements. A heat-map of **K** for the rate coefficient at $E = 62000$ cm^{-1} is given in 2.10. Looking at the first column and recalling the meaning of the K_{ij} elements, one can see that VC is directly converted to all the remaining species except HNC. The highest conversion rate (darkest gray) is towards Int1-III, while the rate of formation of the other two intermediates from VC is slower due to higher activation energies. Direct conversion to product sets containing HCN is also fast. On the contrary, as already mentioned, HNC is not formed directly from VC (blank square in position 7,1). Looking at the whole matrix, the darkest squares are those of the matrix elements connecting Int1-IV and Int1-V to products, due to the associated lowest activation energy. This is in line with the fact that, as also shown by Fig. 2.8, these intermediates evolve rapidly to products.

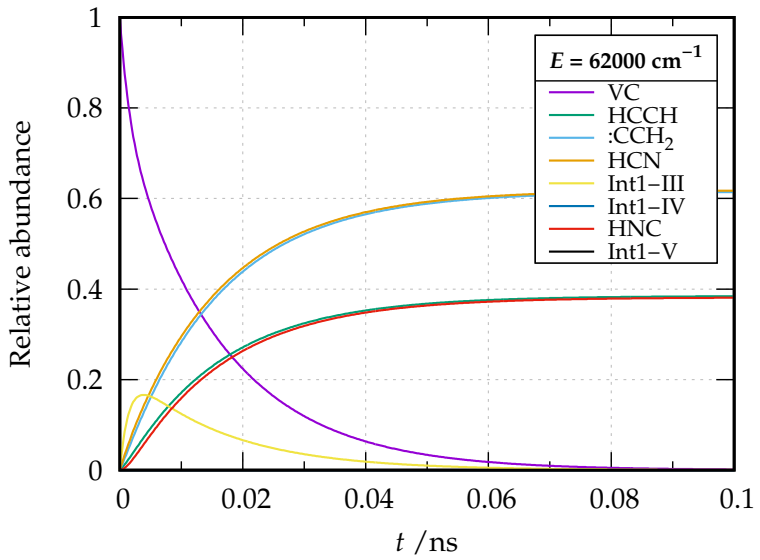

Figure 2.9: Relative abundance of the species involved in the dissociation of vinyl cyanide as a function of time at energy $E = 62000$ cm^{-1} relative to the reactant zero-point energy.

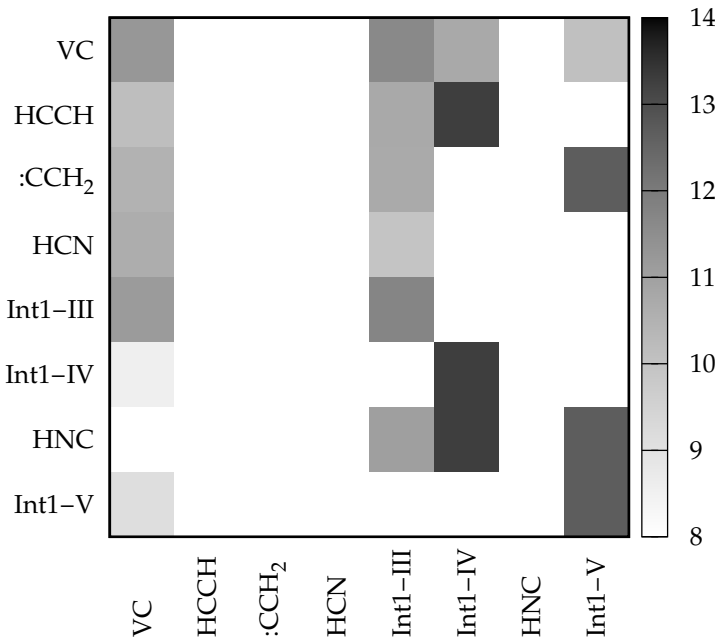

Figure 2.10: Color map of the transition **K** matrix at energy $E = 62000$ cm^{-1} relative to the reactant zero-point energy as visualized in the VMS software. For each element of the matrix, the value of $|\log_{10} K_{ij}|$ in s^{-1} is plotted according to the gray scale at the right-hand-side of the plot area.

2.5 Conclusions

In this paper the implementation of a computer program for chemical kinetics of multi-step reactions and its integration with the graphical interface of the Virtual Multifrequency Spectrometer has been discussed. The developed computational machinery is built around an input/output interface using a hierarchical data structure based on the XML language and shared in common with VMS. Details are given on the implementation of the calculation of microcanonical rate coefficients for the single steps of a unimolecular reaction, and on the modeling of the time evolution of the relative abundance of the involved species. The main features of the program have been illustrated through two example reactions, namely the atmospherically relevant interconversion between hydroxyacetone and 2-hydroxypropanal, and the production of HCN and HNC by dissociation of vinyl cyanide. Work is ongoing in our laboratory to account for bimolecular entrance channels, enhance the potentialities of the program, and integrate it in virtual-reality environments [138, 139].

2.6 New developments

In this section is reported a brief discussion about the implementation in StarRate of new features for the treatment of bimolecular reactions, the tunneling effect, the anharmonicity and the models for the description of the radiative emission which are currently underway.
As regards the bimolecular treatment, the capture models which have already discussed in Sec. 1.3.4 are capable of describing the ion-molecule and radical-molecule reactions. These reaction classes are the most important in Astrochemistry since most of the identified molecular species are ions or radicals. The canonical and microcanonical formulation of the models used to compute the rate constants for these reaction classes have been implemented and are being tested using the LDA and the Gorin formulas. In the following subsection 2.6.1 is provided the microcanonical formulations of the capture models implemented in StarRate, while the canonical formulations have already been given in subsection 1.3.4.
Concerning tunneling, the ZCT model has been implemented and tested only for single-step reactions using the formulation described in Sec. 1.3.5. The implementation of the SCT model is also planned as it has proven to be more accurate for the description of tunneling, which is fundamental at the very low temperatures characterizing the ISM. Indeed, for those multistep reaction channels which have barriers slightly above the reactant limit, tunneling plays a fundamental role in defining the competition with other reactive channels having similar reaction barriers. In Fig. 2.11 is depicted the above mentioned case. The reaction steps involving **TS1** and **TS3**, which are highlighted in red, are the rate determining steps for which the choice of tunneling model will determine the accuracy of the final branching ratios.

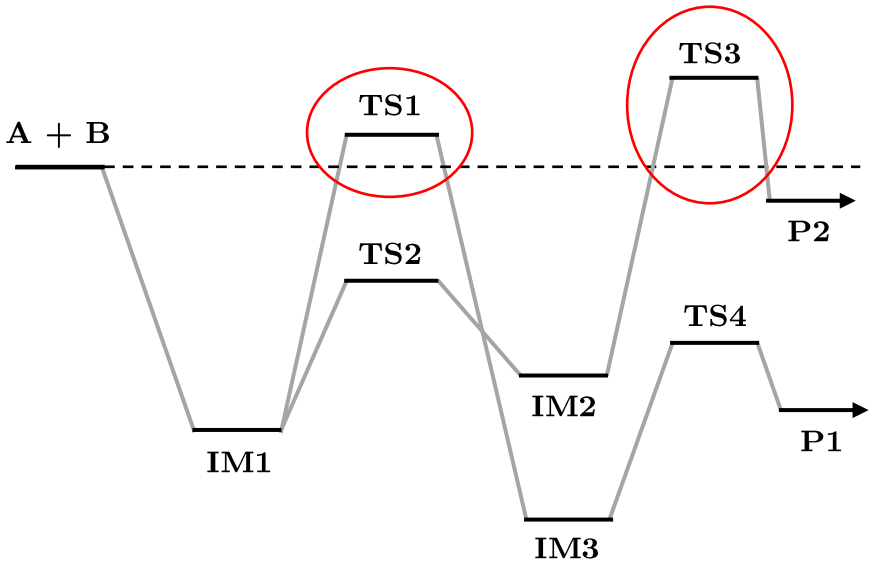

Figure 2.11: Reaction profile of chemical reaction pathways having high energy barriers overcoming the reactants asymptotic limit.

However, for barrierless reactions with submerged transition states, all species involved are highly vibrationally excited. At high values of vibrational energy the effect of anharmonicity on the structure of the vibrational levels of molecular systems becomes stronger and stronger. In Fig. 2.12 is reported an approximate representation of the anharmonic vibrational level of each species involved in a multistep reaction. As can be seen, the anharmonic description of the vibrational levels considerably modifies the DOS for all the species involved in the reaction. It is therefore very important to take these effects into account as they could significantly affect the rate constant values. The accurate computation of the DOS and the partition functions becomes crucial to obtain reliable and accurate rate constants. So, the methodology that will be used to take into account the anharmonic correction performed by StarRate will involve the combination of the anharmonic ZPE, the fundamental vibrational frequencies calculated at the anharmonic level with the Stein-Rabinovitch model to determine the DOS through the separable Morse oscillator model, which is satisfactory for small molecules as is the case for molecules of astrochemical interest[98].

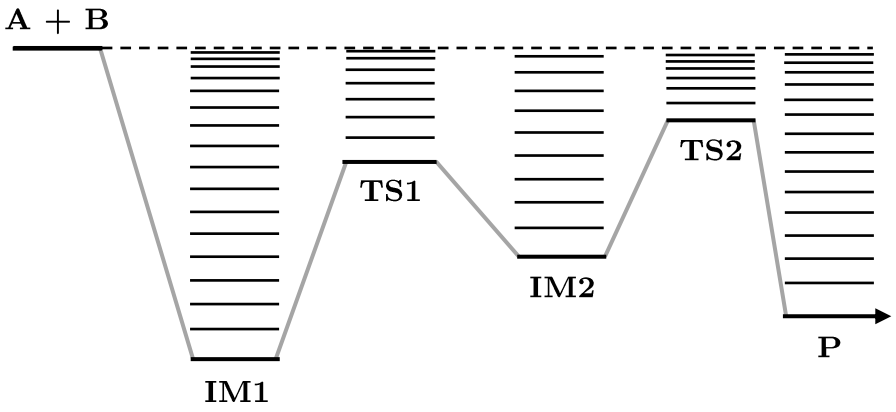

Figure 2.12: Representation of a multistep reaction which highlights the effect of anharmonicity on the distribution of vibrational levels for all stationary points of the reaction profile.

As already discussed in Sec. 1.3.6, given the low pressures characterizing the ISM, the collisional stabilization due to the thermal bath becomes inefficient. To stabilize, reactive systems must therefore release excess vibrational energy through radiative emission, which in the case of radiative association reactions between radicals plays a fundamental role. This process guarantees the depopulation of the most excited vibrational levels making the backward dissociation reaction disfavoured. In Fig.2.13 is shown a graphical representation of the stabilizing effect for an association reaction between two initial reactants A e B. On the left side is depicted the highly vibrationally excited system where all the levels are populated, on the right side the system is represented after that the radiative emission occured indeed the distribution of the population changed and the lower levels results to be more populated.

The stabilizing effect of the radiative emission for the ion-molecule and radical-molecule association processes whose formulation was discussed in section 1.3.6 has

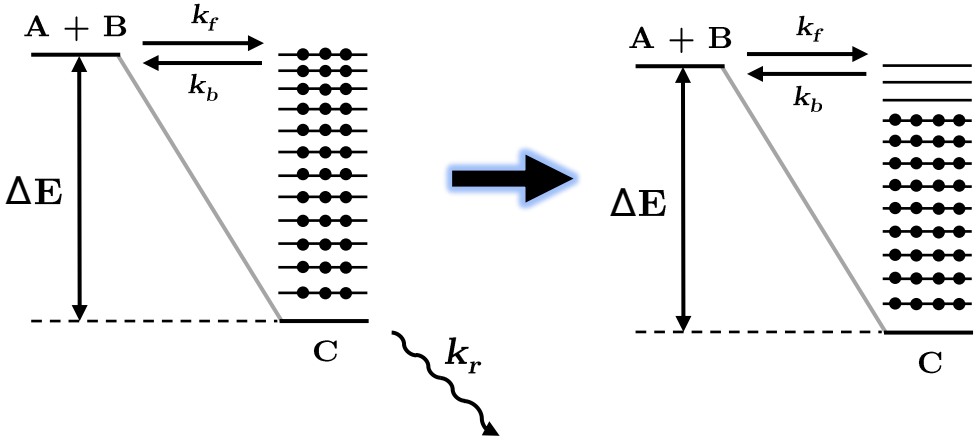

Figure 2.13: Representation of the stabilization effect due to the radiative emission. k_f and k_b are the forward and backward (or back-dissociation) rates for the bimolecular association step.

been implemented and is currently under testing.
In Fig.2.14 is provided a schematic representation of future (currently in progress) implementations.

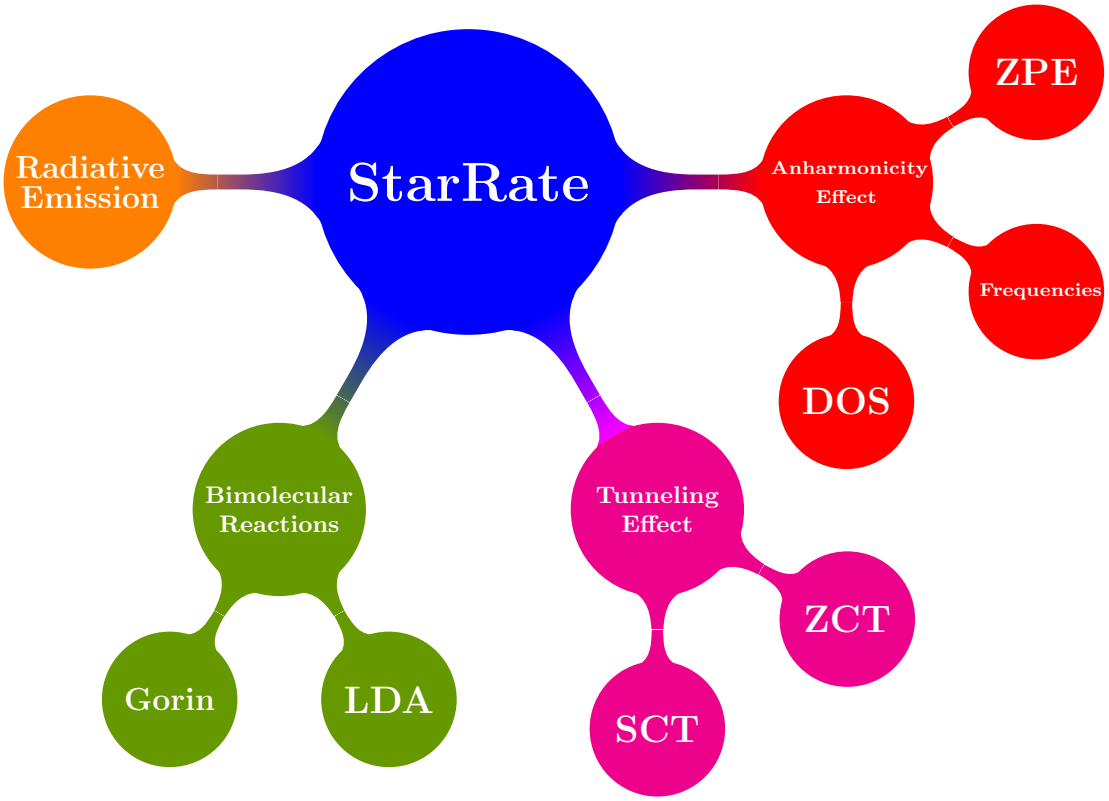

Figure 2.14: Mind map of the features currently under implementation in StarRate.

2.6.1 Bimolecular steps

Given the reversible barrierless association reaction:

$$A + B \underset{k_b}{\overset{k_f}{\rightleftharpoons}} C$$

We can compute k_f using the capture models depending on the nature of the interacting reactants. To compute the back-dissociation rate coefficients we can rely on the detailed balance principle:

$$k_f(A + B \longrightarrow C) * \rho(A + B) = k_b(C \longrightarrow A + B) * \rho(C) \tag{2.11}$$

Depending on the nature of the reactants the derivation and formulation of k_f and k_b will be different. There are two types of bimolecular reactions primarily important in astrochemical context: ion-neutral and neutral-neutral reactions.

Radical-molecule reactions

The capture cross section for the radical-neutral or neutral-neutral collision varies by R^{-6} where, R is the distance between the two neutral fragments. The corresponding microcanonical rate constant is given by:

$$k(E_c) = 3\pi \frac{1}{\sqrt{\mu}} C_6^{\frac{1}{3}} \left(\frac{E_c}{2}\right)^{\frac{1}{6}} \tag{2.12}$$

where, C_6 is the effective collisional coefficient, E_c is the collisional energy, μ is the reduced mass of the two fragments [140].

Ion-molecule reactions

In one of the standard capture models for ion-dipole reactions, based on the locked-dipole approximation (LDA), the dipole moment is assumed to be locked with the energetically favorable orientation along the collision axis, which results in the long range interaction potential:

$$V_{LDA,l}(R) = -\frac{\alpha' e^2}{8\pi\epsilon_0 R^4} - \frac{e\mu_{el}}{4\pi\epsilon_0 R^2} + \frac{\hbar l(l+1)}{2\mu R^2} \tag{2.13}$$

The LDA leads to an expression for the energy dependent rate constant:

$$k_{LDA}\,(E_c) = k_L + \frac{e\mu_{el}}{2^{\frac{3}{2}}\epsilon_0\sqrt{\mu E_c}} \tag{2.14}$$

where k_L is Langevin rate constant which can be rewritten in this way:

$$k_{LDA}\,(E_c) = 2\pi q\sqrt{\frac{\alpha}{\mu}} + \frac{\sqrt{2}\pi q\mu_D}{\sqrt{\mu E_c}} \tag{2.15}$$

where q is the charge of the ion, α is the polarizability of the neutral species, μ is the reduced mass of the ion-neutral pair, μ_D is the permanent dipole moment of the neutral species, E_c is the collisional energy[141].

Chapter 3

Gas-Phase Formation and Isomerization Reactions of Cyanoacetaldehyde, a Prebiotic Molecule of Astrochemical Interest

In this Chapter is proposed a kinetic investigation carried out with the StarRate program of a possible gas-phase formation and isomerization reaction of Cyanoacetaldehyde (NC-CH_2CH=O), a prebiotic molecule of astrochemical interest supposed to be involved in the synthesis of nucleobases when reacts with urea in solution but not yet detected in the ISM. The barrierless radiative association reaction between the two radical fragments formyl(HCO) and cyanomethyl(CH_2CN) has been investigated through a DFT quantum chemical approach combined with the application of the 'Cheap' composite scheme to model the accurate energetics of the reaction pathways. Our results indicate that the direct association of the two reacting radicals (HCO and CH_2CN) is strongly exothermic and thus thermodynamically favoured under the harsh conditions of the ISM. The StarRate program has been employed to compute the relative abundances of the reaction products as a function of time and energy in order to determine which of all the isomers considered in the reaction mechanisms resulted to be the most abundant. Radiative emission rates of the association product have been computed in order to prove that the initial association reaction between the two radical fragments was effective and that the reaction product would not dissociate towards the reactants. From the kinetic results, the two main products of the reaction appear to be the *cis* and *trans* isomers of cyanoacetaldehyde, with a *cis*/*trans* ratio equal to 0.35:0.65 in an energy range compatible with those of the ISM. This Chapter is based on an article already published by Ballotta et. al [142].

3.1 Introduction

The discovery of pyrimidine traces in carbonaceous meteorites in 1979 attracted a lot of attention to the study of possible synthetic pathways for this important scaffold of RNA and DNA bases. During the years, several models have been proposed and experiments have been performed in order to simulate conditions resembling those of the Interstellar Medium (ISM) or primitive Earth for the formation of molecules such as purine and pyrimidine from so-called complex organic molecules (COMs).
In this context, the involvement of cyanoacetaldehyde in the synthesis of the pyrimidine bases has been investigated for a long time. Early experimental studies in aqueous solution were performed already in 1968 by Ferris et al.[143], who suggested a prebiotic synthesis of pyrimidine starting from cyanoacetylene and cyanate, because of their supposed high abundances in the primordial soup and, for HC_3N, also in Titan's atmosphere. However, a few years later (1973) Ferris et al.[144] described an alternative route to formation of the same molecule starting from the condensation of cyanoacetaldehyde and guanidine to form 2,4-diaminopyrimidine that hydrolyzed to cytosine and uracil, and suggested that this route might be favoured with respect to the former one due to the lower tendency of cyanoacetaldehyde and guanidine (with respect to cyanoacetylene and cyanate) to react with other nucleophiles, thus featuring a greater stability as starting materials.
Since then several alternative synthetic routes to pyrimidine have been proposed which included other cyanoacetaldehyde reaction partners such as urea.[145] Robertson et al.[146] suggested to use concentrated urea solutions (similar to those found in evaporating lagoons or in pools on drying beaches on the early Earth) in order to favor the reaction with cyanoacetaldehyde to form cytosine in yields of 30-50%. Additionally, theoretical investigations have been undertaken to study the possible pyrimidine and purine synthetic routes [147]. For example, Kaur and Sharma [148] have performed computational simulations, using Density-Functional Theory (DFT), of the possible free radical ammonia-mediated pathways for cytosine and uracil formation, where cyanoacetaldehyde plays a key role, and, more recently, a computational study of water-catalyzed synthetic route to pyrimidine bases starting from cyanoacetaldehyde and guanidine has been presented [149].
Due to its relevance in the above discussed reactions, cyanoacetaldehyde (and its enolic isomers) has been the subject of computational and experimental IR[150] and Microwave[151] spectroscopic characterization, in order to facilitate its search in the ISM by comparison of laboratory spectra with those recorded by modern and powerful telescopes. These studies also showed that cyanoacetaldehyde conformers are more stable than the enolic isomers due to the presence of a nitrile group which weakly interacts with the hydrogen atom of the carbonyl group.
Despite all these efforts, cyanoacetaldehyde has not yet been detected in the ISM. A mandatory step for a better assessment of the role of this important molecule in the ISM is the investigation of the possible mechanisms for its formation. A computational study reported on a gas-phase model for the cyanoacetylene hydrolysis reaction, considered as a fundamental step for the formation of cyanoacetaldehyde [152]. However, the activation energy for the addition of water to the cyanoacetylene triple bond turned

out to be too high, so that this reaction channel should be closed under the extreme conditions of primitive Earth and ISM. This led the authors to hypothesize a catalytic process on a grain surface which is able to decrease the activation energy.
In the present study we suggest an alternative mechanism for the formation of cyanoacetaldehyde, involving two radicals already detected in the ISM, namely cyanomethyl (CH_2CN) and formyl (HCO), and focus on the chemical evolution of cyanoacetaldehyde. In particular, the isomerization mechanism of cyanoacetaldehyde and its cyanovinylalcohol isomers, which are formed in equilibrium with cyanoacetaldehyde, is also analyzed. Moreover, some cyanoacetaldehyde dissociation reaction paths are investigated in order to determine if such dissociation products are more stable than cyanoacetaldehyde. Finally, in order to provide a quantitative picture of the reaction progress, we modeled the chemical kinetics of the reaction and computed the branching ratios for all the isomers and reaction products with the help of the StarRate computer program, [100, 153] specifically designed to study astrochemical reactions.
The article is organized as follows. In Sec. 3.2, the computational methods are described. In Sec. 3.3, the computed reaction mechanism is discussed with reference to the stationary points of the potential-energy surface (PES). In Sec. 3.4, the kinetics of the reaction is addressed. Sec. 3.5 is devoted to conclusions and perspectives.

3.2 Computational Details

On the grounds of previous experience, [154, 155, 156] geometry optimizations and zero-point corrected electronic energies of reactants, transition states, intermediates, and products along the reaction pathways were obtained by the B2PLYP [157, 158]-D3[159] double-hybrid functional in conjunction with the jun-cc-pVTZ basis set [160]. The stationary points on the reaction pathways were characterized as minima (reactants, intermediates and products) and saddle points (transition states) based on vibrational frequency calculations. The transition states obtained were further confirmed using intrinsic reaction coordinate (IRC) [161] scans at the same levels of theory. For reference purposes, calculations were performed also using the rev-DSD-PBEP86 [162] functional. This combination of functional and basis set will be referred to in the following as rDSD.
After that, for all stationary points computed with the B2PLYP-D3 functional, improved electronic energies were obtained by means of the 'Cheap' composite method, which includes core-valence correlation energy and complete basis set extrapolation at the MP2 [163] level on top of CCSD(T) [164] energies computed with a triple-zeta basis set [165, 166, 167, 168], and has proven to provide absolute deviations from sophisticated HEAT-like composite schemes within 2 kJ mol^{-1}[154, 169]. In detail:

$$E_{\text{Cheap}} = E^{\text{CCSD(T)/VTZ}} + \Delta E^{\text{MP2/CBS}} + \Delta E^{\text{MP2/CV}} \tag{3.1}$$

where

$$\Delta E^{\text{MP2/CBS}} = \frac{4^3 E^{\text{MP2}/QZ} - 3^3 E^{\text{MP2}/TZ}}{4^3 - 3^3} - E^{\text{MP2}/TZ} \tag{3.2}$$

and

$$\Delta E^{\text{MP2/CV}} = E^{\text{MP2/pCVTZ, a.e.}} - E^{\text{MP2/pCVTZ, f.c.}} \tag{3.3}$$

with $\Delta E^{\mathrm{MP2/CV}}$ being the energy correction due to the core correlation evaluated at the MP2/cc-pCVTZ level. In Eq. 3.2, $\Delta E^{\mathrm{MP2/CBS}}$ is the MP2 correlation energy extrapolated to the CBS limit by using n^{-3} extrapolation formula applied to the cc-pVTZ and cc-pVQZ basis sets[170, 171]. A zero-point vibrational energy correction based on B2PLYP-D3 calculations was applied to 'Cheap' electronic energies, and DFT vibrational frequencies obtained with the same functional were used for kinetics calculations. All B2PLYP and rDSD calculations were performed using Gaussian09[172], while 'Cheap' calculations were performed using CFour [173, 174].
Kinetics calculations were performed as described in Sec. 3.4 with the help of the StarRate program [100, 153] interfaced to the Gaussian code through a versatile XML interface (see also Refs. [121, 122] on the issue of interoperability between electronic-structure and dynamics/kinetics programs).

3.3 The potential energy surface

We start the presentation of our results by illustrating the computed mechanism for the formation of cyanoacetaldehyde starting from two radicals widely detected in the ISM, namely formyl (HCO) and cyanomethyl (CH_2CN). A large part of the possible isomerization and dissociation mechanisms of cyanoacetaldehyde has been included in the mechanism, which is shown in full in Fig. 3.1. To simplify the analysis, the mechanism has been divided in four parts, whose reaction mechanisms and PES profiles are illustrated in Figs. 3.2-3.5 and commented in the following. Then, the reaction paths in these four parts that are compatible with ISM conditions have been collected for a comprehensive view in Fig. 3.6. Finally, the zero-point corrected energies of the species involved in the whole reaction are summarized in Table A.1 reported in Appendix A. Before moving to the analysis of the four parts of the overall reaction mechanism, we note that the rDSD calculations outperform the B2PLYP ones when compared to 'Cheap' data, as indicated by root-mean-square (RMS) errors reported in the caption to Table A.1.

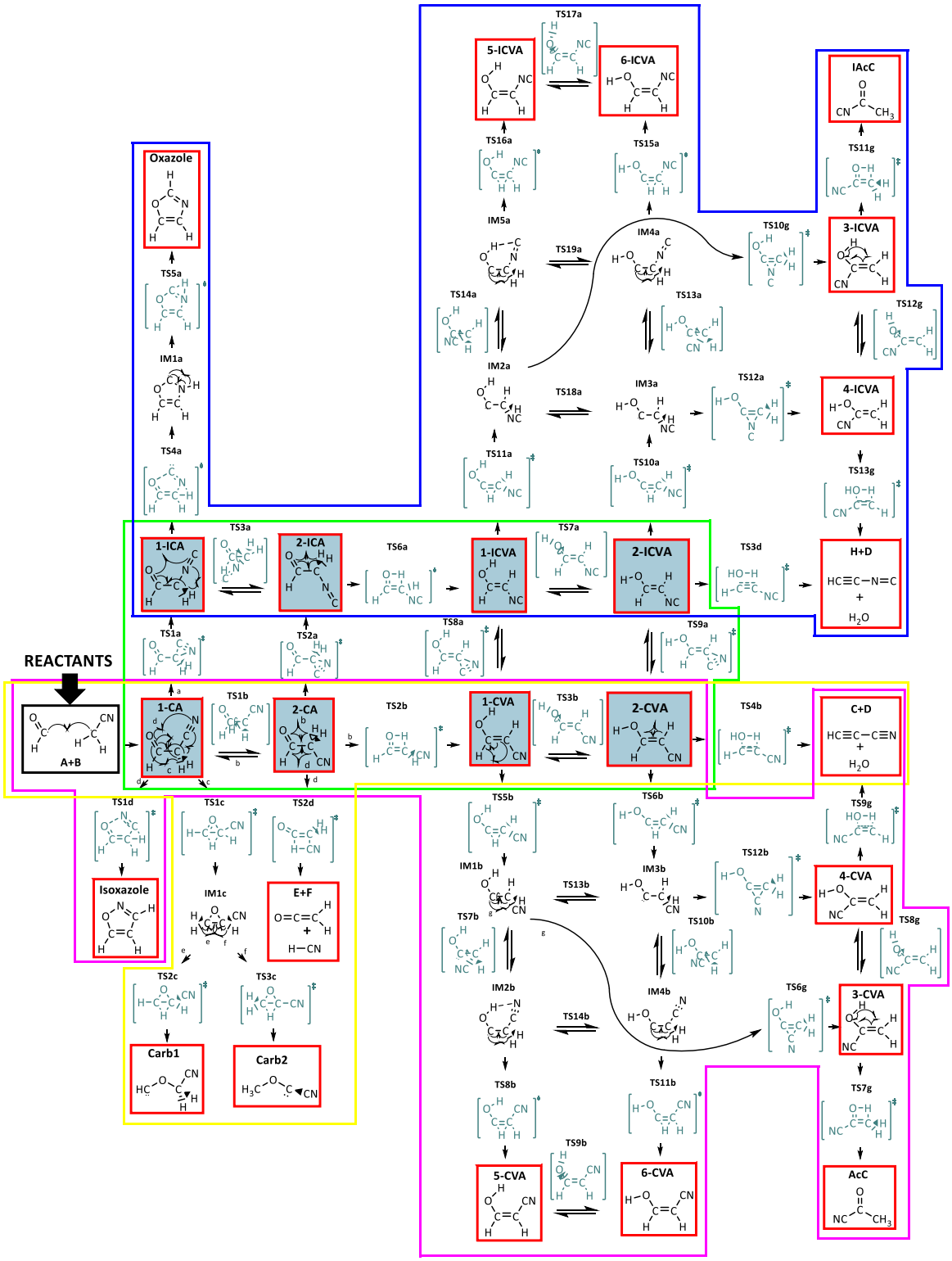

Figure 3.1: Comprehensive view of the reaction mechanism for the formation of cyanoacetaldehyde from the formyl and cyanomethyl radicals considered in this article.

3.3.1 Reaction Channel 1

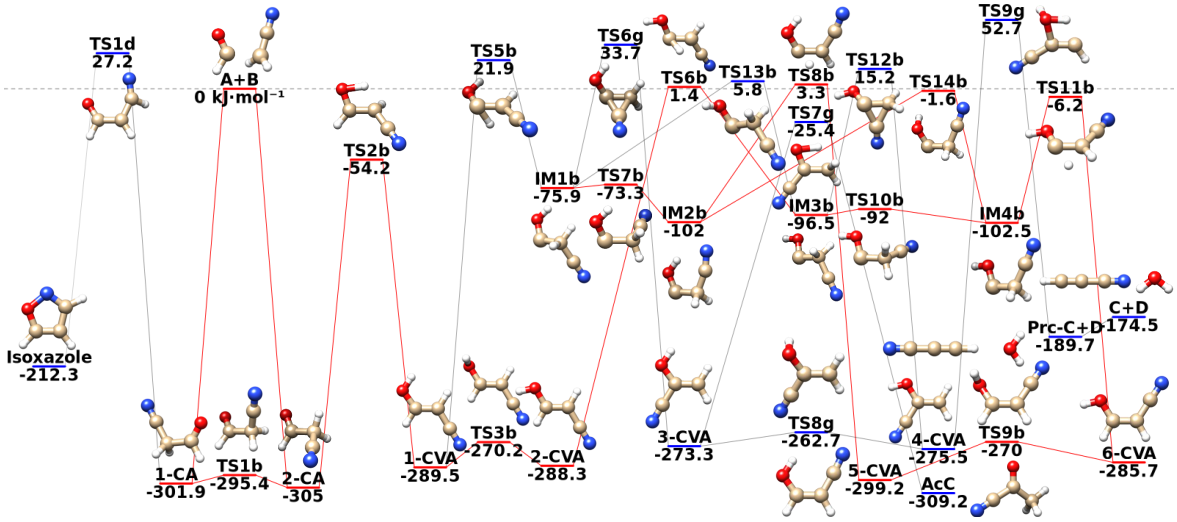

Figure 3.2: Energetics of the isomerization of cyanoacetaldehyde conformers (**1-CA**, **2-CA**), cyanovinylalcohol isomers (**1-CVA**, **2-CVA**, **3-CVA**, **4-CVA**, **5-CVA**, **6-CVA**), **Isoxazole** and acetylcyanide (**AcC**). Dissociation to cyanoacetylene and water (**C+D**) is also included. Energies in kJ mol^{-1} relative to the dissociation limit.

Reaction Channel 1 (violet frame in Fig. 3.1) includes the association and isomerization reaction path of cyanoacetaldehyde conformers (**1-CA**, **2-CA**) to **Isoxazole**, acetylcyanide (**AcC**) and all the cyanovinylalcohol isomers (**1-CVA**, **2-CVA**, **3-CVA**, **4-CVA**, **5-CVA**, **6-CVA**) obtained from keto-enolic tautomerization. The related mechanism and PES profile are reported in Fig. 3.2. The **A+B** critical point in the reaction profile represents the reactant asymptote (algebraic sum of the zero-point corrected energies of the two radical fragments HCO and CH_2CN) or dissociation limit. The notation Prc in this and the following reaction schemes stands for pre-reactive complex. In the following, all energies will be given relative to this value. When the two reactants start to interact, they spontaneously give the two conformers **1-CA** at -301.9 kJ mol^{-1} and **2-CA** at -305.0 kJ mol^{-1}, depending on the initial relative orientation of the incoming radicals. The geometry optimization leads to a barrierless attack of the *sp* C eletrophilic center of HCO to the sp^2 C nucleophilic center in CH_2CN. **1-CA** is slightly less stable than **2-CA** probably due to a destabilizing repulsive electrostatic interaction between oxygen and nitrogen. Interconversion between the two conformers is possible through rotation around the C-C single bond (through **TS1b** with energy -295.4 kJ mol^{-1}). As already mentioned, also the isomerization process from **1-CA** to **Isoxazole** has been studied. The transition state **TS1d**, involving the simultaneous transposition of the hydrogen from methylene to the nitrile carbon and the attack of the nitrile carbon by carbonyl oxygen, has been found at 27.2 kJ mol^{-1} above the reactant asymptote, which makes this pathway unlikely in the ISM. **2-CA** can give keto-enolic tautomerization to **1-CVA** through **TS2b** (involving transposition of the hydrogen from methylene to the carbonyl oxygen) that lays at -54.2 kJ mol^{-1}. From **1-CVA**, two further isomerization pathways have been explored, related to the

conformational isomerization towards **2-CVA** through **TS3b** and the isomerization process towards the carbenic intermediate **IM1b** through **TS5b**. According to our calculations, only the first isomerization process can occur in the ISM because **TS3b** lays below the asymptotic limit at -270.2 kJ mol^{-1}. The other isomerization process cannot occur because **TS5b** lays 21.9 kJ mol^{-1} above the dissociation limit. Finally, several other isomerization processes have been studied, such as the formation of **3-CVA**, **4-CVA** (plus its dissociation to **C**+**D**), **5-CVA**, **6-CVA** and **AcC**. Only the two conformers, **6-CVA** and **5-CVA**, can be formed through a complex isomerization pathway which involves a relatively high energy transition state **TS6b** laying at 1.4 kJ mol^{-1} and two carbenic intermediates **IM3b** and **IM4b**. However, this is not expected to be an efficient path as it involves a relatively high energy barrier of 289.7 kJ mol^{-1}.

3.3.2 Reaction Channel 2

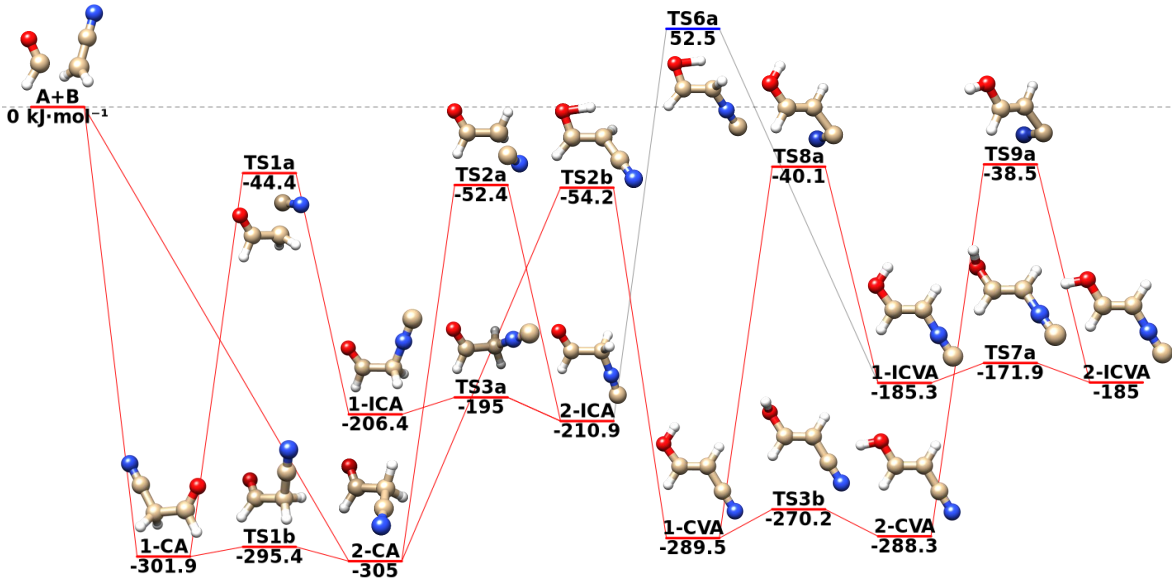

Figure 3.3: Energetics of the isomerization of cyanoacetaldehyde conformers (**1-CA**, **2-CA**) and cyanovinylalcohol isomers (**1-CVA** and **2-CVA**) to isocyanoacetaldehyde conformers (**1-ICA** and **2-ICA**) and isocyanovinylalcohol isomers (**1-ICVA** and **2-ICVA**). Energies in kJ mol^{-1} relative to the dissociation limit.

Reaction Channel 2 (green frame in Fig. 3.1), involves the conversion, through isomerization reactions, of cyano compounds to related isocyano compounds. Mechanisms and PES profile are given in Fig. 3.3. We found that most of the stationary points ruling this reaction channel lay below the dissociation limit, thus offering competitive reaction paths with respect to the isomerization mechanisms of the Reaction channel 1. In analogy with Channel 1, also in Channel 2 the initial barrierless attack of the two reactants to give **1-CA** and **2-CA** and the keto-enolic tautomerization process to give **1-CVA** and **2-CVA** are included in order to make the explanation of the mechanism clearer. Starting from **1-CA** and **2-CA**, two isomerization processes were computed to give **1-ICA** at -206.4 kJ mol^{-1} and **2-ICA** at -210.9 kJ mol^{-1}. **2-ICA** is slightly

more stable than **1-ICA**, probably due to a destabilizing repulsive electrostatic interaction between oxygen and nitrogen in the latter species. Two transition states, **TS1a** and **TS2a**, related to the nitrile/isonitrile isomerization processes, have been found at -44.4 kJ mol^{-1} and at -52.4 kJ mol^{-1}. Also in this case, the interconversion between **1-ICA** and **2-ICA** has been studied. The conformational transition state **TS3a**, related to the interconversion process, has been found at -195.0 kJ mol^{-1}. Moreover, the isomerization from isocyanoacetaldehyde (**2-ICA**) to isocyanovinylalcohol (**1-ICVA**) has been investigated. Two possible pathways have been considered: the keto-enolic tautomerization reaction from **2-ICA** to **1-ICVA** through **TS6a** and the isomerization from **1-CVA** to **1-ICVA** through **TS8a**. Based on our calculations, only the second pathway can occur in ISM conditions, because **TS8a** lays at -40.1 kJ mol^{-1} (**TS6a** shows instead an energy of 52.5 kJ mol^{-1}). Finally, the conformational isomerization of **1-ICVA** into **2-ICVA** has been examined through two possible pathways: the rotation around the dihedral angle included by HOCC, from **1-ICVA** to **2-ICVA** through **TS7a** and the nitrile/isonitrile isomerization from **2-CVA** to **2-ICVA** through **TS9a**. Both pathways can take place in the ISM, as none of them exhibits an energy barrier above the reactant asymptote.

3.3.3 Reaction Channel 3

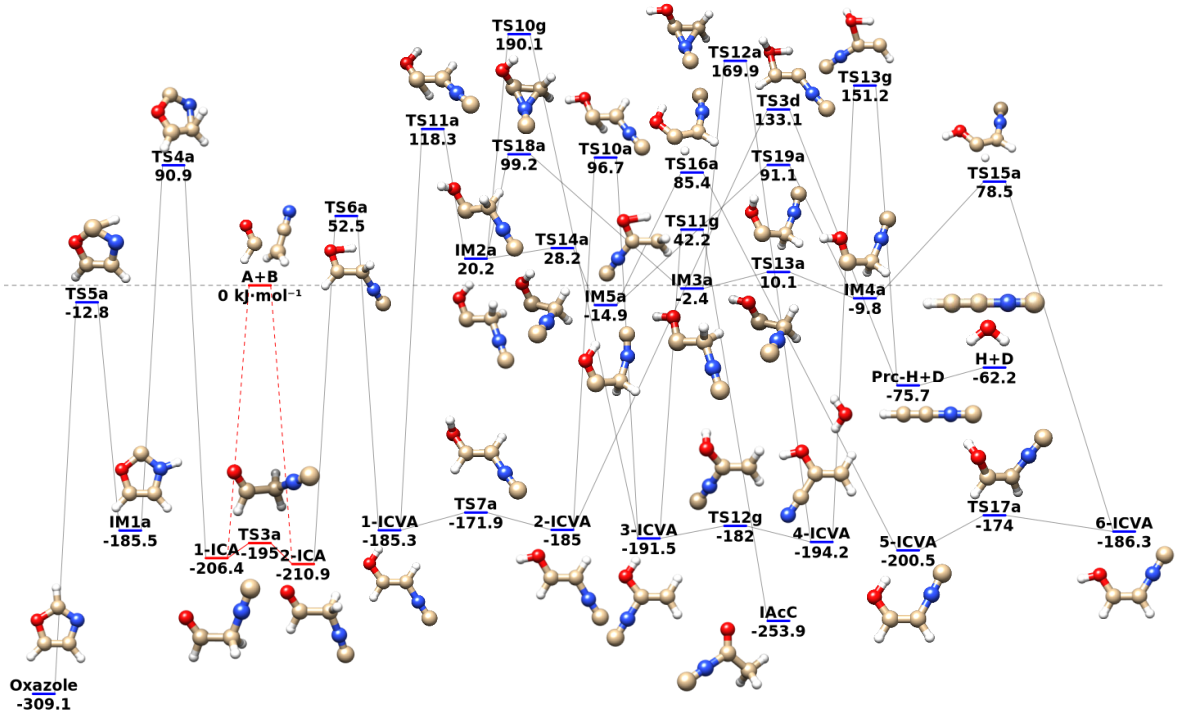

Figure 3.4: Energetics of the isomerization of isocyanoacetaldehyde conformers, isocyanovinylalcohol isomers (**1-ICVA**, **2-ICVA**, **3-ICVA**, **4-ICVA**, **5-ICVA** and **6-ICVA**), **Oxazole** and acetylisocyanide (**IAcC**). Dissociation to **H**+**D** also included. Energies in kJ mol^{-1} relative to the dissociation limit.

Reaction Channel 3 (blue frame in Fig. 3.1) includes the isomerization mechanisms of isocyanoacetaldehyde conformers (**1-ICA** and **2-ICA**) to **Oxazole**, acetylisocyanide (**IAcC**) and all isocyanovinylalcohol isomers (**1-ICVA**, **2-ICVA**, **3-ICVA**, **4-ICVA**, **5-ICVA** and **6-ICVA**) obtained from the keto-enolic tautomerization. Furthermore, the dissociation path from **2-ICVA** to **H**+**D** and the isomerization of **3-ICVA** into **IAcC** are included. Reaction mechanism and PES profile are given in Fig. 3.4, where the dashed lines connecting **A**+**B** to **1-ICA** and **2-ICA** indicate that formation of isocyanoacetaldehyde from the reactants is indirect and proceeds through steps that are not shown in the scheme and that have been discussed in the previous subsections. Based on our calculations none of the above mentioned pathways can take place in the ISM because too high energy barriers are involved.

3.3.4 Reaction Channel 4

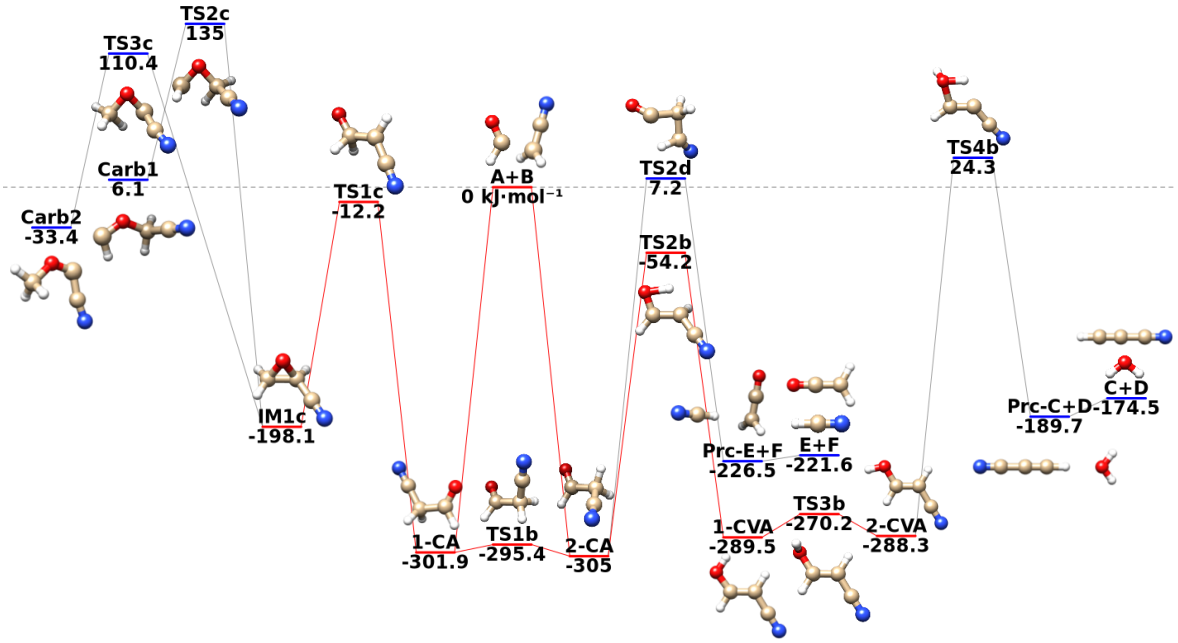

Figure 3.5: Energetics of the dissociation of cyanoacetaldehyde conformers (**1-CA** and **2-CA**) and cyanovinylalcohol isomer (**2-CVA**). Energies in kJ mol^{-1} relative to the dissociation limit.

Reaction Channel 4 (yellow frame in Fig. 3.1) includes some of the possible dissociation reactions of cyanoacetaldehyde to compounds already detected in the ISM such as ketene and hydrogen cyanide (**E**+**F**), cyanoacetylene and water (**C**+**D**), together with an isomerization reaction leading to the formation of carbene compounds (**Carb1**, **Carb2**). Reaction mechanisms and PES profile are given in Fig. 3.5. This portion of reaction mechanism thus features another isomerization reaction and two dissociation mechanisms. The isomerization reaction leads to the formation of two carbenic compounds **Carb1** and **Carb2**, as possible products of a combustion process, however, very unlikely at the ISM conditions. On the other hand, **IM1c**, also known as

oxiranecarbonitrile[175], can be populated, because **TS1c** lays 12.2 kJ mol^{-1} below the reactants. The two dissociation mechanisms (to **C**+**D** and **E**+**F**) lead to the formation of other species widely detected in the ISM: ketene (H_2C_2O), hydrogen cyanide (HCN), cyanoacetylene (HC_3N) and water (H_2O). However, also for such paths too high energy barriers were found. Some additional remarks are in order about the dissociation mechanism which leads to HC_3N + H_2O since our results point out some differences with respect to the pathways proposed by Horn et al[152]. As already mentioned, those authors studied the formation of cyanoacetaldehyde from the cyanoacetylene (HC_3N) hydrolysis, concluding that **1-CVA** is the favoured product issuing from the attack of H_2O to HC_3N. We carried out an IRC computation in order to verify which conformer is preferred upon addition of H_2O to HC_3N. According to our computations, **2-CVA** is the preferred conformer. Moreover, Horn et al. proposed a conversion from cis to trans configuration, which leads to a very unstable transition state. After that, from **1-CVA**, they found a transition state ruling the keto-enolic tautomerization, which leads to the formation of **2-CA**. Our calculations suggest that this is not the most efficient mechanism for the keto-enolic tautomerization reactions. As an alternative, we propose that the cis/trans isomerization is not needed to obtain **2-CA**, but, rather, that **2-CVA** isomerizes to **1-CVA** and then to **2-CA**. This path does not involve the high-energy transition state ruling the cis/trans isomerization. In addition, the comparison of the reaction profile shows a good agreement of the energy barriers involved in both mechanisms, which confirms the validity of our computational procedure. Two further dissociative pathways involving the breaking of C-C, C-O and C-H bonds and leading to astrochemically relevant species were also investigated (though they are not shown in the figure). The first of these involves the dissociation of **6-CVA** to HOCN (cyanic acid) and HCCH (acetylene), two species that have already been detected in the ISM. The second one involves the dissociation of **1-CA** to NCHCCO (cyanoketene, not yet detected in the ISM) and H_2. Both pathways proceed through formation of a transition state and a pre-reactive complex. However, in both cases the transition state lies significantly above the reactant asymptotic limit (120.2 and 18.5 kJ mol^{-1}, respectively), so that both processes have no relevance in the ISM conditions.

3.3.5 Astrochemically relevant reaction pathways

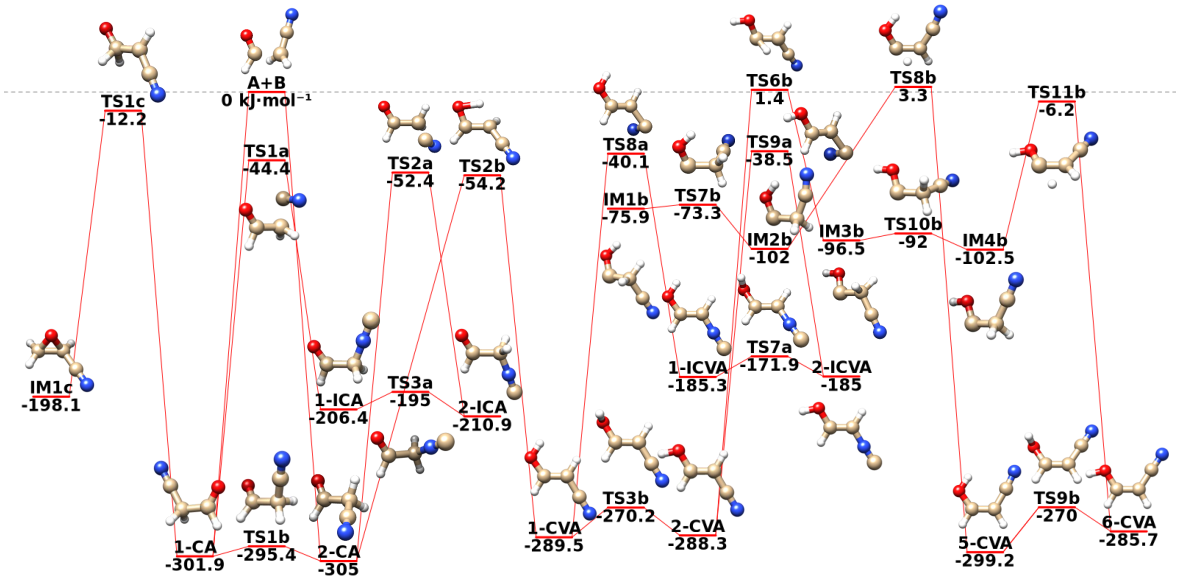

Figure 3.6: Comprehensive view of the astrochemically relevant paths (those highlighted in red in Figs. 3.2-3.5) of the reaction scheme computed in this work.

3.4 Kinetics

The potential energy surface for the reaction of cyanomethyl and formyl radicals computed in this work and presented in Sec. 3.3 gives an in-depth view of the overall mechanism of formation of cyanoacetaldehyde and its possible evolution. However, a comprehensive understanding of the evolution of the reaction along competitive paths can only be attained by modeling the associated reaction kinetics, that provides a detailed description of the reaction progress and helps in predicting the chemical traces that might be detected experimentally in interstellar space. In principle, the time evolution of a chemical reaction should be addressed through a quantum treatment of the underlying nuclear motion. However, exact quantum-dynamics calculations are only achievable for very small systems [102, 104, 105, 106]. Approximate quantum-dynamical methods are able to extend this limit to slightly larger systems but are definitely out of reach for the reactions such as that reported in this article. More affordable, yet reasonably accurate, approaches are either a (quasi-)classical treatment [109, 110, 111] of the nuclear motion or simpler approximations rooted into some flavour of the transition-state theory (TST), where the kinetic information is obtained from the stationary points characterizing the PES. In the present case, the branching ratios among the several reaction products were obtained from unimolecular kinetics calculations in the Rice-Ramsperger-Kassel-Marcus (RRKM) framework[112, 113, 114] for all the steps following the bimolecular association. The reaction rates issuing from those

computations are next combined in a master equation treatment. The microcanonical rate constants (k(E)) of each unimolecular step are given by

$$k(E) = \frac{N^{\ddagger}(E)}{h\rho(E)} \tag{3.4}$$

where, E is the energy, $N^{\ddagger}(E)$ is the rovibrational sum of states of the transition state, h is the Planck's constant and $\rho(E)$ is the rovibrational density of states of the reactant species. The vibrational densities of states were calculated by the Stein-Rabinovitch algorithm [128] and are then convoluted with classical rotor densities of states to obtain the final rovibrational densities. Sums of states were computed by a simple integration of the corresponding densities. Then, the chemical master equation is constructed by using all the individual rate constants for each step. In this framework, the evolution of the relative abundance of each involved species as a function of time can be described by an ordinary first order differential equation

$$\frac{\mathrm{d}\mathbf{c}(t)}{\mathrm{d}t} = \mathbf{K}\mathbf{c}(t) \tag{3.5}$$

where $\mathbf{c}(t)$ is the vector of the concentration of the species at time t, and $\mathbf{K}$ is a square matrix containing proper combinations of the microcanonical rate constants for each step at a given energy. Accordingly, the time evolution of the species concentrations can be obtained by matrix diagonalization techniques according to

$$\mathbf{c}(t) = \mathbf{Z}e^{\mathbf{\Lambda}t}\mathbf{Z}^{-1}\mathbf{c}(0) \tag{3.6}$$

where, $\mathbf{c}(0)$ is the species concentration at $t = 0$, $\mathbf{\Lambda}$ is the eigenvalue vector and $\mathbf{Z}$ is the eigenvector matrix. The readers are referred to Refs. [100, 153] for further details about the StarRate implementation. As described in detail in Sec. 3.3, the title reaction starts with formation of **1-CA** from association of cyanomethyl (CH_2CN) and formyl radicals (HCO). This species can isomerize to **2-CA**, and both isomers can further evolve along several different pathways. Several reaction channels are, however, ruled by energy barriers laying above the reactant asymptote, thus being unlikely in the ISM. According to the results discussed in the preceding sections, only the following species can be formed by reactions involving only submerged barriers: **1-CA**, **2-CA**, **1-CVA**, **2-CVA**, **1-ICA**, **2-ICA**, **1-ICVA**, **2-ICVA**, and **IM1c**.
This last species, however, is far less relevant than the others as it is accessed by a reaction step from **1-CA** through **TS1c** involving a very high energy barrier (289.7 kJ mol^{-1}). In order to investigate the kinetics of the isomerization reactions of cyanoacetaldehyde, we addressed an energy range from 0 to 6 kJ mol^{-1} (equivalent temperature 720 K), corresponding to the typical accuracy of popular composite schemes and representing a conservative upper bound to the accuracy of the computed energy barriers. In the following, we first show for illustrative purposes the time evolution of the relative abundances of the several involved species for a selected energy of 5 kJ mol^{-1} (enough to open up a 'non-submerged' reaction path), and then discuss the final populations (those resulting in the infinite future) over the entire considered energy range. As shown in Fig. 3.6, at 5 kJ mol^{-1} additional reaction channels open up leading to 1)

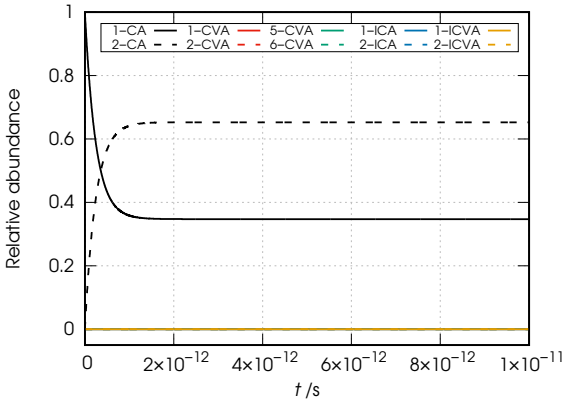

Figure 3.7: Relative abundance (arbitrary unit) vs time plot at 5 kJ mol^{-1}.

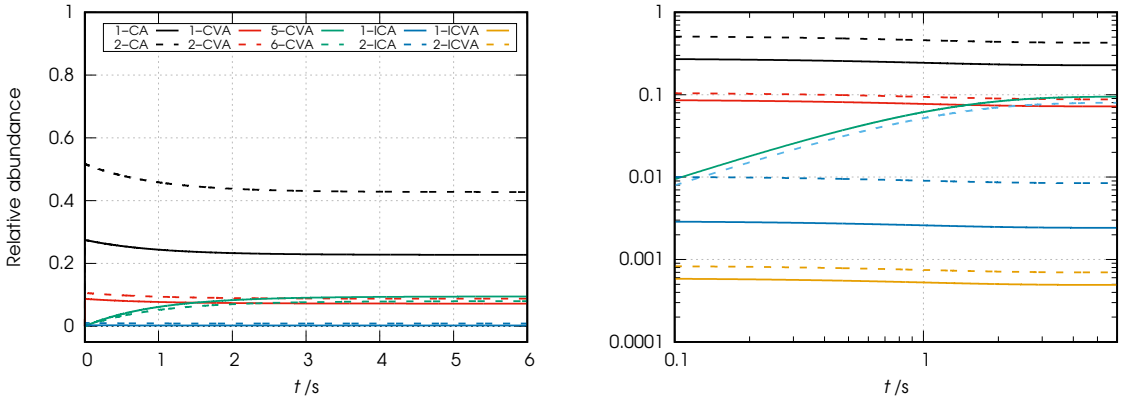

Figure 3.8: Relative abundance (arbitrary unit) vs time plot at 5 kJ mol^{-1}.

formation of **5-CVA** and **6-CVA** through **TS6b** (laying at 1.4 kJ mol^{-1}), **IM3b** and **IM4b**, and 2) formation of **IM1b** and **IM2b** through **TS8b** (laying at 3.3 kJ mol^{-1}). Among these species, only **5-CVA** and **6-CVA** turned out to be non-negligibly involved in the reaction, while all others (including the previously mentioned **IM1c**) resulted in relative abundances well below 0.1%. We will therefore from now on focus our analysis on the following ten species: **1-CA**, **2-CA**, **1-CVA**, **2-CVA**, **1-ICA**, **2-ICA**, **1-ICVA**, **2-ICVA**, **5-CVA** and **6-CVA**.

In Fig. 3.7, the relative abundance of the ten main products outlined above is plotted as a function of time in a very short time frame at the beginning of the reaction (10^{-11} s) for an energy of 5 kJ mol^{-1}. The figure shows that rapidly (in a time frame of less than 2×10^{-12} s), the **1-CA**-**2-CA** isomerization process occurs (in agreement with its very low activation energy) and a **1-CA**:**2-CA** ratio of 0.35:0.65 is soon established. This picture undergoes slight changes when moving to the analysis of a larger time frame. In the left panel of Fig. 3.8, the relative abundances for the same species at the same energy of 5 kJ mol^{-1} are plotted as a function of time up to 6 s. The right panel reproduces the same plot using a logarithm scale for both axes. In this figure, the detail on the conversion between **1-CA** and **2-CA** is lost, but additional information is gained on the progress of the overall reaction. In fact, as more visible in the right panel of the figure, formation of other species occurs at different time scales, whereby,

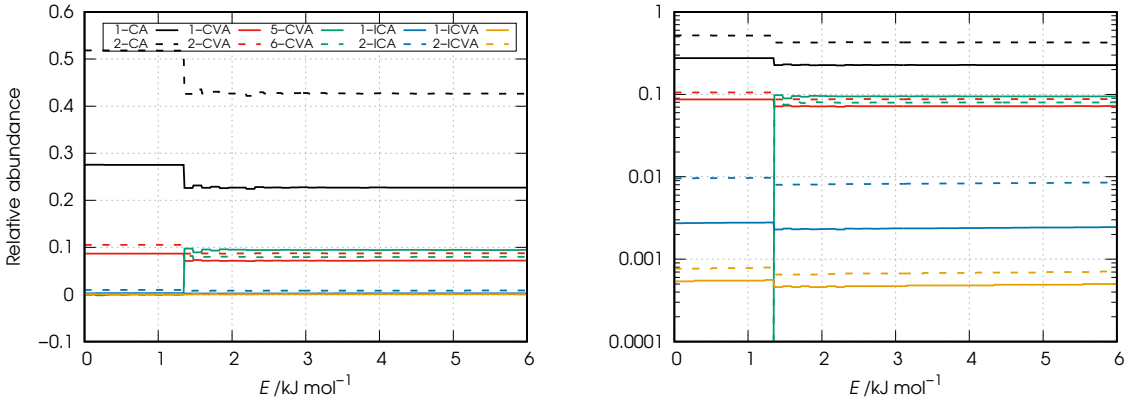

Figure 3.9: Final populations for all the species for an energy range of 6 kJ mol^{-1} above the dissociation limit.

for instance, **1-ICA** and **2-ICA** rapidly reach a relative abundance of $\sim 10\%$, while those of **5-CVA** and **6-CVA** reach a comparable plateau only after about 2 seconds. The relative abundance of **1-CA** and **2-CA** is of course affected by the population of the other species as the reaction proceeds (decreasing to values of 0.23 and 0.43, respectively), however their ratio keeps almost constant at a value of 0.35:0.65. In order to assess how these results are affected by the available energy and obtain a more informative picture, we plot in the left panel of Fig. 3.9 the final populations for an energy range up to 6 kJ mol^{-1} (corresponding, as already mentioned, to an upper bound for the accuracy of the computed energy barriers).
The right panel of the figure shows the same plot using a logarithm scale for the relative abundances. It is apparent that the picture is essentially the same for all considered energies, with the relative abundance of **2-CA** almost doubling that of **1-CA**, and with the relative abundances of the minor species undergoing minor changes, except near an energy of 1.4 kJ mol^{-1} where the channel leading to formation of **5-CVA** and **6-CVA** opens up. According to these results, the ratio between the abundances of the two main conformers **1-CA** and **2-CA** is far from thermodynamic equilibrium under the physical conditions characterizing the ISM. In fact, while the thermodynamic **1-CA**:**2-CA** ratio (which can be straightforwardly determined by the energy difference between the conformers) is 0.42:0.58 at a temperature of 10 K and 0.47:0.53 a temperature of 24 K, the kinetically determined one keeps an almost constant value of about 0.35:0.65 in an energy range up to an equivalent temperature of 720 K. Of course, the lack of collisional relaxation processes in the ISM due to low-pressure conditions implies that the effective formation of the discussed complexes entirely relies on radiative stabilization mechanisms [176, 177]. These have indeed been shown to play a key role in association reactions leading to complexes with several number of vibrational modes and accessible isomers [178] such as those targeted in this work. Vuitton et al. [179] have estimated that at low temperatures the rate coefficients for exothermic processes leading to radiative association are close to the collision limit for adducts having as few as four C atoms, predicting an association rate of 1.1×10^{-10} cm^3 s^{-1} at 150 K for complexes having five 'heavy' atoms such as cyanoacetaldehyde. As pointed out in Ref. [177], in the low-pressure limit the effective association rate is given by

$k_{\text{eff}} = k_f k_r/(k_b+k_r)$, where k_f is the forward association rate, k_b is the back-dissociation rate, and k_r is the radiative stabilization rate. In order to assess the importance of radiative stabilization for the reaction considered in this work, we computed the **1-CA** association rate (forward rate, k_f) using a capture model for a long range potential of the form $-C_6/R^6$ using the approach outlined in Ref. [180]. To this purpose, a C_6 coefficient of 182.92 Hartree ${a_0}^6$ was obtained by performing energy calculations for several points along the entrance coordinate for the HCO + CH_2CN reaction and by fitting the energies to a $V = V_0 - C_6/R^6$ law. An estimate of the rate constant for radiative stabilization (k_r) was obtained within a harmonic approximation from the ir absorption intensities for the $v = 0$ to $v = 1$ transition of the various vibrational modes of the complex as described in Ref. [177]. In an energy range of 0.12-1.32 kJ mol^{-1} (range of equivalent temperatures: 15-160 K), k_f varies from 3.5×10^{-10} to 4.8×10^{-10} cm^3 s^{-1}. On the other hand, the k_r calculated on the corresponding interval of equivalent temperatures ranges from 4.68×10^{-9} to 9.5×10^{-4} s^{-1}. Now, as can be argued from the above expression of k_{eff}, any value of k_b significantly lower than k_r (up to the limiting case of $k_b = 1.0 \times 10^{-23}$ and 5.1×10^{-21} s^{-1} obtained for the extremes of the mentioned energy range by computing k_b from k_f through the principle of detailed balance as done in Ref. [180]) would lead to a rate equal to k_f. Thus in the considered astrochemically relevant energy range the effective association rate for the process studied in this work is expected to be in the range 3.5-4.8 $\times 10^{-10}$ cm^3 s^{-1}, which is in good agreement with the prediction by Vuitton et al. of 1.1×10^{-10} cm^3 s^{-1} at 150 K [179].

3.5 Conclusions

In this paper we have modeled a gas-phase route leading to the formation of cyanoacetaldehyde, an important molecule considered a forerunner of the pyrimidine bases cytosine and uracil. The computed mechanism starts from reaction of the formyl (HCO) and cyanomethyl (CH_2CN) radicals and involves several isomerization and dissociation pathways. The potential-energy surface for such reaction has been explored by quantum chemical computations employing double-hybrid density functionals and further refined by single-point calculations exploiting the 'Cheap' composite scheme. According to our results, the direct association of the HCO and CH_2CN radicals is strongly exothermic and thus thermodynamically favoured under the harsh conditions of the ISM. Kinetic calculations show that the main products of the reaction are the two conformers of cyanoacetaldehyde (nitrile and carbonyl groups in a cis or trans configuration) in a cis:trans ratio of about 0.35:0.65 (resulting from relative abundances of 0.28 and 0.52, respectively, in an energy range below 1.4 kJ mol^{-1}) for energy ranges compatible with the ISM conditions. Some other products are also found, including isomers of isocyanoacetaldehyde, cyanovinylalcohol and isocyanovinylalcohol with relative abundances not exceeding 10%. The computed ratio between the two main conformers of cyanoacetaldehyde differs from that computed at thermodynamical equilibrium and reflects the complexity of the overall reaction mechanism. Such ratio in the effective conditions of the ISM may be further affected by different destruction rates for the two conformers by reaction with the abundant atomic hydrogen, as shown for the much

simpler case of Z- and E-cyanomethanimine in Ref. [181]. This prompts further work which is ongoing in our group for examining this aspect through the modeling of the more challenging reaction of cyanoacetaldehyde with atomic hydrogen.

Chapter 4

Toward the detection of cyanoketene in the interstellar medium: new hints from quantum chemistry and rotational spectroscopy

In this Chapter is proposed a detailed quantum chemical investigation of a new reaction mechanism possibly leading to the formation of cyanoketene in the ISM, for which different reaction channels have been found by the AutoMeKin program and the structures and harmonic force fields of the key stationary points have been characterized at the DFT level employing last-generation double hybrid functionals. Finally, single point computations at those geometries by state-of-the-art composite wave-function methods provided accurate energies for the evaluation of thermochemical and kinetic parameters in the framework of an Ab-Initio Transition State Theory based Master Equation (AITSTME) strategy. Our results indicate that the barrier-less association reaction of the formyl radical (HCO) to the cyanocarbene radical (HCCN) can lead to the formation of cyanoketene under the harsh conditions of the ISM. Canonical rate constants computed for temperatures up to 600 K show that the most abundant product is indeed cyanoketene. Furthermore, to aid the search of cyanoketene, still undetected in the ISM, its rotational spectrum was recorded up to 530 GHz. The refined set of spectroscopic constants obtained in this way allows spectral predictions from the microwave to the terahertz region, particularly for the bright b-type transitions, which can be targeted for the identification of cyanoketene in spectral line surveys. Despite cyanoketene was already sought in a variety of astronomical sources, we suggest to look for it in those sources where HCO or HCCN have been already detected, namely W3, NGC2024, W51, K3-50, IRC+2016 and TMC-1. This Chapter is based on an article already published by Ballotta et. al [182].

4.1 Introduction

A recent joint laboratory-observational paper [183] addressed the issue of the presence of cyanoketene in the interstellar medium (ISM). The rationale for the search of this molecule was the 44-year-old detection of ketene [184] and the existence of several CN-containing molecules in the ISM[12], such as cyanoformaldehyde [185], aminoacetonitrile [186, 187], benzonitrile [188], and many cyanopolyynes [189, 190, 191, 192]. Searched for in several star-forming regions, cyanoketene was not detected and its chemical formation route was discussed by Margulès et al.,[183], who suggested three possible pathways: (i) the addition of the CN radical to ketene or (ii) to the ketenyl radical HC_2O, and (iii) the reaction of the C_3N radical with water. While the third reaction would probably lead to different products [183], the first two reactions represent plausible formation pathways for cyanoketene in the ISM. Indeed, the reaction between the CN radical and a neutral partner has already been shown to be an effective formation route for some other molecules in the ISM (see, e.g., Vazart et al.[193] for cyanomethanimine and Tonolo et al.[194] for cyanoformaldehyde). Anyway, computational and experimental studies for the addition of CN to ketene by Zhang and Du, Sun et l., Edwards and Hershberger[195, 196, 197] showed that this reaction leads to the formation of $CO+H_2C_2N$ through a dissociative recombination process. Since reaction (ii) is a radiative association process, the final product is expected to be stabilized by photon emission, otherwise the excess energy would lead to back dissociation to the initial reactants, as already proposed in the case of the formation cyanoacetaldehyde [142]. For this reason Margulés et al. considered this reaction unlikely in the ISM, but possible on grain surfaces. Finally, a computational investigation of reaction (iii) by Xie et al.[198] showed that it cannot occur at very low temperatures because of a non-negligible energy barrier for the hydrogen abstraction. The same authors studied also the catalytic effect of water on the reaction and found that increasing the number of catalyzing water molecules the reaction becomes barrier-less. However, due to the very low pressure characterizing the ISM, reactions between more than two reactants are very unlikely, so that this reaction channel seems not plausible for cyanoketene synthesis.

In addition to these possibilities, a computational study of Xie et al.[199] found NC-CHCO as an intermediate of the reaction between atomic oxygen and cyanoacetylene (HC_3N) in the gas phase and on water ice. By investigating both gas-phase and water ice catalyzed reactivity, it was shown that the activation energy governing the gas-phase process can be strongly lowered by the catalytic activity of water, up to producing a barrier-less process. Another mechanism, involving the reaction between NCO and C_2H_2, was proposed by Xie et al.[200] and leads to cyanoketene as one of the possible products. Unfortunately, this process involves a non-negligible energy barrier, which cannot be overcome under the ISM conditions. Furthermore the authors performed a kinetic analysis and the result demonstrated that the preferred products are HCN and HC_2O.

In the present work we suggest an alternative mechanism for the formation of cyanoketene, which involves two reactants already detected in the ISM, namely the cyanocarbene (HCCN)[201] and formyl (HCO)[202] radicals. In order to obtain an accurate descrip-

tion of reaction energies and activation barriers, a full quantum-mechanical investigation of different reaction paths has been carried out combining state-of-the-art density functionals and wave-function composite methods [168]. Exploiting these data, a kinetic analysis has been next performed employing a Master Equation (ME) approach to compute the formation rate constants of the products and to prove the effectiveness of the mechanism proposed.
Additionally, we have extended the study of the rotational spectrum of cyanoketene into the sub-millimeter-wave range in order to facilitate its astronomical observation. Although most of the first interstellar detections relied on low-frequency observations [12], the higher-frequency spectral windows covered by modern facilities (such as ALMA[1] or SOFIA[2]) offer further chances to detect additional complex organic molecules (COMs), i.e., molecules containing at least one carbon atom and a total of at least six atoms. Their capabilities have been demonstrated recently by the discovery of interstellar species (including COMs) observable only in the THz domain [203, 204, 205] by exploiting high frequencies ALMA Band 10 spectral line surveys [206, 207].
Based on these premises, the rotational spectrum of cyanoketene has been measured up to 530 GHz, with the inclusion of additional *b*-type *Q* branch transitions with respect to the data reported by Margulés et al.[183]. These improvements allowed a refinement of all the spectroscopic constants and a precise determination of the purely K_a dependent centrifugal distortion constants up to the eighth order. On the whole, the newly determined set of spectroscopic parameters extends the range of reliable spectral predictions up to the ALMA Band 9 (602–720 GHz).

4.2 Computational Details

4.2.1 Reaction mechanism discovery

Feasible reaction paths have been generated by means of the AutoMeKin [49, 50, 2] program, designed for the automated reaction mechanism discovery. The program is based on the application of methods and concepts rooted in the graph theory, reactive molecular dynamics and electronic structure. The dynamic simulations needed to obtain the initial structures of the transition states (TS) governing putative reaction mechanisms were performed using the semi-empirical PM7 method [55] implemented in the MOPAC package [51]. 100 trajectories per iteration (keyword *ntraj*) were calculated for a total of 10 iterations. The screening parameters used to avoid redundant structures included a value of 100 cm^{-1} for the smallest accepted imaginary frequency (keyword *imagmin*) in order to take into account also torsional transition states and a value of 0.1 for the lowest eigenvalue of the Laplacian used to differentiate the structures resulting from the fragmentation of an intermediate (keyword *eigLmax*). Two other parameters (MAPE max and BAPE max) used to compare the descriptors characterizing the different structures obtained from the molecular dynamics simulations, were set to 0.002 and 1.5, respectively. Further details about these screening parameters can be found in ref. [37]. After this step, optimized geometries and zero-point

[1] Atacama Large Millimeter/submillimeter Array
[2] Stratospheric Observatory for Infrared Astronomy

corrected electronic energies of reactants, transition states, intermediates, and products along the reaction pathways were obtained by the rev-DSD-PBEP86[162]-GD3BJ[69] double-hybrid functional in conjunction with the jun-cc-pVTZ basis set. [160] This combination of functional and basis set will be referred to in the following as rDSD. Diagonalization of analytical rDSD Hessians[208] allowed also to characterize all the critical points belonging to the reaction pathways as minima (reactants, intermediates and products) and saddle points (transition states). The different elementary steps were further characterized following rDSD intrinsic reaction coordinates (IRCs)[161] starting from the different TSs.
The results of the simulations have been analyzed using the AMK tool [57], which allows to examine the extremely complex reaction networks generated by AutoMeKin, to visualize molecular structures with their vibrational normal modes and to check the potential energy profiles of the reaction mechanisms investigated. Thanks to AMK, it has been possible to find the reaction pathways which lead to the formation of cyanoketene and to select the structures of all the critical points ruling these paths. For such structures, improved electronic energies were obtained by single point computations exploiting the junChS-F12 composite scheme described in more detail in the next subsection.

4.2.2 junChS-F12 Composite scheme

It is well-known that for systems not showing strong multireference character the coupled-cluster (CC) model including single, double and perturbative estimate of triple excitations (CCSD(T))[209] delivers accurate electronic energies provided that complete basis set (CBS) extrapolation and core valence (CV) correlation are taken into the proper account. The key idea of the reduced cost Cheap scheme (ChS)[210, 165, 168, 36] is that, starting from frozen core (fc) CCSD(T) computations in conjunction with a (partially augmented) triple-zeta basis set[170, 171, 211, 212], CBS and CV terms can be computed with good accuracy and negligible additional cost employing second order Møller-Plesset perturbation theory (MP2)[213]. In particular, the CBS extrapolation by the standard n^{-3} two-point formula[214] employs MP2/jun-cc-pV(X+d)Z energies with X = T and Q, whereas the CV contribution is incorporated as the difference between all-electron (ae) and fc MP2 calculations, both with the cc-pCVW(T+d)Z basis set [215]. Replacement of conventional methods by the explicitly correlated (F12) variants[58, 60] leads to our current standard version of the approach, which is referred to as junChS-F12[1, 216, 217]. Comparison with the most accurate results available for reaction energies and activation barriers [168, 1, 217] showed that junChS-F12 energy evaluations at rDSD optimized geometries provide average absolute errors of the order of 1 kJ mol^{-1}. Therefore, this approach was employed for all the stationary points in conjunction with anharmonic zero-point vibrational energy corrections computed in the framework of second-order vibrational perturbation theory [218] employing rDSD anharmonic force fields.
All DFT calculations were performed using Gaussian16[52], while junChS-F12 calculations were performed using MOLPRO [63, 62, 61].

4.2.3 Kinetics

Global and channel-specific rate constants have been computed in the framework of the Ab Initio Transition State Theory based Master Equation approach (AITSTME) employing the MESS software [85] to solve the multiwell one-dimensional master equation by the chemically significant eigenvalue (CSE) method. The collisional energy transfer probability is described using the exponential down model[219] with a temperature dependent $< \Delta E_{down} >$ of $260 \times (\mathrm{T}/298)^{0.875}$ cm^{-1} in an argon bath.
For elementary steps governed by distinct saddle points, rate coefficients are determined by the conventional transition- state theory (TST) within the rigid-rotor harmonic-oscillator (RRHO) approximation and including tunneling as well as non-classical reflection effects using the Eckart model[84].
Instead, rate constants for barrier-less elementary reactions are computed employing the phase space theory (PST)[44, 45]. The long-range interaction between the incoming reactants is described by an isotropic attractive potential $V(R) = -C_6/R^6$ [75]. The C_6 parameter (90.12 ${a_0}^6 E_\mathrm{h}$) has been obtained by a least-square fitting of rDSD electronic energies computed at different values of the HOC-CHCN distance. It is well known that Phase Space Theory (PST) can overestimate the rate of barrier-less association reactions leading to uncertainties of up to a factor of 2-3 on the total reaction rates with respect to experimental data and/or theoretical estimations obtained by more sophisticated methods.[220, 76] However, the main aim of our work is to provide a semi-quantitative support to the suggested reaction mechanism. In this context, the above mentioned uncertainty does not impair the comparison between different products since the entrance channel is common to all of them. This comment does not detract, of course, from the possibility of applying in forthcoming studies more elaborate methods, which have proved to be more reliable in the quantitative determination of the reaction rates.
Rate constants have been evaluated for a pressure 1×10^{-8} bar in the 10–600 K temperature range to mimic the typical conditions of different regions of the ISM. Next, the rate constants at different temperatures have been fitted to a three-parameter modified Arrhenius equation, namely the Arrhenius–Kooij expression[221, 222]:

$$k(T) = A(\frac{T}{300})^n e^{-\frac{E}{RT}}$$

where A, n, and E are the fitting parameters and R is the universal gas constant.
The key results of the kinetic analysis have been further checked by computations performed with the StarRate program, specifically designed for reactions of astrochemical interest.[90, 3].

4.3 The potential energy surface

A schematic diagram of the potential energy surface (PES) generated by AutoMeKin is shown in Figure 4.1. The initial reactants, **Rx1**, are the HCO and HCCN radicals, whose electronic ground states are a doublet and a triplet, respectively. In analogy with the formation route of ethanimine investigated by Balucani et al.[223] and Baiano et

al.[224], a total of six spin states are thus possible, including the two components of the reactive doublet state which can bring to the formation of a chemical bond and the four components of the non-reactive quartet state.

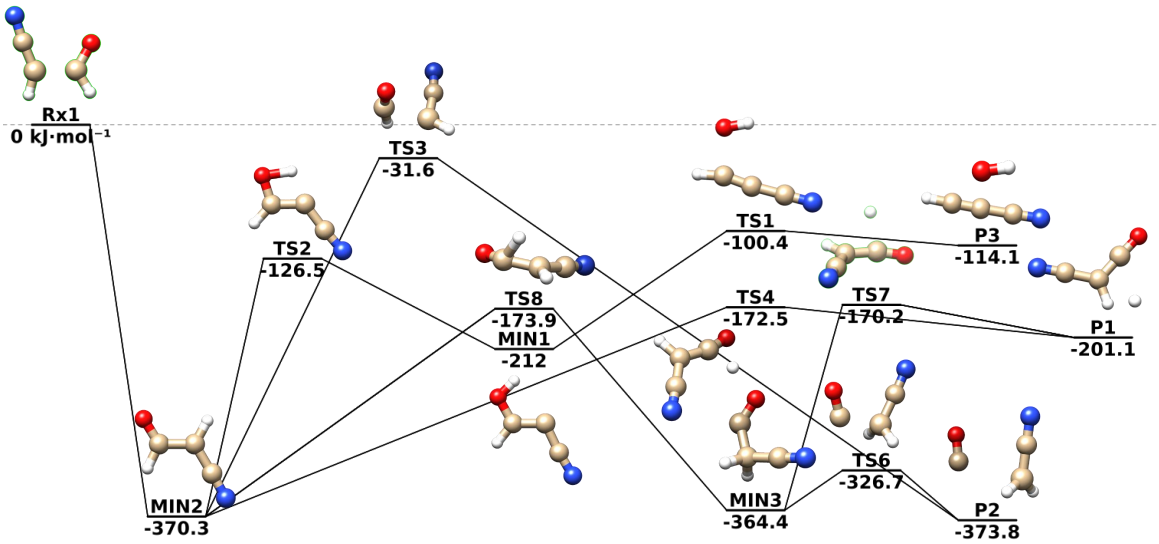

Figure 4.1: Energetics of the reaction: junChS-F12 electronic energies augmented by rDSD anharmonic ZPE corrections. Energies in kJ mol^{-1} relative to the reactants limit.

4.3.1 Description of the reaction mechanism

We recall that both the reactants representing the asymptotic limit (AL), namely HCCN (triplet state) and HCO (doublet state) have been detected in the ISM. As shown in Figure B.1 reported in Appendix B, the formyl radical carries out a barrierless attack on the sp^2 carbon of cyanocarbene radical, which brings to the formation of the new C-C bond and leads to a strong stabilization of the system. The intermediate reached at the end of this step (**MIN2**), which lies 370.3 kJ mol^{-1} below the AL. **MIN2**, can next undergo a hydrogen transposition, which leads to the formation of another (less stable) reaction intermediate **MIN1** and subsequently, through the breaking of the C-O bond, leads to the **P3** products, i.e. cyanoacetylene (HC_3N) and the hydroxyl radical(OH).
Another reactive pathway that can originate from **MIN2** is the dissociation with the simultaneous hydrogen transfer reaction leading to the formation of **P2** at -373.8 kJ mol^{-1}, i.e. carbon monoxide (CO) and cyanomethyl radical (H_2C_2N the thermodynamically most stable products of the reaction mechanism shown in Figure 4.1.
A third possible reaction channel is the transposition of hydrogen from **MIN2** to **MIN3** through the transition state **TS8** at -173.9 kJ mol^{-1} and the subsequent dissociation of **MIN3** to **P2** through the transition state **TS6** at -326.7 kJ mol^{-1}. The elimination of a hydrogen atom from **MIN2** gives the final product by overcoming a barrier of 197.8 kJ mol^{-1}. In the corresponding transition state **TS4**, (172.5 kJ mol^{-1}

below the AL) a π bond is being formed between the two carbon atoms. The **P1** products, namely cyanoketene and a hydrogen atom, are 201.1 kJ mol^{-1} more stable than the reactants. Since the process is exothermic and the whole energy profile lies below the AL, our computations suggest that this pathway represents a plausible mechanism for the formation of cyanoketene in the ISM. The relative electronic energies of all the stationary points obtained at the rDSD and junChS-F12 levels are reported in Table B.1 reported in Appendix B.

4.4 Rate constants

In order to prove that the reaction mechanism proposed in this work could justify the formation of cyanoketene in the ISM, it is necessary to perform kinetic computations. The rate constants as a function of temperature for the products **P1**, **P2**, **P3** obtained for the reaction between HCCN and HCO is shown in Figure 4.2. The parameters of the corresponding Arrhenius-Kooij fits are collected in Table 4.1.

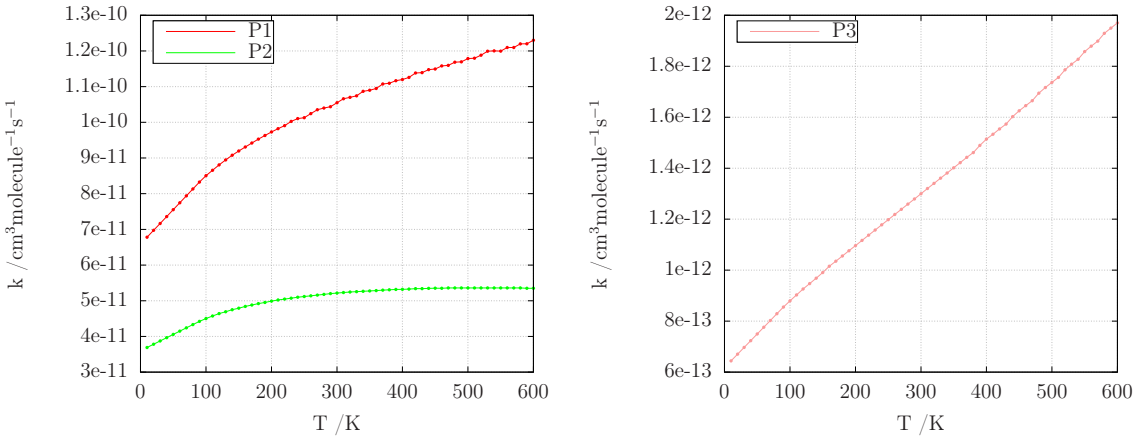

Figure 4.2: Temperature-dependence plots of the **P1**, **P2** and **P3** products of the HCCN˙+ HCO reaction.

	P1	**P2**	**P3**
A/cm^{3}molecule^{-1}s^{-1}	1.04×10^{-10}	5.48×10^{-11}	1.11×10^{-12}
n	0.22	0.02	0.68
E/kJmol^{-1}	-44.60	132.46	-444.62
rms[a]	2.90×10^{-13}	2.83×10^{-13}	1.86×10^{-14}

[a] rms stands for root-mean-square deviation of the fit.

Table 4.1: The Arrhenius-Kooij Parameters for the HCCN + HCO reaction.

Inspection of the results reported in Figure 4.2 shows that the formation rate of **P1** ranges between 6.8×10^{-11} and 1.22×10^{-11}cm^{3}molecule^{-1}s^{-1} and is higher than the formation rates of **P2** and **P3** in the whole interval of temperatures (0-600 K). This is

mainly due to the nature of the reaction pathways leading to **P1**, which includes the single-step path **MIN2-TS4-P1**, governed by one of the lowest activation energies of all the reaction channels of **MIN2** towards the possible products. The other single step reaction pathway is **MIN2-TS3-P2**, and in this case the very high activation energy (about 340 kJ mol^{-1}) makes it the most kinetically disfavored. All the other pathways found by AutoMeKin involve multi-step reactions leading to the formation of **P1**, **P2** and **P3**. Indeed, the second most competitive route is the transposition of hydrogen through **MIN2-TS8-MIN3**. Although **TS8** is the lowest energy transition state, the multi-step nature of the corresponding reaction channel makes this route less favorable with respect to the **MIN2-TS4-P1** pathway. **P2** is the second most favored product since its formation rate takes values between 3.6×10^{-11} and 5.4×10^{-11} $cm^3molecule^{-1}s^{-1}$. Finally, the formation rate of **P3** assumes values between 2.0×10^{-13} and 6.6×10^{-13} $cm^3molecule^{-1}s^{-1}$, which is the lowest of the all products of the reaction. This is probably due to the nature of the **P3** formation pathway, which involves the highest activation barriers.
In summary, a detailed kinetic analysis shows that, in spite of the greater stability of **P2** with respect to other possible products, cyanoketene is formed preferentially under the typical physical-chemical conditions of the interstellar medium.

4.5 Experiment

4.5.1 The millimeter/submillimeter-wave spectrometer

The rotational spectrum of cyanoketene has been recorded by means of a millimeter-/submillimeter-wave frequency-modulation spectrometer, described in details elsewhere [225, 226]. Here, only a short summary is provided. A Gunn diode emitting in the W band ($80 - 115$ GHz) was used as primary source of radiation, whose frequency was locked *via* a phase-lock-loop to a radio-frequency local oscillator referenced to a 5 MHz rubidium atomic-clock. Passive multipliers (doublers and triplers) were used in cascade to achieve spectral coverage at higher frequencies. The output radiation was sine-wave modulated at $f = 48$ kHz and fed to the free-space glass absorption cell of the spectrometer, connected to the pyrolysis apparatus at one end and to a pumping system at the other end. Finally, the signal was detected by a liquid-He cooled InSb hot electron Bolometer (QMC Instruments Ltd.) and demodulated by a Lock-in amplifier set at twice the modulation frequency ($2f$), so that the second derivative of the actual spectrum was displayed. In this work, the uncertainty associated to our measurements ranges from 15 to 40 kHz depending on the line-width and the signal to noise ratio of the spectral line.

4.5.2 Production of cyanoketene

As pointed out in previous papers [227, 228], substituted ketenes can be formed via Flash Vacuum Pyrolysis (FVP) of different precursors, namely Meldrum's acid derivatives, isoxazolone compounds, or acetic acid derivatives. In the present work, cyanoketene was produced by the pyrolysis of gaseous methyl cyanoacetate (Sigma

Aldrich, 99% purity) in the same apparatus previously employed for the study of other unstable molecules [229, 230, 231, 232]. The best yield of cyanoketene was attained by flowing the precursor's vapors through a quartz tube heated at 1430 K by a tubular furnace. The pyrolysis products were continuously injected into the cell and subsequently pumped out from it, where the pressure was maintained at about 10 Pa.
No unexpected or unusually high safety hazards were encountered.

4.5.3 Spectrum analysis and results

Cyanoketene is a near-prolate asymmetric rotor ($\kappa = -0.98$) belonging to the C_s symmetry point group. All atoms lie in a plane defined by the two principal inertial axes a and b and only two components, μ_a and μ_b, contribute to the total dipole moment $\mu = 3.542(15)$ D, with values of 2.844(12) D and 2.112(9) D, respectively [233]. The rotational energies of cyanoketene can be derived using the standard semi-rigid Hamiltonian for an asymmetric rotor:

$$\mathscr{H} = \mathscr{H}_{rot} + \sum_n \mathscr{H}_{cd}^{(n^{th})} \tag{4.1}$$

The rigid rotor part $\mathscr{H}_{rot}$ contains the angular momentum operator $\hat{J}^2$ and its components:

$$\begin{aligned} \mathscr{H}_{rot} = & \tfrac{1}{2}(B+C)\,\hat{J}^2 + \left[A - \tfrac{1}{2}(B+C)\right]\hat{J}_z^2 \\ & + \tfrac{1}{2}(B-C)\left(\hat{J}_x^2 - \hat{J}_y^2\right), \end{aligned} \tag{4.2}$$

where A, B, and C are the rotational constants and are related to the moments of inertia about the pertinent axes. The centrifugal distortion effects are recovered by adding several $\mathscr{H}_{cd}^{(n^{th})}$ terms, up to the required power n. Here, the terms with $n = 4$ and 6 are expressed using the Watson-type S-reduced Hamiltonian in terms of the quartic (D and d) and sextic (H and h) centrifugal distortion constants:

$$\begin{aligned} \mathscr{H}_{cd}^{S} = & -D_J(\hat{J}^2)^2 - D_{JK}\hat{J}^2\hat{J}_z^2 - D_K\hat{J}_z^4 \\ & + d_1\hat{J}^2\left(\hat{J}_+^2 + \hat{J}_-^2\right) + d_2\left(\hat{J}_+^4 + \hat{J}_-^4\right) \\ & + H_J(\hat{J}^2)^3 + H_{JK}(\hat{J}^2)^2\hat{J}_z^2 \\ & + H_{KJ}\hat{J}^2\hat{J}_z^4 + H_K\hat{J}_z^6 + h_1(\hat{J}^2)^2\left(\hat{J}_+^2 + \hat{J}_-^2\right) \\ & + h_2\hat{J}^2\left(\hat{J}_+^4 + \hat{J}_-^4\right) + h_3\left(\hat{J}_+^6 + \hat{J}_-^6\right), \end{aligned} \tag{4.3}$$

Higher order distortion terms have the general form[234]:

$$\mathscr{H}_{cd}^{(n^{th})} = \sum_{i=0}^{n/2} X_i (\hat{J}^2)^{(n/2-i)} \hat{J}_z^{2i} + \sum_{i=1}^{n/2} x_i (\hat{J}^2)^{(n/2-i)} \left(\hat{J}_+^{2i} + \hat{J}_-^{2i} \right) \tag{4.4}$$

This work started when the spectroscopic parameters of NCCHCO were available only from Hanh et al.[233], who investigated the microwave spectrum of cyanoketene below 40 GHz. Their set of constants were used to obtain an initial guess of the rotational spectrum above 80 GHz. By employing the spectrometer described in Section 4.5.1, a systematic search of the rotational transitions of cyanoketene was performed in selected frequency ranges between 80 and 530 GHz. A total number of 525 transitions (353 a-type and 172 b-type) has been recorded and analyzed, together with those observed by Hanhn et al.[233], in a weighted least-squares procedure as implemented in the SPFIT/SPCAT suite of program [235].

After the completion of this analysis, however, we became aware of the work published by Margulés et al.[183]. Their study focused on the spectral region below 330 GHz and reported an extended analysis of several hundreds of a-type transitions, while the investigation of the b-type spectrum was more limited than in our work. Therefore, because of the different information brought by different types of transitions, we decided to perform a global fit of all the available rotational transitions of cyanoketene, in order to further improve the accuracy of its spectroscopic parameters.

The determination of the complete set of octic centrifugal distortion constants is the major improvement achieved in our global fit. In particular, the determination of the L_K constant – together with the accurate values obtained for several purely K_a dependent centrifugal distortion parameters, such as D_K and H_K – is of great importance for predicting b-type ^rR transitions, whose intensity is the highest at any temperature up to 300 K.

The root-mean-square (RMS) error of the residuals of our analysis is 0.027 MHz, which is comparable to the accuracy of the experimental measurements, the fit standard deviation (σ) being 0.90. A comparison of the final set of our spectroscopic parameters with those determined by Margulés et al.[183] is shown in Table 4.2.

A re-formatted version of the FIT output file is provided as SI. The new set of spectroscopic parameters allows to reproduce and predict the rotational spectrum of cyanoketene in a wide frequency range, up to the ALMA Band 9. The newly predicted frequencies can assist future astronomical search for cyanoketene in a huge frequency range, since the uncertainty in the line positions is generally lower than the typical spectral resolution of radio-telescopes working in the millimeter/submillimeter domain.

Parameter	Present work	[183]
A	29601.18220(77)[a]	29601.17783(98)
B	2812.149125(48)	2812.14944(11)
C	2563.721998(43)	2563.72222(11)
$D_J \times 10^3$	1.538791(19)	1.539026(76)
$D_{JK} \times 10^3$	-115.00852(48)	-115.00801(47)
$D_K \times 10^3$	2814.456(35)	2813.778(55)
$d_1 \times 10^6$	-368.8083(61)	-368.8395(72)
$d_2 \times 10^6$	-9.1506(18)	-9.1383(12)
$H_J \times 10^6$	0.0061426(35)	0.006213(22)
$H_{JK} \times 10^6$	-0.21744(15)	-0.21768(16)
$H_{KJ} \times 10^6$	-24.0662(27)	-24.0191(27)
$H_K \times 10^6$	834.52(61)	807.50(86)
$h_1 \times 10^9$	2.3411(16)	2.3535(20)
$h_2 \times 10^9$	0.13843(73)	0.13074(31)
$h_3 \times 10^9$	0.04192(15)	0.04377(17)
$L_J \times 10^{12}$	-0.03119(23)	-0.0382(22)
$L_{JJK} \times 10^{12}$	1.431(15)	1.555(17)
$L_{JK} \times 10^9$	-0.03184(25)	-0.05033(14)
$L_{KKJ} \times 10^9$	10.2005(95)	10.0790(97)
$L_K \times 10^9$	-315.6(32)	
$l_1 \times 10^{15}$	-14.37(14)	-15.85(18)
$l_2 \times 10^{15}$	-1.178(71)	
$l_3 \times 10^{15}$	-0.704(28)	-1.17(38)
$l_4 \times 10^{15}$	-0.0988(63)	-0.0579(7)
$P_{KKJ} \times 10^{12}$	-3.353(10)	-3.206(10)
No. of distinct lines	2050	
RMS / kHz	27.0	
σ	0.90	

[a] Values in parentheses are standard errors in units of the last quoted digits.

Table 4.2: Spectroscopic parameters[a] of cyanoketene.

4.6 Discussion and conclusions

In this work, we have proposed a new formation route for cyanoketene involving two species already detected in the interstellar medium, namely the formyl and cyanocarbene radicals. The doublet potential energy surface starting from those reactants has been examined by an accurate yet feasible computational approach combining last generation density functionals and composite wave-function methods. In order to help the astronomical search of this molecule, we carried out also laboratory measurements of its rotational spectrum up to 530 GHz.

Since the results of our theoretical kinetic analysis support the conclusion that cyanoketene can be formed from HCO and HCCN by means of a hydrogen eliminitation reaction, we suggest to search for cyanoketene in the ISM regions where HCO and HCCN have been already detected. Unfortunately, to the best of our knowledge, those two radicals have been never detected in the same interstellar region. Anyway, the regions where

at least one of those molecules has been detected are: W3, NGC2024, W51, K3-50, IRC+2016 and TMC-1. Among them, only TMC-1 has been investigated by Margulés et al.[183] so we suggest to search for this molecule in the other aforementioned regions. The second major outcome of this work is an improved set of spectroscopic constants, which can be used to refine the spectral predictions of cyanoketene from the microwave to the terahertz region. In particular, *b*-type transitions (which are expected to be bright across the whole spectrum) can be targeted with high precision and can unequivocally proof the presence of cyanoketene in spectral line surveys. High-mass star forming regions represent the most suitable sources [236, 237] for performing future astronomical searches.

Chapter 5

Competition between abstraction and addition channels for the reaction between the OH radical and vinyl alcohol in the interstellar medium

In this Chapter is proposed a detailed quantum chemical study of possible reaction channels starting from the interaction between the OH radical and both conformers of Vy (*syn* and *anti*) in order to understand if it is a possible path for the formation of (Z)1,2-ethenediol (Et), a molecule recently identified in the ISM. Et, the enolic form of glycolaldehyde, is considered a key precursor for the formation of sugars in both interstellar and prebiotic chemistry. The formation of a pre-reactive complex always represents the first step of the reaction, which can then proceed through the attack to the double bond (leading in turn to the formation of different dissociation products), or through hydrogen abstraction, which eventually produces a radical species and water. Then, a master equation approach based on ab-initio transition state theory has been employed to calculate the reaction rate constants of different products for temperatures up to 500 K. Comparison of the kinetic results for the different reaction channels shows that hydrogen abstraction is strongly favoured for both Vy conformers and leads to the formation of water and CH_2CHO radical. As a matter of fact, formation of Et is strongly disfavoured under the harsh conditions of the ISM by both kinetic and thermodynamic points of view because of the high activation energy and strong endothermicity of the corresponding reaction path. This Chapter is based on a manuscript submitted to the *ACS Earth and Space Chemistry* by Ballotta et al.

5.1 Introduction

A large number of studies have shown that vinyl alcohol (Vy) and hydroxyl radical OH) are involved in various types of gas-phase processes like, for instance, the oxidation and combustion of hydrocarbons [238], the formation of organic acids in the atmosphere and troposphere[239], or the formation of complex organic molecules (COM) in the interstellar medium (ISM)[240]. While these molecules have been identified in environments characterized by different physical-chemical conditions, the experimental procedures required for their synthesis and isolation are so challenging that a precise characterization of the chemistry of these compounds is very involved and, sometimes, even impossible. Vy is the simplest enol and belongs to the family of C_2H_4O species, which includes also acetaldehyde and oxirane. The synthesis of Vy can be performed by a pyrolytic elimination reaction of water starting from ethylene glycol at low pressure and at a temperature of 900 K[241]. The conversion of Vy into the more stable acetaldehyde isomer is governed by a high energy barrier, but the reaction is very fast at room temperature and pressure in the presence of acid or basic catalysts. The tautomerization can also take place through a photochemical process at the low pressures and temperatures characterizing Earth atmosphere and stratosphere [242, 243]. However, under these conditions, the Vy lifetime is strongly enhanced by the synergistic effect of its intrinsic kinetic stability and the absence of chemical agents able to catalyze conversion into acetaldehyde. This situation increases, in turn, the probability of Vy reactions with other chemical species and, indeed, the involvement of Vy in the production of organic acids in the atmosphere has been demonstrated unambiguously[244, 245]. These findings led da Silva et al.[246] to compute accurately the thermodynamic properties of Vy in order to characterize its reactivity in the atmosphere with OH and molecular oxygen (O_2). In even more extreme environments, such as those characteristic of the ISM, the kinetic stability and lifetime of thermodynamically unstable species increase considerably. In fact, both conformers of Vy (*syn* and *anti*) were identified in the molecular cloud of Sagittarius B2 thanks to accurate infrared and rotational spectroscopic investigations [247]. Both conformers were recently detected also in the giant molecular cloud G+ 0.693-0.027 by Jiménez-Serra et al.[248], who were able to derive the relative abundances and the column densities of all the members of the family of C_2H_4O compounds. Careful analysis of the spectroscopic data showed that the most stable *syn* conformer of Vy is also the most abundant one. Several reaction mechanisms involving reactions on cosmic dust, interaction with galactic cosmic rays, or the gas-phase keto-enol tautomerization of acetaldehyde have been proposed as possible formation routes of Vy[249, 250]. However neither theoretical nor experimental conclusive proofs of the viability of specific reaction mechanisms have been provided so far. The other molecular hero of the present work is the OH radical, whose central role in combustion processes, in the chemistry of the atmosphere, and in the ISM has been confirmed by several studies. Indeed OH, which has been identified in the ISM already in 1963 toward Cas A [251, 252], is considered a key radical in the interstellar chemistry of oxygen, because of its ability to react with several other molecules under the harsh conditions of the ISM[253, 254]. OH radical formation routes include dissociative recombinations of electrons and molecular cations formed by ion-neutral

reactions (e.g., in cold interstellar clouds), photodesorption from the surface of icy grains and, at much higher temperatures, gas-phase atom-molecule collisions like, e.g., O + H_2 and H + H_2O [255]. Photodissociation of H_2O, in the gas phase or in the mantle of icy grains, is another potential OH source[256]. Recently, gas-phase reaction mechanisms involving Vy and the OH radical have been proposed as possible formation routes of (Z) 1,2-ethenediol (Et), a molecule recently detected in the ISM [257]. Et is the enolic form of glycolaldehyde and is considered a key precursor in the formation of sugars in both interstellar and prebiotic chemistry, possibly through the so-called formose reaction. Rivilla et al.[257] proposed another formation path for this molecule in the gas phase, namely the reaction between formaldehyde and hydroxyl methyl radical (CH_2OH), a species not yet identified in the ISM. Based on these premises, we decided to perform a comprehensive study of the reaction between Vy and OH by means of a computational protocol[182] based on the generation of plausible reaction mechanisms with the help of unsupervised explorations of reactive potential energy surfaces (PES), the refinement of structural and energetic parameters by a composite quantum chemical method, and the computation of kinetic parameters (reaction rate constants and branching ratios) by the master equation (ME) approach based on ab-initio transition state theory (TST). The article is organized as follows. In Section 2, the computational methods are described. In Section 3, the computed reaction mechanisms are discussed with reference to the stationary points of the pertinent reactive PESs. In Section 4, the kinetics of all the reactions is addressed. In Section 5, the main conclusion and perspectives are summarized.

5.2 Computational Details

5.2.1 Reaction mechanism discovery

The AutoMeKin (AMK) program [49, 50, 2] was used for the unsupervised generation of plausible reaction mechanisms. Unlike other programs that require the initial optimization of the energy minima characterizing the mechanism and then the calculation of the transition states (TSs), the methodology on which AMK is built relies on the initial optimization of TS structures. Then, the connected minima are obtained from each TS by computing intrinsic reaction coordinates (IRC) [161]. In this way, plausible reaction mechanisms can be generated by connecting all energy minima through the initially calculated TSs. In this framework, a very effective workflow is obtained in AMK by combining molecular dynamics (MD) simulations, post-processing, and careful selection of the TS molecular structures obtained with MD. MD simulations have been performed using the semi-empirical PM7 method [55] implemented in the MOPAC software [51]. 100 trajectories per iteration were set through the keyword *ntraj* for a total of 10 iterations. The following values were set for the parameters employed by AMK to minimize the redundancy of the guess TS structures: 100 cm^{-1} for the lowest imaginary frequency (*imagmin* keyword); 0.1 for the lowest eigenvalue of the Laplacian (*eigLmax* keyword) in order to differentiate the structures resulting from the fragmentation of an intermediate; 0.002 and 1.5 (*mapemax* and *bapemax* keywords, respectively) for the descriptors employed in the screening of the structures obtained from the MD simula-

tions. Optimized geometries and zero-point corrected electronic energies of reactants, TSs, intermediates, and products along the different reaction pathways were obtained using the rev-DSD-PBEP86[162]-GD3BJ[69] double-hybrid functional in conjunction with the jun-cc-pVTZ basis set[160]. This combination of functional and basis set will be referred to in the following simply as rDSD. All the critical points belonging to the reaction pathways were characterized as minima (reactants, intermediates, and products) and saddle points (TSs) based on the diagonalization of analytical rDSD Hessians[158]. The nature of the minima connected by the TSs obtained in this way was determined by following intrinsic reaction coordinates (IRCs) at the same level of theory. Several studies have shown that this combination of functional and basis set provides accurate geometrical structures [258, 259] and vibrational frequencies [260]. The results of the simulations were analyzed using amk_tools [57], a graphic visualizer that allows for the examination of the extremely complex reaction networks generated by AMK. A typical reaction network drawn by amk_tools is shown in Figure 5.1. The same software was used to visualize molecular structures with their vibrational normal modes and to check the potential energy profiles of the different reaction mechanisms. In this way it was possible to find the reaction pathways leading to the formation of all the dissociation products and to select all the structures of the critical points involved in each reaction path. For such structures, electronic energies were refined by exploiting the junChS-F12 composite scheme[168] described in more detail in the next subsection.

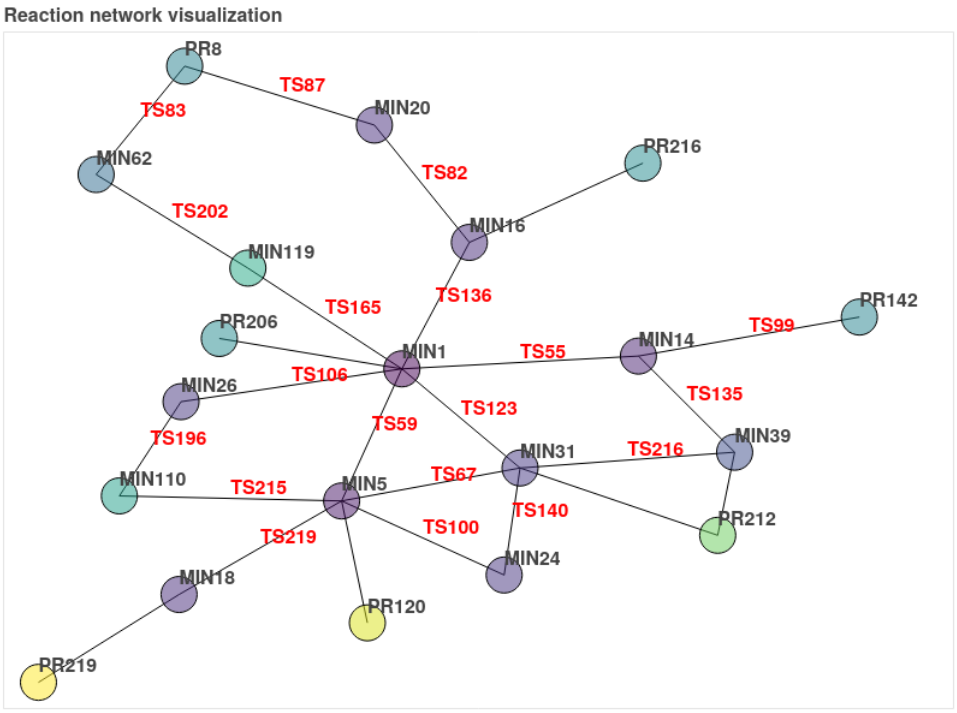

Figure 5.1: An example of reaction network generated by amk_tools. The circles are the energy minima of the reaction network, while the connecting lines are the TSs.

5.2.2 junChS-F12 composite scheme

It is widely acknowledged that the coupled-cluster (CC) model including single, double, and perturbative estimate of triple excitations (CCSD(T))[209] delivers highly accurate electronic energies for systems that do not exhibit strong multi-reference character, provided that complete basis set (CBS) extrapolation and core valence (CV) correlation are taken into account. The reduced cost Cheap Scheme (ChS)[210, 165, 168, 36] is based on the idea that accurate CBS and CV terms can be obtained at negligible additional cost by utilizing second-order Møller-Plesset perturbation theory (MP2)[163] on top of frozen core (fc) CCSD(T) computations with (partially augmented) triple-zeta basis sets[170, 171, 160, 212]. The junChS-F12 variant, in which conventional MP2 and CCSD(T) methods are replaced by their explicitly correlated (F12) counterparts[58, 60], is currently the most accurate version of the approach [1, 216, 217]. In details:

$$E_{\text{jChS-F12}} = E^{\text{CCSD(T)-F12/3Z}} + \Delta E^{\text{MP2-F12/CBS}} + \Delta E^{\text{MP2-F12/CV}} \tag{5.1}$$

where

$$\Delta E^{\text{MP2-F12/CBS}} = \frac{4^3 E^{\text{MP2-F12/4Z}} - 3^3 E^{\text{MP2-F12/3Z}}}{4^3 - 3^3} - E^{\text{MP2-F12/3Z}} \tag{5.2}$$

and

$$\Delta E^{\text{MP2-F12/CV}} = E^{\text{MP2-F12/3CZ, a.e.}} - E^{\text{MP2-F12/3CZ, f.c.}} \tag{5.3}$$

In Eq. 5.2, $\Delta E^{\text{MP2-F12/CBS}}$ is the MP2-F12 correlation energy extrapolated to the CBS limit by using the n^{-3} formula [261] applied to jun-cc-pVTZ (3Z) and jun-cc-pVQZ (4Z) basis sets [170, 171]. Instead, the CV contribution ($\Delta E^{\text{MP2-F12/CV}}$) is incorporated as the difference between all-electron (ae) and fc MP2/F12 calculations, both with the cc-pCVTZ (3CZ) basis set [212]. The junChS-F12 energy evaluations at rDSD optimized geometries provide average absolute errors well within the so called chemical accuracy (about 4 kJ mol^{-1}), as shown by comparison with the most accurate results available for reaction energies and activation barriers[168, 1, 217]. Therefore, this approach was utilized for all stationary points, together with anharmonic zero-point energy (ZPE) contributions computed in the framework of second-order vibrational perturbation theory[218] employing rDSD anharmonic force fields.
All DFT calculations were carried out using the Gaussian16 code[52], while junChS-F12 calculations were performed using the MOLPRO program[63, 62, 61].

5.2.3 Kinetics

Global and channel-specific rate constants were computed in the framework of the Ab Initio Transition State Theory based Master Equation approach (AITSTME), as implemented in the MESS software [85]. MESS solves the multiwell one-dimensional master equation using the chemically significant eigenvalue (CSE) method, treating bimolecular products and reactants as sources and sinks. Collisional energy relaxation was described using the exponential down model[219] with a temperature-dependent $< \Delta E_{down} >$ of $260 \times (\text{T}/298)^{0.875}$ cm^{-1} in an argon bath. Barrierless reaction rate constants were calculated through phase space theory (PST)[44, 45], approximating the long-range interaction between incoming reactants with an isotropic attractive

potential $V(R) = -C_6/R^6$[75]. The C_6 parameters were obtained by a least-square fit of rDSD electronic energies computed at different values of intermolecular distances. In Table 5.1 are reported the values of the C_6 parameters for all the pre-reactive complexes involved in the reaction mechanisms.

	PrC1	**PrC2**	**PrC4**
syn	292.05	181.96	966.24
anti	30.62	123.75	29.78

Table 5.1: C_6 parameters in $a_0^6 E_\mathrm{h}$ for all the pre-reactive complexes.

Rate constants of elementary steps involving distinct transition states were computed using the conventional transition-state theory. Calculations were carried out in the framework of the rigid-rotor harmonic-oscillator (RRHO) approximation and included tunneling as well as non-classical reflection effects using the Eckart model[84]. Kinetic simulations were performed for the conditions typical of different regions of the ISM, namely a pressure of 1×10^{-8} bar and temperatures in the range 20–500 K. The temperature dependence of the rate constants was fitted by the three-parameter Arrhenius–Kooij equation, [221, 222]:

$$k(T) = A(\frac{T}{300})^n e^{-\frac{E}{RT}}$$

where A, n, and E are the fitting parameters and R is the universal gas constant. The results of the kinetic analysis were further verified by calculations performed with the StarRate program, specifically designed for reactions of astrochemical interest.[100, 153].

5.3 Results

All the reaction profiles analyzed in the following subsections start with the stabilization of the reactants through non-covalent intermolecular interactions, which lead to the formation of several pre-reactive complexes[262]. Detailed tables in the SI report the electronic energies calculated at the junChS-F12 and rDSD levels corrected for anharmonic ZPEs calculated at the rDSD level for all the stationary points located in the different reaction paths. Although rDSD energies are not employed in the computation of thermodynamic and kinetic parameters, the fair agreement with junChS-F12 results gives further support to the use of rDSD optimized geometries and vibrational frequencies.

5.3.1 Mechanism of abstraction reactions

Hydrogen abstraction reactions from *syn*-Vy can lead to the formation of water together with four different radical species, **P1**, **P2**, **P3**, and **P4**.
Inspection of the reaction profile in Figure 5.2 shows that the initial reaction step is the formation of pre-reactive complexes (**PrC1**, **PrC2**, or **PrC4**, lying 13.9, 14.4,

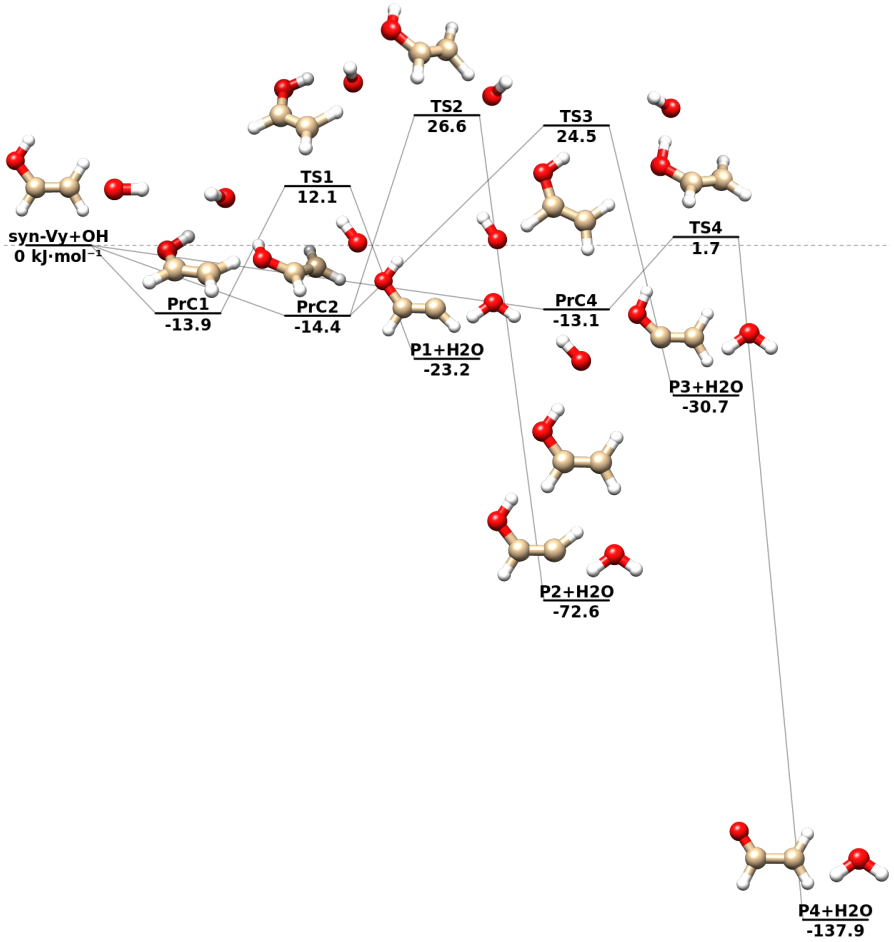

Figure 5.2: Energetics of the abstraction reactions between *syn*-Vy and OH: junChS-F12 energies augmented by rDSD anharmonic ZPEs. Energies in kJ mol^{-1} relative to the reactants limit.

and 13.1 kJ mol^{-1}, respectively below the reactants). Starting from these pre-reactive complexes the reaction can further proceed through 4 different transition states, **TS1**, **TS2**, **TS3** and **TS4**, corresponding to the attack of the **OH** radical to the four non-equivalent hydrogen atoms of *syn*-Vy. Noted is that either **TS2** or **TS3** can be reached from **PrC2** in which the OH radical forms a bifurcated hydrogen bond involving both the hydrogen atoms of the Vy CH_2 moiety. The lowest energy barrier (**TS4**) lies 14.8 kJ mol^{-1} above the corresponding pre-reactive complex **PrC4** (1.7 kJ mol^{-1} above the reactants) and governs the abstraction of the hydroxyl hydrogen. The transition states ruling the other hydrogen abstractions are **TS1**, **TS2**, and **TS3**, which lie 26.0, 41.0, and 38.9 kJ mol^{-1} above the corresponding pre-reactive complexes (**PrC1** and **PrC2**). The high energy barriers governing these three processes indicate that formation of **P4** is kinetically favoured. Noted is that the same trend would be obtained in terms of thermodynamic control since **P4** lies -137.9 kJ mol^{-1} below the reactants, whereas the exothermicity of the reactions leading to **P1**, **P2** and **P3** are 23.2, 72.6, and 30.7 kJ mol^{-1}, respectively. The preference for the route leading to **P4** can be traced back

to the lower strength of the OH bond with respect to its CH counterparts and to the stabilization of the CH_2CHO radical by π-electron delocalization in the C-C-O moiety. In analogy with the case of *syn*-Vy, also the abstraction reactions involving the *anti* conformer start with the stabilization of the initial reagents through the formation of a pre-reactive complexes (**PrC1**, **PrC2**, or **PrC4**).

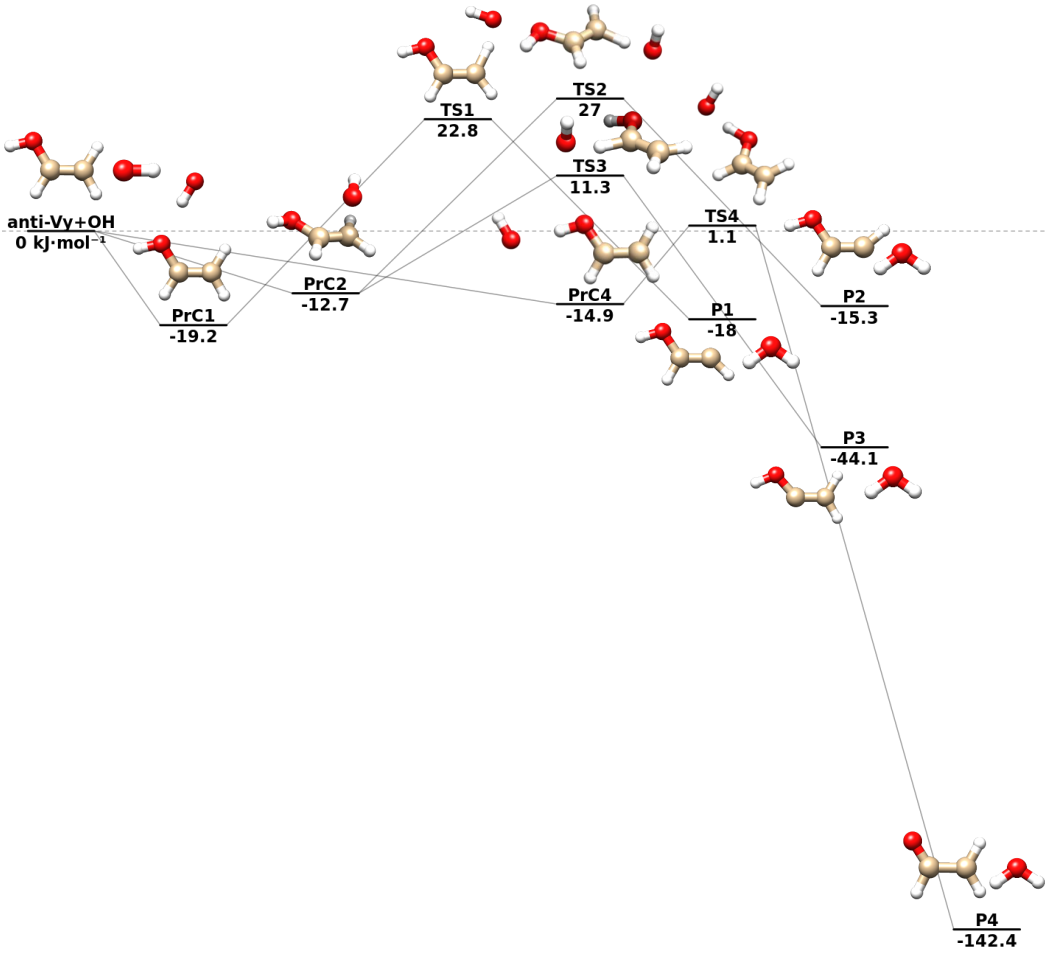

Figure 5.3: Energetics of the abstraction reaction between *anti*-Vy and OH: junChS-F12 energies augmented by rDSD anharmonic ZPEs. Energies in kJ mol^{-1} relative to the reactants limit.

The most stable complex is **PrC1** which lies 19.2 kJ mol^{-1} below the reactants, whereas **PrC2** and **PrC4** lie 12.7 and 14.9 kJ mol^{-1}, respectively below the reactants. The reaction then proceeds through the attack of OH to one of the hydrogen atoms of *anti*-Vy overcoming the corresponding transition state (**TS1**, **TS2**, **TS3**, or **TS4**). Inspection of the energy barriers collected in Figure 5.3 shows that the favored abstraction process leads to the formation of **P4** following the **PrC4** $\longrightarrow$ **TS4** $\longrightarrow$ **P4** path. In fact **TS4** is found 1.1 kJ mol^{-1} above the reactants, whereas **TS1**, **TS2** and **TS3** lie 22.8, 27.0, and 11.3 kJ mol^{-1} above the reactants. All the reactions are exothermic, but all the paths except that leading to **P4** are governed by energy barriers higher than 10 kJ

mol^{-1}. As a consequence, the reactants would have to acquire from the surrounding environment a significant energy, with this being a highly unlikely process under the harsh conditions of the ISM.

5.3.2 Mechanism of addition reactions

The initial step of all the addition reactions of OH to *syn*-Vy is the formation of the same pre-reactive complex (**PrC1**) already discussed for the corresponding abstraction reactions, which lies 13.9 kJ mol^{-1} below the reactants.

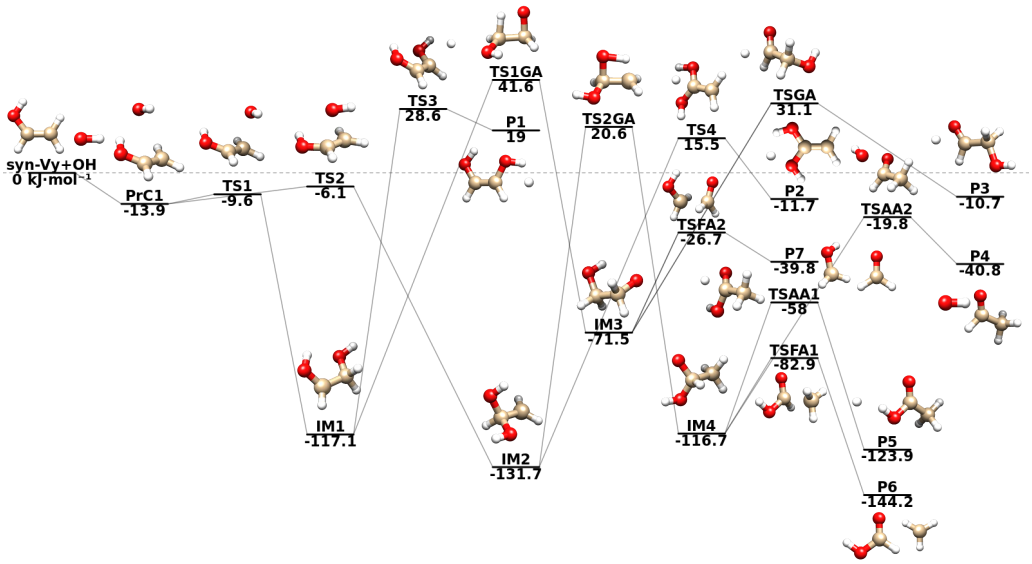

Figure 5.4: Energetics of the addition reactions between *syn*-Vy and OH: junChS-F12 energies augmented by rDSD anharmonic ZPEs. Energies in kJ mol^{-1} relative to the reactants limit.

Next, the OH radical can attack one of the two ends of the double bond overcoming either the **TS1** or **TS2** transition state, which lie 9.6 and 6.1 kJ mol^{-1}, respectively below the reactants. Then, the reaction intermediate **IM1** or **IM2** can be formed by strongly exothermic processes (117.1 or 131.7 kJ mol^{-1} respectively below the reactants). Several reactive pathways start from these two intermediates, corresponding to isomerization and dissociation reactions leading to the formation of molecules not yet detected in the ISM, but also to already identified species. In details, the reaction can proceed through the isomerization reaction by transposition of hydrogen from **IM1** to **IM3** or from **IM2** to **IM4**, with **IM3** (71.5 kJ mol^{-1} below the reactants) and **IM4** (116.8 kJ mol^{-1} below the reactants) being less stable than the other two intermediates. These processes are governed by the two transition states **TS1GA** and **TS2GA**, which lie 41.6 and 20.6 kJ mol^{-1}, respectively above the reactants. Two other reactive pathways can be followed starting from **IM1** and **IM2**, namely the dissociation reactions which lead to the formation of the 1,2 (**P1**) and 1,1 (**P2**) isomers of ethenediol shown in Figure 5.4, overcoming the corresponding transition states **TS3**

and **TS4** which lie 28.6 and 15.5 kJ mol^{-1}, respectively above the reactants. However, formation of **P1** in the ISM is unlikely in view of the non negligible endothermicity (19.0 kJ mol^{-1}) of the reaction. On the other hand, **P2** lies below the asymptotic limit of the reactants by about 11.7 kJ mol^{-1}. Then, dissociation of **IM3** and **IM4** can lead to hydroxymethyl radical and formaldehyde (**P7**), formic acid and methyl radical (**P6**), acetic acid and atomic hydrogen (**P5**), acetaldehyde and hydroxyl radical (**P4**), or glycolaldehyde and atomic hydrogen (**P3**). While all these processes are exothermic, the high energy of the corresponding transition states (**TS1GA**, **TS2GA**, **TSGA**) indicate that these reaction channels are closed in the typical ISM conditions. The first step of all addition reactions involving the *anti*-Vy conformer is the formation of the same pre-reactive complex (**PrC2**) already discussed for the corresponding abstraction reactions and lying 12.7 kJ mol^{-1} below the reactants.

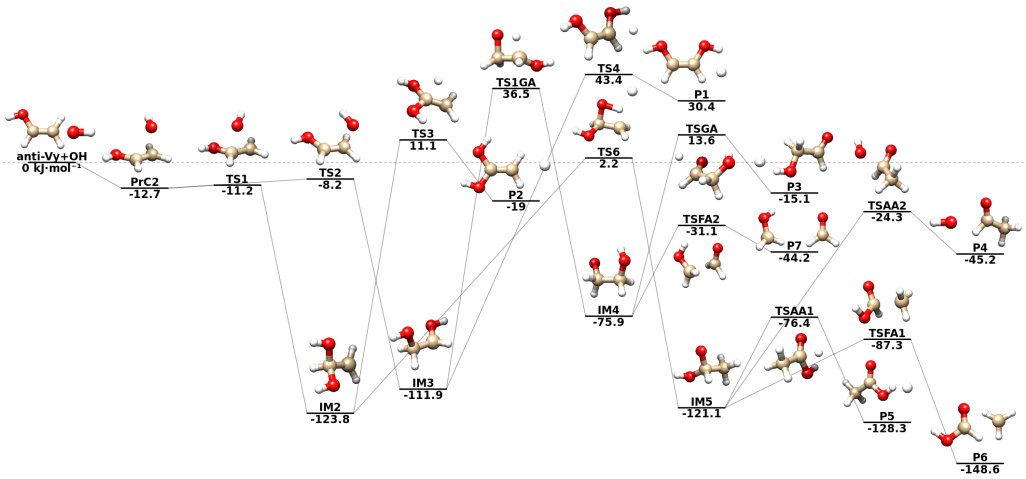

Figure 5.5: Energetics of the addition reactions between *anti*-Vy and OH: junChS-F12 energies augmented by rDSD anharmonic ZPEs. Energies in kJ mol^{-1} relative to the reactants limit.

The reactions then proceed with the attack of the OH radical to the double bond of Vy, which can lead to the formation of two different reaction intermediates, **IM2** or **IM3**, lying 123.8 and 111.9 kJ mol^{-1}, respectively below the reactants. Next, **IM2** can isomerize to **IM5** through **TS6**, and **IM3** can isomerize to **IM4** through **TS1GA**. Inspection of Figure 5.5 shows that the **IM2**$\longrightarrow$**TS6**$\longrightarrow$**IM5** channel is the favored one, since it involves energy barriers significantly lower than those governing the alternative pathway leading to the formation of **P2**. Starting from **IM5**, acetaldehyde (**P4**), acetic acid (**P5**), or formic acid (**P6**) can be produced through the transition states **TSAA2**, **TSAA1** and **TSFA1**, which lye respectively 24.3, 76.4, and 87.3 kJ mol^{-1} below the reactants. Two other dissociation pathways have been identified, which start from the higher energy intermediate **IM4** and lead to the formation of glycolaldehyde (**P3**) through a hydrogen elimination process governed by an energy barrier of 13.6 kJ mol^{-1} above the reactants (**TSGA**), or to the formation of formic acid (**P7**) through **TSFA2**, which lies 31.1 kJ mol^{-1} below the asymtotic limit. Also in this case all the reaction channels shown in Figure 5.5 are unlikely to be open in

the ISM in view of the high energy barriers (well above the asymptotic limit of the reactants) to be overcome.

5.3.3 Rate constants

The rate constants for the abstraction and addition reactions of both Vy conformers are depicted as Arrhenius plots in Figure 5.6, 5.7, 5.8, 5.9 in order to give a better and more comprehensible graphical representation of the kinetic results. In Tables 5.2, 5.3, 5.4, 5.5 are collected the parameters of the corresponding Arrhenius-Kooij fits. Starting from abstraction reactions involving *syn*-Vy, inspection of the results reported in Figure 5.6 and Table 2 shows that the rate constant governing the formation of **P4** (which ranges between 1.40×10^{-12} and 3.70×10^{-11} $cm^3molecule^{-1}s^{-1}$) is higher than the rate constants governing the formation of **P1**, **P2** and **P3** in the whole interval of temperatures (20-500 K). This trend parallels that of the energy barriers involved in the reaction pathways leading to the various products, which are all single-step reactions. In fact, the energy barrier governing the formation of **P4** is 14.8 kJ mol^{-1}, to be compared to values of 26.0, 38.9, and 41.0 kJ mol^{-1} for the channels leading to **P1**, **P3** and **P2**, respectively. In agreement with those barriers, the second most kinetically favoured single-step reaction pathway is **PrC1-TS1-P1**, whose rate constant ranges between 1.40×10^{-14} and 9.63×10^{-13} $cm^3molecule^{-1}s^{-1}$. The rate constant for the reaction channel leading to **P3** ranges between 4.20×10^{-15} and 2.25×10^{-13} $cm^3molecule^{-1}s^{-1}$. Finally, the rate constant governing the formation of **P2** ranges between 3.20×10^{-16} and $1.68\times10^{-14}cm^3molecule^{-1}s^{-1}$.

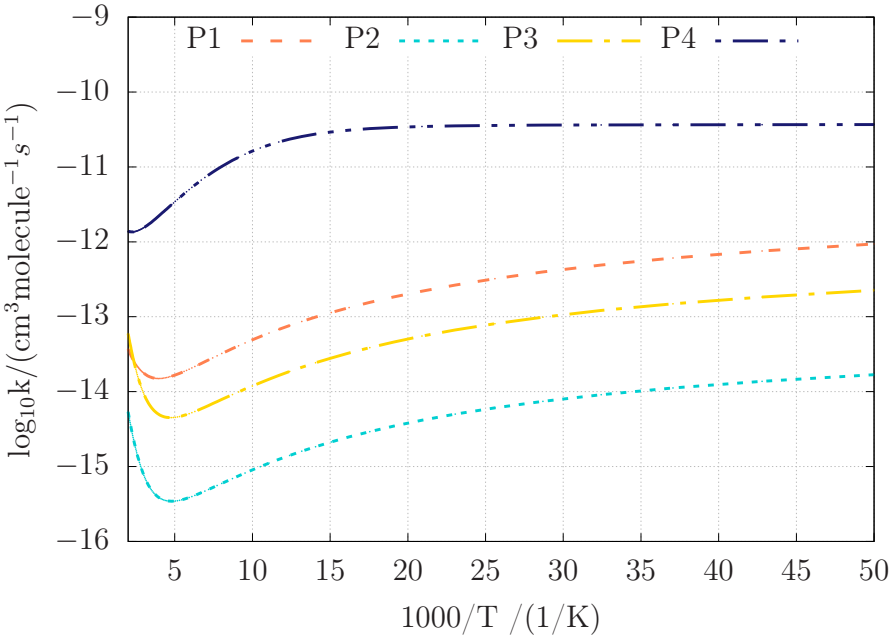

Figure 5.6: Arrhenius plot of the rate constants for the abstraction reactions involving *syn*-Vy and OH leading to **P1**, **P2**, **P3**, **P4**.

	A/cm^{3}molecule^{-1}s^{-1}	n	E/kJmol^{-1}	rms[a]
P1	9.49×10^{-1}	2.66	459.65	1.42×10^{-15}
P2	1.43×10^{10}	3.05	20084.77	4.97×10^{-17}
P3	6.80×10^{9}	3.02	20270.54	1.19×10^{-15}
P4	1.21×10^{-11}	2.19	-1382.16	2.82×10^{-14}

[a] rms stands for root-mean-square deviation of the fit.

Table 5.2: Arrhenius-Kooij Parameters for the abstraction reactions involving *syn*-Vy.

Figure 5.7 and Table 3 show that also for the abstraction reactions involving the *anti* isomer the fastest process leads to the formation of **P4** in the whole interval of temperatures (20-500 K) and its rate constant ranges between 8.8×10^{-13} and 2.50×10^{-11}cm^{3}molecule^{-1}s^{-1}. Once again the trend of rate constants parallels that of energy barriers. Accordingly, the second highest rate constant (ranging between 5.80×10^{-14} and 2.90×10^{-12}cm^{3}molecule^{-1}s^{-1}) governs the formation of **P3**, with the barrier associated to this abstraction process being about 24.0 kJ mol^{-1}. Next, formation of **P1** is governed by an energy barrier of 42.0 kJ mol^{-1} and its rate constant ranges between 1.70×10^{-15} and 8.38×10^{-14}cm^{3}molecule^{-1}s^{-1}. Finally, the slowest process is the formation of **P2**, which is ruled by an energy barrier of 39.7 kJ mol^{-1} and has a rate constant ranging between 1.15×10^{-16} and 4.13×10^{-15} cm^{3}molecule^{-1}s^{-1}. Noted is that the energy barrier governing the formation of **P2** is actually lower than that of **P1**, but the corresponding transition states are reached from two different intermediates (**PrC2** and **PrC1**), so that **TS2** is less stable than **TS1** with respect to the energy of the reactants. At the low-pressures characterizing the ISM, the excess energy of pre-reactive complexes cannot be dissipated by intermolecular interactions with the surrounding gas, so that the correct energy reference is that of reactants. This point is further analyzed in the general discussion section.

	A/cm^{3}molecule^{-1}s^{-1}	n	E/kJmol^{-1}	rms[a]
P1	4.03×10^{8}	3.01	16428.82	9.95×10^{-17}
P2	3.79×10^{11}	3.03	20379.33	9.42×10^{-17}
P3	1.44×10^{-2}	2.94	5147.99	8.46×10^{-16}
P4	2.35×10^{-11}	1.86	-1454.88	3.02×10^{-14}

[a] rms stands for root-mean-square deviation of the fit.

Table 5.3: Arrhenius-Kooij Parameters for the abstraction reactions involving *anti*-Vy.

Coming to addition reactions, the results reported in Figure 5.8 and Table 4 show that in the whole interval of temperatures (20-500 K) the formation of **P6** is governed by the highest rate constant, which ranges between 2.10×10^{-16} and 1.66×10^{-12}cm^{3}molecule^{-1}s^{-1}. All the other products are formed by multi-step reaction pathways governed by rate constants decreasing in the order **P5** > **P2** > **P7** > **P4**. The slowest reaction channel leads to the formation of Et (**P1**), whose rate constant ranges between 1.70×10^{-30} and 1.82×10^{-16}cm^{3}molecule^{-1}s^{-1} in the whole temperature range. This finding is re-

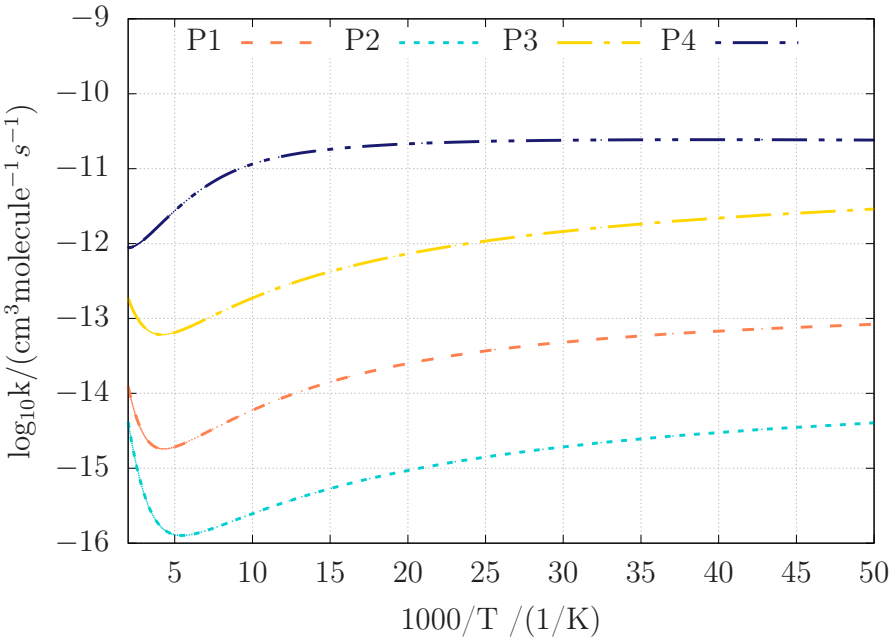

Figure 5.7: Arrhenius plot of the rate constants for the abstraction reactions involving *anti*-Vy and OH leading to **P1**, **P2**, **P3**, **P4**.

lated to both the significant endothermicity of the process (30.4 kJ mol^{-1}) and to the presence of the highest energy barrier (**TS4**, 43.4 kJ mol^{-1}). A small rate constant characterizes also the reaction channel leading to **P3** (between 1.04×10^{-27} and $1.09\times10^{-20}cm^3molecule^{-1}s^{-1}$), which, despite being exothermic (15.1 kJ mol^{-1}), is a multi-step process involving a high energy barrier for the rate determining step (**TS1GA**, 36.5 kJ mol^{-1}).

	A/cm^{3}molecule^{-1}s^{-1}	**n**	**E/kJmol^{-1}**	**rms**[a]
P1	5.42×10^{-10}	3.31	18097.41	7.54×10^{-19}
P2	8.09×10^{-3}	2.54	8222.08	2.83×10^{-18}
P3	1.10×10^{13}	6.94	28929.39	1.99×10^{-23}
P4	1.99	5.06	8305.40	9.42×10^{-22}
P5	2.95×10^{4}	2.64	12223.05	2.54×10^{-20}
P6	3.86×10^{5}	1.20	15365.07	4.29×10^{-19}
P7	1.30×10^{23}	4.52	20867.25	6.13×10^{-20}

[a] rms stands for root-mean-square deviation of the fit.

Table 5.4: Arrhenius-Kooij Parameters for the addition reactions involving *syn*-Vy.

While the general trend of the rate constants governing addition reactions to *anti-Vy* is analogous to that of the *syn* isomer, the reaction pathways discovered by AutoMeKin involve different energy barriers, which lead to non negligible quantitative differences. In any case, the results reported in Figure 5.9 and Table 5 show that in the whole temperature interval the highest rate constant (between 2.00×10^{-13} and

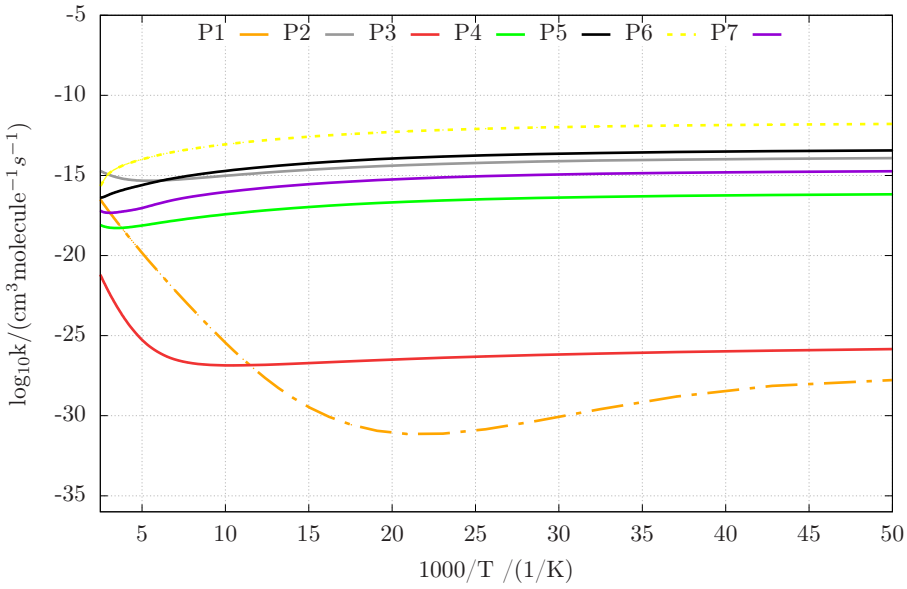

Figure 5.8: Arrhenius plots of the constants for the addition reactions involving *syn*-Vy and OH leading to **P1**, **P2**, **P3**, **P4**, **P5**, **P6**, **P7**.

1.01×10^{-11}cm^{3}molecule^{-1}s^{-1}) governs again the formation of **P6**, while the formation of 1,1- and 1,2-ethenediol isomers (**P1** and **P2**, respectively) is kinetically disadvantaged. In particular, the rate constant for the formation of **P1** ranges between 1.10×10^{-34}cm^{3}molecule^{-1}s^{-1} and 7.40×10^{-18}cm^{3}molecule^{-1}s^{-1}, whereas that of **P2** ranges between 2.9×10^{-15} cm^3 molecule^{-1} s^{-1} and 6.3×10^{-14} cm^3 molecule^{-1} s^{-1}.

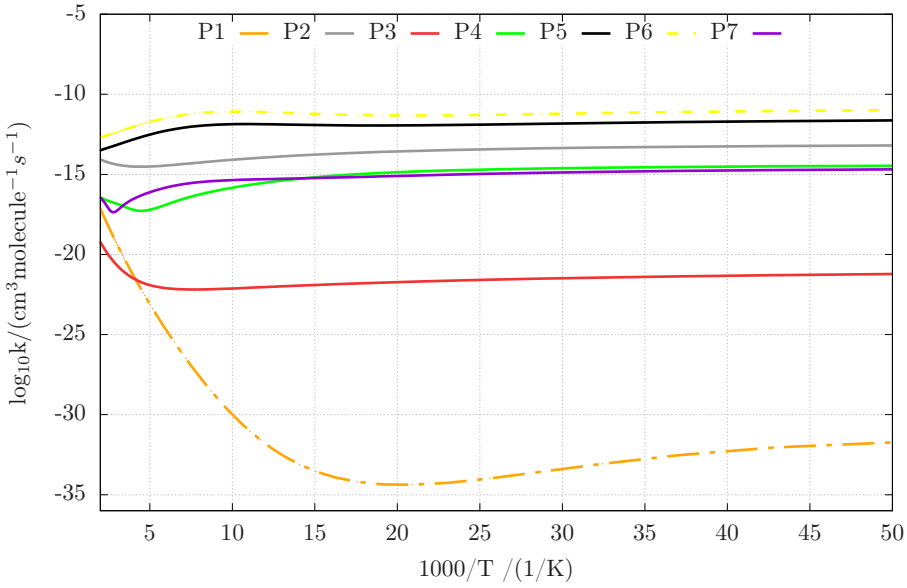

Figure 5.9: Arrhenius plots of the rate constants for the addition reactions involving *anti*-Vy and OH leading to **P1**, **P2**, **P3**, **P4**, **P5**, **P6**, **P7**.

	$A/cm^3molecule^{-1}s^{-1}$	n	$E/kJmol^{-1}$	rms[a]
P1	8.93×10^{-7}	2.61	36638.56	1.84×10^{-20}
P2	9.78×10^{-7}	2.39	3740.35	6.36×10^{-18}
P3	1.00×10^{12}	4.85	25123.29	5.77×10^{-23}
P4	9.78×10^{-14}	5.36	-9872.98	4.11×10^{-20}
P5	$1{,}04\times10^{-13}$	1.51	-3746.10	1.60×10^{-17}
P6	8.89×10^{-13}	0.86	-2477.75	6.02×10^{-17}
P7	7.01×10^{17}	3.03	21657.89	6.94×10^{-20}

[a] rms stands for root-mean-square deviation of the fit.

Table 5.5: Arrhenius-Kooij Parameters for the addition reactions involving *anti*-Vy.

5.4 General discussion and conclusions

Vinylalcohol has two conformers (*syn* and *anti*) with a computed energy difference of 4.7 kJ mol^{-1} and an interconversion barrier lying 18.0 kJ mol^{-1} above the more stable (*syn*) species. Both conformers have been detected in different regions of the ISM and the observed relative populations (8.3/1) [248, 247] agree with their computed counterparts at temperatures close to 60 K. These findings suggest that interconversion between the conformers is unlikely. Furthermore, only one structure exists for CH_2CHO (**P4**), whereas *syn* and *anti* conformers are possible for other intermediates and products. In particular, the *syn* conformer of Et (**P1** in Figure 5.4) is more stable than its *anti* counterpart (**P1** in Figure 5.5) by 16.1 kJ mol^{-1}. The results of the previous sections show unambiguously that hydrogen abstraction reactions are kinetically favored with respect to additions and lead preferentially to the formation of the CH_2CHO radical (**P4**) from both vinyl alcohol conformers. The reaction channels leading to formation of Et (**P1** in Figures 5.4 and 5.5) turn out to be the most kinetically disadvantaged, in agreement with the endothermicity of the corresponding reactions. In analogy with the reaction of OH with saturated alcohols [263, 264], the addition reaction (producing in the present case formic acid and methyl radical, **P6**) becomes competitive with the abstraction reaction at high temperatures. However, this feature is not significant for the ISM regions, which are the reference environments in the present investigation. While some of the reaction channels starting from the *anti* conformer are marginally faster than those starting from the *syn* conformer, this finding has no consequence on the general trends due to the small quantitative difference and the negligible initial population of the *syn* conformer (about 10% at 60 K, as mentioned above).

Since all the reaction paths involve emerged energy barriers, these channels can be open at the low temperatures of the ISM only in the presence of effective tunneling contributions. From the analysis of the tunneling coefficients calculated with the Eckart model for the hydrogen abstraction processes of both *syn* and *anti* conformers shown in Figure 5.10, it is apparent that tunneling plays a dominant role in the range of temperatures characteristic of the ISM (typically between 50 and 200 K), and then decays very rapidly for temperatures higher than about 200 K. Furthermore, the rate

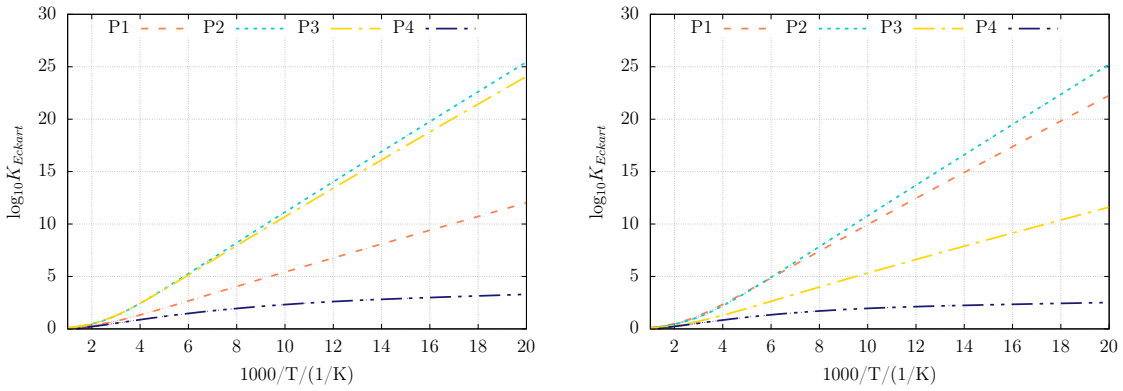

Figure 5.10: Eckart tunneling coefficients as a function of temperature for the abstraction reactions involving the *syn* conformer on the left and the *anti* conformer on the right.

constants governing the formation of all the products have a negative dependence on the temperature in the very low pressure and temperature regime. As already addressed by Guo et al.[263] and Zheng et al.[264], always in the context of hydrogen abstraction reactions, this is due to the lack of collisional stabilization of the pre-reactive complex. Indeed, as shown in Figure 5.11, for sufficiently high pressures the stabilization of the pre-reactive complex is favored, with this allowing deep tunneling starting from its zero point energy and leading, at the same time, to an increase of the rate constant with the temperature. However, in the absence of stabilizing collisions (as is the case for very low pressures) tunneling can take place only at energies above that of the reagents, with this limitation reducing the value of the rate constant with respect to its high-pressure counterpart. Indeed, in such a situation, rate constants approach the value of the capture rate constant for the formation of the pre-reactive complex from the initial reagents. While the treatment of tunneling employed in the present study (zero-curvature model based on an Eckart potential) delivers qualitatively correct results, quantitative computation would require more advanced models [265]. However, these refinements are outside the scope of the present paper, which is mainly devoted to the analysis of possible formation routes of Et at low-pressures and temperatures. In this framework, the predominance of abstraction over addition with the consequent preferential formation of the CH_2CHO radical (**P4**) over Et (**P1**) has been proven beyond any reasonable doubt. Therefore, we suggest to search for this radical species in the ISM regions where Vy and OH have been detected, i.e. Sagittarius B2 and G+0.693-0.027.

Our analysis led to the identification among the possible products of a couple of reactants, formaldehyde and hydroxymethyl radical (**P7**), suggested by Rivilla et al.[257] as possible precursors of Et. However, also the reaction leading from **P7** to **P1** is endothermic (by about 30 kJ mol^{-1}) and, therefore, unlikely to be feasible under the conditions of the ISM. Therefore, the results of our computational study suggest the search of alternative reactions in the gas-phase able to produce Et, or to investigate possible formation routes on grain surfaces. Together with the intrinsic interest of the studied formation routes, the computational strategy proposed in the present study

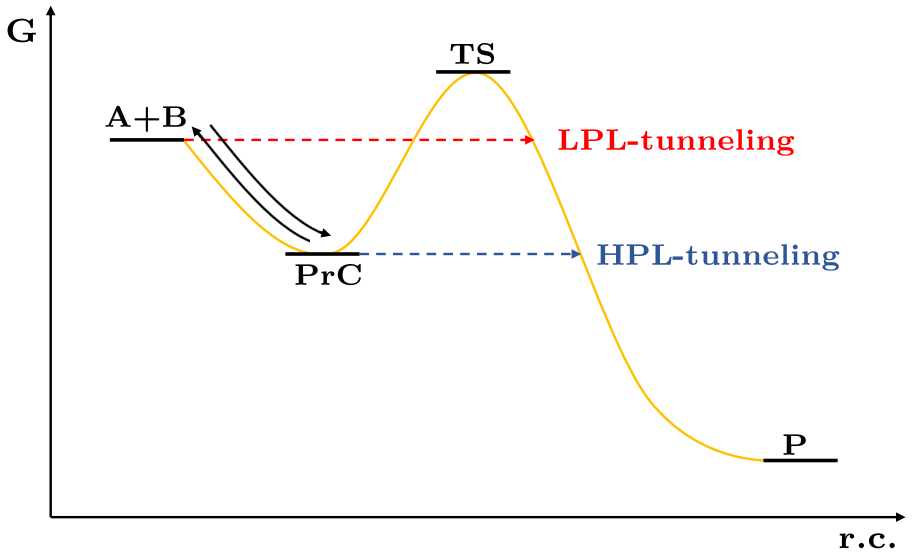

Figure 5.11: Representation of the low-temperature kinetics for high- and low-pressure limits (HPL and LPL, respectively).

paves the way toward systematic investigations of reaction paths for complex organic molecules in the interstellar medium by effective user-friendly tools.

Chapter 6

Computational kinetic investigation of the reaction between vinyl alcohol and CN radical in the interstellar medium

In this Chapter the same methodology applied in Chapter 4 and 5 has been employed to study the reaction between Vinyl alcohol (VyA) conformers and radical CN, two relatively abundant molecules identified in the ISM. Our results indicate that VyA's conformers feature a similar reactivity with CN for both addition and abstraction reactions. For both conformers, the barrierless association reaction to the double bond shows a strong exothermicity which leads to the formation of an intermediate more than -220.0 kJ mol^{-1} below the reactant asymptote. After that, the reaction can evolve towards the formation of several products through isomerization, dissociation and hydrogen elimination steps. The kinetics of abstraction and addition reactions have been investigated with the help of the MESS program taking into the proper account internal rotations for the various TSs involved int the reaction mechanisms. Rate constants computed for temperature up to 600 K show that the most kinetically favoured product of these reactions is cyanoacetaldehyde, a prebiotic molecule not yet detected in the ISM.

6.1 Introduction

In the last decades, thanks to ever more precise detection systems, such as radio telescopes and satellites, more than 200 molecules have been detected in the ISM [266]. Among these, a class of molecules called interstellar Complex Organic Molecules (iCOMs) has attracted much attention, because they are supposed to be the chemical precursors of the more complex building blocks of life, such as amino acids or nucleobases [267, 5]. Given the predominance of gaseous matter in the ISM (about 99% while the remaining 1% is composed of grains) it is hypothesized that the gaseous phase may play a central role in the formation of these molecules [268]. However, given the extreme thermodynamic conditions that characterize the ISM, high vacuum and very low temperatures, reactions in the gaseous phase can only take place if there are no energy barriers higher than the energy of the initial reactants. The unusual chemistry characterizing these environments involves highly reactive ionic and radical species which can react to form more complex molecules [269]. Furthermore, despite the many efforts that have been made to understand how these iCOMs can form in the ISM, the reaction mechanisms which bring to their formation are still not clear. However, in the last decades, simulations of reaction mechanisms and computational kinetics investigations have proved to be of great help in obtaining accurate and reliable information on the reaction mechanisms that can lead to the formation of iCOMs [270]. Moreover, from these analyses it is also possible to obtain theoretical parameters useful for the simulation of the chemical evolution of astrophysical objects, such as molecular clouds which represent the initial stage of the star formation process and for which the chemistry that occurs during these processes is still poorly known. In this paper we study the reaction between vinyl alcohol (VyA) conformers, *syn* and *anti*, and cyanide (CN) radical which are two relatively abundant molecules present in the ISM. In particular, VyA's microwave transitions have been detected in emission toward the dense molecular cloud Sagittarius B2(N) (SgrB2N) which is one of the most studied by astronomers because it is rich in prebiotic iCOMs [247]. VyA is the enolic tautomer of acetaldehyde, another very abundant species in the ISM and both belong to the family of C_2H_4O isomers together with oxirane also identified in the ISM. VyA can exist in two rotameric forms, *syn* and *anti*, depending on the value assumed by the dihedral angle φ (C-C-O-H), which defines the position of the hydroxyl hydrogen with respect to the double bond [271]. Over the years much work has been done regarding its spectroscopic characterization and its presence in various astronomical objects has been researched [272, 273]. Possible reaction mechanisms have also been hypothesized using experimental and computational approaches to account for the relative abundances of the two isomers *anti* and *syn* [274, 249, 275]. Furthermore, enols together with aldehydes are assumed to serve as key tracers of a non-equilibrium chemistry driven by cosmic rays leading to COMs[240]. CN radical has also been detected in SgrB2N and other regions of the ISM as reported by McGuire [276]. It is supposed to be involved in several gas-phase reaction mechanisms for the formation of iCOMs as investigated by Tonolo et al.[194], Alessandrini et al. [277], Puzzarini et al. [6] and Lupi et al.[154]. We present a gas-phase model of the barrierless reactions of VyA's conformers with CN, which to our knowledge has never been investigated before. The thermochemistry

and the reactive PES governing the reactions have been characterized through a quantum mechanical approach based on the double hybrid rev-DSDPBEP86 functional and then refined by the junChS-F12 composite scheme. Our results indicate that VyA's conformers feature a similar but still different reactivity with CN. For both reactions the barrierless association reaction to the double bond shows a strong exothermicity leading to the formation of very highly stabilized reaction intermediates lying at low energies respect with the reactant asymptote. After that, for both isomers the reaction can evolve towards the formation of several products through isomerization and dissociation steps which bring to the formation of several molecular species detected and not yet detected in the ISM. Rate constants have been computed with the help of the MESS program in a range of temperatures typical of the ISM. From the kinetic simulations the most favoured products for both conformers are cyanoacetaldehyde, a prebiotic molecule not yet detected in the ISM but for which several reaction mechanisms have been proposed [142, 152] and the dissociation product composed by vinylcyanide and hydroxyl radical, both molecules have already been detected in the ISM. The article is organized as follows. In Section 2, the computational methods are described. In Section 3, the computed reaction mechanisms are discussed with reference to the stationary points of the potential energy surface (PES). In Section 4, the kinetics of the reactions are addressed. Section 5 is devoted to conclusions.

6.2 Computational Details

The computational protocol used to study the aforementioned reactive system is the same used in chapters 5 and 6 of this thesis. Below is a brief summary of the computational details.

6.2.1 Reaction mechanism discovery

All the reaction mechanisms shown in this work have been automatically generated by means of the AutoMeKin [49, 50, 2] (AMK) program. Unlike other programs for the automatic discovery of the reaction mechanism which involve the initial optimization of the minima characterizing the mechanism and then the calculation of the transition states (TSs), the methodology on which AMK is built is based on the initial optimization of the structures of transition states and then obtain the connected minima from each TS via IRC calculations. In this way the program builds the reaction mechanism by interconnecting all minima through the initially calculated TSs. To do that, AMK relies on the combination of molecular dynamics simulations (MD), post-processing and selection of the TS molecular structures obtained with MD and the re-optimization of the molecular structures through DFT calculations. MD simulations have been performed using the semi-empirical method PM7 [55] implemented in MOPAC [51]. Geometry optimizations and zero-point corrected electronic energies of reactants, transition states, intermediates, and products along the reaction pathways were obtained by the rev-DSD-PBEP86[162]-GD3BJ[69] double-hybrid functional in conjunction with the jun-cc-pVTZ basis set [160] (here after rDSD). All the critical points belonging to the reaction pathways were characterized as minima (reactants,

intermediates and products) and saddle points (transition states) based on vibrational frequency calculations. The transitions states obtained were further confirmed using intrinsic reaction coordinate (IRC) [161] scans at the same level of theory. The results of the simulations have been analyzed using AMK tools [57], a graphic visualizer which allow to examine the extremely complex reaction networks generated by AutoMeKin, to visualize molecular structures with their vibrational normal modes and check the potential energy profiles of the reaction mechanisms investigated. Thanks to AMK tools, it has been possible to select all the structures of the critical points involved in the reaction pathways. For such structures, improved electronic energies have been obtained by exploiting the junChS-F12a composite scheme which will be explained in more detail in the next subsection.

6.2.2 Electronic structure calculations

It is well known that for systems not showing strong multireference character the coupled-cluster (CC) model which takes into account for single, double and triple excitations through a perturbative treatment (CCSD(T))[209] lead to an accurate estimation of the electronic energies if complete basis set (CBS) extrapolation and core valence (CV) correlation are taken into account appropriately. Starting from the optimized geometries obtained through rDSD, the basic idea of the reduced cost Cheap scheme (ChS)[210, 165, 168, 278] is to compute single point frozen core (fc) CCSD(T) calculation in conjunction with a partially augmented triple-zeta basis set[170, 171, 160, 212]. CBS and CV terms computed employing second order Møller-Plesset theory (MP2). The replacement of conventional methods by the explicitly correlated (F12) variants leads to the jun-ChS-F12 scheme.
The comparison with the most accurate results available for reaction energies and activation barriers [168, 1, 217] showed that jun-ChS energy evaluations at rDSD optimized geometries provide average absolute errors of the order of 1 kJ mol^{-1}. Therefore, for all stationary points, this approach was employed in conjunction with anharmonic zero-point vibrational energy corrections computed in the framework of second-order vibrational perturbation theory [218] employing rDSD anharmonic force fields. All rev-DSD-PBEP86 calculations were performed using Gaussian16[52], while 'junChS-F12a' calculations were performed using MOLPRO [63, 62, 61].

6.2.3 Kinetics

To determine which among the possible products of the two reactions was the more kinetically favored, a kinetic analysis was performed employing an Ab Initio Transition State Theory based on Master Equation approach (AITSTME) by means of the MESS software [85] to compute the global and channel-specific rate constants. To do that MESS solves the multiwell one-dimensional master equation by the chemically significant eigenvalue (CSE) method and bimolecular products and reactants are treated as sources and sinks. The collisional energy relaxation is described using the exponential down model [219] with a temperature dependent $< \Delta E_{down} >$ of $260 \times (T/298)^{0.875}$ cm^{-1} in an argon bath. Barrier-less reaction rate constants have been computed

through the phase space theory (PST)[44, 45] which relies on the approximation that the long-range interaction between the incoming reactants is described by an isotropic attractive potential $V(R) = -C_6/R^6$ [75]. To obtain the C_6 parameters for both *anti* and *syn* conformers (63.49 and 64.09 $a_0^6 E_\mathrm{h}$, respectively) a least-square fit of rDSD electronic energies computed at different values of the NC-CH2CHOH distance have been performed. The rate coefficients of the elementary steps governed by distinct transition states have been computed by the conventional transition-state theory (TST). Calculations have been carried out assuming a rigid-rotor harmonic-oscillator (RRHO) approximation and including tunneling as well as non-classical reflection effects using the Eckart model[84]. For all the transition states internal rotation (IR) modes have been identified by the use of redundant internal coordinates. For each IR, rotation potentials have been calculated by means of constrained scan calculations. Depending on the nature and number of IR modes identified in the TSs, one-dimensional decoupled hindered rotor models or, in the case of internal rotations coupled with other rotation modes, multi-dimensional rotors were employed. Kinetic simulations have been performed setting the temperature and pressure conditions typical of different regions of the ISM. A pressure of 1×10^{-8} bar in a range of temperatures between 30–600 K have been set to compute the rate constants. The resulting rate constants computed in the above mentioned temperature range have been fitted to a three-parameter modified Arrhenius equation, namely the Arrhenius–Kooij expression[221, 222]:

$$k(T) = A(\frac{T}{300})^n e^{-\frac{E}{RT}}$$

where A is s pre-exponential factor, n is a constant, T is the temperature, E defines a linear variation of the activation energy (E_a) with the temperature, $E_a/R = E + nT$, and R is the universal gas constant.
A, n and E are the fitting parameters.
However, the Arrhenius-Kooij expression cannot be used for all reaction channels.

6.3 Results

We start the presentation of our results by illustrating the computed reaction mechanism of the abstraction and addition processes of the VyA conformers, namely *syn* and *anti*, with the radical cyanide (CN), all these species have been detected in the ISM. To simplify the analysis, the first PESs presented here concern the abstraction reaction between the VyA conformers and CN. After that, the PESs regarding the addition reactions between VyA conformers and CN are reported.

6.3.1 Mechanism of abstraction reactions

Hydrogen abstraction reactions from *syn*-VyA can lead to the formation of hydrogen cyanide together with four different radical species, **P1A**, **P2A**, **P3A**, and **P4A**.

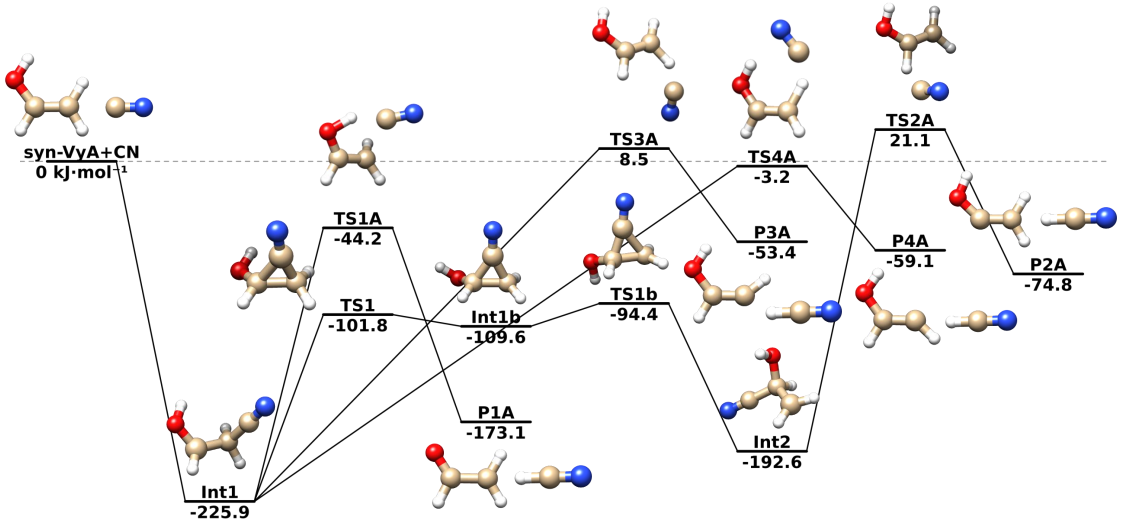

Figure 6.1: Energetics of the abstraction reactions between the *syn*-VyA and CN: junChS-F12 energies augmented by anharmonic rDSD ZPE corrections.

Inspection of the reaction profile in Figure 6.1 shows that the initial reaction step is the formation of an intermediate **Int1** lying 225.9 kJ mol^{-1}, respectively below the reactants. Starting from this intermediate the reaction can further proceed through 4 different transition states, **TS1A**, **TS2A**, **TS3A** and **TS4A**, corresponding to the attack of the **CN** radical to the four non-equivalent hydrogen atoms of *syn*-VyA. The lowest energy barrier (**TS1**) lies 181.7 kJ mol^{-1} above **Int1** (44.2 kJ mol^{-1} below the reactants) and governs the abstraction of the hydroxyl hydrogen. The transition states ruling the other hydrogen abstractions are **TS2A**, **TS3A**, and **TS4A**, which lie 247.0, 234.4, and 222.7 kJ mol^{-1} above the intermediate **Int1**. The high energy barriers governing these three processes indicate that formation of **P1** is kinetically favoured. Noted is that the same trend would be obtained in terms of thermodynamic control since **P1** lies -173.1 kJ mol^{-1} below the reactants, whereas the exothermicity of the reactions leading to **P2A**, **P3A** and **P4A** are 74.8, 53.4, and 59.1 kJ mol^{-1},

respectively. The preference for the route leading to **P1A** can be traced back to the lower strength of the OH bond with respect to its CH counterparts and to the stabilization of the CH_2CHO radical by π-electron delocalization in the C-C-O moiety. In analogy with the case of *syn*-VyA, also the abstraction reactions involving the *anti* conformer start with the formation of a reaction intermediate **Int1** lying 230.3 kJ mol^{-1} below the initial reactants.

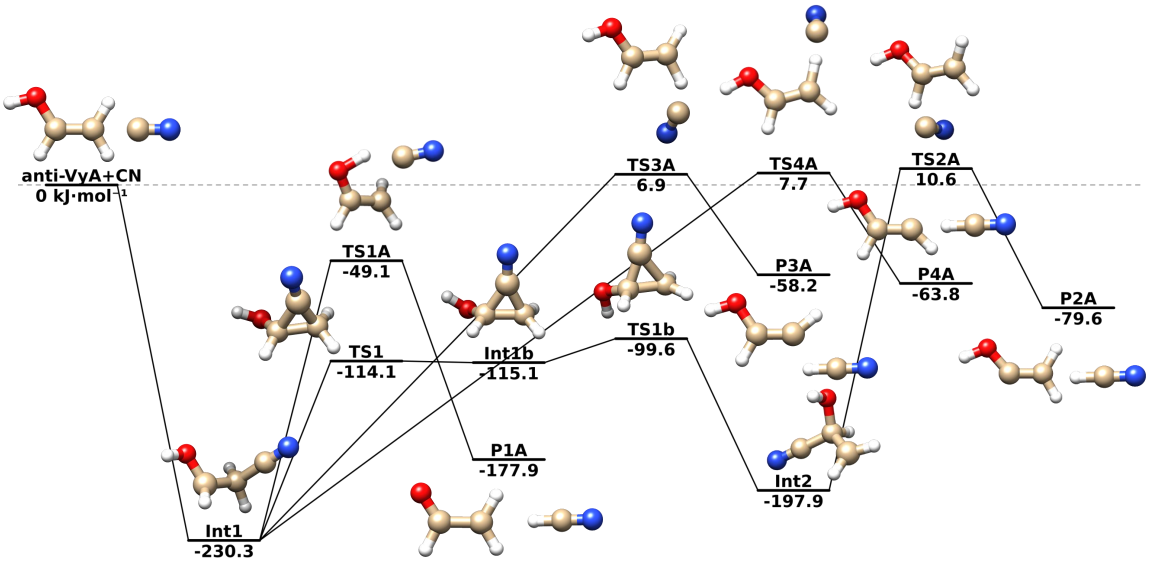

Figure 6.2: Energetics of the abstraction reactions between the *anti*-VyA and CN: junChS-F12 energies augmented by anharmonic rDSD ZPE corrections.

The reaction then proceeds through the attack of CN to one of the hydrogen atoms of *anti*-VyA overcoming the corresponding transition state (**TS1A**, **TS2A**, **TS3A**, or **TS4A**). Inspection of the energy barriers collected in Figure 6.2 shows that the favored abstraction process leads to the formation of **P1A** following the **Int1** $\longrightarrow$ **TS1** $\longrightarrow$ **P1A** path. In fact **TS1A** is found 49.1 kJ mol^{-1} below the reactants, whereas **TS2A**, **TS3A** and **TS4A** lie 10.6, 6.9, and 7.7 kJ mol^{-1} above the reactants. All the reactions are exothermic, but all the paths except that leading to **P1A** are governed by energy barriers higher than the initial reactants asymptotic limit. As a consequence, the reactants would have to acquire from the surrounding environment a significant energy, with this being a highly unlikely process under the harsh conditions of the ISM.

The reaction between *syn*-VyA with radical CN shown in Figure 6.3 is characterized by an initial highly exothermic barrierless attack of CN to the double bond of *syn*-VyA which bring to the formation of **Int1** at -225.9 kJ mol^{-1}. The reaction can subsequently progress with the elimination of atomic hydrogen through two different TSs, the **TS4** at -73.1 kJ mol^{-1} and **TS8** at -68.1 kJ mol^{-1}, to lead to the formation of one of the isomers of cyanovinylalcohol **P1** at -94.3 kJ mol^{-1}, or of cyanoacetaldehyde **P3** at -109.6 kJ mol^{-1}. Otherwise the reaction can proceed with the transposition of hydrogen to form another more stable intermediate **Int3** at about -231.3 kJ mol^{-1} through the **TS3** overcoming a barrier of 165.0 kJ mol^{-1}, or the transposition of the

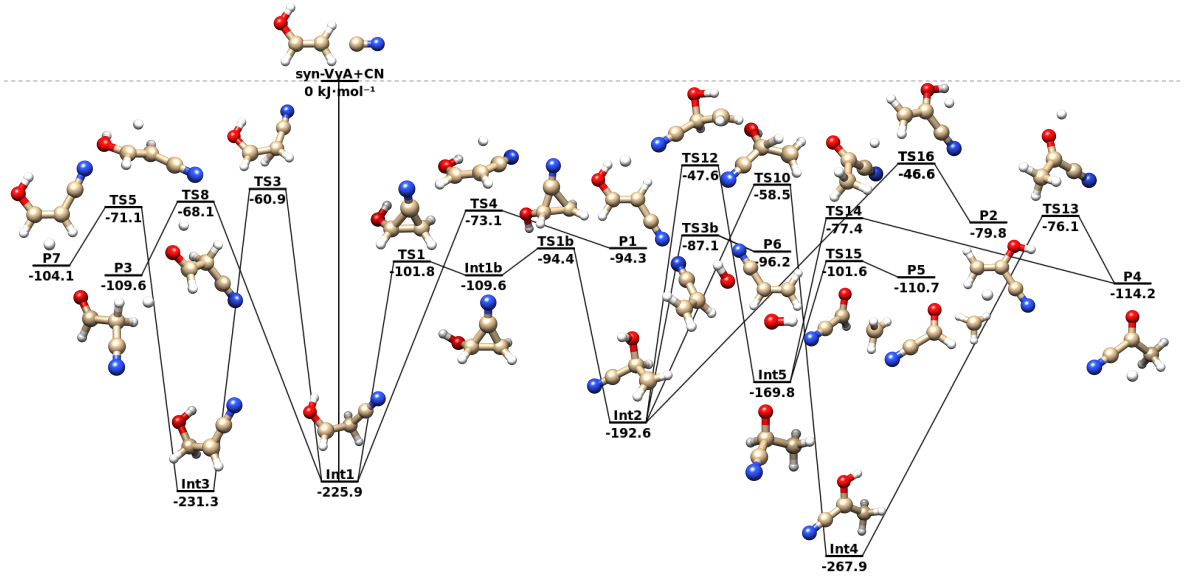

Figure 6.3: Energetics of the reaction between the *syn*-VyA and CN: junChS-F12 energies augmented by anharmonic rDSD ZPE corrections.

cyanide group passing through the **Int1b** at -109.6 kJ mol^{-1} to arrive at the formation of **Int2** at about -192.6 kJ mol^{-1}. After that, those three intermediates through several isomerization and dissociation paths can lead to the formation of many other products, like other cyanovinylalcohol isomers, **P2** and **P7**, respectively at -79.8 kJ mol^{-1} and -104.1 kJ mol^{-1}, the vinylcyanide **P6** at -96.2 kJ mol^{-1}, the formylcyanide **P5** at -110.7 kJ mol^{-1} and the acetylcyanide **P4** at -114.2 kJ mol^{-1}. As can be seen, all the dissociation products of the aforementioned processes show a strong exothermicity, a necessary condition for their formation in the ISM. It is also worth pointing out that only few of the possible products are molecular species already detected in the ISM, in paticular in SgrB2N, such as the formylcyanide[185] and vinylcyanide[279].
Also for *anti*-VyA in Figure 6.4the initial reaction stage provides for the barrierless attack of CN to the π system of the VyA, to lead to the formation of the reaction intermediate **Int1** at -230.30 kJ mol^{-1}. From **Int1** the reaction can evolve through hydrogen elimination reactions to form **P1** at -98.60 kJ mol^{-1} and **P3** at -114.90 kJ mol^{-1}, passing through **TS4** and **TS8**, respectively. Otherwise **Int1** can evolve through isomerization steps which involve the transposition of the CN radical or the hydrogen atom through the **TS1** at -114.1 kJ mol^{-1} and **TS3** at -63.60 kJ mol^{-1} to form two others reaction intermediates, **Int2** at -197.90 kJ mol^{-1} and **Int3** at -234.70 kJ mol^{-1}. From **Int3** another hydrogen elimination process can bring to the formation of **P7** through **TS5** with energy barrier of 157.80 kJ mol^{-1}. From **Int2** a possible dissociation pathway can bring to the formation of **P6**, through **TS3b**. Also two isomerization steps can occur through hydrogen transposition mechanisms through **TS10** and **TS12**, which bring to the formation of **Int4** at -273.20 kJ mol^{-1} and **Int5** at -175.10 kJ mol^{-1}. From **Int4** the hydrogen elimination can bring to the formation of **P4** through **TS13** with an energy barrier of 191.80 kJ mol^{-1}. From **Int5** two possible dissociation pathways can occur which brign to the formation of **P4** and **P5** at -119.50

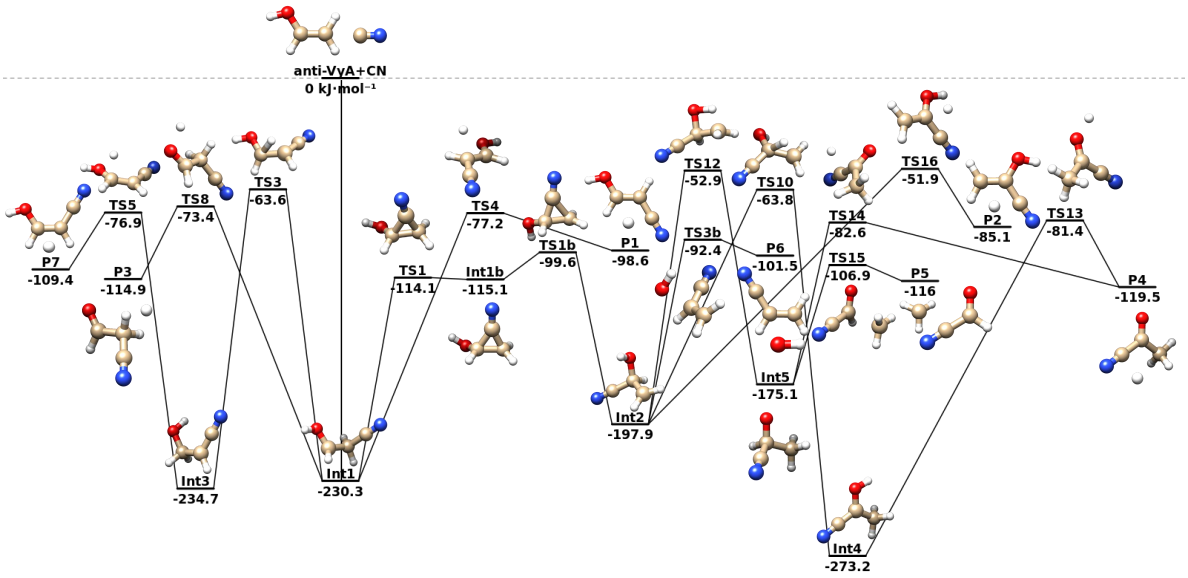

Figure 6.4: Energetics of the reaction between the *anti*-VyA and CN radical: junChS-F12 energies augmented by anharmonic rDSD ZPE corrections.

kJ mol^{-1} and -116.00 kJ mol^{-1} respectively. It is useful to observe that also in this case all the processes of formation of the reaction products are strongly exothermic and that some of the products turn out to be, as in the case of the previous reaction, molecules already identified in the ISM while most of them are not , such as cyanoacetyladehyde (**P3**), isomers of cyanovinyl alcohol (**P1**, **P2**, **P7**) and acetylcyanide (**P4**).

6.3.2 Rate constants

In order to prove which of the all possible products of the reaction between the two VyA conformers and CN at the ISM thermodynamic conditions is the most kinetically favoured one is necessary to perform kinetic computations. The Arrhenius plot for all the abstraction products **P1A**, **P2A**, **P3A**, **P4A** and the addition products **P1**, **P2**, **P3**, **P4**, **P5**, **P6**, **P7** for the reactions *syn*-VyA+CN and *anti*-VyA+CN, are shown in Figures 6.5, 6.6, 6.7 and 6.8. The parameters of the Arrhenius-Kooij and NTS fits are given in Table 7.7, 7.8, 7.9, 7.10 reported in Appendix D. These have been obtained by fitting the global rate constants and the transitivities computed in the 30–600 K range.

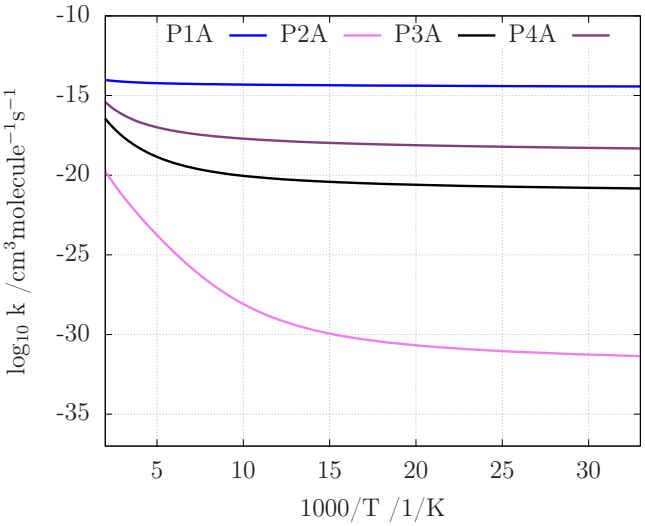

Figure 6.5: Arrhenius plot of the formation rate constants of the products **P1A**, **P2A**, **P3A**, **P4A** of the *syn*-VyA + CN abstraction reactions.

Starting from abstraction reactions involving *syn*-VyA, inspection of the results reported in Figure 6.5 shows that the rate constant governing the formation of **P1A** (which ranges between 3.13×10^{-13} and 1.00×10^{-12} $cm^3molecule^{-1}s^{-1}$) is higher than the rate constants governing the formation of **P2A**, **P3A** and **P4A** in the whole interval of temperatures (30-600 K). The trend reflects the effect of the energy barriers and the nature of their reaction pathways involved in leading to the various products. In fact, the formation pathways of **P1A** and **P4A** show submerged TSs lying 44.2 and 3.2 kJ mol^{-1} below the reactants, while **P2A** and **P3A** show TSs which lye above it. Furthermore the formation pathway of **P2A** involve three different intermediates and high energy barriers, which make it the most kinetically disfavoured process. The formation rate constant for the reaction channel leading to **P4A** ranges between 4.26×10^{-20} and 8.41×10^{-16} $cm^3molecule^{-1}s^{-1}$. For **P3A** ranges between 1.11×10^{-19} and 8.05×10^{-15} $cm^3molecule^{-1}s^{-1}$. Finally, the rate constant governing the formation of **P2A** ranges between 1.62×10^{-32} and $5.36\times10^{-26}cm^3molecule^{-1}s^{-1}$.
Figure 6.6 shows that also for the abstraction reactions involving the *anti* conformer the fastest process leads to the formation of **P1A** in the whole interval of temperatures (30-600 K) and its rate constant ranges between 3.70×10^{-15} and 1.07×10^{-14}

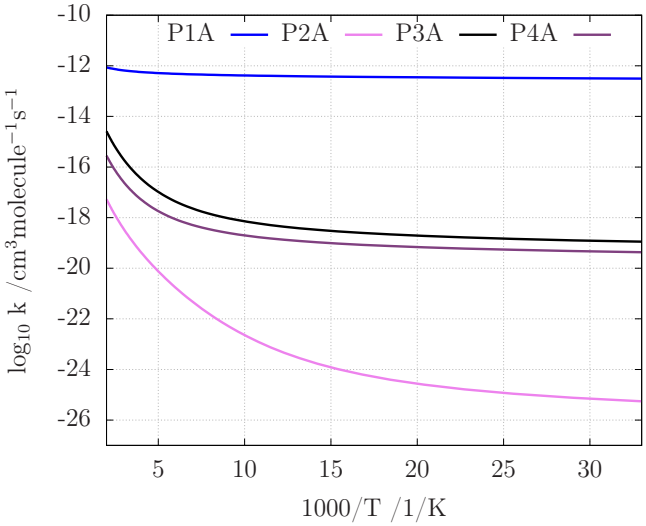

Figure 6.6: Arrhenius plot of the formation rate constants of the products **P1A**, **P2A**, **P3A**, **P4A** of the *anti*-VyA + CN abstraction reactions.

$cm^3molecule^{-1}s^{-1}$. Once again the trend of rate constants parallels that of energy barriers and the single/multi step nature of the reaction path. Accordingly, the second highest rate constant (ranging between 1.46×10^{-21} and 1.09×10^{-16} $cm^3molecule^{-1}s^{-1}$) is the formation of **P3A**, with the barrier associated to this abstraction process being about 24.0 kJ mol^{-1}. Next, formation of **P4A** is governed by an energy barrier of 42.0 kJ mol^{-1} and its rate constant ranges between 4.76×10^{-19} and 9.16×10^{-16} $cm^3molecule^{-1}s^{-1}$. Finally, the slowest process is the formation of **P2A**, which is ruled by an energy barrier of 39.7 kJ mol^{-1} and has a rate constant ranging between 4.30×10^{-32} and $6.69\times10^{-20}cm^3molecule^{-1}s^{-1}$.

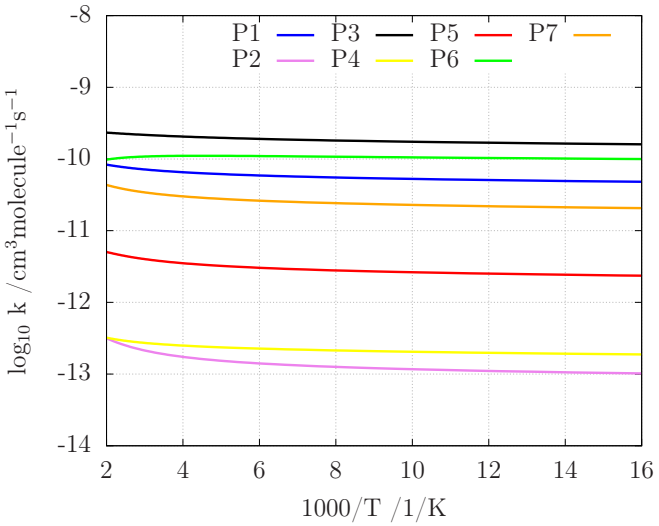

Figure 6.7: Arrhenius plot of the formation rate constants of the products **P1**, **P2**, **P3**, **P4**, **P5**, **P6** and **P7** of the *syn*-VyA + CN addition reaction.

For addition reactions, the results reported in Figure 6.7 show that in the whole interval of temperatures (30-600 K) the formation of **P3**, which is the cyanoacetaldehyde, is governed by the highest rate constant, which ranges between 1.40×10^{-10} and 2.40×10^{-10}cm^{3}molecule^{-1}s^{-1}. All the other products are formed by multi-step reaction pathways governed by rate constants decreasing in the order **P6** > **P1** > **P7** > **P5** > **P4** > **P2**, which correspond to vinylcyanide and radical hydroxyl, a (E)-cyanovinylalcohol, (Z)-cyanovinylalcohol, formylcyanide and radical methyl, acetylcyanide, 2-hydroxy-2-propenitrile.
While the general trend of the rate constants governing addition reactions to *anti-Vy* is analogous to that of the *syn* conformer, the reaction pathways discovered by AutoMeKin involve different energy barriers, which lead to non negligible quantitative differences. In any case, the results reported in Figure 6.8 shows that in the whole temperature interval the highest rate constant (between 2.83×10^{-13} and 4.74×10^{-10}cm^{3}molecule^{-1}s^{-1}) governs again the formation of **P3**.

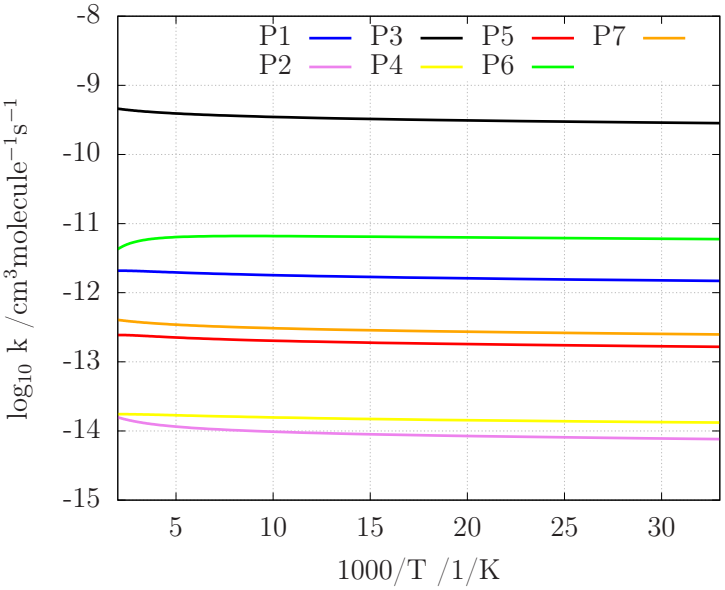

Figure 6.8: Arrhenius plot of the formation rate constants of the products **P1**, **P2**, **P3**, **P4**, **P5**, **P6** and **P7** of the *anti*-VyA + CN addition reaction.

6.3.3 Interpretation

For some abstraction reaction channels the analysis of the trend of the transitivity functions $\gamma(\beta)$, which correspond to the reciprocal of the activation energy $(1/E_a)$ with $\beta = 1/RT$ show a sub-Arrhenius behavior typical of low-temperature reactions in which tunneling influences the rate constants[280].
Since the E_a can be expressed as

$$E_a = -\frac{\partial \ln k(T)}{\partial \beta} \tag{6.1}$$

we analyzed the trends of $\gamma(\beta)$ by using the $k(T)$ obtained by the kinetic simulations. The general classification proposed in ref. 280 allows us to understand the importance that tunneling has in tuning the rate constants.
For this purpose the "crossover temperatures", T_c have been calculated by using the following expression[281, 282]

$$T_c = \frac{\hbar v^{\ddagger}}{R} \tag{6.2}$$

in which $v^{\ddagger}$ is the value of the imaginary frequency at the TS, R is the universal gas constant and $\hbar$ is the reduced Planck's constant. Depending on the value assumed by T_c it was possible to define in which tunneling regime the various reactive paths were located in the investigate temperature range T: classical, for $T > 4T_c$, negligible, for $4T_c > T > 2T_c$, moderate, for $2T_c > T > T_c$ and deep, for $T_c > T$.
In Table 6.1 are reported the values of T_c for all the barrier above the reactants limit which bring to the formation of **P2A**, **P3A** and **P4A** for both VyA's conformers.

	T_c/**K**		T_c/**K**
P2A	16.6	**P2A**	17.9
P3A	34.7	**P3A**	36.2
P4A	39.5	**P4A**	26.1

Table 6.1: Crossover temperatures for the *syn*-VyA (left) and *anti*-VyA (right) abstraction processes.

For all the processes it was therefore possible to define that the temperature range considered in the kinetic simulations defined a tunneling regime ranging from deep to classical, except for the **P2A** formation processes and **P4A** formation process for *anti*-VyA which range from moderate to classical.
So, we used the Nakamura-Takayanagi-Sato (NTS)[283, 284] transitivity function $\gamma(\beta)$ to fit our data. NTS is expressed as

$$\gamma(\beta) = \frac{1}{\varepsilon^{\ddagger}} \left[1 + (RT_0)^2 \beta^2\right]^{\frac{3}{2}}$$

in which $\varepsilon^{\ddagger}$ and T_0 are the fitting parameters and are defined as the Arrhenius-Eyring energy barrier and the Vogel-Fulcher-Tammann temperature (VFT-temperature), R is the universal gas constant and β, which is expressed as $\beta = \frac{1}{RT}$, it is often referred as to the Lagrange parameter. In Appendix D, Figures 7.3 and 7.4 show the comparison plots between our data and the fitted NTS function.

6.4 General discussion and conclusions

In this work a computational kinetic study between the vinyl alcohol conformers and the CN radical is proposed. Specifically, the hydrogen addition and abstraction channels were analyzed by an automated search for possible reaction mechanisms using the AMK program. After the refinement through the use of the junChS-F12 composite

schemes of the energetics of the reactive PESs, a kinetic analysis of all the reactive channels was then performed in a typical temperature range of the ISM by means of the MESS program. The results show that the formation of **P3** is favoured for both conformers in the entire temperature range even if TSs at higher energies are involved than other reaction pathways shown in the Figure 6.3 and 6.4. This is due to the presence of low-frequency vibrational motions associated with hindered rotations characterizing various involved TSs, including **TS8** involved in the cyanoacetaldehyde formation pathway.
In more detail in Table 6.2 the models used for all the TSs involved in the reaction mechanisms of the two conformers *syn* and *anti* are indicated.

***anti*-VyA + CN**		***syn*-VyA + CN**	
TS	**Model**	**TS**	**Model**
TS1	1D-HR	**TS1**	1D-HR
TS1b	1D-HR	**TS1b**	1D-HR
TS3	1D-HR	**TS3**	MD-HR
TS3b	MD-HR	**TS3b**	MD-HR
TS4	1D-HR	**TS4**	1D-HR
TS5	1D-HR	**TS5**	1D-HR
TS8	MD-HR	**TS8**	MD-HR
TS10	1D-HR	**TS10**	1D-HR
TS12	MD-HR	**TS12**	MD-HR
TS13	Free	**TS13**	Free
TS14	1D-HR	**TS14**	1D-HR
TS15	1D-HR	**TS15**	1D-HR
TS16	MD-HR	**TS16**	MD-HR
TS1A	Free	**TS1A**	Free
TS2A	Free	**TS2A**	Free
TS3A	Free	**TS3A**	Free
TS4A	Free	**TS4A**	Free

Table 6.2: List of the TSs involved in all the reaction mechanisms with the model used to treat the internal rotations, i.e., one-dimensinal free rotor (Free), one-dimensional hindered rotor (1D-HR) and multi-dimensional coupled hindered rotors (MD-HR).

As far as the Tunnel effect is concerned, it can be hypothesized that for the addition mechanisms it does not play an important role since all the TSs lye below the asymptotic limit of the reactants. The same hypothesis can be made for the **P1A** formation mechanism of abstraction mechanisms for both conformers and **P4A** product of the *syn*-VyA conformer. In any case, it can be stated that tunneling affects only the formation mechanisms of **P2A**, **P3A** and **P4A** for the *anti* conformer and of **P2A** and **P3A** for the conformal *syn*.
From the nature of the reaction mechanisms reported in this work, characterized by thermodynamically very stable reaction intermediates and numerous submerged TSs, it is possible to state that the Tunnel effect cannot decisively condition the value assumed

by the rate constants. On the contrary, given that all the species involved in the various mechanisms are strongly excited vibrationally, the effect of the internal rotations of the different TSs plays a fundamental role affecting the final value assumed by the rate constants.
Mechanistic analysis of hydrogen abstraction channels shows similarity to another system analyzed by Balucani et al. [285] involving ethylene and radical cyanide. Also in this case the association without barriers is strongly favoured, leading to the formation of thermodynamically very stable reaction intermediates. In the case of hydrogen abstraction, given that for ethylene the hydrogens are all equivalent to each other, this process is associated with only one transition state which according to the reported results is about 5 kJ mol^{-1} above the reactants. In the case of VyA there are no equivalent hydrogens, in fact four different transition states have been identified. From the results obtained, the kinetically most favored abstraction process is also the one involved in the weakest bond, the hydrogen of the hydroxyl group which leads to the formation of **P4A** for both VyA conformers.
This study brings new insights into a possible mechanism of formation of a prebiotic molecule not yet identified in the ISM, cyanoacetaldehyde. We therefore suggest to look for this molecule in those regions where both VyA and CN have been identified, i.e. Sagittarius B2N and G+0.693-0.027.

Chapter 7

Conclusions and future perspectives

In this dissertation, a computational protocol for the modeling of reaction mechanism and kinetics of gas-phase reactions of astrochemical interest have been developed and presented. The three main pillars of this protocol involve: (i) the automated reaction mechanism discovery through the AutoMeKin program, (ii) the energy refinement of the electronic energies by means of the 'cheap' family schemes and (iii) the kinetic analysis of the reaction mechanism obtained through the StarRate program in conjunction with the MESS program for kinetic calculations through AITSTME approach.
For (i) the starting point is the construction of PESs using the AutoMeKin program for the automated search of reaction mechanisms. It has been demonstrated that thanks to this program it is possible to obtain a more detailed description of the reaction mechanisms that can lead to the formation of iCOMs and to discover formation channels for molecules of astrochemical interest that had not yet been previously considered. The program is also able to analyze in detail the barrierless reaction channels which allow to obtain an extensive list of possible starting reagents, like radicals and ions, which are fundamental for the chemistry of the ISM.
For (ii), the 'cheap' family of composite schemes has been applied to obtain accurate energetic characterization of the reactive PES discovered by AutoMeKin. All of these methods begin by computing the molecular geometries and vibrational frequencies using spin-component scaled double hybrid density functionals with dispersion corrections and triple-quality basis sets with diffuse functions. All of these schemes' variations have their roots in the coupled cluster ansatz, to which complete basis set and core-valence corrections are included and both are evaluated at the MP2 level of theory in an effort to cut down on computational costs without compromising accuracy. In fact, the aforementioned approaches have since been compared to a wide range of benchmark reaction barriers and molecular architectures. According to the findings, the standard deviation is within 1.25 kJ mol^{-1}.
For (iii), two programs, StarRate and MESS, have been used in conjunction in order to obtain a kinetic analysis of the complex reaction networks obtained in (i) and (ii). More specifically, the development and the features already implemented and several new features, concerning multidimensional tunneling (ZCT, SCT), radiative emission stabilization and anharmonicity models which are currently under implementation in StarRate have been discussed in Chapter 2. After that, StarRate has been used also to

investigate the kinetics of the reactive systems studied in Chapters 3, and in Chapters 4 and 5 also with MESS.
This protocol has been applied to study four reactive systems, (a) the radiative association reaction between the radicals HCO and H_2CCN, (b) the dissociative recombination between the radicals HCO and HCCN, (c-d) the competition between the addition and abstraction channels for the reaction between Vy conformers and the CN and OH radicals have been reported and discussed.
For none of the above reactions there are other computational or experimental studies in the literature. From our results, for what concerns (a), radiative emission stabilization plays a central role in the formation of Cyanoacetaldehyde at the very harsh conditions of the ISM. More generally, the effectiveness of the radiative emission effect can grow as the number of degrees of freedom of the analyzed molecular system increases. We will study this effect in more detail and for larger reactive systems in the future. In (b) a plausible formation reaction pathway of the Cyanoketene starting from the radical species HCO and HCCN has been discussed. The kinetic analysis of the mechanism confirms that, Cyanoketene is not the thermodynamically favored product, it appears to be the kinetically most favored one. For (c), the investigation of the reaction between Vy and OH has been carried out in order to prove that (Z)1,2-Ethendiol cannot be formed through addition reaction channels, instead hydrogen abstraction is kinetically favored which bring to the formation of vynoxy radical, a molecule not yet detected in the ISM. For (d), the reaction between Vy and CN have been investigated through abstraction and addition reaction channels which led to the discovery of a plausible dissociative recombination route for the formation of Cyanoacetaldehyde in the ISM.
In general terms, most of the objectives outlined in the Introduction have been reached satisfactorily. Of course, the computational strategy proposed in this thesis can be further improved.
A future step forward will be the development of an interface capable of automating the various steps of the protocol developed in this thesis in order to obtain a computational tool capable of providing a detailed description both at the mechanistic and kinetic level of the reactive system under investigation.
As regards the accuracy of the kinetic models used, the simulations carried out for the various reactive systems presented above are not intended to provide a precise quantitative description, but to provide a semi-quantitative analysis of the formation channels of molecules not yet identified in the ISM. The methodology presented here paves the way for the systematic computational study of the formation mechanisms of iCOMs. In this way it will also be possible to work in synergy with the spectroscopists to give indications on which molecule to look for and in which area of the ISM. Thanks to this protocol it is possible to obtain a detailed description at a mechanistic level and a good estimation of the reaction rates which are both of paramount importance to model the chemical evolution of astrophysical objects. We therefore believe that the protocol presented in this dissertation could be of considerable utility in the computational study of the gas phase chemical reactivity of the ISM, both as regards the understanding of the iCOM formation mechanisms, and as regards the search for molecules not yet identified in the ISM.

Bibliography

[1] Jacopo Lupi, Silvia Alessandrini, Cristina Puzzarini, and Vincenzo Barone. junchs and junchs-f12 models: Parameter-free efficient yet accurate composite schemes for energies and structures of noncovalent complexes. *Journal of Chemical Theory and Computation*, 17(11):6974–6992, 2021. PMID: 34677974.

[2] Emilio Martínez-Núñez, George L. Barnes, David R. Glowacki, Sabine Kopec, Daniel Peláez, Aurelio Rodríguez, Roberto Rodríguez-Fernández, Robin J. Shannon, James J. P. Stewart, Pablo G. Tahoces, and Saulo A. Vazquez. Automekin2021: An open-source program for automated reaction discovery. *Journal of Computational Chemistry*, 42(28):2036–2048, 2021.

[3] Surajit Nandi, Bernardo Ballotta, Sergio Rampino, and Vincenzo Barone. A general user-friendly tool for kinetic calculations of multi-step reactions within the virtual multifrequency spectrometer project. *Applied Sciences*, 10(5), 2020.

[4] Malgorzata Biczysko, Julien Bloino, and Cristina Puzzarini. Computational challenges in astrochemistry. *WIREs Computational Molecular Science*, 8(3):e1349, 2018.

[5] Cristina Puzzarini. Grand challenges in astrochemistry. *Frontiers in Astronomy and Space Sciences*, 7, 2020.

[6] Cristina Puzzarini and Vincenzo Barone. The challenging playground of astrochemistry: an integrated rotational spectroscopy – quantum chemistry strategy. *Phys. Chem. Chem. Phys.*, 22:6507–6523, 2020.

[7] Eric Herbst. The chemistry of interstellar space. *Chem. Soc. Rev.*, 30:168–176, 2001.

[8] Satoshi Yamamoto. *Introduction to Astrochemistry*, page 286. Springer Tokyo, 2017.

[9] Christian P. Endres, Stephan Schlemmer, Peter Schilke, Jürgen Stutzki, and Holger S.P. Müller. The cologne database for molecular spectroscopy, cdms, in the virtual atomic and molecular data centre, vamdc. *Journal of Molecular Spectroscopy*, 327:95–104, 2016. New Visions of Spectroscopic Databases, Volume II.

[10] Holger S.P. Müller, Frank Schlöder, Jürgen Stutzki, and Gisbert Winnewisser. The cologne database for molecular spectroscopy, cdms: a useful tool for astronomers and spectroscopists. *Journal of Molecular Structure*, 742(1):215–227, 2005. MOLECULAR SPECTROSCOPY AND STRUCTURE.

[11] Müller, H. S. P., Thorwirth, S., Roth, D. A., and Winnewisser, G. The cologne database for molecular spectroscopy, cdms. *A&A*, 370(3):L49–L52, 2001.

[12] Brett A. McGuire. 2018 census of interstellar, circumstellar, extragalactic, protoplanetary disk, and exoplanetary molecules. *The Astrophysical Journal Supplement Series*, 239(2):17, nov 2018.

[13] Eric Herbst. Chemistry of star-forming regions. *The Journal of Physical Chemistry A*, 109(18):4017–4029, 2005. PMID: 16833724.

[14] Eleonora Bianchi, Cecilia Ceccarelli, Claudio Codella, Juan Enrique-Romero, Cecile Favre, and Bertrand Lefloch. Astrochemistry as a tool to follow protostellar evolution: The class i stage. *ACS Earth and Space Chemistry*, 3(12):2659–2674, 2019.

[15] Yao Wang, Fujun Du, Dmitry Semenov, Hongchi Wang, and Juan Li. Chemical modeling of the complex organic molecules in the extended region around sagittarius b2. *Astronomy & Astrophysics*, 648:16, 2021.

[16] Paola Caselli and Cecilia Ceccarelli. Our astrochemical heritage. *The Astronomy and Astrophysics Review*, 20:1–68, 2012.

[17] Cristina Puzzarini and Vincenzo Barone. Interstellar Complex Organic Molecules: A Step Toward Biomolecule Building Blocks in the Skies. In *Prebiotic Photochemistry: From Urey–Miller-like Experiments to Recent Findings*. The Royal Society of Chemistry, 06 2021.

[18] Cristina Puzzarini. Gas-phase chemistry in the interstellar medium: The role of laboratory astrochemistry. *Frontiers in Astronomy and Space Sciences*, 8, 2022.

[19] Eric Herbst. Unusual chemical processes in interstellar chemistry: Past and present. *Frontiers in Astronomy and Space Sciences*, 8, 2021.

[20] V .Wakelam, I.W.M Smith, and E .Herbst. Reaction networks for interstellar chemical modelling: Improvements and challenges. *Space science review*, 156:13–72, 2010.

[21] André Canosa, Fabien Goulay, Ian R. Sims, and Bertrand R. Rowe. *Gas Phase Reactive Collisions at Very Low Temperature: Recent Experimental Advances and Perspectives*, pages 55–120. Russian Chemical Reviews, 2008.

[22] B. McCall, A. Huneycutt, and R. Saykally. An enhanced cosmic-ray flux towards ζ persei inferred from a laboratory study of the h3+–e- recombination rate. *Nature*, 422:500–502, 2003.

[23] Manfred A. Biondi and Sanborn C. Brown. Measurement of electron-ion recombination. *Phys. Rev.*, 76:1697–1700, Dec 1949.

[24] Per-Olov Löwdin. *Correlation Problem in Many-Electron Quantum Mechanics I. Review of Different Approaches and Discussion of Some Current Ideas*, pages 207–322. John Wiley I& Sons, Ltd, 1958.

[25] Attila G. Császár, Wesley D. Allen, and Henry F. Schaefer. In pursuit of the ab initio limit for conformational energy prototypes. *The Journal of Chemical Physics*, 108(23):9751–9764, 1998.

[26] Amir Karton and Jan M. L. Martin. Explicitly correlated wn theory: W1-f12 and w2-f12. *The Journal of Chemical Physics*, 136(12):124114, 2012.

[27] Kirk A. Peterson, David Feller, and David A. Dixon. Chemical accuracy in ab initio thermochemistry and spectroscopy: current strategies and future challenges. *Theoretical Chemistry Accounts*, 131:1–20, 2012.

[28] Amir Karton. A computational chemist's guide to accurate thermochemistry for organic molecules. *WIREs Computational Molecular Science*, 6(3):292–310, 2016.

[29] Michael E. Harding, Juana Vázquez, Branko Ruscic, Angela K. Wilson, Jürgen Gauss, and John F. Stanton. High-accuracy extrapolated ab initio thermochemistry. iii. additional improvements and overview. *The Journal of Chemical Physics*, 128(11):114111, 2008.

[30] Yannick J. Bomble, Juana Vázquez, Mihály Kállay, Christine Michauk, Péter G. Szalay, Attila G. Császár, Jürgen Gauss, and John F. Stanton. High-accuracy extrapolated ab initio thermochemistry. ii. minor improvements to the protocol and a vital simplification. *The Journal of Chemical Physics*, 125(6):064108, 2006.

[31] Attila Tajti, Péter G. Szalay, Attila G. Császár, Mihály Kállay, Jürgen Gauss, Edward F. Valeev, Bradley A. Flowers, Juana Vázquez, and John F. Stanton. Heat: High accuracy extrapolated ab initio thermochemistry. *The Journal of Chemical Physics*, 121(23):11599–11613, 2004.

[32] Larry A. Curtiss, Paul C. Redfern, and Krishnan Raghavachari. Gn theory. *WIREs Computational Molecular Science*, 1(5):810–825, 2011.

[33] Larry A. Curtiss, Paul C. Redfern, and Krishnan Raghavachari. Gaussian-4 theory. *The Journal of Chemical Physics*, 126(8):084108, 2007.

[34] J. A. Montgomery, J. W. Ochterski, and G. A. Petersson. A complete basis set model chemistry. iv. an improved atomic pair natural orbital method. *The Journal of Chemical Physics*, 101(7):5900–5909, 1994.

[35] J. A. Montgomery, M. J. Frisch, J. W. Ochterski, and G. A. Petersson. A complete basis set model chemistry. vii. use of the minimum population localization method. *The Journal of Chemical Physics*, 112(15):6532–6542, 2000.

[36] Vincenzo Barone, Jacopo Lupi, Zoi Salta, and Nicola Tasinato. Development and validation of a parameter-free model chemistry for the computation of reliable reaction rates. *Journal of Chemical Theory and Computation*, 17(8):4913–4928, 2021. PMID: 34228935.

[37] Stuart C. Althorpe and David C. Clary. Quantum scattering calculations on chemical reactions. *Annual Review of Physical Chemistry*, 54(1):493–529, 2003. PMID: 12651964.

[38] M.H. Beck, A. Jäckle, G.A. Worth, and H.-D. Meyer. The multiconfiguration time-dependent hartree (mctdh) method: a highly efficient algorithm for propagating wavepackets. *Physics Reports*, 324(1):1–105, 2000.

[39] Ian R. Craig and David E. Manolopoulos. Chemical reaction rates from ring polymer molecular dynamics. *The Journal of Chemical Physics*, 122(8):084106, 2005.

[40] Gilles H. Peslherbe, Haobin Wang, and William L. Hase. *Monte Carlo Sampling for Classical Trajectory Simulations*, pages 171–201. John Wiley I& Sons, Ltd, 1999.

[41] M Baer. *Theory of chemical reaction dynamics. Volume 3.* CRC Press, 1 1985.

[42] Henry Eyring. The activated complex in chemical reactions. *The Journal of Chemical Physics*, 3(2):107–115, 1935.

[43] M. G. Evans and M. Polanyi. Some applications of the transition state method to the calculation of reaction velocities, especially in solution. *Trans. Faraday Soc.*, 31:875–894, 1935.

[44] Philip Pechukas and John C. Light. On detailed balancing and statistical theories of chemical kinetics. *The Journal of Chemical Physics*, 42(9):3281–3291, 1965.

[45] Walter J. Chesnavich. Multiple transition states in unimolecular reactions. *The Journal of Chemical Physics*, 84(5):2615–2619, March 1986.

[46] M. J. Pilling and P. W. Seakins. *Reaction kinetics.* Oxford University Press, 1996.

[47] Junwei Lucas Bao and Donald G. Truhlar. Variational transition state theory: theoretical framework and recent developments. *Chem. Soc. Rev.*, 46:7548–7596, 2017.

[48] Aurelio Rodríguez, Roberto Rodríguez-Fernández, Saulo A. Vázquez, George L. Barnes, James J. P. Stewart, and Emilio Martínez-Núñez. tsscds2018: A code for automated discovery of chemical reaction mechanisms and solving the kinetics. *Journal of Computational Chemistry*, 39(23):1922–1930, 2018.

[49] Emilio Martínez-Núñez. An automated method to find transition states using chemical dynamics simulations. *Journal of Computational Chemistry*, 36(4):222–234, 2015.

[50] Emilio Martínez-Núñez. An automated transition state search using classical trajectories initialized at multiple minima. *Phys. Chem. Chem. Phys.*, 17:14912–14921, 2015.

[51] J. J. P. Stewart. Mopac2016.

[52] M. J. Frisch, G. W. Trucks, H. B. Schlegel, G. E. Scuseria, M. A. Robb, J. R. Cheeseman, G. Scalmani, V. Barone, G. A. Petersson, H. Nakatsuji, X. Li, M. Caricato, A. V. Marenich, J. Bloino, B. G. Janesko, R. Gomperts, B. Mennucci, H. P. Hratchian, J. V. Ortiz, A. F. Izmaylov, J. L. Sonnenberg, D. Williams-Young, F. Ding, F. Lipparini, F. Egidi, J. Goings, B. Peng, A. Petrone, T. Henderson, D. Ranasinghe, V. G. Zakrzewski, J. Gao, N. Rega, G. Zheng, W. Liang, M. Hada, M. Ehara, K. Toyota, R. Fukuda, J. Hasegawa, M. Ishida, T. Nakajima, Y. Honda, O. Kitao, H. Nakai, T. Vreven, K. Throssell, J. A. Montgomery, Jr., J. E. Peralta, F. Ogliaro, M. J. Bearpark, J. J. Heyd, E. N. Brothers, K. N. Kudin, V. N. Staroverov, T. A. Keith, R. Kobayashi, J. Normand, K. Raghavachari, A. P. Rendell, J. C. Burant, S. S. Iyengar, J. Tomasi, M. Cossi, J. M. Millam, M. Klene, C. Adamo, R. Cammi, J. W. Ochterski, R. L. Martin, K. Morokuma, O. Farkas, J. B. Foresman, and D. J. Fox. Gaussian˜16 Revision C.01, 2016. Gaussian Inc. Wallingford CT.

[53] Kenichi Fukui. The path of chemical reactions - the irc approach. *Accounts of Chemical Research*, 14(12):363–368, 1981.

[54] Daniel T Gillespie. A general method for numerically simulating the stochastic time evolution of coupled chemical reactions. *Journal of Computational Physics*, 22(4):403–434, 1976.

[55] J. J. P. Stewart. Optimization of parameters for semiempirical methods vi: more modifications to the nddo approximations and re-optimization of parameters. *Journal of Molecular Modeling*, pages 1–32, 2013.

[56] William L. Hase, Daniel G. Buckowski, and Kandadai N. Swamy. Dynamics of ethyl radical decomposition. 3. effect of chemical activation vs. microcanonical sampling. *The Journal of Physical Chemistry*, 87(15):2754–2763, 1983.

[57] Diego Garay-Ruiz, Moises Álvarez Moreno, Carles Bo, and Emilio Martínez-Núñez. New tools for taming complex reaction networks: The unimolecular decomposition of indole revisited. *ACS Physical Chemistry Au*, 2(3):225–236, 2022.

[58] Hans-Joachim Werner, Thomas B. Adler, and Frederick R. Manby. General orbital invariant mp2-f12 theory. *The Journal of Chemical Physics*, 126(16):164102, 2007.

[59] Gerald Knizia, Thomas B. Adler, and Hans-Joachim Werner. Simplified ccsd(t)-f12 methods: Theory and benchmarks. *The Journal of Chemical Physics*, 130(5):054104, 2009.

[60] Thomas B. Adler, Gerald Knizia, and Hans-Joachim Werner. A simple and efficient ccsd(t)-f12 approximation. *The Journal of Chemical Physics*, 127(22):221106, 2007.

[61] H.-J. Werner, P. J. Knowles, G. Knizia, F. R. Manby, M. Schütz, P. Celani, W. Györffy, D. Kats, T. Korona, R. Lindh, A. Mitrushenkov, G. Rauhut, K. R. Shamasundar, T. B. Adler, R. D. Amos, S. J. Bennie, A. Bernhardsson, A. Berning, D. L. Cooper, M. J. O. Deegan, A. J. Dobbyn, F. Eckert, E. Goll, C. Hampel, A. Hesselmann, G. Hetzer, T. Hrenar, G. Jansen, C. Köppl, S. J. R. Lee, Y. Liu, A. W. Lloyd, Q. Ma, R. A. Mata, A. J. May, S. J. McNicholas, W. Meyer, T. F. Miller III, M. E. Mura, A. Nicklass, D. P. O'Neill, P. Palmieri, D. Peng, K. Pflüger, R. Pitzer, M. Reiher, T. Shiozaki, H. Stoll, A. J. Stone, R. Tarroni, T. Thorsteinsson, M. Wang, and M. Welborn. Molpro, version , a package of ab initio programs.

[62] Hans-Joachim Werner, Peter J. Knowles, Frederick R. Manby, Joshua A. Black, Klaus Doll, Andreas Heßelmann, Daniel Kats, Andreas Köhn, Tatiana Korona, David A. Kreplin, Qianli Ma, Thomas F. Miller, Alexander Mitrushchenkov, Kirk A. Peterson, Iakov Polyak, Guntram Rauhut, and Marat Sibaev. The molpro quantum chemistry package. *The Journal of Chemical Physics*, 152(14):144107, 2020.

[63] Hans-Joachim Werner, Peter J. Knowles, Gerald Knizia, Frederick R. Manby, and Martin Schütz. Molpro: a general-purpose quantum chemistry program package. *WIREs Computational Molecular Science*, 2(2):242–253, 2012.

[64] P. Hohenberg and W. Kohn. Inhomogeneous electron gas. *Phys. Rev.*, 136:B864–B871, Nov 1964.

[65] W. Kohn and L. J. Sham. Self-consistent equations including exchange and correlation effects. *Phys. Rev.*, 140:A1133–A1138, Nov 1965.

[66] John P. Perdew and Karla Schmidt. Jacob's ladder of density functional approximations for the exchange-correlation energy. *AIP Conference Proceedings*, 577(1):1–20, 2001.

[67] Stefan Grimme, Jens Antony, Stephan Ehrlich, and Helge Krieg. A consistent and accurate ab initio parametrization of density functional dispersion correction (dft-d) for the 94 elements h-pu. *The Journal of Chemical Physics*, 132(15):154104, 2010.

[68] Daniel G. A. Smith, Lori A. Burns, Konrad Patkowski, and C. David Sherrill. Revised damping parameters for the d3 dispersion correction to density functional theory. *The Journal of Physical Chemistry Letters*, 7(12):2197–2203, 2016. PMID: 27203625.

[69] Stefan Grimme, Stephan Ehrlich, and Lars Goerigk. Effect of the damping function in dispersion corrected density functional theory. *Journal of Computational Chemistry*, 32(7):1456–1465, 2011.

[70] Bruce W Morrissey. Microscopic reversibility and detailed balance. an overview. *Journal of Chemical Education*, 52(5):296, 1975.

[71] Bruce H Mahan. Microscopic reversibility and detailed balance. an analysis. *Journal of Chemical Education*, 52(5):299, 1975.

[72] James A. Miller, Raghu Sivaramakrishnan, Yujie Tao, C. Franklin Goldsmith, Michael P. Burke, Ahren W. Jasper, Nils Hansen, Nicole J. Labbe, Peter Glarborg, and Judit Zádor. Combustion chemistry in the twenty-first century: Developing theory-informed chemical kinetics models. *Progress in Energy and Combustion Science*, 83:100886, 2021.

[73] Stephen J. Klippenstein, Vijay S. Pande, and Donald G. Truhlar. Chemical kinetics and mechanisms of complex systems: A perspective on recent theoretical advances. *Journal of the American Chemical Society*, 136(2):528–546, 2014. PMID: 24283502.

[74] Eugenia Dzib and Gabriel Merino. The hindered rotor theory: A review. *WIREs Computational Molecular Science*, 12(3):e1583, 2022.

[75] Antonio Fernández-Ramos, James A. Miller, Stephen J. Klippenstein, and Donald G. Truhlar. Modeling the kinetics of bimolecular reactions. *Chemical Reviews*, 106(11):4518–4584, 2006. PMID: 17091928.

[76] Andriana Tsikritea, Jake A. Diprose, Timothy P. Softley, and Brianna R. Heazlewood. Capture theory models: An overview of their development, experimental verification, and applications to ion–molecule reactions. *The Journal of Chemical Physics*, 157(6):060901, 2022.

[77] Friedrich Hund. Zur deutung der molekelspektren. i. *Zeitschrift für Physik*, 40(10):742–764, 1927.

[78] Friedrich Hund. Zur deutung der molekelspektren. iii. bemerkungen über das schwingungs-und rotationsspektrum bei molekeln mit mehr als zwei kernen. *Zeitschrift für Physik*, 43:805–826, 1927.

[79] Eugen Merzbacher. The early history of quantum tunneling. *Physics Today*, 55(8):44–50, 2002.

[80] Edward U Condon. Tunneling—how it all started. *American Journal of Physics*, 46(4):319–323, 1978.

[81] George Gamow. The quantum theory of nuclear disintegration. *Nature*, 122(3082):805–806, 1928.

[82] Malcolm P Applebey and Geoffrey Ogden. 33. the electrolytic preparation of deuterium and the separation coefficient α. *Journal of the Chemical Society (Resumed)*, pages 163–168, 1936.

[83] RP Bell. The kinetics of proton transfer reactions. *Transactions of the Faraday Society*, 34:229–236, 1938.

[84] Carl Eckart. The penetration of a potential barrier by electrons. *Phys. Rev.*, 35:1303–1309, Jun 1930.

[85] Yuri Georgievskii, James A. Miller, Michael P. Burke, and Stephen J. Klippenstein. Reformulation and solution of the master equation for multiple-well chemical reactions. *The Journal of Physical Chemistry A*, 117(46):12146–12154, 2013. PMID: 24053787.

[86] David R. Glowacki, Chi-Hsiu Liang, Christopher Morley, Michael J. Pilling, and Struan H. Robertson. Mesmer: An open-source master equation solver for multi-energy well reactions. *The Journal of Physical Chemistry A*, 116(38):9545–9560, 2012. PMID: 22905697.

[87] David M. Golden, John R. Barker, and Lawrence L. Lohr. Master equation models for the pressure- and temperature-dependent reactions ho + no2 $\rightarrow$ hono2 and ho + no2 $\rightarrow$ hoono. *The Journal of Physical Chemistry A*, 107(50):11057–11071, 2003.

[88] John R. Barker. Energy transfer in master equation simulations: A new approach. *International Journal of Chemical Kinetics*, 41(12):748–763, 2009.

[89] Alan D. Isaacson, Donald G. Truhlar, Sachchida N. Rai, Rozeanne Steckler, Gene C. Hancock, Bruce C. Garrett, and Michael J. Redmon. Polyrate: A general computer program for variational transition state theory and semiclassical tunneling calculations of chemical reaction rates. *Computer Physics Communications*, 47(1):91–102, 1987.

[90] Surajit Nandi, Danilo Calderini, Julien Bloino, Sergio Rampino, and Vincenzo Barone. A modern-fortran program for chemical kinetics on top of anharmonic vibrational calculations. In Sanjay Misra, Osvaldo Gervasi, Beniamino Murgante, Elena Stankova, Vladimir Korkhov, Carmelo Torre, Ana Maria A.C. Rocha, David Taniar, Bernady O. Apduhan, and Eufemia Tarantino, editors, *Computational Science and Its Applications – ICCSA 2019*, pages 401–412, Cham, 2019. Springer International Publishing.

[91] William H. Miller, Nicholas C. Handy, and John E. Adams. Reaction path Hamiltonian for polyatomic molecules. *The Journal of Chemical Physics*, 72(1):99–112, 07 1980.

[92] David Ferro-Costas, Donald G. Truhlar, and Antonio Fernández-Ramos. Pilgrim: A thermal rate constant calculator and a chemical kinetics simulator. *Computer Physics Communications*, 256:107457, 2020.

[93] Thomas J Millar and David Arnold Williams. *Rate Coefficients in Astrochemistry: Proceedings of a Conference Held at Umis, Manchester, UK September 21–24, 1987*, volume 146. Springer Science & Business Media, 2012.

[94] Stephen J. Klippenstein, Yu-Chuan Yang, Victor Ryzhov, and Robert C. Dunbar. Theory and modeling of ion–molecule radiative association kinetics. *The Journal of Chemical Physics*, 104(12):4502–4516, 1996.

[95] Daniel T Gillespie. Exact stochastic simulation of coupled chemical reactions. *The journal of physical chemistry*, 81(25):2340–2361, 1977.

[96] Terry Beyer and DF Swinehart. Algorithm 448: number of multiply-restricted partitions. *Communications of the ACM*, 16(6):379, 1973.

[97] Stephen E Stein and BS Rabinovitch. Accurate evaluation of internal energy level sums and densities including anharmonic oscillators and hindered rotors. *The Journal of Chemical Physics*, 58(6):2438–2445, 1973.

[98] Thanh Lam Nguyen and John R. Barker. Sums and densities of fully coupled anharmonic vibrational states: A comparison of three practical methods. *The Journal of Physical Chemistry A*, 114(10):3718–3730, 2010. PMID: 20170143.

[99] James A. Miller and Stephen J. Klippenstein. Master equation methods in gas phase chemical kinetics. *The Journal of Physical Chemistry A*, 110(36):10528–10544, 2006. PMID: 16956234.

[100] Surajit Nandi, Danilo Calderini, Julien Bloino, Sergio Rampino, and Vincenzo Barone. A modern-fortran program for chemical kinetics on top of anharmonic vibrational calculations. *Lecture Notes in Computer Science*, 11624:401–412, 2019.

[101] Stuart C. Althorpe and David C. Clary. Quantum scattering calculations on chemical reactions. *Annual Review of Physical Chemistry*, 54(1):493–529, 2003.

[102] Sergio Rampino, Noelia Faginas Lago, Antonio Laganà, and Fermín Huarte-Larrañaga. An extension of the grid empowered molecular simulator to quantum reactive scattering. *Journal of Computational Chemistry*, 33(6):708–714, 2012.

[103] Sergio Rampino. Configuration-space sampling in potential energy surface fitting: A space-reduced bond-order grid approach. *The Journal of Physical Chemistry A*, 120(27):4683–4692, 2016.

[104] Sergio Rampino, Dimitris Skouteris, and Antonio Laganà. Microscopic branching processes: The O + O_2 reaction and its relaxed potential representations. *International Journal of Quantum Chemistry*, 110(2):358–367, 2010.

[105] Sergio Rampino, Dimitris Skouteris, and Antonio Laganà. The O + O_2 reaction: quantum detailed probabilities and thermal rate coefficients. *Theoretical Chemistry Accounts: Theory, Computation, & Modeling*, 123(3/4):249–256, 2009.

[106] Antonio Laganà, Noelia Faginas Lago, Sergio Rampino, Fermín Huarte Larrañaga, and Ernesto García. Thermal rate coefficients in collinear versus bent transition state reactions: the N + N_2 case study. *Physica Scripta*, 78(5):058116, 2008.

[107] M. H. Beck, A. Jäckle, G. A. Worth, and H.-D. Meyer. The multiconfiguration time-dependent Hartree (MCTDH) method: a highly efficient algorithm for propagating wavepackets. *Physics Reports*, 324(1):1–105, 2000.

[108] Ian R. Craig and David E. Manolopoulos. Chemical reaction rates from ring polymer molecular dynamics. *The Journal of Chemical Physics*, 122(8):084106, 2005.

[109] Sergio Rampino, Mariachiara Pastore, Ernesto Garcia, Leonardo Pacifici, and Antonio Laganà. On the temperature dependence of the rate coefficient of formation of C_2^+ from C + CH^+. *Monthly Notices of the Royal Astronomical Society*, 460(3):2368–2375, 2016.

[110] Leonardo Pacifici, Mariachiara Pastore, Ernesto Garcia, Antonio Laganà, and Sergio Rampino. A dynamics investigation of the C + $CH^+ \rightarrow C_2^+$ + H reaction on an *ab initio* bond-order like potential. *The Journal of Physical Chemistry A*, 120(27):5125–5135, 2016.

[111] Sergio Rampino and Yury V. Suleimanov. Thermal rate coefficients for the astrochemical process C + $CH^+ \rightarrow C2^+$ + H by ring polymer molecular dynamics. *The Journal of Physical Chemistry A*, 120(50):9887–9893, 2016.

[112] Oscar Knefler Rice and Herman C. Ramsperger. Theories of unimolecular gas reactions at low pressures. *Journal of the American Chemical Society*, 49(7):1617–1629, 1927.

[113] L. S. Kassel. Studies in homogeneous gas reactions. I. *The Journal of Physical Chemistry*, 32(2):225–242, 1927.

[114] R. A. Marcus. Unimolecular dissociations and free radical recombination reactions. *The Journal of Chemical Physics*, 20(3):359–364, 1952.

[115] Vincenzo Barone. The virtual multifrequency spectrometer: a new paradigm for spectroscopy. *WIREs Computational Molecular Science*, 6(2):86–110, 2016.

[116] Julien Bloino, Malgorzata Biczysko, and Vincenzo Barone. General perturbative approach for spectroscopy, thermodynamics, and kinetics: Methodological background and benchmark studies. *Journal of Chemical Theory and Computation*, 8(3):1015–1036, 2012.

[117] Julien Bloino and Vincenzo Barone. A second-order perturbation theory route to vibrational averages and transition properties of molecules: General formulation and application to infrared and vibrational circular dichroism spectroscopies. *J. Chem. Phys.*, 136(12):124108, 2012.

[118] Daniele Licari, Alberto Baiardi, Malgorzata Biczysko, Franco Egidi, Camille Latouche, and Vincenzo Barone. Implementation of a graphical user interface for the virtual multifrequency spectrometer: The VMS-Draw tool. *Journal of Computational Chemistry*, 36(5):321–334, 2015.

[119] F Syntax Rules. http://www.fortran.com/F/F_bnf.html. (Archived on 5 February 2020).

[120] Michael Metcalf and John Reid. *The F Programming Language*. Oxford University Press, Inc., New York, NY, USA, 1996.

[121] Elda Rossi, Stefano Evangelisti, Antonio Laganà, Antonio Monari, Sergio Rampino, Marco Verdicchio, Kim K. Baldridge, Gian Luigi Bendazzoli, Stefano Borini, Renzo Cimiraglia, Celestino Angeli, Peter Kallay, Hans P. Lüthi, Kenneth Ruud, José Sanchez-Marin, Anthony Scemama, Peter G. Szalay, and Attila Tajti. Code interoperability and standard data formats in quantum chemistry and quantum dynamics: The Q5/D5Cost data model. *Journal of Computational Chemistry*, 35(8):611–621, 2014.

[122] Sergio Rampino, Antonio Monari, Elda Rossi, Stefano Evangelisti, and Antonio Laganà. A priori modeling of chemical reactions on computational grid platforms: Workflows and data models. *Chemical Physics*, 398(0):192–198, 2012.

[123] FoX in Fortran Wiki. http://fortranwiki.org/fortran/show/FoX. (Archived on 5 February 2020).

[124] Nadezhda I. Butkovskaya, Nicolas Pouvesle, Alexander Kukui, Yujing Mu, and Georges Le Bras. Mechanism of the OH-initiated oxidation of hydroxyacetone over the temperature range 236-298 K. *The Journal of Physical Chemistry A*, 110(21):6833–6843, 2006.

[125] Jing Sun, Sui So, and Gabriel da Silva. The gas phase aldose-ketone isomerization mechanism: Direct interconversion of the model hydroxycarbonyls 2-hydroxypropanal and hydroxyacetone. *International Journal of Quantum Chemistry*, 117(20):e25434, 2017.

[126] Mark Brouard. *Reaction Dynamics*. Oxford Chemistry Primers. OUP Oxford, 1998.

[127] Nicholas J. B. Green. Chapter 1 - introduction. In Nicholas J.B. Green, editor, *Unimolecular Kinetics*, volume 39 of *Comprehensive Chemical Kinetics*, pages 1 – 53. Elsevier, 2003.

[128] Stephen Stein and B. S. Rabinovitch. Accurate evaluation of internal energy level sums and densities including anharmonic oscillators and hindered rotors. *The Journal of Chemical Physics*, 58(6):2438–2445, 1973.

[129] Terry Beyer and D. F. Swinehart. Algorithm 448: Number of multiply-restricted partitions. *Communications of the ACM*, 16(6):379, June 1973.

[130] William H. Miller. Tunneling corrections to unimolecular rate constants, with application to formaldehyde. *Journal of the American Chemical Society*, 101(23):6810–6814, 1979.

[131] D. M. Kooij. Über die Zersetzung des Gasförmigen phosphorwasserstoffs. *Zeitschrift für Physikalische Chemie, Abteilung B*, 12:155–161, 1893.

[132] K. Laidler. A glossary of terms used in chemical kinetics, including reaction dynamics (iupac recommendations 1996). *Pure and Applied Chemistry*, 68(1):149–192, 1996.

[133] Zahra Homayoon, Saulo A. Vázquez, Roberto Rodríguez-Fernández, and Emilio Martínez-Núñez. Ab initio and RRKM study of the HCN/HNC elimination channels from vinyl cyanide. *The Journal of Physical Chemistry A*, 115(6):979–985, 2011.

[134] Struan H. Robertson, Michael J. Pilling, Luminita C. Jitariu, and Ian H. Hillier. Master equation methods for multiple well systems: application to the 1-,2-pentyl system. *Physical Chemistry Chemical Physics*, 9:4085–4097, 2007.

[135] John R. Barker and Ralph E. Weston. Collisional energy transfer probability densities $p(e, j; e', j')$ for monatomics colliding with large molecules. *The Journal of Physical Chemistry A*, 114(39):10619–10633, 2010.

[136] Michael J. Wilhelm, Matthew Nikow, Laura Letendre, and Hai-Lung Dai. Photodissociation of vinyl cyanide at 193 nm: Nascent product distributions of the molecular elimination channels. *The Journal of Chemical Physics*, 130(4):044307, 2009.

[137] Agnes Derecskei-Kovacs and Simon W. North. The unimolecular dissociation of vinylcyanide: A theoretical investigation of a complex multichannel reaction. *The Journal of Chemical Physics*, 110(6):2862–2871, 1999.

[138] Andrea Salvadori, Marco Fusè, Giordano Mancini, Sergio Rampino, and Vincenzo Barone. Diving into chemical bonding: An immersive analysis of the electron charge rearrangement through virtual reality. *Journal of Computational Chemistry*, 39(31):2607–2617, 2018.

[139] Marta Martino, Andrea Salvadori, Federico Lazzari, Lorenzo Paoloni, Surajit Nandi, Giordano Mancini, Vincenzo Barone, and Sergio Rampino. Chemical promenades: Exploring potential-energy surfaces with immersive virtual reality. *Journal of Computational Chemistry*, 2020. DOI: 10.1002/JCC.26172.

[140] Yuval Shagam, Ayelet Klein, Wojciech Skomorowski, Renjie Yun, Vitali Averbukh, Christiane P. Koch, and Edvardas Narevicius. Molecular hydrogen interacts more strongly when rotationally excited at low temperatures leading to faster reactions. *Nature Chemistry*, 7:921–926, 2015.

[141] Valentina Zhelyazkova, Fernanda BV Martins, Josef A Agner, Hansjürg Schmutz, and Frédéric Merkt. Ion-molecule reactions below 1 k: Strong enhancement of the reaction rate of the ion-dipole reaction he++ ch 3 f. *Physical Review Letters*, 125(26):263401, 2020.

[142] Bernardo Ballotta, Surajit Nandi, Vincenzo Barone, and Sergio Rampino. Gas-phase formation and isomerization reactions of cyanoacetaldehyde, a prebiotic molecule of astrochemical interest. *ACS Earth and Space Chemistry*, 5(5):1071–1082, 2021.

[143] James P. Ferris, Robert A. Sanchez, and Leslie E. Orgel. Studies in prebiotic synthesis: III. Synthesis of pyrimidines from cyanoacetylene and cyanate. *J. Mol. Biol.*, 33(3):693–704, 1968.

[144] J. P. Ferris, O. S. Zamek, A. M. Altbuch, and H. Freiman. Chemical evolution: Xviii. synthesis of pyrimidines from guanidine and cyanoacetaldehyde. *J. Mol. Evol.*, 3(4):301–309, 1974.

[145] Kevin E. Nelson, Michael P. Robertson, Matthew Levy, and Stanley L Miller. Concentration by evaporation and the prebiotic synthesis of cytosine. *Origins of Life and Evolution of the Biosphere*, 31(3):221–229, 2001.

[146] Michael P. Robertson and Stanley L. Miller. An efficient prebiotic synthesis of cytosine and uracil. *Nature*, 375(6534):772–774, 1995.

[147] Tianfang Wang and John H. Bowie. Can cytosine, thymine and uracil be formed in interstellar regions? a theoretical study. *Org. Biomol. Chem.*, 10:652–662, 2012.

[148] Sarabjeet Kaur and Purshotam Sharma. Cyanoacetaldehyde as a building block for prebiotic formation of pyrimidines. *Int. J. Quantum. Chem.*, 119(22):e25886, 2019.

[149] Joong Chul Choe. Formation of cytosine and uracil from cyanoacetylaldehyde and guanidine: A computational study. *Bull. Korean Chem. Soc.*, 41(3):382–384, 2020.

[150] Abdessamad Benidar, Robert Georges, Jean-Claude Guillemin, Otilia Mó, and Manuel Yáñez. Infrared spectra of cyanoacetaldehyde ($NCCH_2CHO$): A potential prebiotic compound of astrochemical interest. *ChemPhysChem*, 14(12):2764–2771, 2013.

[151] Harald Møllendal, Laurent Margulès, Roman A. Motiyenko, Niels Wessel Larsen, and Jean-Claude Guillemin. Rotational spectrum and conformational composition of cyanoacetaldehyde, a compound of potential prebiotic and astrochemical interest. *J. Phys. Chem. A*, 116(16):4047–4056, 2012.

[152] Anne Horn, Harald Møllendal, and Jean-Claude Guillemin. A quantum chemical study of the generation of a potential prebiotic compound, cyanoacetaldehyde,

and related sulfur containing species. *J. Phys. Chem. A*, 112(43):11009–11016, 2008.

[153] Surajit Nandi, Bernardo Ballotta, Sergio Rampino, and Vincenzo Barone. A general user-friendly tool for kinetic calculations of multi-step reactions within the virtual multifrequency spectrometer project. *Applied Sciences*, 10(5):1872, 2020.

[154] Jacopo Lupi, Cristina Puzzarini, Carlo Cavallotti, and Vincenzo Barone. State-of-the-art quantum chemistry meets variable reaction coordinate transition state theory to solve the puzzling case of the H_2s + cl system. *J. Chem. Theory. Comput.*, 16(8):5090–5104, 2020.

[155] Vincenzo Barone, Giorgia Ceselin, Marco Fusè, and Nicola Tasinato. Accuracy meets interpretability for computational spectroscopy by means of hybrid and double-hybrid functionals. *Front. Chem.*, 8:859, 2020.

[156] Fan Xie, Marco Fusè, Arsh S Hazrah, Wolfgang Jaeger, Vincenzo Barone, and Yunjie Xu. Discovering the elusive global minimum in a ternary chiral cluster: rotational spectra of propylene oxide trimer. *Angew. Chem., Int. Ed.*, 59(50):22427–22430, 2020.

[157] Stefan Grimme. Semiempirical hybrid density functional with perturbative second-order correlation. *J. Chem. Phys.*, 124(3):034108, 2006.

[158] Malgorzata Biczysko, Pawel Panek, Giovanni Scalmani, Julien Bloino, and Vincenzo Barone. Harmonic and anharmonic vibrational frequency calculations with the double-hybrid b2plyp method: Analytic second derivatives and benchmark studies. *J. Chem. Theory. Comput.*, 6(7):2115–2125, 2010.

[159] Stefan Grimme, Jens Antony, Stephan Ehrlich, and Helge Krieg. A consistent and accurate ab initio parametrization of density functional dispersion correction (dft-d) for the 94 elements h-pu. *J. Chem. Phys.*, 132(15):154104, 2010.

[160] Ewa Papajak, Jingjing Zheng, Xuefei Xu, Hannah R. Leverentz, and Donald G. Truhlar. Perspectives on basis sets beautiful: Seasonal plantings of diffuse basis functions. *J. Chem. Theory. Comput.*, 7(10):3027–3034, 2011.

[161] Kenichi Fukui. The path of chemical reactions - the irc approach. *Acc. Chem. Res.*, 14(12):363–368, 1981.

[162] Sebastian Kozuch and Jan M. L. Martin. DSD-PBEP86: in search of the best double-hybrid DFT with spin-component scaled MP2 and dispersion corrections. *Phys. Chem. Chem. Phys.*, 13:20104–20107, 2011.

[163] Chr. Moller and M. S. Plesset. Note on an approximation treatment for many-electron systems. *Phys. Rev.*, 46:618–622, Oct 1934.

[164] George D. Purvis and Rodney J. Bartlett. A full coupled-cluster singles and doubles model: The inclusion of disconnected triples. *J. Chem. Phys.*, 76(4):1910–1918, 1982.

[165] Cristina Puzzarini, Malgorzata Biczysko, Vincenzo Barone, Laura Largo, Isabel Peña, Carlos Cabezas, and José Luis Alonso. Accurate characterization of the peptide linkage in the gas phase: A joint quantum-chemical and rotational spectroscopy study of the glycine dipeptide analogue. *J. Phys. Chem. Letters*, 5(3):534–540, 2014.

[166] Cristina Puzzarini and Malgorzata Biczysko. Microsolvation of 2-thiouracil: Molecular structure and spectroscopic parameters of the thiouracil–water complex. *J. Phys. Chem. A*, 119(21):5386–5395, 2015.

[167] Lorenzo Spada, Nicola Tasinato, Giulio Bosi, Fanny Vazart, Vincenzo Barone, and Cristina Puzzarini. On the competition between weak oh$\cdots$f and ch$\cdots$f hydrogen bonds, in cooperation with ch$\cdots$o contacts, in the difluoromethane – tert-butyl alcohol cluster. *J. Mol. Spectrosc.*, 337:90–95, 2017.

[168] Silvia Alessandrini, Vincenzo Barone, and Cristina Puzzarini. Extension of the "cheap" composite approach to noncovalent interactions: The jun-chs scheme. *J. Chem. Theory. Comput.*, 16(2):988–1006, 2020.

[169] Zoi Salta, Nicola Tasinato, Jacopo Lupi, Rahma Boussessi, Alice Balbi, Cristina Puzzarini, and Vincenzo Barone. Exploring the maze of $c_2n_2h_5$ radicals and their fragments in the interstellar medium with the help of quantum-chemical computations. *ACS Earth Space Chem.*, 4(5):774–782, 2020.

[170] Thom H. Dunning. Gaussian basis sets for use in correlated molecular calculations. i. the atoms boron through neon and hydrogen. *J. Chem. Phys.*, 90(2):1007–1023, 1989.

[171] David E. Woon and Thom H. Dunning. Gaussian basis sets for use in correlated molecular calculations. v. core-valence basis sets for boron through neon. *J. Chem. Phys.*, 103(11):4572–4585, 1995.

[172] M. J. Frisch, G. W. Trucks, H. B. Schlegel, G. E. Scuseria, M. A. Robb, J. R. Cheeseman, G. Scalmani, V. Barone, G. A. Petersson, H. Nakatsuji, X. Li, M. Caricato, A. V. Marenich, J. Bloino, B. G. Janesko, R. Gomperts, B. Mennucci, H. P. Hratchian, J. V. Ortiz, A. F. Izmaylov, J. L. Sonnenberg, D. Williams-Young, F. Ding, F. Lipparini, F. Egidi, J. Goings, B. Peng, A. Petrone, T. Henderson, D. Ranasinghe, V. G. Zakrzewski, J. Gao, N. Rega, G. Zheng, W. Liang, M. Hada, M. Ehara, K. Toyota, R. Fukuda, J. Hasegawa, M. Ishida, T. Nakajima, Y. Honda, O. Kitao, H. Nakai, T. Vreven, K. Throssell, J. A. Montgomery, Jr., J. E. Peralta, F. Ogliaro, M. J. Bearpark, J. J. Heyd, E. N. Brothers, K. N. Kudin, V. N. Staroverov, T. A. Keith, R. Kobayashi, J. Normand, K. Raghavachari, A. P. Rendell, J. C. Burant, S. S. Iyengar, J. Tomasi, M. Cossi, J. M. Millam, M. Klene, C. Adamo, R. Cammi, J. W. Ochterski, R. L. Martin,

K. Morokuma, O. Farkas, J. B. Foresman, and D. J. Fox. Gaussian 09 Revision A.02, 2016. Gaussian Inc. Wallingford CT.

[173] J. F. Stanton, J. Gauss, L. Cheng, M. E. Harding, D. A. Matthews, and P. G. Szalay. CFOUR, Coupled-Cluster techniques for Computational Chemistry, a quantum-chemical program package.

[174] Devin A. Matthews, Lan Cheng, Michael E. Harding, Filippo Lipparini, Stella Stopkowicz, Thomas-C. Jagau, Péter G. Szalay, Jürgen Gauss, and John F. Stanton. Coupled-cluster techniques for computational chemistry: The cfour program package. *J. Chem. Phys.*, 152(21):214108, 2020.

[175] Markus Behnke, Ivan Medvedev, Manfred Winnewisser, Frank C. De Lucia, and Eric Herbst. The millimeter- and submillimeter-wave spectrum of oxiranecarbonitrile. *Astrophys. J. Suppl. Ser.*, 152(1):97–101, may 2004.

[176] David R Bates and Eric Herbst. Radiative association. In *Rate Coefficients in Astrochemistry: Proceedings of a Conference held at Umis, Manchester, UK September 21–24, 1987*, pages 17–40. Springer, 1988.

[177] Stephen J. Klippenstein, Yu-Chuan Yang, Victor Ryzhov, and Robert C. Dunbar. Theory and modeling of ion-molecule radiative association kinetics. *J. Chem. Phys.*, 104(12):4502–4516, 1996.

[178] Eric Herbst and Robert C. Dunbar. A global view of radiative association as a function of product size: interstellar implications. *Mon. Not. R. Astron. Soc.*, 253(2):341–349, 11 1991.

[179] V Vuitton, R V Yelle, P Lavvas, and S J Klippenstein. Rapid association reactions at low pressure: Impact on the formation of hydrocarbons on titan. *Astrophys. J.*, 744:11, 2012.

[180] Fanny Vazart, Camille Latouche, Dimitrios Skouteris, Nadia Balucani, and Vincenzo Barone. Cyanomethanimine isomers in cold interstellar clouds: Insights from electronic structure and kinetic calculations. *Astrophys. J.*, 810(2):111, 2015.

[181] Christopher N. Shingledecker, Germán Molpeceres, Víctor M. Rivilla, Liton Majumdar, and Johannes Kästner. Isomers in interstellar environments. i. the case of z- and e-cyanomethanimine. *Astrophys. J.*, 897(2):158, jul 2020.

[182] Bernardo Ballotta, Tainah D. Marforio, Sergio Rampino, Emilio Martínez-Núñez, Vincenzo Barone, Mattia Melosso, Andrea Bottoni, and Luca Dore. Toward the detection of cyanoketene in the interstellar medium: New hints from quantum chemistry and rotational spectroscopy. *ACS Earth Space Chem.*, page doi:10.1021/acsearthspacechem.3c00060, 2023.

[183] L. Margulès, B. A. McGuire, R. A. Motiyenko, C. Brogan, T. Hunter, A. Remijan, and J. C. Guillemin. Millimeter wave spectroscopy of cyanoketene

(NC−CH=C=O) and an observational search in the ism. *Astron. Astrophys.*, 638:A3, 2020.

[184] B. E. Turner. Microwave Detection of Interstellar Ketene. *Astrophys. J. Lett.*, 213:L75–L79, April 1977.

[185] Anthony J Remijan, JM Hollis, FJ Lovas, Wilmer D Stork, PR Jewell, and DS Meier. Detection of interstellar cyanoformaldehyde (cncho). *Astrophys. J. Lett.*, 675(2):L85, 2008.

[186] A Belloche, KM Menten, CHSP Comito, HSP Müller, P Schilke, J Ott, S Thorwirth, and C Hieret. Detection of amino acetonitrile in sgr b2 (n). *Astron. Astrophys.*, 492(3):769–773, 2008.

[187] M Melosso, A Belloche, M-A Martin-Drumel, O Pirali, F Tamassia, L Bizzocchi, RT Garrod, HSP Müller, KM Menten, L Dore, and C Puzzarini. Far-infrared laboratory spectroscopy of aminoacetonitrile and first interstellar detection of its vibrationally excited transitions. *Astron. Astrophys.*, 641:A160, 2020.

[188] Brett A McGuire, Andrew M Burkhardt, Sergei Kalenskii, Christopher N Shingledecker, Anthony J Remijan, Eric Herbst, and Michael C McCarthy. Detection of the aromatic molecule benzonitrile (c-C_6H_5CN) in the interstellar medium. *Science*, 359(6372):202–205, 2018.

[189] Gisbert Winnewisser and CM Walmsley. The detection of HC_5N and HC_7N in irc+ 10216. *Astron. Astrophys.*, 70:L37–L39, 1978.

[190] Luca Bizzocchi, Filippo Tamassia, Jacob Laas, Barbara M Giuliano, Claudio Degli Esposti, Luca Dore, Mattia Melosso, Elisabetta Canè, Andrea Pietropolli Charmet, Holger SP Müller, H Spahn, A Belloche, P Caselli, Karl M Menten, and Robin T Garrod. Rotational and high-resolution infrared spectrum of HC_3N: Global ro-vibrational analysis and improved line catalog for astrophysical observations. *Astrophys. J. Suppl. Ser.*, 233, 2017.

[191] V M Rivilla, L Colzi, F Fontani, M Melosso, P Caselli, L Bizzocchi, F Tamassia, and L Dore. DC_3N Observations towards High-Mass Star-Gorming Regions. *Mon. Not. R. Astron. Soc.*, 06 2020. staa1616.

[192] Ryan A Loomis, Andrew M Burkhardt, Christopher N Shingledecker, Steven B Charnley, Martin A Cordiner, Eric Herbst, Sergei Kalenskii, Kin Long Kelvin Lee, Eric R Willis, Ci Xue, Anthony J Remijan, Michael C McCarthy, and Brett A McGuire. An investigation of spectral line stacking techniques and application to the detection of $hc_{11}n$. *arXiv preprint arXiv:2009.11900*, 2020.

[193] Fanny Vazart, Camille Latouche, Dimitrios Skouteris, Nadia Balucani, and Vincenzo Barone. Cyanomethanimine isomers in cold interstellar clouds: Insights from electronic structure and kinetic calculations. *Astrophys. J.*, 810(2):111, 2015.

[194] Francesca Tonolo, Jacopo Lupi, Cristina Puzzarini, and Vincenzo Barone. The quest for a plausible formation route of formyl cyanide in the interstellar medium: a state-of-the-art quantum-chemical and kinetic approach. *Astrophys. J.*, 900(1):85, 2020.

[195] Weichao Zhang and Benni Du. Ab initio quantum chemical studies of reaction mechanism for cn with ch2co. *International Journal of Quantum Chemistry*, 106(5):1076–1085, 2006.

[196] Hao Sun, Hong-Qing He, Bo Hong, Ying-Fei Chang, Zhe An, and Rong-Shun Wang. Theoretical study of the mechanism of ch2co + cn reaction. *International Journal of Quantum Chemistry*, 106(4):894–905, 2006.

[197] Michael A. Edwards and John F. Hershberger. Kinetics of the cn+ch2co and nco+ch2co reactions. *Chemical Physics*, 234(1):231–237, 1998.

[198] H. B. Xie, G. S. Shi, and Y. H. Ding. Chemical behavior of polycyanoacetylene radicals on gaseous and ice water: A computational perspective. *The Astrophysical Journal*, 662(1):758, jun 2007.

[199] H. B. Xie, Y. H. Ding, and C. C. Sun. Reaction mechanism of oxygen atoms with cyanoacetylene in the gas phase and on water ice. *Astrophys. J.*, 643(1):573–581, may 2006.

[200] H. B. Xie, J. Wang, S. W. Zhang, Y. H. Ding, and C. C. Sun. An ignored but most favorable channel for nco+c2h2 reaction. *The Journal of Chemical Physics*, 125(12):124317, 2006.

[201] M Guélin and J Cernicharo. Astronomical detection of the hccn radical-toward a new family of carbon-chain molecules? *Astronomy and Astrophysics*, 244:L21–L24, 1991.

[202] LE Snyder, JM Hollis, and BL Ulich. Radio detection of the interstellar formyl radical. *The Astrophysical Journal*, 208:L91–L94, 1976.

[203] Rolf Güsten, Helmut Wiesemeyer, David Neufeld, Karl M Menten, Urs U Graf, Karl Jacobs, Bernd Klein, Oliver Ricken, Christophe Risacher, and Jürgen Stutzki. Astrophysical detection of the helium hydride ion HeH^+. *Nature*, 568(7752):357–359, 2019.

[204] M Melosso, L Bizzocchi, O Sipilä, BM Giuliano, L Dore, F Tamassia, M-A Martin-Drumel, O Pirali, E Redaelli, and P Caselli. First detection of NHD and ND_2 in the interstellar medium - amidogen deuteration in iras 16293–2422. *Astron. Astrophys.*, 641:A153, 2020.

[205] A Bacmann, A Faure, P Hily-Blant, K Kobayashi, H Ozeki, S Yamamoto, L Pagani, and F Lique. Deuterium fractionation of nitrogen hydrides: Detections of NHD and ND_2. *Mon. Not. R. Astron. Soc.*, 499(2):1795–1804, 2020.

[206] Brett A McGuire, Crystal L Brogan, Todd R Hunter, Anthony J Remijan, Geoffrey A Blake, Andrew M Burkhardt, P Brandon Carroll, Ewine F van Dishoeck, Robin T Garrod, Harold Linnartz, Christopher N Shingledecker, and Eric R Willis. First results of an alma band 10 spectral line survey of ngc 6334i: Detections of glycolaldehyde ($HC(O)CH_2OH$) and a new compact bipolar outflow in HDO and CS. *Astrophys. J. Lett.*, 863(2):L35, 2018.

[207] Mattia Melosso, Luca Dore, Filippo Tamassia, Crystal L Brogan, Todd R Hunter, and Brett A McGuire. The sub-millimeter rotational spectrum of ethylene glycol up to 890 GHz and application to ALMA Band 10 spectral line data of NGC 6334I. *J. Phys. Chem. A*, 124:240–246, 2020.

[208] Malgorzata Biczysko, Pawel Panek, Giovanni Scalmani, Julien Bloino, and Vincenzo Barone. Harmonic and anharmonic vibrational frequency calculations with the double-hybrid b2plyp method: Analytic second derivatives and benchmark studies. *J. Chem. Theory Comput.*, 6:2115–2125, 2010.

[209] K. Raghavachari, G. W. Trucks, J. A. Pople, and M. Head-Gordon. A fifth-order perturbation comparison of electron correlation theories. *Chem. Phys. Lett.*, 157:479 – 483, 1989.

[210] C. Puzzarini and V. Barone. Extending the molecular size in accurate quantum-chemical calculations: The equilibrium structure and spectroscopic properties of uracil. *Phys. Chem. Chem. Phys.*, 13:7189–7197, 2011.

[211] Ewa Papajak, Jingjing Zheng, Xuefei Xu, Hannah R. Leverentz, and Donald G. Truhlar. Perspectives on basis sets beautiful: Seasonal plantings of diffuse basis functions. *J. Chem. Theory Comput.*, 7:3027–3034, 2011.

[212] Kirk A. Peterson and Thom H. Dunning. Accurate correlation consistent basis sets for molecular core-valence correlation effects: The second row atoms al-ar, and the first row atoms b-ne revisited. *J. Chem. Phys.*, 117:10548–10560, 2002.

[213] Chr. Møller and M. S. Plesset. Note on an approximation treatment for many-electron systems. *Phys. Rev.*, 46:618–622, 1934.

[214] Trygve Helgaker, Wim Klopper, Henrik Koch, and Jozef Noga. Basis-set convergence of correlated calculations on water. *J. Chem. Phys.*, 106(23):9639–9646, 1997.

[215] J. Grant Hill, Shivnath Mazumder, and Kirk A. Peterson. Correlation consistent basis sets for molecular core-valence effects with explicitly correlated wave functions: The atoms b–ne and al–ar. *The J. Chem. Phys.*, 132:054108, 2010.

[216] V. Barone, , M. Fusè, R. Aguado, S. Potenti, I. Leon, E. R. Alonso, S. Mata, F. Lazzari, G. Mancini, L. Spada, A. Gualandi, P. G. Cozzi, C. Puzzarini, J. l. Alonso, and V. Barone. Bringing machine-learning enhanced quantum chemistry and microwave spectroscopy to conformational landscape exploration: the

paradigmatic case of 4-fluoro-threonine. *Chemistry, Europ. J.*, page e202203990, 2022.

[217] V. Barone, S. Di Grande, and C. Puzzarini. Toward accurate yet effective computations of rotational spectroscopy parameters for biomolecule building blocks. *Molecules*, 28:913, 2023.

[218] Julien Bloino, Malgorzata Biczysko, and Vincenzo Barone. General perturbative approach for spectroscopy, thermodynamics, and kinetics: Methodological background and benchmark studies. *Journal of Chemical Theory and Computation*, 8(3):1015–1036, 2012. PMID: 26593363.

[219] D. C. Tardy and B. S. Rabinovitch. Collisional energy transfer. thermal unimolecular systems in the low-pressure region. *The Journal of Chemical Physics*, 45(10):3720–3730, 1966.

[220] Jacopo Lupi, Cristina Puzzarini, Carlo Cavallotti, and Vincenzo Barone. State-of-the-art quantum chemistry meets variable reaction coordinate transition state theory to solve the puzzling case of the h2s + cl system. *J. Chem. Theory Comput.*, 16(8):5090–5104, 2020.

[221] D. M. Kooij. Über die zersetzung des gasförmigen phosphorwasserstoffs. *Zeitschrift für Physikalische Chemie*, 12U:155–161, 1893.

[222] K. J. Laidler. A glossary of terms used in chemical kinetics, including reaction dynamics (iupac recommendations 1996). *Pure and Applied Chemistry*, 68:149–192, 1996.

[223] Nadia Balucani, Dimitrios Skouteris, Cecilia Ceccarelli, Claudio Codella, Stefano Falcinelli, and Marzio Rosi. A theoretical investigation of the reaction between the amidogen, nh, and the ethyl, c2h5, radicals: a possible gas-phase formation route of interstellar and planetary ethanimine. *Molecular Astrophysics*, 13:30–37, 2018.

[224] Carmen Baiano, Jacopo Lupi, Nicola Tasinato, Cristina Puzzarini, and Vincenzo Barone. The role of state-of-the-art quantum-chemical calculations in astrochemistry: Formation route and spectroscopy of ethanimine as a paradigmatic case. *Molecules*, 25:2873, 2020.

[225] Mattia Melosso, Beatrice Conversazioni, Claudio Degli Esposti, Luca Dore, Elisabetta Cané, Filippo Tamassia, and Luca Bizzocchi. The pure rotational spectrum of $^{15}ND_2$ observed by millimetre and submillimetre-wave spectroscopy. *J. Quant. Spectrosc. Ra.*, 222:186–189, 2019.

[226] Mattia Melosso, Luca Bizzocchi, Filippo Tamassia, Claudio Degli Esposti, Elisabetta Canè, and Luca Dore. The rotational spectrum of ^{15}ND. isotopic-independent Dunham-Type analysis of the imidogen radical. *Phys. Chem. Chem. Phys.*, 21:3564–3573, 2019.

[227] DWJ Moloney, MW Wong, R Flammang, and C Wentrup. Cyanoketene and iminopropadienones. *J. Org. Chem.*, 62(13):4240–4247, 1997.

[228] C Wentrup. Flash vacuum pyrolysis: Techniques and reactions. *Angew. Chem. Int. Edit.*, 56(47):14808–14835, 2017.

[229] Luca Dore, Luca Bizzocchi, Claudio Degli Esposti, and Jürgen Gauss. The magnetic hyperfine structure in the rotational spectrum of H_2CNH. *J. Mol. Spectrosc.*, 263(1):44–50, 2010.

[230] Mattia Melosso, Brett A McGuire, Filippo Tamassia, Claudio Degli Esposti, and Luca Dore. Astronomical search of vinyl alcohol assisted by submillimeter spectroscopy. *ACS Earth Space Chem.*, 3(7):1189–1195, 2019.

[231] Claudio Degli Esposti, Mattia Melosso, Luca Bizzocchi, Filippo Tamassia, and Luca Dore. Determination of a semi-experimental equilibrium structure of 1-phosphapropyne from millimeter-wave spectroscopy of CH_3CP and CD_3CP. *J. Mol. Struct.*, 1203:127429, 2020.

[232] Alessio Melli, Simone Potenti, Mattia Melosso, , Sven Herbers, Lorenzo Spada, Andrea Gualandi, Kevin G Lengsfeld, Luca Dore, Philipp Buschmann, Pier Giorgio Cozzi, Jens-Uwe Grabow, Vincenzo Barone, and Cristina Puzzarini. A journey from thermally-tunable synthesis to spectroscopy of phenylmethanimine in gas-phase and solution. *Chem. Eur. J.*, 26:1–8, 2020.

[233] M Hahn, H-K Bodenseh, and M Ferner. Cyanoketene: the microwave spectrum and structure of an unstable molecule. *J. Mol. Spectrosc.*, 223(2):138–147, 2004.

[234] Walter Gordy and Robert L. Cook. *Microwave Molecular Spectra.* Wiley, 3rd edition edition, 1984.

[235] Herbert M Pickett. The fitting and prediction of vibration-rotation spectra with spin interactions. *J. Mol. Spectrosc.*, 148(2):371–377, 1991.

[236] Jes K. Jørgensen, Arnaud Belloche, and Robin T. Garrod. Astrochemistry during the formation of stars. *Annual Review of Astronomy and Astrophysics*, 58(1):727–778, 2020.

[237] A Coletta, F Fontani, VM Rivilla, C Mininni, L Colzi, Á Sánchez-Monge, and MT Beltrán. Evolutionary study of complex organic molecules in high-mass star-forming regions. *Astron. Astrophys.*, 641:A54, 2020.

[238] Terrill A. Cool, Koichi Nakajima, Toufik A. Mostefaoui, Fei Qi, Andrew McIlroy, Phillip R. Westmoreland, Matthew E. Law, Lionel Poisson, Darcy S. Peterka, and Musahid Ahmed. Selective detection of isomers with photoionization mass spectrometry for studies of hydrocarbon flame chemistry. *J. Chem. Phys.*, 119(16):8356–8365, 2003.

[239] Alex T. Archibald, Max R. McGillen, Craig A. Taatjes, Carl J. Percival, and Dudley E. Shallcross. Atmospheric transformation of enols: A potential secondary source of carboxylic acids in the urban troposphere. *Geophys. Res. Lett.*, 34(21), 2007.

[240] Matthew J. Abplanalp, Samer Gozem, Anna I. Krylov, Christopher N. Shingledecker, Eric Herbst, and Ralf I. Kaiser. A study of interstellar aldehydes and enols as tracers of a cosmic ray-driven nonequilibrium synthesis of complex organic molecules. *Proc. Nat. Acad. Sci.*, 113(28):7727–7732, 2016.

[241] J Clayden, N Greeves, , and S. Warren. *Organic Chemistry*. Oxford University Press, 2nd edition edition, 2012.

[242] B Heazlewood, A Maccarone, and D. Andrews. Near-threshold h/d exchange in cd3cho photodissociation. *Nature Chem.*, 3(6):443–448, 2011.

[243] Duncan U. Andrews, Brianna R. Heazlewood, Alan T. Maccarone, Trent Conroy, Richard J. Payne, Meredith J. T. Jordan, and Scott H. Kable. Phototautomerization of acetaldehyde to vinyl alcohol: A potential route to tropospheric acids. *Science*, 337(6099):1203–1206, 2012.

[244] Xiaoyang Lei, Weina Wang, Jiemiao Gao, Sainan Wang, and Wenliang Wang. Atmospheric chemistry of enols: The formation mechanisms of formic and peroxyformic acids in ozonolysis of vinyl alcohol. *J. Phys. Chem. A*, 124(21):4271–4279, 2020.

[245] Sui So, Uta Wille, and Gabriel da Silva. Atmospheric chemistry of enols: A theoretical study of the vinyl alcohol + oh + o2 reaction mechanism. *Envir. Sci. Technol.*, 48(12):6694–6701, 2014.

[246] Gabriel da Silva, Chol-Han Kim, and Joseph W. Bozzelli. Thermodynamic properties (enthalpy, bond energy, entropy, and heat capacity) and internal rotor potentials of vinyl alcohol, methyl vinyl ether, and their corresponding radicals. *J. Phys. Chem. A*, 110(25):7925–7934, 2006.

[247] B. E. Turner and A. J. Apponi. Microwave detection of interstellar vinyl alcohol, ch2=choh. *Astrophys. J.*, 561(2):L207, oct 2001.

[248] Izaskun Jiménez-Serra, Lucas F. Rodríguez-Almeida, Jesús Martín-Pintado, Víctor M. Rivilla, Mattia Melosso, Shaoshan Zeng, Laura Colzi, Yoshiyuki Kawashima, Eizi Hirota, Cristina Puzzarini, Belén Tercero, Pablo de Vicente, Fernando Rico-Villas, Miguel A. Requena-Torres, and Sergio Martín. Precursors of fatty alcohols in the ism: Discovery of n-propanol. *Astron. Astrophys.*, 663(A181):15, 2022.

[249] N. Fabian Kleimeier and Ralf I. Kaiser. Interstellar enolization-acetaldehyde (ch3cho) and vinyl alcohol (h2cch(oh)) as a case study. *Chem. Phys. Chem*, 22(12):1229–1236, 2021.

[250] Jozef Peeters, Vinh Son Nguyen, and Jean-François Müller. Atmospheric vinyl alcohol to acetaldehyde tautomerization revisited. *J. Phys. Chem. Lett.*, 6(20):4005–4011, 2015.

[251] Alan H. Barrett. Radio observations of interstellar hydroxyl radicals. *Science*, 157(3791):881–889, 1967.

[252] Sander Weinreb, Alan H. Barrett, M. Littleton Meeks, and John C. Henry. *97. Radio Observations of OH in the Interstellar Medium*, pages 666–670. Harvard University Press, Cambridge, MA and London, England, 1979.

[253] David Hollenbach and Christopher F McKee. Molecule formation and infrared emission in fast interstellar shocks. i physical processes. *Astrophys. J. Suppl. Ser.*, 41:555–592, 1979.

[254] David A Neufeld and A Dalgarno. Fast molecular shocks. i-reformation of molecules behind a dissociative shock. *Astrophys. J.*, 340:869–893, 1989.

[255] Ewine F Van Dishoeck, Eric Herbst, and David A Neufeld. Interstellar water chemistry: from laboratory to observations. *Chem. Rev.*, 113(12):9043–9085, 2013.

[256] Y Chang, Y Yu, and H Wang. Hydroxyl super rotors from vacuum ultraviolet photodissociation of water. *Nature Commun.*, 10(1250), 2019.

[257] V. M. Rivilla, l. Colzi, I. Jiménez-Serra, J. Martin-Pintadol, A. Megias, M. Melosso, L. Bizzocchi, A. López-Gallifa, A. Martínez-Henares, B. Massalkhi, S.and Tercero, P. de Vicente, J.-C. Guillemin, J. García de la Concepción, F. Rico-Villas, S. Zeng, s. Martin, M. a. Requena-Torres, F. Tonolo, S. Alessandrini, L. Dore, V. Barone, and C. Puzzarini. Precursors of the rna world in space: Detection of (z)-1,2-ethenediol in the interstellar medium, a key intermediate in sugar formation. *Astrophys. J. Lett.*, 929:L11, 2022.

[258] Giorgia Ceselin, Vincenzo Barone, and Nicola Tasinato. Accurate biomolecular structures by the nano-LEGO approach: Pick the bricks and build your geometry. *J. Chem. Theory Comput.*, 17:7290–7311, 2021.

[259] V. Barone, M. Fusè, F. Lazzari, and G. Mancini. Benchmark structures and conformational landscapes of amino acids in the gas phase: a joint venture of machine learning, quantum chemistry, and rotational spectroscopy. *J. Chem. Theory Comput.*, 19:DOI:10.1021/acs.jctc.2c01143, 2023.

[260] Vincenzo Barone, Giorgia Ceselin, Marco Fusè, and Nicola Tasinato. Accuracy meets interpretability for computational spectroscopy by means of hybrid and double-hybrid functionals. *Front. Chem.*, 8:584203, 2020.

[261] Trygve Helgaker, Wim Klopper, Henrik Koch, and Jozef Noga. Basis-set convergence of correlated calculations on water. *J. Chem. Phys.*, 106(23):9639–9646, 1997.

[262] Oksana Tishchenko, Sonia Ilieva, and Donald G. Truhlar. Communication: Energetics of reaction pathways for reactions of ethenol with the hydroxyl radical: The importance of internal hydrogen bonding at the transition state. *J. Chem. Phys.*, 133(2):021102, 2010.

[263] Xuan Guo, Rui Ming Zhang, Lu Gem Gao, Xin Zhang, and Xuefei Xu. Computational kinetics of the hydrogen abstraction reactions of n-propanol and isopropanol by oh radical. *Phys. Chem. Chem. Phys.*, 21:24458–24468, 2019.

[264] Jingjing Zheng, Gbenga A. Oyedepo, and Donald G. Truhlar. Kinetics of the hydrogen abstraction reaction from 2-butanol by oh radical. *The Journal of Physical Chemistry A*, 119(50):12182–12192, 2015.

[265] Lu Gem Gao, Jingjing Zheng, Antonio Fernández-Ramos, Donald G. Truhlar, and Xuefei Xu. Kinetics of the methanol reaction with oh at interstellar, atmospheric, and combustion temperatures. *J. Am. Chem. Soc.*, 140(8):2906–2918, 2018.

[266] Malgorzata Biczysko, Julien Bloino, and Cristina Puzzarini. Computational challenges in astrochemistry. *WIREs Computational Molecular Science*, 8(3):e1349, 2018.

[267] Scott A. Sandford, Michel Nuevo, Partha P. Bera, and Timothy J. Lee. Prebiotic astrochemistry and the formation of molecules of astrobiological interest in interstellar clouds and protostellar disks. *Chemical Reviews*, 120(11):4616–4659, 2020. PMID: 32227889.

[268] Eric Herbst and John T. Jr. Yates. Introduction: Astrochemistry. *Chemical Reviews*, 113(12):8707–8709, 2013.

[269] Eric Herbst. Unusual chemical processes in interstellar chemistry: Past and present. *Frontiers in Astronomy and Space Sciences*, 8, 2021.

[270] Vincenzo Barone and Cristina Puzzarini. Toward accurate formation routes of complex organic molecules in the interstellar medium: The paradigmatic cases of acrylonitrile and cyanomethanimine. *Frontiers in Astronomy and Space Sciences*, 8, 2022.

[271] Martin Rodler and A. Bauder. Structure of syn-vinyl alcohol determined by microwave spectroscopy. *Journal of the American Chemical Society*, 106(14):4025–4028, 1984.

[272] Hayley Bunn, Killian Hull, Isaac Miller, and Paul L. Raston. Far-infrared synchrotron spectroscopy of a potentially important interstellar isotopologue of vinyl alcohol: Ch2chod. *The Journal of Physical Chemistry A*, 124(4):704–710, 2020. PMID: 31922411.

[273] Mattia Melosso, Brett A. McGuire, Filippo Tamassia, Claudio Degli Esposti, and Luca Dore. Astronomical search of vinyl alcohol assisted by submillimeter spectroscopy. *ACS Earth and Space Chemistry*, 3(7):1189–1195, 2019.

[274] Vladimir A. Basiuk and Kensei Kobayashi. Formation of interstellar vinyl alcohol via simple radical processes: Theoretical study. *International Journal of Quantum Chemistry*, 97(2):713–718, 2004.

[275] Chris J. Bennett, Yoshihiro Osamura, Matt D. Lebar, and Ralf I. Kaiser. Laboratory studies on the formation of three c2h4o isomers—acetaldehyde (ch3cho), ethylene oxide (c-c2h4o), and vinyl alcohol (ch2choh)—in interstellar and cometary ices. *The Astrophysical Journal*, 634(1):698, nov 2005.

[276] Brett A. McGuire. 2021 census of interstellar, circumstellar, extragalactic, protoplanetary disk, and exoplanetary molecules. *The Astrophysical Journal Supplement Series*, 259(2):30, mar 2022.

[277] Silvia Alessandrini and Mattia Melosso. Fate of the gas-phase reaction between oxirane and the cn radical in interstellar conditions. *Frontiers in Astronomy and Space Sciences*, 8, 2021.

[278] V. Barone, J. Lupi, Z. Salta, and N. Tasinato. Development and validation of a parameter-free model chemistry for the computation of reliable reaction rates. *J. Chem. Theory Comput.*, 17:4913–4928, 2021.

[279] FF Gardner and G Winnewisser. The detection of interstellar vinyl cyanide/acrylonitrile. *The Astrophysical Journal*, 195:L127–L130, 1975.

[280] Valter H. Carvalho-Silva, Nayara D. Coutinho, and Vincenzo Aquilanti. Temperature dependence of rate processes beyond arrhenius and eyring: Activation and transitivity. *Frontiers in Chemistry*, 7, 2019.

[281] Ronald Percy Bell. *The tunnel effect in chemistry*. Springer, 2013.

[282] St G Christov. The characteristic (crossover) temperature in the theory of thermally activated tunneling processes. *Quantum Systems in Chemistry and Physics. Trends in Methods and Applications*, pages 109–147, 1997.

[283] Kazutaka Nakamura, Toshiyuki Takayanagi, and Shin Sato. A modified arrhenius equation. *Chemical Physics Letters*, 160(3):295–298, 1989.

[284] Shin Sato. Tunneling in bimolecular reactions. *Chemical Physics*, 315(1):65–75, 2005.

[285] Nadia Balucani, Francesca Leonori, Raffaele Petrucci, Xingan Wang, Piergiorgio Casavecchia, Dimitrios Skouteris, Alessandra F. Albernaz, and Ricardo Gargano. A combined crossed molecular beams and theoretical study of the reaction cn+c2h4. *Chemical Physics*, 449:34–42, 2015.

Appendices

Appendix A

Supporting Data for Chapter 3

	B2PLYP-D3	rDSD	Cheap		B2PLYP-D3	rDSD	Cheap
A+B	0	0	0	**TS2c**	151.4	132.1	135.0
1-CA	-290.3	-307.8	-301.9	**TS3c**	122.9	104.3	110.4
2-CA	-293.5	-310.7	-305.0	**TS1b**	-283.6	-300.9	-295.4
1-CVA	-279.5	-294.3	-289.5	**TS2b**	-48.9	-64.3	-54.2
2-CVA	-277.9	-292.6	-288.3	**TS3b**	-257.4	-272.4	-270.2
3-CVA	-259.8	-276.0	-273.3	**TS4b**	32.1	19.7	24.3
4-CVA	-262.0	-277.9	-275.5	**TS5b**	33.9	19.0	21.9
5-CVA	-289.0	-304.0	-299.2	**TS6b**	14.2	-1.4	1.4
6-CVA	-275.1	-289.9	-285.7	**TS7b**	-55.8	-72.0	-73.3
Prc-C+D	-180.7	-187.9	-189.7	**TS8b**	15.2	0.2	3.3
C+D	-164.0	-170.8	-174.5	**TS9b**	-248.2	-272.4	-270.0
Isoxazole	-198.0	-220.2	-212.3	**TS10b**	-73.6	-91.0	-92.0
AcC	-299.8	-316.5	-309.2	**TS11b**	6.0	-9.4	-6.2
Prc-E+F	-224.5	-230.8	-226.5	**TS12b**	24.8	8.4	15.2
E+F	-218.2	-223.8	-221.6	**TS13b**	24.2	9.2	5.8
Carb1	18.3	5.5	6.1	**TS14b**	15.6	0.6	-1.6
Carb2	-26.1	-37.1	-33.4	**TS6g**	42.4	26.6	33.7
IM1c	-183.8	-206.2	-198.1	**TS7g**	-22.2	-37.2	-25.4
IM1b	-58.6	-74.5	-75.9	**TS8g**	-248.2	-264.1	-262.7
IM2b	-84.7	-101.3	-102.0	**TS9g**	60.6	49.2	52.7
IM3b	-78.4	-95.5	-96.5	**TS10g**	200.7	190.0	190.1
IM4b	-84.7	-102.2	-102.5	**TS11g**	48.6	34.6	42.2
1-ICA	-193.5	-209.3	-206.4	**TS12g**	-165.4	-180.4	-182.0
2-ICA	-197.9	-213.6	-210.9	**TS13g**	144.2	150.5	151.2
1-ICVA	-172.5	-186.5	-185.3	**TS1a**	-30.9	-47.3	-44.4
2-ICVA	-171.7	-185.5	-185.0	**TS2a**	-39.9	-55.9	-52.4
3-ICVA	-176.0	-191.1	-191.5	**TS3a**	-181.2	-197.1	-195.0
4-ICVA	-178.5	-193.4	-194.2	**TS4a**	104.9	84.7	90.9
5-ICVA	-187.4	-201.6	-200.5	**TS5a**	4.3	-17.6	-12.8
6-ICVA	-173.1	-187.0	-186.3	**TS6a**	59.5	45.4	52.5
Prc-H+D	-64.0	-69.5	-75.7	**TS7a**	-156.7	-170.8	-171.9
H+D	-49.3	-54.5	-62.2	**TS8a**	-25.9	-39.2	-40.1
Oxazole	-291.9	-314.7	-309.1	**TS9a**	-24.1	-37.5	-38.5
IAcC	-242.5	-258.1	-253.9	**TS10a**	111.3	97.2	96.7
IM1a	-165.0	-187.1	-185.5	**TS11a**	132.1	118.6	118.3
IM2a	39.0	24.6	20.2	**TS12a**	181.6	170.4	169.9
IM3a	17.1	1.4	-2.4	**TS13a**	30.4	14.3	10.1
IM4a	8.6	-7.1	-9.8	**TS14a**	47.7	32.9	28.2
IM5a	3.0	-11.9	-14.9	**TS15a**	92.2	78.2	78.5
TS1d	40.3	42.8	27.2	**TS16a**	99.1	85.5	85.4
TS2d	10.7	-3.1	7.2	**TS17a**	-159.0	-173.1	-174.0
TS3d	144.3	132.9	133.1	**TS18a**	119.0	105.5	99.2
TS1c	17.7	13.1	-12.2	**TS19a**	108.6	95.4	91.1

Table A.1: Zero-point corrected energies (in kJ mol^{-1}) relative to the dissociation limit for the all species involved in the HCO + CH_2CN addition reaction computed using the 3 different levels of theory discussed in Sec. 3.2. The RMS deviation of B2PLYP-D3 and rDSD data from Cheap values is 14.0 and 5.3 kJ mol^{-1}, respectively.

Appendix B

Supporting Data for Chapter 4

Species	rDSD	junChS-F12
Rx1	0.0	0.0
MIN1	-190.4	-212.0
MIN2	-384.6	-370.3
MIN3	-381.9	-364.4
TS1	-102.6	-100.4
TS2	-143.6	-126.5
TS3	-50.2	-31.6
TS4	-193.7	-172.5
TS6	-338.7	-326.7
TS7	-189.1	-170.2
TS8	-194.2	-173.9
P1	-227.7	-201.1
P2	-382.5	-373.8
P3	-127.4	-114.1

Table B.1: Anharmonic Zero-Point corrected Energies (in kJ mol^{-1}) relative to the Asymptotic Limit for all the species involved in the reaction computed using the two different levels of theory discussed in Section 4.2. The RMS deviation of rDSD results from their junChS-F12 counterparts is 16.5 kJ mol^{-1}.

Scan of Barrierless Reaction

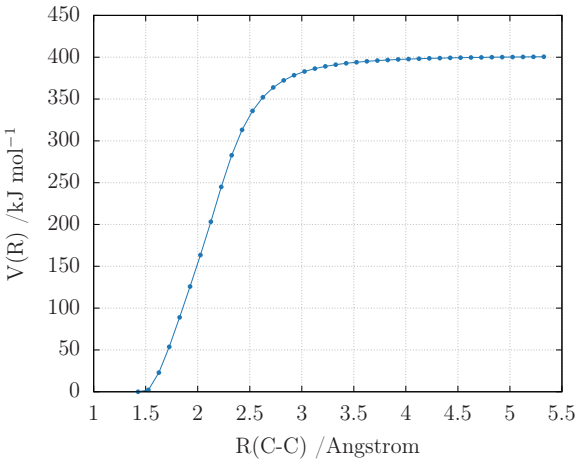

Figure B.1: One-dimensional potential energy profile as a function of C–C bond formation (Å) for the reaction of HCCN + HCO $\longrightarrow$ MIN2 computed at the rDSD level.

Appendix C

Supporting Data for Chapter 5

Addition reactions

***anti*-VyA + OH**			***syn*-VyA + OH**		
Species	**rDSD**	**junChS-F12**	**Species**	**rDSD**	**junChS-F12**
***anti*-Vy+OH**	0.0	0.0	***syn*-Vy+OH**	0.0	0.0
PrC	-11.0	-12.6	**PrC**	-13.9	-13.9
IM2	-124.6	-123.8	**IM1**	-117.9	-117.1
IM3	-113.5	-111.9	**IM2**	-132.1	-131.7
IM4	-77.3	-75.9	**IM3**	-72.7	-71.5
IM5	-120.0	-121.1	**IM4**	-115.4	-116.7
TS1	-3.2	-11.2	**TS1**	-2.5	-9.6
TS1GA	39.0	36.5	**TS1GA**	44.2	41.6
TS2	-0.8	-8.2	**TS2**	2.6	-6.1
TS3	16.0	11.1	**TS2GA**	8.9	20.6
TS4	45.1	43.4	**TS3**	30.4	28.6
TS6	4.3	2.2	**TS4**	20.5	15.5
TSAA2	-14.1	-24.3	**TSAA1**	-72.9	-58.0
TSFA2	-36.3	-31.1	**TSAA2**	-9.6	-19.8
TSFA1	-89.5	-87.3	**TSFA2**	-31.7	-26.7
TSAA1	-77.4	-76.4	**TSFA1**	-84.9	-82.9
TSGA	11.6	13.6	**TSGA**	28.5	31.1
P1	26.2	30.4	**P1**	15.6	19.0
P2	-23.1	-19.0	**P2**	-18.5	-11.7
P3	-23.6	-15.1	**P3**	-19.1	-10.7
P4	-50.6	-45.2	**P4**	-46.0	-40.8
P5	-136.9	-128.3	**P5**	-132.3	-123.9
P6	-153.3	-148.6	**P6**	-148.8	-144.2
P7	-48.0	-44.2	**P7**	-43.4	-39.8

Table C.1: Anharmonic Zero-point Corrected Energies (in kJ mol^{-1}) Relative to the Dissociation Limit for All the Species Involved in the *anti*-Vy + OH and *syn*-Vy + OH Abstraction Reactions Computed Using the Two Different Levels of Theory Discussed in Section 5.2.

Abstraction reactions

***anti*-VyA + OH**			***syn*-VyA + OH**		
Species	**rDSD**	**junChS-F12**	**Species**	**rDSD**	**junChS-F12**
***anti*-Vy+OH**	0.0	0.0	***syn*-Vy+OH**	0.0	0.0
PrC1	-18.9	-19.2	**PrC1**	-13.8	-13.9
PrC2	-11.0	-12.7	**PrC2**	-13.9	-14.1
PrC4	-15.3	-14.9	**PrC4**	-19.9	-13.1
TS1	28.0	22.8	**TS1**	16.9	12.1
TS2	30.2	27.0	**TS2**	30.3	26.6
TS3	17.2	11.3	**TS3**	29.2	24.5
TS4	15.8	1.1	**TS4**	27.0	1.7
P1	-12.2	-18.0	**P1**	-17.7	-23.2
P2	-10.3	-15.3	**P2**	-67.1	-72.6
P3	-39.7	-44.1	**P3**	-35.1	-39.7
P4	-140.9	-142.4	**P4**	-136.3	-137.9

Table C.2: Anharmonic Zero-point Corrected Energies (in kJ mol^{-1}) Relative to the Dissociation Limit for All the Species Involved in the *syn*-VyA + OH and *anti*-VyA + OH Abstraction Reactions Computed Using the Two Different Levels of Theory Discussed in Section 5.2.

Appendix D

Supporting Data for Chapter 6

Addition reactions

***anti*-VyA + CN**			***syn*-VyA + CN**		
Species	**rDSD**	**junChS-F12**	**Species**	**rDSD**	**junChS-F12**
A+B	0.0	0.0	**A+B**	0.0	0.0
Int1	-247.9	-230.3	**Int1**	-242.9	-225.9
Int1b	-122.7	-115.1	**Int1b**	-117.7	-109.6
Int2	-214.7	-197.9	**Int2**	-209.7	-192.6
Int3	-249.3	-234.7	**Int3**	-246.4	-231.3
Int4	-289.1	-273.2	**Int4**	-284.1	-267.9
Int5	-183.2	-175.1	**Int5**	-187.1	-169.8
TS1	-123.2	-114.1	**TS1**	-112.7	-101.8
TS1b	-109.5.1	-99.6	**TS1b**	-104.1	-94.4
TS3	-81.3	-66.2	**TS3**	-77.1	-60.9
TS3b	-97.6	-92.4	**TS3b**	-92.0	-87.1
TS4	-91.4	-77.2	**TS4**	-87.2	-73.1
TS5	-88.8	-76.9	**TS5**	-84.5	-71.1
TS8	-89.3	-73.4	**TS8**	-85.5	-68.1
TS10	-77.4	-63.8	**TS10**	-73.3	-58.5
TS12	-69.3	-52.9	**TS12**	-63.2	-47.6
TS13	-100.2	-81.4	**TS13**	-96.3	-76.1
TS14	-101.6	-82.6	**TS14**	-96.4	-77.4
TS15	-126.4	-106.9	**TS15**	-121.3	-101.6
TS16	-72.1	-51.9	**TS16**	-56.4	-46.6
P1	-121.8	-98.6	**P1**	-116.7	-94.3
P2	-105.8	-85.1	**P2**	-100.4	-79.8
P3	-138.4	-114.9	**P3**	-134.6	-109.6
P4	-145.3	-119.5	**P4**	-140.1	-114.2
P5	-138.5	-116.0	**P5**	-131.6	-110.7
P6	-118.1	-101.5	**P6**	-112.0	-96.2
P7a	-131.5	-109.4	**P7a**	-125.9	-104.1

Table D.1: Anharmonic Zero-point Corrected Energies (in kJ mol^{-1}) Relative to the Dissociation Limit for All the Species Involved in the *syn*-VyA + CN and *anti*-VyA + CN Addition Reactions Computed Using the Two Different Levels of Theory Discussed in Section 6.2. The RMS deviation of rDSD results from their junChS-F12 counterparts for *anti* and *syn* are 17.1 and 17.2 kJ mol^{-1}, respectively.

Abstraction reactions

anti-VyA + CN			*syn*-VyA + CN		
Species	**rDSD**	**junChS-F12**	**Species**	**rDSD**	**junChS-F12**
A+B	0.0	0.0	**A+B**	0.0	0.0
Int1	-247.9	-230.3	**Int1**	-242.9	-225.9
TS1	-42.4	-23.2	**TS1**	-64.7	-44.2
TS2	-6.3	10.6	**TS2**	5.0	21.0
TS3	-6.5	6.9	**TS3**	-5.3	8.5
TS4	-4.9	7.7	**TS4**	-16.9	-3.2
P1	-192.2	-177.9	**P1**	-187.6	-173.1
P2	-91.0	-79.6	**P2**	-86.4	-74.8
P3	-61.6	-58.2	**P3**	-57.0	-53.4
P4	-63.5	-63.8	**P4**	-58.9	-59.0

Table D.2: Anharmonic Zero-point Corrected Energies (in kJ mol^{-1}) Relative to the Dissociation Limit for All the Species Involved in the *syn*-VyA + CN and *anti*-VyA + CN Abstraction Reactions Computed Using the Two Different Levels of Theory Discussed in Section 6.2. The RMS deviation of rDSD results from their junChS-F12 counterparts for *syn*-VyA + CN and *anti*-VyA + CN is 3.1 and 3.2 kJ mol^{-1}, respectively.

Scan of Barrierless Reaction

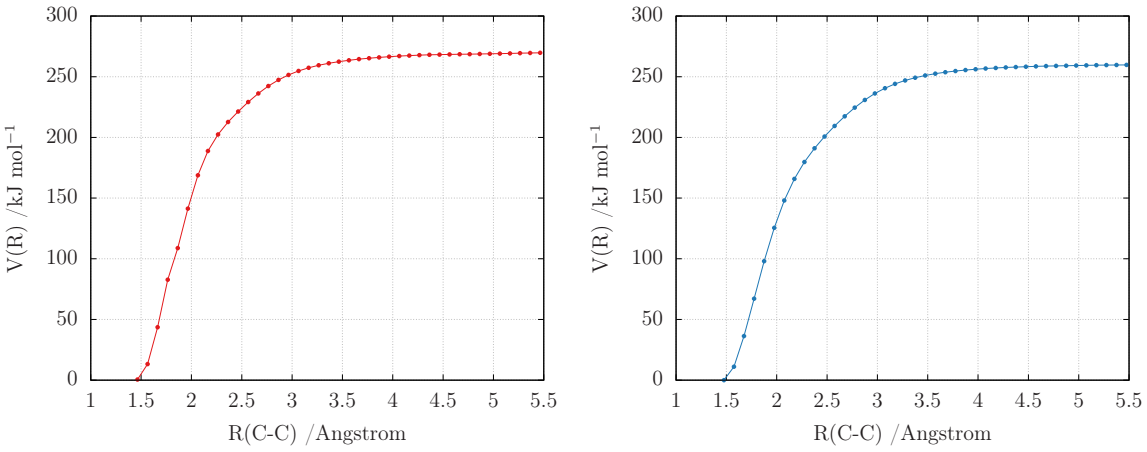

Figure D.1: One-dimensional potential energy "curves" as a function of C−C bond formation (Å) for the reactions *anti*-VyA + CN ⟶ Int1 in red and *syn*-VyA + CN ⟶ Int1 in blue computed at the level rev-DSDPBEP86-GD3(BJ)/jun-cc-pVTZ.

NTS Parameters

	$\varepsilon^{\ddagger}$/**kJmol**$^{-1}$	**T**$_0$/**K**	**rms**[a]
P2A	2158.36	12.78	5.04×10^{-4}
P3A	309.52	8.52	1.78×10^{-2}
P4A	240.15	7.97	2.22×10^{-3}

[a] rms stands for root-mean-square deviation of the fit.

Table D.3: The NTS parameters for the *syn*-VyA + CN abstraction reaction.

	$\varepsilon^{\ddagger}$/**kJmol**$^{-1}$	**T**$_0$/**K**	**rms**[a]
P2A	1515.76	10.89	3.87×10^{-4}
P3A	326.34	8.66	1.66×10^{-3}
P4A	303.42	8.89	2.17×10^{-3}

[a] rms stands for root-mean-square deviation of the fit.

Table D.4: The NTS parameters for the *anti*-VyA + CN abstraction reaction.

Arrhenius-Kooij Parameters

	A/**cm**^{3}**molecule**$^{-1}$**s**$^{-1}$	**n**	**E**/**kJmol**$^{-1}$	**rms**[a]
P1	6.68×10^{-11}	0.37	-114.69	1.09×10^{-12}
P2	1.67×10^{-13}	1.02	-484.24	1.08×10^{-14}
P3	2.12×10^{-10}	0.19	-3.46	5.32×10^{-13}
P4	2.54×10^{-13}	0.39	-139.00	6.44×10^{-15}
P5	3.56×10^{-12}	0.57	-214.95	8.98×10^{-14}
P6	1.14×10^{-10}	-0.17	187.72	3.79×10^{-12}
P7	3.03×10^{-11}	0.59	-236.25	1.02×10^{-12}
P1A	5.45×10^{-13}	0.72	-370.04	1.81×10^{-14}

[a] rms stands for root-mean-square deviation of the fit.

Table D.5: The Arrhenius-Kooij parameters for the *syn*-VyA + CN addition reaction.

	$A/cm^3molecule^{-1}s^{-1}$	n	$E/kJmol^{-1}$	rms[a]
P1	2.08×10^{-12}	0.05	69.23	2.39×10^{-14}
P2	1.26×10^{-14}	0.38	-103.58	1.39×10^{-16}
P3	4.19×10^{10}	0.18	-4.28	3.64×10^{-13}
P4	1.77×10^{14}	0.02	70.05	1.60×10^{-16}
P5	2.40×10^{-13}	0.07	65.10	3.62×10^{-15}
P6	6.21×10^{-12}	-0.47	327.34	3.61×10^{-13}
P7	3.69×10^{-13}	0.18	-3.10	4.17×10^{-16}
P1A	6.63×10^{-17}	0.59	-224.19	1.80×10^{-16}

[a] rms stands for root-mean-square deviation of the fit.

Table D.6: The Arrhenius-Kooij parameters for the *anti*-VyA + CN addition reaction.

$\gamma(\beta)$ vs NTS fitting plots

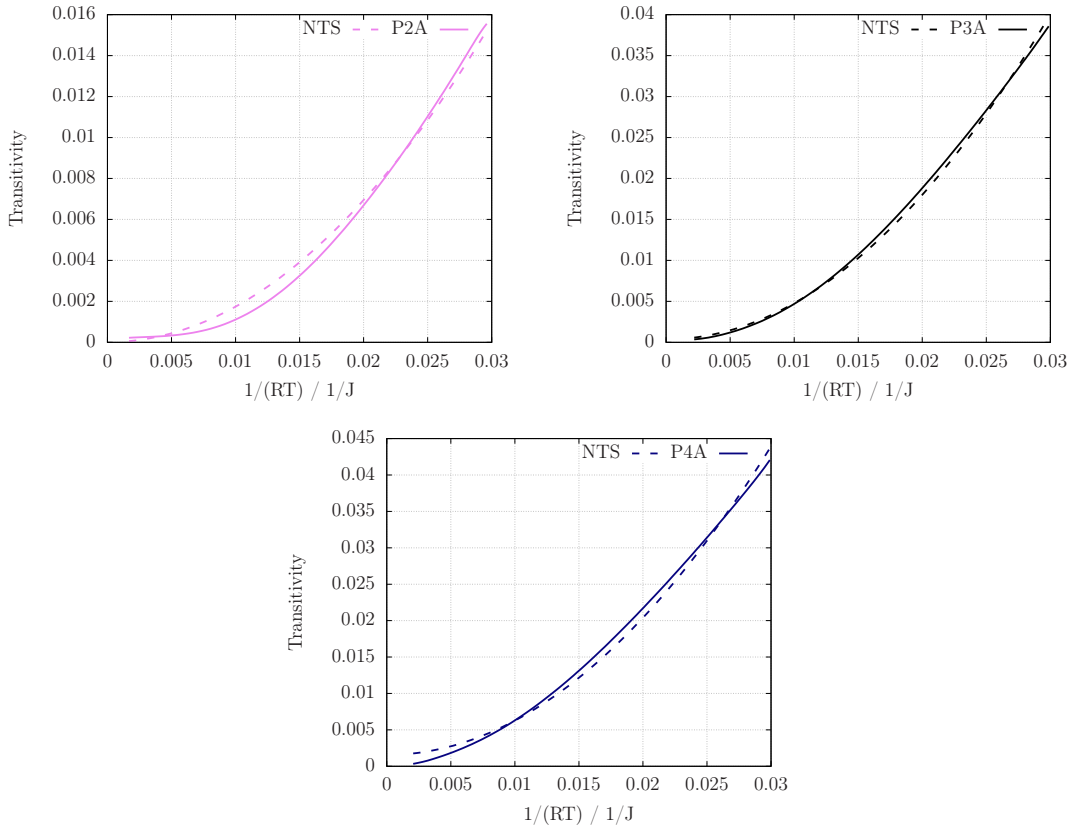

Figure D.2: Comparison between NTS fitting function and transitivity data obtained from the kinetic simulations for the abstraction reactions between *anti*-VyA + CN.

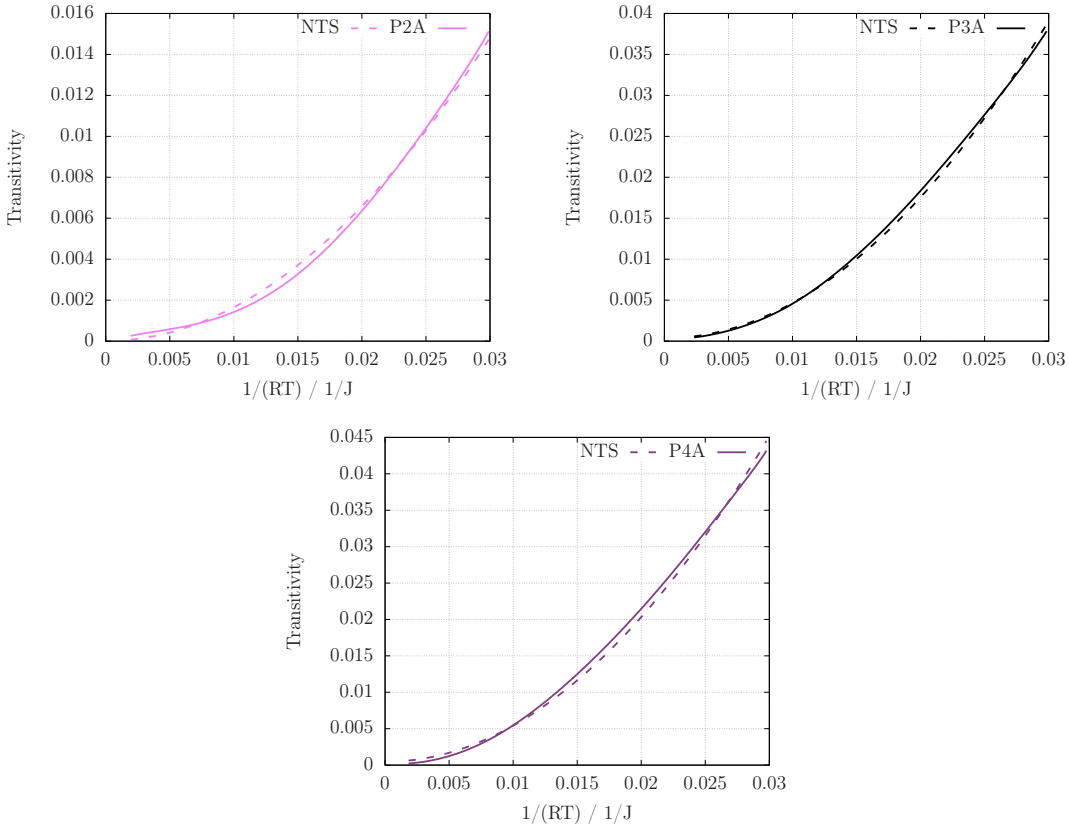

Figure D.3: Comparison between NTS fitting function and transitivity data obtained from the kinetic simulations for the abstraction reactions between *syn*-VyA + CN.